Towards the Next Generation of Location-Aware Communications

Zohair M. Abu-Shaban

M.Sc. (Imperial College London), D.I.C., B.Eng.

April, 2018

A thesis submitted for the degree of
Doctor of Philosophy
of The Australian National University

Research School of Engineering
College of Engineering and Computer Science
The Australian National University

Dedicated to my loving wife, Rola
and
our dear children, Mustafa and Elsy.

Declaration

The content of this thesis is the result of original research and have not been submitted for a higher degree to any other university or institution. Much of this work has either been published or submitted for publications as journal papers and conference proceedings. Following is a list of these papers.

Journal Publications

- **Z. Abu-Shaban**, X. Zhou, T. Abhayapala, "A Novel TOA-based Mobile Localization Technique under Mixed LOS/NLOS Conditions for Cellular Networks," *IEEE Transactions on Vehicular Technology*, vol. 65, no. 11, pp. 8841-8853, Nov 2016.

- **Z. Abu-Shaban**, X. Zhou, T. Abhayapala, G. Seco-Granados, H. Wymeersch, "Error Bounds for Uplink and Downlink 3D Localization in 5G mmWave Systems," Accepted in *IEEE Transactions on Wireless Communication*, April 2018.

- **Z. Abu-Shaban**, H. Wymeersch, T. Abhayapala, G. Seco-Granados, "Single-Anchor Two-Way Localization Bounds for 5G mmWave Systems: Two Protocols," to be submitted to *IEEE Transactions on Wireless Communication*, May 2018.

Conference Proceedings

- **Z. Abu-Shaban**,H. Wymeersch, X. Zhou, G. Seco-Granados, T. Abhayapala "Random-Phase Beamforming for Initial Access in the Millimeter-Wave Cellular Networks" in the proceedings of *2016 IEEE Global Communications Conf. (GLOBECOM)*, Washington, DC, pp. 1-6, Dec 2016.

- **Z. Abu-Shaban**, X. Zhou, T. Abhayapala, G. Seco-Granados, H. Wymeersch "Location and Orientation Estimation Performance with Uplink and Downlink 5G mmWave Multipath Signals" in the proceedings of *IEEE Wireless Communications and Networking Conf. (WCNC)*, Barcelona, Spain, April 2018.

- **Z. Abu-Shaban**, H. Wymeersch, T. Abhayapala, G. Seco-Granados, "Single-Anchor Two-Way Localization Bounds for 5G mmWave Systems," to be submitted to *2018 IEEE Global Communications Conf. (GLOBECOM Workshops)*, Abu Dhabi, UAE, Dec 2018.

The following papers are also results of my Ph.D. study, but not included in this thesis:

Journal Publications

- R. Mendrzik, , H. Wymeersch, G. Bauch, **Z. Abu-Shaban**, "Harnessing NLOS Components for Position and Orientation Estimation in 5G mmWave MIMO," Second round of review after major revisions at *IEEE Transactions on Wireless Communication*, Nov 2017.

Conference Proceedings

- T. Abhayapala, H. Chen, **Z. Abu-Shaban**, "Three Dimensional Beamforming for 5G Networks Using Planar (2D) Antenna Arrays," To be submitted *European Signal Processing Conference (EUSIPCO)*, Feb 2018.

The research work presented in this thesis has been performed jointly with Prof. Thushara D. Abhayapala (ANU), Dr. Xiangyun Zhou (ANU), Prof. Henk Wymeersch (Chalmers, Sweden), and Prof. Gonzalo Seco-Granados (UAB, Spain). At least, 75% of this work is my own.

Zohair Abu-Shaban
Research School of Engineering
The Australian National University
Canberra ACT 2601
April, 2018

Acknowledgments

First and foremost, all praise belongs to God, who has always been there to give me guidance, patience and endurance to keep going. Furthermore, this work would not have been possible, without the support of many people, and for that I would like to express my gratitude, and acknowledge each and every one of them:

- My supervisor Prof. Thushara Abhayapala for his solid support for me during my PhD, starting from the application process, arranging a top-up scholarship, to finally writing my thesis. I appreciate him giving me confidence and freedom to be an independent researcher eventually. Moreover, I enjoyed learning from his wisdom during our informal tea chats.

- My co-supervisor, Dr. Sean Zhou, for his thought-provoking opinions and constructive criticism that gave me other angles to look into my work.

- My research collaborator, Prof. Henk Wymeersch, of Chalmers University of Technology, Sweden, for providing timely and eye-opining feedback on my work, helping me penetrate a research field that is still in its infancy, and providing me with a stimulating research environment during my visit to his group.

- My research collaborator, Prof. Gonzalo Seco-Granados, of the Universitat Autónoma de Barcelona, Spain, for his research collaboration, which was instrumental to my work, for his friendly and welcoming attitude when I visited his research group, and for providing accommodation for me and my family during that visit.

- The Australian National University (ANU), and the Australian Government's

Research Training Program (RTP) for granting me generous scholarships to help me realize my dream of pursuing a PhD.

- The Vice-Chancellor of ANU, and the Dean of the ANU's College of Engineering and Computer Science, for partially sponsoring me with a 4-month travel grant to pursue overseas research visits that were a crucial stage during my PhD.

- My colleagues and fellow PhD students in CECS, for being a source of inspiration, and advice whenever I needed them.

- My strong and unique parents, Mustafa and Sawsan, for their endless and unconditioned love and support, for having high expectations of me and pushing me to excel in every task I do. I cannot thank them enough for that.

- Last but not least, the love of my life, Rola and our two children, Mustafa and Elsy. Having been surrounded by their love, encouragement, patience, and understanding, they never failed to turbo-charge me to do my best. For that, I consider them to be the "angel" co-authors of this thesis.

Abstract

This thesis is motivated by the expected implementation of the next generation mobile networks (5G) from 2020, which is being designed with a radical paradigm shift towards millimeter-wave technology (mmWave). Operating in 30–300 GHz frequency band (1–10 mm wavelengths), massive antenna arrays that provide a high angular resolution, while being packed on a small area will be used. Moreover, since the abundant mmWave spectrum is barely occupied, large bandwidth allocation is possible and will enable low-error time estimation. With this high spatiotemporal resolution, mmWave technology readily lends itself to extremely accurate localization that can be harnessed in the network design and optimization, as well as utilized in many modern applications. Localization in 5G is still in early stages, and very little is known about its performance and feasibility.

In this thesis, we contribute to the understanding of 5G mmWave localization by focusing on challenges pertaining to this emerging technology. Towards that, we start by considering a conventional cellular system and propose a positioning method under outdoor LOS/NLOS conditions that, although approaches the Cramér-Rao lower bound (CRLB), provides accuracy in the order of meters. This shows that conventional systems have limited range of location-aware applications. Next, we focus on mmWave localization in three stages. Firstly, we tackle the initial access (IA) problem, whereby user equipment (UE) attempts to establish a link with a base station (BS). The challenge in this problem stems from the high directivity of mmWave. We investigate two beamforming schemes: directional and random. Subsequently, we address 3D localization beyond IA phase. Devices nowadays have higher computational capabilities and may perform localization in the downlink. However, beamforming on the UE side is sensitive to the device orientation. Thus, we study localization in both the uplink and downlink under

multipath propagation and derive the position (PEB) and orientation error bounds (OEB). We also investigate the impact of the number of antennas and the number of beams on these bounds. Finally, the above components assume that the system is synchronized. However, synchronization in communication systems is not usually tight enough for localization. Therefore, we study two-way localization as a means to alleviate the synchronization requirement and investigate two protocols: distributed (DLP) and centralized (CLP).

Our results show that random-phase beamforming is more appropriate IA approach in the studied scenarios. We also observe that the uplink and downlink are not equivalent, in that the error bounds scale differently with the number of antennas, and that uplink localization is sensitive to the UE orientation, while downlink is not. Furthermore, we find that NLOS paths generally boost localization. The investigation of the two-way protocols shows that CLP outperforms DLP by a significant margin. We also observe that mmWave localization is mainly limited by angular rather than temporal estimation.

In conclusion, we show that mmWave systems are capable of localizing a UE with sub-meter position error, and sub-degree orientation error, which asserts that mmWave will play a central role in communication network optimization and unlock opportunities that were not available in the previous generation.

List of Acronyms

BS	Base Station
CDF	Cumulative Distribution Function
CLP	Centralized Localization Protocol
CRLB	Cramér-Rao lower bound
DBF	Directional Beamforming
DLP	Distributed Localization Protocol
DOA	Direction-of-Arrival
DOD	Direction-of-Departure
(E)FIM	(Equivalent) Fisher Information Matrix
IA	Initial Access
mmWave	Millimeter-wave Technology
MSE	Mean Square Error
(N)LOS	(None-)line-of-sight
OEB	Orientation Error Bound
PDF	Probability Density Function
PEB	Position Error Bound
PSD	Power Spectral Density
RMSE	Root Mean Square Error
RPBF	Random-Phase Beamforming
RSS	Received Signal Strength
SNR	Signal-to-Noise Ratio
TDOA	Time-Difference-of-Arrival
TOA	Time-of-Arrival
UE	User Equipment
ULA	Uniform Linear Array
URA	Uniform Rectangular Array

Notations and Symbols

j	$\sqrt{-1}$
a	Scalar
$\mathbf{a}$	Column vector
$\mathbf{A}$	Matrix
$[\mathbf{A}]_{m,n}$	Element in the mth row and nth column of $\mathbf{A}$
$(\cdot)^{\mathrm{T}}$	Vector and matrix transpose operator
$(\cdot)^{\mathrm{H}}$	Vector and matrix complex conjugate transpose operator
$\det(\mathbf{A})$	Determinant of a square matrix
$\mathrm{diag}(\mathbf{A})$	Diagonal of a square matrix
$\mathrm{diag}(\mathbf{a})$	Square matrix with $\mathbf{a}$ as main diagonal
$\mathrm{Tr}(\mathbf{A})$	Trace of a square matrix
$\|\cdot\|$	ℓ_2 norm of a vector
$\|\cdot\|_{\mathrm{F}}$	Frobenius norm of a matrix
$\mathbf{0}_N$	All-zeros column vector of length N
$\mathbf{0}_{N\times N}$	All-zeros matrix of size $N \times N$
$\mathbf{1}_N$	All-ones column vector of length N
$\mathbf{1}_{N\times N}$	All-ones matrix of size $N \times N$
$\mathbf{I}_N$	Identity matrix of size $N \times N$
$\mathbb{E}\{\cdot\}$	Expectation operator
$\Re\{\cdot\}$	Real part
$\Im\{\cdot\}$	Imaginary part
$\odot$	Hadamard product
$\otimes$	Kronecker product
$\mathbb{R}^N$	N-dimensional real vector space
$\mathbb{R}^{N\times M}$	$N \times M$ dimensional real matrix space
$\mathbb{C}^N$	N-dimensional complex vector space
$\mathbb{C}^{N\times M}$	$N \times M$ dimensional complex matrix space

λ	Wavelength
c	Speed of light ($= 3 \times 10^8$)
τ	Time-of-arrival
β	Complex path gain
θ	Elevation angle measure w.r.t positive z-axis
ϕ	Azimuth angle measure w.r.t positive x-axis
$\mathbf{a}_{\mathrm{R}}(\theta, \phi)$	Receiver array response vector in the direction (θ, ϕ)
$\mathbf{a}_{\mathrm{T}}(\theta, \phi)$	Transmitter array response vector in the direction (θ, ϕ)
$\mathbf{k}(\theta, \phi)$	Wavenumber vector in the direction (θ, ϕ)
$\mathbf{p}$	User equipment position.
$\mathbf{o}$	User equipment orientation.
$\mathbf{F}$	Transmit beamforming matrix.
$\mathbf{W}$	Receive beamforming matrix.
$\mathbf{s}(t)$	Transmitted signal vector.
$\mathbf{r}(t)$	Received signal vector at the antenna array.
$\mathbf{y}(t)$	Received signal vector after receive beamforming.
$\boldsymbol{\varphi}$	Vector of unknown parameters.
$\widehat{\boldsymbol{\varphi}}$	Estimator of $\boldsymbol{\varphi}$.
$\mathbf{J}_{\boldsymbol{\varphi}}$	Fisher Information Matrix of $\boldsymbol{\varphi}$.
$\mathbf{J}^{\mathrm{e}}_{\boldsymbol{\varphi}}$	Equivalent Fisher Information Matrix of $\boldsymbol{\varphi}$.
$\boldsymbol{\Upsilon}$	Parameter transformation matrix.
B	Clock bias of the clock of D_2 w.r.t the clock of D_1.
W	System bandwidth
W_{eff}	Effective bandwidth
E_{t}	Transmitted energy per symbol.
T_{s}	Symbol duration.
N_0	Noise power spectral density.
N_{R}	Number of antennas at the receiver.
N_{T}	Number of antennas at the transmitter.
N_{B}	Number of transmitted beams.
N_{s}	Number of pilot symbols or measurements.
$f_X(x)$	Probability density function of a random variable x.

Contents

List of Figures

List of Tables

Chapter 1

Introduction

1.1 Evolution of Localization

"Where are you?" is probably one of the questions most asked on a daily basis. Since the beginning of history, humans sought knowledge of their locations for different reasons. Using notable landscapes, like mountains, hills and shores, they were able to know their position on land. Later, with the aid of instruments such as astrolabes [2], kamals [3], and sextants [4], they observed astronomical objects, e.g., the stars and the sun, in order to infer location information, which helped them navigate the high seas, survive the vast deserts, and explore the world. The broad concept applied back then was to take some measurements and observations relative to some *anchors*, whose positions were known, and then use these measurements to somehow coarsely determines one's location.

With tremendous human efforts, although continued to use the same concept of relative measurements, today's localization[1] methods use extremely more complex tools to take these measurements, need minimal usage efforts, and are greatly more accurate. Since the discovery of electromagnetic waves and the subsequent radio technology, localization using radio signals replaced the older methods. The first attempt known to employ radio signals in localization dates back to 1906 when The Stone Radio and Telegraph Company installed a direction-finding nav-

[1]Localization is studied in many disciplines differently. For example, it can be used in audio or underwater applications. However, in this thesis, localization, radio localization, positioning and geolocation are used interchangeably to refer to localization using wireless signals.

igation prototype on an American naval ship [5]. Subsequently, with the advent of satellites later in the 20th century, the first satellite navigation system, Transit, was made operational by the USA in 1962, and provided an accuracy of about 25 meter [6]. Later on by 1985, the USA fully put in orbit the Global Positioning System (GPS) we know nowadays [7]. More recently, the Russian GLONASS, and the European Galileo, and several other national systems followed [7]. Although the above systems were mainly motivated by military use initially, location determination eventually found its way to civilian applications, particularly after the adoption of mobile communication networks for civilian purposes.

For the last few decades, localization has been used in an abundance of indoor and outdoor applications, including

- *Emergency intervention:* Twenty years ago, the US started using mobile localization to determine the location from which an emergency call is made. This would provide the emergency department with more precise information to act more rapidly [8, 9].

- *Civilian navigation:* GPS was made available for civilian use, and became very popular for route guidance in aviation, maritime and land travel [7].

- *People localization:* This includes geofencing applications such as locating lost children in parks, zoos, or theme parks, or vulnerable individuals leaving a predefined area [10–12]. It also includes locating prisoners trying to escape [13].

- *Asset management:* Localization has been useful in managing and storing goods in warehouses [14–16]. Moreover, using radio frequency tags, a store can locate unpaid items when a customer departs [17].

- *Workforce management:* Tracking firemen during a mission [18], knowing the location of workers in a warehouse, or patients and staff at hospitals [19] are all applications of radio localization.

- *Other location-based services:* Location-based marketing especially in social networks [20, 21], and location-based billing [22].

For cellular networks, location services were supported in 2G and 3G through radio resource control, radio resource location services protocol, and IS-801 standard to meet the requirements of emergency services and commercial applications [23]. Later in the 4G, long-term evolution (LTE) standards define three positioning techniques [23–25], namely, assisted GNSS that integrates satellite systems with terrestrial cellular networks, observed time-difference-of-arrival (TDOA) that requires cooperation amongst multiple anchors using the so-called Positioning Reference Signals, and the enhanced cell ID that combines angular and temporal information using the uplink signals. These three techniques together compose the LTE Positioning Protocol, which is implemented to enable positioning over LTE.

With active research being done on 5G millimeter-wave (mmWave) mobile *communication*, and the expected launch of 5G in 2020, 5G *localization* is receiving a growing attention [26–28] due to the unique features 5G mmWave technology enjoys. With the possible extremely large bandwidth allocation and the utilization of array of large number of antennas at both the BS and UE, mmWave 5G is expected to facilitate high-accuracy localization, which not only paves the way to a wide range of applications that were not possible in previous generations [29–32], but will also enable an optimized network design and performance due to the possible integration of location information in the network paradigm [26, 33–35].

1.2 Classification of Localization Systems

A localization system is an estimator that determines the location of an agent using one or more anchors. In this context, the *agent* is the device with unknown position. For example, it can be a mobile station in cellular networks, a laptop in WiFi localization, or a sensing node in wireless sensor networks. A generic term often used to refer to an agent is *user equipment* (UE). On the other hand, an *anchor* is an active device that has a known location, and attempts to estimate the location of a UE. An anchor can be a base station (BS) in cellular networks, an access point in WiFi localization, or a reference node in wireless sensor networks. We can broadly view localization from nine angles summarized below [36–39]:

1. **Infrastructure:** Localization can be implemented on different platforms,

depending on the application.

- *Satellite positioning* is more suitable for aviation and maritime navigation systems.
- *Cellular networks* are more suitable for responding to emergency calls, location-aware billing services, and communication systems optimization.
- *WiFi localization* was initially more suited for indoor localization applications in warehouses, hospitals, and office spaces, where WiFi infrastructure is already installed. However, with the spread of WiFi access points in outdoor, and the growing application of Internet-of-Things (IoT), WiFi has also been used in outdoor localization [40].
- *Wireless sensor networks* (WSN) are a considerably active area of localization, particularly for monitoring the environment, industrial plants, and traffic systems.
- *Proximity devices*, such as radio frequency identification tags (RFID) and Bluetooth devices, have been used to implement indoor localization and provided an accuracy of 1 meter.

2. **Localization Technique:**

- *Fingerprinting:* The basic idea of fingerprinting is to build a database containing location-based features (e.g., received power) for some area of interest, in a process called calibration. Subsequently, the location of a user can be determined by pattern recognition methods that match the user features with the best database entry. This method is widely used in indoor WiFi localization, although it suffers from some shortcomings, including the overhead time-consuming calibration process. It is also sensitive to environment changes such as moving people and layout alternation, in which case calibration needs to be done regularly.
- *Proximity Detection* is the simplest localization technique in which the anchor (e.g., BS) makes a boolean decision based on the received signal strength (RSS) to determine whether the user is within a predefined

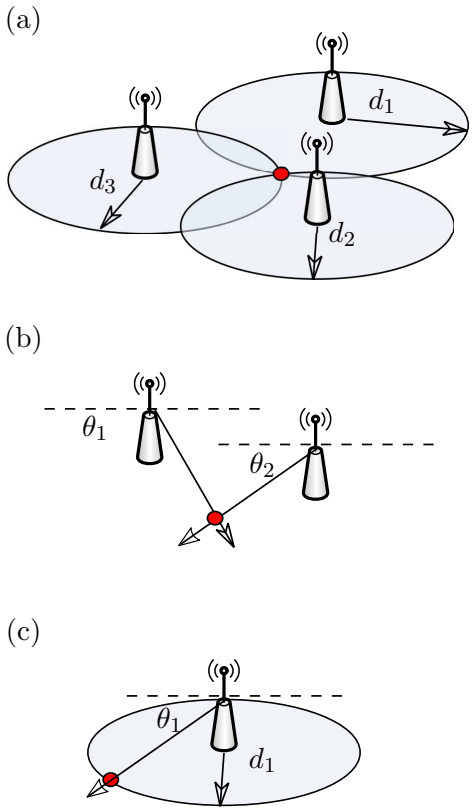

Figure 1.1: (a) Multilateration localization with TOA ranging in 2D, (b) Multiangulation localization with DOA in 2D, (b) Hybrid localization wth angle and range measurements. The red dot represents the UE location.

range. Proximity detection is widely used in mobile networks, e.g., for handover and other resources allocation procedures. It is also used in shoplifting prevention using RFID tags, and in vehicles proximity keys.

- *Multilateration* requires multiple anchors depending of the dimension of localization 2-dimensional (2D) or 3-dimensional (3D). Each of these anchors estimates its range from the UE, and uses this estimate to determine the locus of the UE with respect to this anchor. The UE location is then determined at a processing center as, ideally, the intersection of the loci provided by the participating anchors. Measurements can be obtained using time-of arrival (TOA), time-difference-of-arrival (TDOA),

RSS, or round-trip time (RTT). One popular application of this method is the GPS, in which a receiver should be in the vicinity of at least 4 satellites, and determines its location as the intersection created by 4 corresponding spheres. In mobile communication networks, where 2D position is to be estimated, three BSs participate to collectively localize a UE. As shown in Figure 1.1.a, each BS estimates the range of the UE and defines a circle, whose radius is equal to the estimated range. The UE position is then taken as the intersection point of the three circles. The accuracy of this approach is subject to the accuracy of the range estimation. One promising field of application using TOA is in ultra wideband (UWB) systems, where the massive bandwidth provides cm-level accuracy [36].

- *Multiangulation* requires two or more anchors to cooperate and localize a UE. Equipped with an antenna array, each anchor estimates the direction-of-arrival (DOA) with respect to its own array, by measuring the phase difference of signals arriving at different antennas of the array. DOA is then used to define a straight line, as shown in Figure 1.1.b. The UE location is then taken as the intersection point of the lines defined by different DOAs.
- *Hybrid Localization* combines range and angular measurements. As in multilateration, a range estimate is obtained through TOA, TDOA, RTT or RSS measurements, and used to define a circle as shown in Figure 1.1.c. Moreover, an angle estimate is obtained at the same anchor. The UE position is then taken as the intersection of the line and the circle defined by these estimates. Note that this approach inherently requires an anchor with an antenna array.

3. **User Equipment Participation:** Localization can be either active, when the UE participates in the localization process, or passive when it does not. Active localization, depending on where the UE location is estimated, can be either uplink localization when the anchor estimates the UE location, or downlink localization if the location is estimated at the UE itself. On the other hand, localization is passive when it is done without exchanging

messages. Also known as device-free localization, passive localization usually applied to estimating the location of obstacles such as scatterers, from which an environment map can then be created.

4. **Processing Location:** When more than one anchor are involved, localization systems can be classified based on the premises where the estimation process takes place, as centralized of distributed (cooperative). Centralized systems are those which collect measurements at different anchors and then the whole location estimation process takes place at a dedicated processing center. This is the traditional approach applied in cellular networks. On the contrary, in distributed localization, each anchor participates in the localization process by exchanging useful information with neighboring anchors till the unknown location is determined. This approach is widely used in WSNs.

5. **User Environment:** This environment can be either indoor or outdoor. Each of these two environments has its own requirements in terms of accuracy, algorithm complexity, and suitable infrastructure.

6. **Number of Anchors:** Depending on the technique used, a localization system can comprise a single or multiple anchors. Single-anchor localization systems can use fingerprinting, proximity or hybrid techniques. On the other hand, by definition, multilateration and multiangulation are built with multiple anchors.

7. **Number of Users:** A localization system can be a single-user or multiuser.

8. **User Movement:** A localization system can serve a stationary, or a moving user. In the latter case, the localization process is referred to as *tracking*.

9. **Antenna Configuration:** Single antenna localization is useful when angle measurements are not involved, in which case an antenna array is required.

The classification of the localization systems is summarized in Figure 1.2.

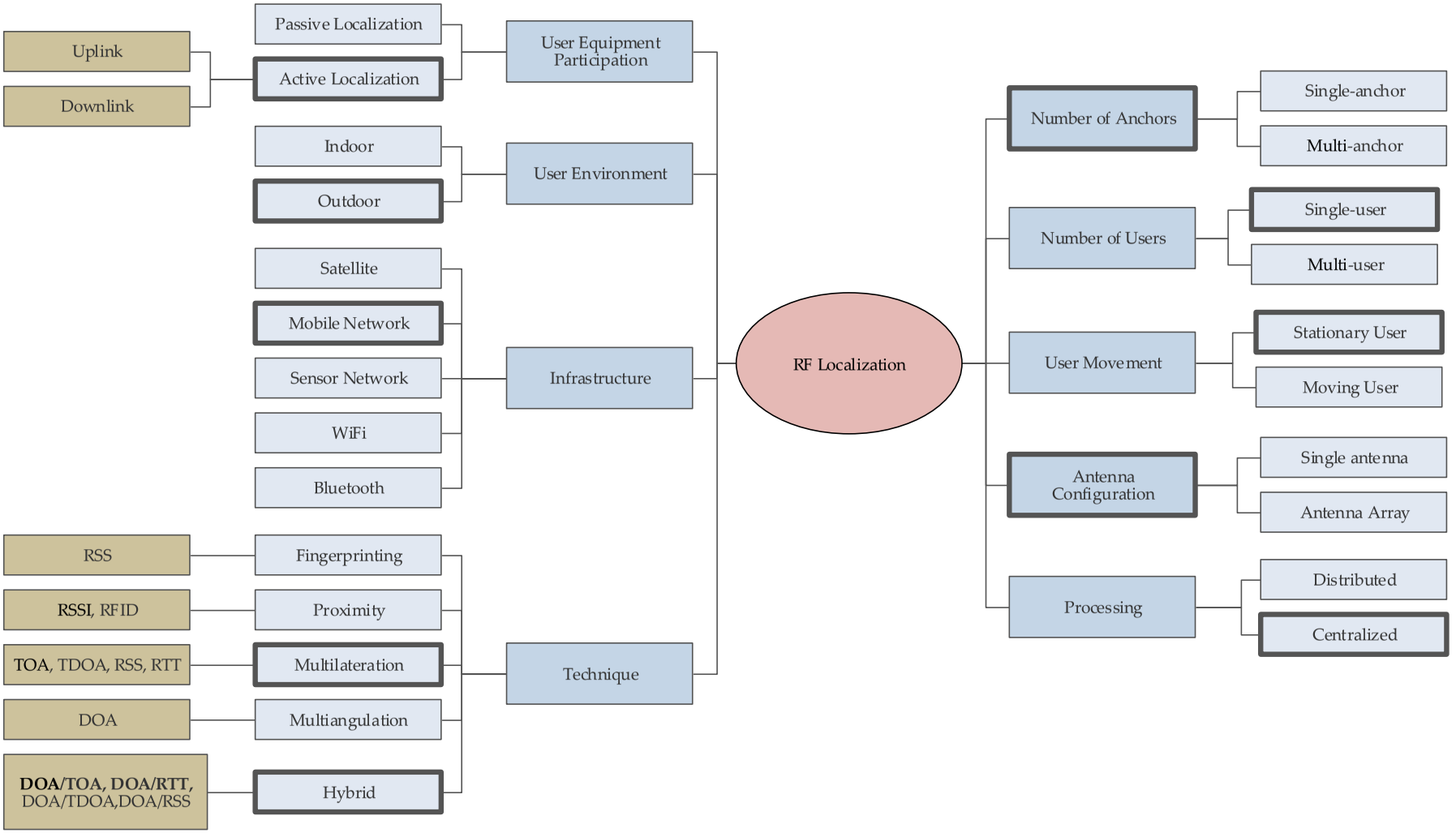

Figure 1.2: Spidergram summarizing the different classifications of localization. The boxes with thicker borders are the ones considered in this thesis.

1.3 Challenges Facing Localization Systems

From our discussion so far, it can be seen that localization is highly dependent on accurate channel and transceiver models in order to take accurate measurement of time, phase, power level, or a combination of them. However, sometimes these models are not sufficiently accurate, which may deteriorate the expected performance if the underlying impairments are not properly addressed. In this section, we discuss the main challenges a localization system may face.

One of the main challenges in this context is the presence of none-line-of-sight (NLOS) paths between the transmitter and receiver [41, 42]. In many of the localization methods, measurement of TOA, DOA or RSS of the line-of-sight (LOS) are needed to establish the location of the UE. However, in a multipath environment, the measurements may not be related to the LOS. Moreover, NLOS signals travel longer distances than LOS, which introduces a positive range bias on the measurements. Therefore, the presence of NLOS paths can cause significant performance deterioration or even the collapse of the localization process, and thus must be remedied to preserve the robustness. One way to deal with this issue is the "identify and mitigate", in which a path is identified statistically to be either LOS or NLOS, before incorporating this information in the localization process [43–47]. On the other hand, the "identify and discard" approach cleans the signal by retaining the information of the LOS path only [42, 48, 49]. Moreover, convex optimization tools have also been used to estimate the UE location in the presence of NLOS paths, without the need to identify the link status [1, 50–55].

Another challenge that usually faces localization is the tight synchronization requirement between the anchors and the UE. TOA measurements, and the resulting range measurements, are only useful if the time at which the signal departed the transmitter is known. Therefore, the clocks of the receiver and the transmitter should be synchronized to guarantees a sample-rate at the receiver similar to that at the transmitter, with no excess time offset [36, 56, 57]. Similarly, DOA measurements are based on measurements of the signal phase of arrival [58], which means that timing and carrier frequency offsets should be synchronized in that case. Although communication systems are synchronized in most cases, the level of synchronization is not usually high enough to suit localization. This being said, there

are applications that do not require time synchronization, such as those involving RSS and TDOA[2] [36].

Systems relying on DOA estimation must be equipped with antenna arrays. For reliable positioning using DOA, the array must have antennas with known electric characteristics such as gain and phase. The antenna locations and inter-antenna spacing should also be known. However, in reality the antenna electric characteristics may vary over time, and it is hard to guarantee the array element locations exactly as the design values. Therefore, for robust localization performance using antenna array, a process called *array calibration* is sometimes necessary [59]. Compensating for the gain, phase or antenna elements location errors, array calibration is achieved using pilots of known nature transmitted from known locations [59, 60].

In many localization applications, the UE to be localized is assumed to be stationary. However, applications based on this assumption, may not work if the user is moving in a car or a train for example. Relative motion of the receiver with respect to the transmitter is known to introduce the Doppler effect which affects the synchronization and consequently the localization accuracy [39]. To overcome this issue, systems with potentially moving users observe signals over a very short period of time, or use tracking methods, such as Kalman filter, to obtain and predict the location of the UE [29] [38].

Finally, localization algorithms, especially those involving antenna arrays and 3D localization, can be very demanding in terms of device processing resources and physical size. Thus, most algorithms are traditionally designed to be executed at the anchors that have superior computation powers, or resort to a design trade-off between performance and complexity. Nevertheless, with the smart devices having a growing processing power, more complexity is being pushed in the UE nowadays, especially in device-to-device communication paradigms [61].

1.4 5G: Localization Opportunities and Challenges

Mobile technology is one of the most successful ambient technologies. This is why, recently there has been a significant increase in the bandwidth requirement. Not

[2]In TDOA, synchronization between the UE and BSs is not required. However, the different BSs must be synchronized, which is easy to achieve [36].

only the number of users increased but also the number of devices (phone, tablets, smart watches,... etc.) per user and the data volume per device have also immensely increased. While internet access from a mobile device was initially for browsing and other low-to-medium size data usages, nowadays with the ubiquity of social networks and video-on-demand services, users expect to be able to stream network-demanding contents such as ultra high-definition movies, and video calls with high quality. Advanced techniques to optimize the latest mobile communication have almost been depleted, whether using orthogonal frequency-division multiplexing (OFDM), multiple-input multiple-output (MIMO), multi-user diversity, link adaptation, turbo code, or hybrid automatic repeat request (HARQ) [62]. Therefore, a move to a new generation (5G) is necessary, and would involve radical adoption of disruptive technologies including: massive MIMO and mmWave [61].

MmWave 5G systems are characterized by frequencies of 30–300 GHz. At these high frequencies, the path loss becomes more significant than in the sub-6 GHz bands [62–65]. Therefore, the use of dedicated techniques to provide sufficient gain will be necessary to counter-act the increasing path loss. By virtue of mmWave tiny wavelengths, a large number of antennas can be packed in a small area. Thus, beamforming at the transmitter and receiver will be a natural techniques to use. Moreover, mmWave channels have no diffraction, are sensitive to blockage, and enjoy a low scattering/reflective nature, causing the channel to be sparse, with the number of paths limited to just a few [64, 66]. The small number of paths and the use of beamforming mean that mmWave communication is dominated by LOS and limited NLOS communication, hence, can be considered quasi-optical [67]. Furthermore, moving to higher carrier frequencies in bands that are barely occupied, mmWave will employ a very large bandwidth supporting 1 Gbps data rate, and providing reduced latency [62].

From a localization point-of-view, the large number of antennas and the large bandwidth facilitate estimating the DOA, DOD and TOA with a high degree of accuracy, leading to the following implications:

1. UE position Estimation using a single anchor can potentially be very accurate.

2. The low-error estimate of location will unlock a wide range of location-aware applications, including vehicle-to-vehicle and vehicle-to-everything commu-

nications [30, 31], intelligent health systems [68], environment mapping [69], targeted content delivery [70], and public safety applications [32].

3. Due to the highly directive nature of mmWave channels, incorporating localization in the network design and optimization will be an indispensable feature [26]. In fact, 5G will be the first generation of mobile communication to do that [26], with many research nowadays investigating the possibilities. For example, it has been shown that location-awareness can boost the network performance if pilots are assigned based on the user location [34]. Moreover, location determination assists in more efficient beamforming schemes [33, 71]. Furthermore, spatial-devision multiple access can be better optimized when the user location is known [35].

High performance localization schemes in 5G, will not be possible without efficient beamforming techniques. However, there are mainly three challenges in 5G mmWave beamforming. Firstly, due to the high directivity of mmWave channels, beam alignment of the UE and BS in the *initial access (IA) to the network*(network discovery phase) becomes an important issue to address [64,72]. On the other hand, analog-to-digital converters are known to be highly power dissipating. Therefore, it will be infeasible to employ *all-digital beamforming*, especially with the large number of antennas. Towards that, analog beamforming, or hybrid beamforming architecture have been proposed for 5G mmWave devices [64]. Moreover, beamforming at UE is highly sensitive to the *device orientation*, since steering the device away from the BS, may point beams towards directions not useful for localization.

In addition to the challenges of a classical a localization system discussed in Section 1.3, to meet accuracy requirements, 5G localization systems need to address the high computational and processing complexity stemming from the large number of antennas and large bandwidth. Handover and location information fusion from different localization methods will also be a challenge [26]. Finally, since a UE is usually associated with one person, the abundance of location-aware communication will raise legal issues regarding privacy as it would reveal the user location, speed, and means of transport [73].

Finally, it is worth mentioning that during a late phase of writing this thesis, the first 5G standard was approved by 3GPP in December 2017. Under the New

Radio (NR) series, the 5G NR Release 15 [74] defines actual baseline physical layer components, system specifications and radio access functionalities up to 52.5 GHz. As the work on 5G localization incorporated in this thesis started in 2015, when 5G was in its infancy, reflecting this standard in the current thesis was not possible.

1.5 Thesis Scope and Overview

The next generation of mobile communication systems (5G) is expected to provide an excellent platform of a wide range applications of location-aware communication. In this context, localization can be seen as a key enabler of such systems. Therefore, it is imperative to study localization in the context of 5G mmWave systems. [3]Although localization techniques have been an actively-researched topic over the past decades, there are still many open problems which researchers have not solved or understood yet. With focus on outdoor mobile localization, this thesis contributes to the field's aggregated knowledge by providing applied and fundamental research results that address open areas of localization with more focus on 5G mmWave systems. The thesis studies NLOS localization in various outdoor environments of conventional communication systems (sub-6 GHz). Subsequently, focusing on 5G mmWave systems, which is still in its infancy, the thesis explores fundamental performance bounds of location estimation, and provides a deep understanding of the factors that together affect these bounds, and shows how this understanding can be exploited to better design 5G communication systems and localization algorithms.

The main contribution this thesis provides is a fundamental understanding of how 5G mmWave technology can enable extremely accurate localization. By studying theoretical performance bounds, we aim to provide insights on the feasibility and the factors that need to be considered when designing 5G localization systems in order to achieve the required high location accuracy. The localization systems considered in this thesis follow the classifications in Figure 1.2, highlighted with thicker box borders. That is, we consider single-stationary-user active outdoor lo-

[3]It is commonly understood that the first commercial deployments of 5G technology will focus on centimeter-wave technology. However, we focus on 5G systems that are related to the highly anticipated mmWave systems

calization for mobile communications networks using multilateration and hybrid approaches.

Research Questions

The research presented in this thesis seeks to address the following research questions:

1. *In sub-6 GHz, given an environment with a given scattering richness, what is the best expected performance? How can we exploit the NLOS propagation models to better design localization algorithm with performance that approaches the best performance?*

2. *Focusing on 5G mmWave communications systems, and considering the initial network access problem, how can we use a blind beamforming technique that provides the UE with a reasonable access to the network?*

3. *Beyond the IA phase, is it better to perform localization at the BS (Uplink) or at the UE (downlink)? How does the unique mmWave channel features impact this performance? What is the best positioning performance that can be achieved?*

4. *What are the system parameters that need to be tuned in order to boost the performance of 5G mmWave localization? How do these parameters affect the performance?*

5. *Building on the results of questions 3 and 4, how can we account for synchronization issues in mmWave?*

Thesis Overview

The remainder of this thesis is organized as follows:

- **Chapter 2** provides the background necessary to understand the thesis. This includes a brief revision of relevant notions from array signal processing, a review of some concepts of estimation theory, and an overview with some example on how to compute the Cramér-Rao lower bound (CRLB). CRLB is

a performance metric widely-used to judge and benchmark estimation problems, of which localization is one.

- **Chapter 3** proposes a trilateration-based localization scheme applicable in conventional cellular systems and accounts for different NLOS environments. Towards that, we devise an unbiased ranging method that is based on a distance-dependent bias model. Then, incorporating range estimate from 3 BSs, we localize UE. We perform an error analysis and compare it with the distance CRLB that is obtained using numerical statistical methods. We do that for mixed LOS/NLOS scenarios in four environments, ranging from bad urban environment to rural environment.

- **Chapter 4** focuses on the initial access problem in 5G mmWave networks, when no channel-side information is available at the UE that attempts to gain network access. In this regard, the chapter investigates two blind beamforming schemes, referred to as random-phase beamforming (RPBF) and directional beamforming (DBF). Since the subsequent step to initial access would be channel estimation, we compare the performance of DBF and RPBF in terms of CRLB of the channel parameters. We show that under the considered scenarios, RPBF is more appropriate.

- **Chapter 5** considers the 3D positioning error bound of 5G mmWave systems in multipath propagation, both uplink and downlink, beyond the initial access phase. It analyzes the impact of system parameters, and the interaction between different paths in terms of information gain. It also explores the role of reflectors, and scatterers on the localization limits. The problem of jointly estimating the UE location and orientation is considered, since beamforming at the UE in mmWave systems (hence, systems performance) depends on the UE orientation. The results in this chapter imply that uplink and downlink are not equivalent, and that NLOS paths assist localization in general. Moreover, we show that mmWave systems can provide a sub-meter position and sub-degree orientation errors, if the systems parameters are tuned appropriately.

- **Chapter 6** extends the results in Chapter 5 by focusing on LOS scenarios,

and accounting for the time-offset bias issue. It proposes two-way localization protocols, distributed and centralized and compares them in terms of the uplink and downlink position error bounds in the presence of receive beamforming and spatially correlated noise. We deduce that the centralized protocol outperforms the distributed protocol, with the cost of requiring coarse synchronization.

- **Chapter 7** provides a summary of the important results of the thesis and sheds some light on related future research directions.

Chapter 2

Background Concepts

Overview: *The reader of this thesis encounters many concepts of array signal processing and classical estimation theory. Therefore, it is meaningful to cover these concepts in this Chapter. The Chapter starts by giving an overview on the field of array signal processing, where the coordinate system is defined, and the concept of array manifold vector is introduced. Subsequently, analog beamforming and the resulting channel model useful in 5G mmWave are described. In the second part of the Chapter, the basics of estimation theory are covered, and the measurement model is discussed. The assessment of the estimation performance is highlighted thereafter. The concepts of Cramér-Rao Lower Bound (CRLB) and Fisher Information Matrix (FIM) are frequently encountered throughout this thesis. Therefore, they are introduced later in this Chapter. Moreover, we observe one variable sometimes, but are interested in another, which is a function of the observed one. Towards that, we discuss the transformation of parameters. To conclude this Chapter, the equivalent FIM (EFIM) is briefed at the end. To make the concepts in this chapter clearer, some relevant examples were designed and included herein. We stress that this Chapter is not to meant to be all-inclusive, and that only background relevant to the thesis is provided. However, we provide highlights to guide the reader to other resources, should more comprehensive background be necessary.*

2.1 Background on Array Signal Processing

As the name suggests, array signal processing is a branch of signal processing that focuses on signals received by a group of sensors. These sensors are spatially "arrayed" by a specific geometry that affects the behavior of the sensors ensemble. In the context of this thesis, the sensors we are focusing on are antennas, as traducers of electromagnetic waves into electrical signals. Since the signal arrives at the array elements in delayed versions, the signal received at the output of an antenna array carries two-part information: spatial and temporal. Employing this spatiotemporal information, array signal processing addresses four problems [75]. Firstly, the *detection* problem is concerned with estimating the number of emitting sources. Secondly, the DOA *estimation* problem, known as direction finding, employs the spatial information of the received signal to infer information on the direction from which the signal is impinging on the array. Then in combination with TOA estimation, the location of the transmitter can therefore be determined. Moreover, the *reception* problem addresses the design of beamforming schemes to extract the desired signal and cancel the interference. Finally, *environment mapping* seeks to create a map of the surrounding environment based on the received signal features such as signal density based on the spatial coordinates. In this thesis, we focus on the location estimation bounds, and beamforming. Thus, only array processing basics that are related to these two concepts are introduced in this chapter. However, a reader interested in comprehensive background on array processing is referred to the books [58, 75–79], which cover a wide range of topics with varying levels of complexity, while [80] provides a good overview on the topic.

2.1.1 Array Manifold Vector

Firstly, we need to understand how the antenna array behaves as an ensemble. Towards that, the *array manifold vector*, provides us with this understanding [58, 75]. It is reasonable to expect the array manifold vector to depend on the array geometry. Therefore, we start by defining the standard spherical coordinate system, used in this thesis. From Figure 2.1, for $0 \leq \theta \leq \pi$, $0 \leq \phi < 2\pi$, and $\varrho \geq 0$, we

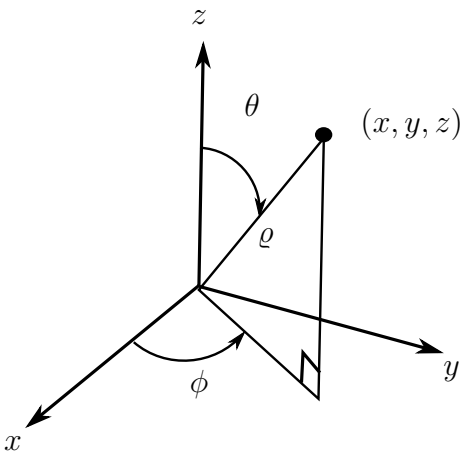

Figure 2.1: Spherical coordinate system.

can write

$$x = \varrho \sin\theta \cos\phi, \tag{2.1a}$$

$$y = \varrho \sin\theta \sin\phi, \tag{2.1b}$$

$$z = \varrho \cos\theta. \tag{2.1c}$$

Based on this notation, we define a unit vector pointing towards (x, y, z) as $\mathfrak{u} \triangleq [\sin\theta\cos\phi, \sin\theta\sin\phi, \cos\theta]^{\mathrm{T}}$, from which the wavenumber vector can be defined as

$$\mathbf{k}(\theta, \phi) \triangleq \frac{2\pi}{\lambda}\mathfrak{u} = \frac{2\pi}{\lambda}[\sin\theta\cos\phi, \sin\theta\sin\phi, \cos\theta]^{\mathrm{T}}, \tag{2.2}$$

where $\lambda = c/f_c$ is the wavelength, c is the propagation speed, and f_c is the carrier frequency. Furthermore, considering an array of N_{R} antennas, denote the location of the n^{th} antenna, $1 \leq n \leq N_{\mathrm{R}}$, in Cartesian coordinates by $\mathbf{u}_n = [x_n, y_n, z_n]^{\mathrm{T}} \in \mathbb{R}^3$. The the antenna location matrix is given by

$$\mathbf{\Delta}_{\mathrm{R}} = [\mathbf{u}_1, \mathbf{u}_2, \cdots, \mathbf{u}_{N_{\mathrm{R}}}] \in \mathbb{R}^{3\times N_{\mathrm{R}}}. \tag{2.3}$$

Consequently, the array manifold vector is defined by [58, 75]

$$\mathbf{a}_{\mathrm{R}}(\theta, \phi) \triangleq \widetilde{\mathbf{g}}(\theta, \phi) \odot \exp\left(-j\mathbf{\Delta}_{\mathrm{R}}^{\mathrm{T}}\mathbf{k}(\theta, \phi)\right), \tag{2.4}$$

where $\odot$ denotes the Hadamard product, and $\widetilde{\mathbf{g}}(\theta,\phi) \in \mathbb{C}^{\mathrm{N_R}}$ is a vector specifying the directional gain and phase of each antenna element. In our work, as the case with most literature, we will assume that the antennas radiation pattern is isotropic. That is,

$$\mathbf{a}_{\mathrm{R}}(\theta,\phi) = \frac{1}{\sqrt{N_{\mathrm{R}}}} \exp\left(-j\boldsymbol{\Delta}_{\mathrm{R}}^{\mathrm{T}}\mathbf{k}(\theta,\phi)\right), \tag{2.5}$$

Note that we use $\sqrt{N_{\mathrm{R}}}$ to normalize $\mathbf{a}_{\mathrm{R}}(\theta,\phi)$, such that $\mathbf{a}_{\mathrm{A}}^{\mathrm{T}}(\theta,\phi)\mathbf{a}_{\mathrm{R}}(\theta,\phi) = 1$. Moreover, observe that $\mathbf{a}_{\mathrm{R}}(\theta,\phi)$, encapsulates the phase difference of arrival at each antenna. Finally, note that usually the term "array manifold vector" is used as a unified term that applies to both transmitter and receiver. However, "array response vector" is the popular used with receiving arrays, while "array steering vector" is the one used with transmitting arrays. After all, these three terms describe the vector defined in (2.5).

In the following, we show how to obtain the array manifold vector for example geometries.

Uniform Rectangular Array (URA)

A URA is a 2D array of sensors as illustrated in Figure 2.2 (right). The total number of antennas is $N_{\mathrm{R}} = N_{\mathrm{R,x}}N_{\mathrm{R,z}}$, where $N_{\mathrm{R,x}}$ and $N_{\mathrm{R,z}}$ are the number of antennas in the x- and z-directions, respectively. We denote the inter-element spacing in these direction by d_{x} and d_{z}. Using the general form in (2.5), we can write

$$\boldsymbol{\Delta}_{\mathrm{R}}^{\mathrm{T}} = [d_{\mathrm{x}}\mathbf{x}_{\mathrm{R}}, \quad \mathbf{0}_{N_{\mathrm{R}}}, \quad d_{\mathrm{z}}\mathbf{z}_{\mathrm{R}}] \tag{2.6}$$

where

$$\mathbf{x}_{\mathrm{R}} = \mathbf{1}_{N_{\mathrm{R,z}}} \otimes \widetilde{\mathbf{x}}_{\mathrm{R}}, \tag{2.7a}$$

$$\mathbf{z}_{\mathrm{R}} = \widetilde{\mathbf{z}}_{\mathrm{R}} \otimes \mathbf{1}_{N_{\mathrm{R,x}}}, \tag{2.7b}$$

$$\widetilde{\mathbf{x}}_{\mathrm{R}} \triangleq \left[-\frac{N_{\mathrm{R,x}}-1}{2}, -\frac{N_{\mathrm{R,x}}-1}{2}+1, \cdots, \frac{N_{\mathrm{R,x}}-1}{2}\right]^{\mathrm{T}}, \tag{2.7c}$$

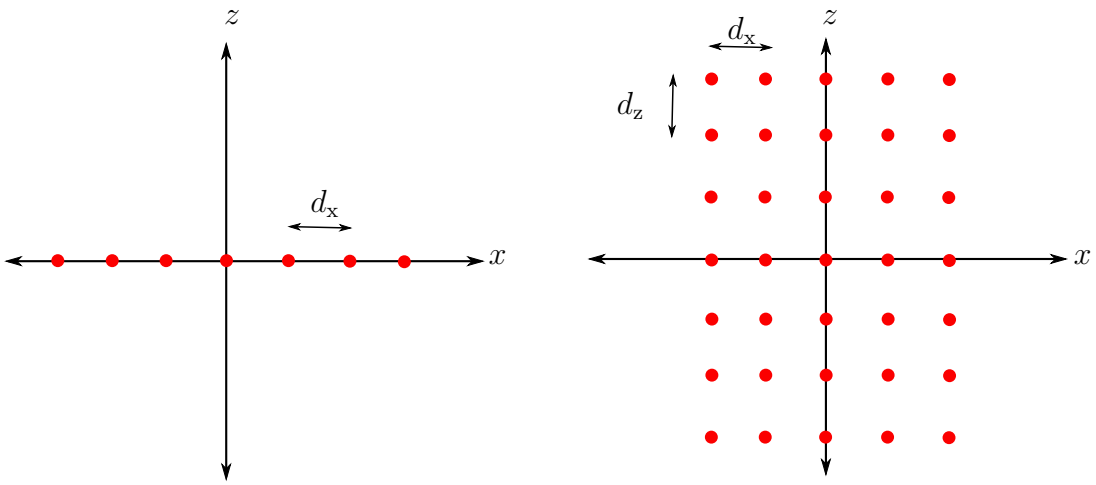

Figure 2.2: Left: ULA with 9 antennas and d_x inter-element spacing. When $d_x = \lambda/2$ it is called SLA. Right: URA of 45 antennas, consisting of 9 ULAs, each with 5 antennas and d_x inter-element spacing. Spacing between adjacent arrays is d_z.

$$\widetilde{\mathbf{z}}_{\mathrm{R}} \triangleq \left[-\frac{N_{\mathrm{R,z}}-1}{2}, -\frac{N_{\mathrm{R,z}}-1}{2}+1, \cdots, \frac{N_{\mathrm{R,z}}-1}{2}\right]^{\mathrm{T}}. \tag{2.7d}$$

and $\otimes$ denotes the Kronecker product. Consequently, we obtain

$$\mathbf{a}_{\mathrm{R}}(\theta,\phi) = \frac{1}{\sqrt{N_{\mathrm{R}}}} \exp\left(-j\frac{2\pi}{\lambda}\left(d_{\mathrm{x}} \sin\theta\cos\phi\ \mathbf{x}_{\mathrm{R}} + d_{\mathrm{z}}\cos\phi\ \mathbf{z}_{\mathrm{R}}\right)\right). \tag{2.8}$$

Note that when $d_{\mathrm{x}} = d_{\mathrm{z}} = \lambda/2$, and $N_{\mathrm{R,x}} = N_{\mathrm{R,z}}$, the array is called standard square array (SSA).

Uniform Linear Array (ULA)

A ULA is an 1-dimensional array of sensor with equispaced antennas as illustrated in Figure 2.2 (left). It is easy to see that a ULA is a special case URA with $N_{\mathrm{R,z}} = 1$. Therefore,

$$\mathbf{x}_{\mathrm{R}} = \widetilde{\mathbf{x}}_{\mathrm{R}}, \qquad \mathbf{z}_{\mathrm{R}} = \mathbf{0}_{N_{\mathrm{R}}}, \qquad \theta = \frac{\pi}{2}. \tag{2.9}$$

Thus, the array response vector is given by

$$\mathbf{a}_{\mathrm{R}}(\phi) \triangleq \frac{1}{\sqrt{N_{\mathrm{R}}}} \exp\left(-j\frac{2\pi d_{\mathrm{x}}}{\lambda}\cos\phi\ \mathbf{x}_{\mathrm{R}}\right), \tag{2.10}$$

Note that when $d_{\mathrm{x}} = \lambda/2$, the ULA is called standard linear array (SLA).

2.1.2 Analog Beamforming

One of the great advantages of array signal processing is enabling us to focus the transmission or reception on some specific areas by steering the beams electronically, rather than mechanically as in traditional radar systems. We can achieve that through a process called *beamforming*, whereby we scale the signal on each antenna by some complex weight to alter its magnitude and phase, so that the overall antenna gain is higher in the desired areas than in the other areas [76]. In mmWave systems, analog beamforming will be implemented using phase-shifters only. Therefore, in this thesis, we restrict our discussion on beamforming only to analog beamforming with constant magnitude but varying phase.

The simplest form of beamforming is when the antennas are uniformly weighted. Considering a URA lying the xz-plane as shown in Figure 2.2, under this beamforming scheme, the radiation pattern of the beam points towards $\theta = \phi = 90°$. Similarly, in the case of a ULA along the x-axis, it points towards the broadside direction, $\phi = 90°$ [58]. An example radiation pattern of a 12-antenna ULA is shown in Figure 2.3. This radiation pattern is often called an *array factor*, which is the radiation pattern of an "unsteered" beam [58].

Mathematically, for any beamforming vector $\mathbf{f}$, the beam gain in the direction (θ, ϕ) is given [76]

$$G(\theta,\phi)[\mathrm{dB}] = 20\log_{10}\left(\frac{\|\mathbf{f}^{\mathrm{H}}\mathbf{a}(\theta,\phi)\|}{\|\mathbf{f}\|}\right). \tag{2.11}$$

Consider a transmitting array with N_{T} antennas, and assume that we want to transmit a beam towards a direction (θ_0, ϕ_0). In that case, we can design $\mathbf{f}$ to be

$$\mathbf{f}(\theta_0,\phi_0) = \mathbf{a}_{\mathrm{T}}(\theta_0,\phi_0) \triangleq \frac{1}{\sqrt{N_{\mathrm{T}}}} \exp\left(-j\boldsymbol{\Delta}_{\mathrm{T}}^{\mathrm{T}}\mathbf{k}(\theta_0,\phi_0)\right). \tag{2.12}$$

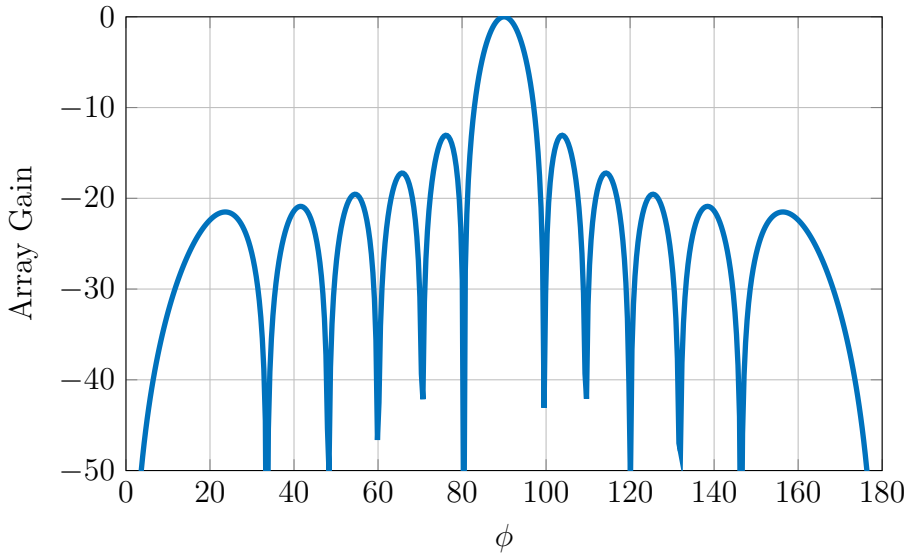

Figure 2.3: An array factor of a 12-antenna standard ULA.

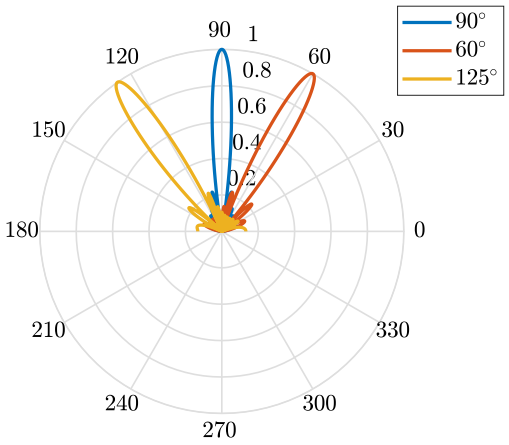

Figure 2.4: Radiation Pattern of a 12-antenna ULA, steered to 60°, and 125°.

Throughout this thesis, we will refer to this type of beamforming as *directional beamforming*. The array factor of the 12-antenna ULA shown in Figure 2.3 is replotted in polar form in Figure 2.4 (blue), steered to the directions 60°, and 125°.

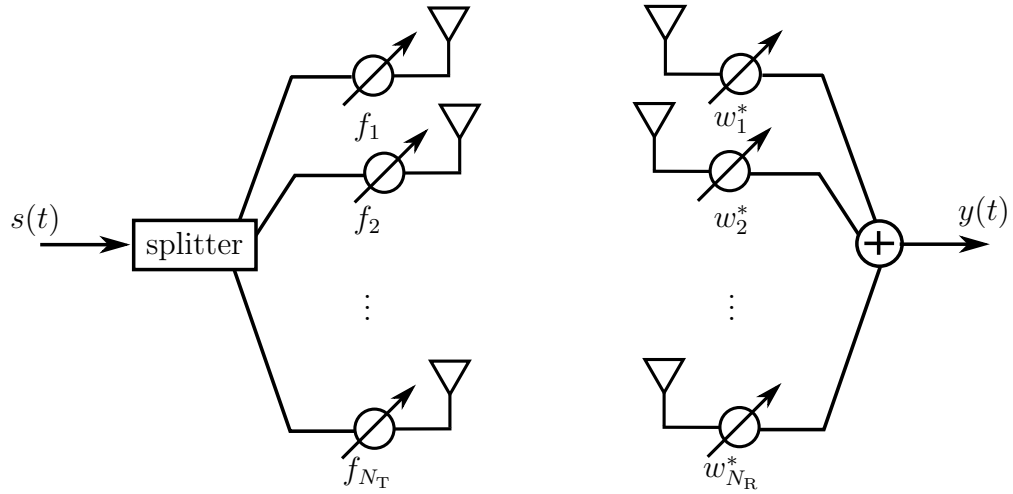

Figure 2.5: Analog transmit and receive beamforming structure.

2.1.3 Received Signal Model

In this subsection, we introduce the end-to-end channel model based on the analog beamforming structure, shown in Figure 2.5. Due to the infeasibility of all-digital beamforming, this model is a candidate structure for 5G mmWave communication [64]. Consider a transmitter and a receiver equipped with N_T, and N_R antennas, respectively. For the simplicity of presentation, let us consider initially the transmission of a single signal, $s(t)$, over a single beam through a single path. The transmit beamforming, denoted by $\mathbf{f}(\theta_\mathrm{f}, \phi_\mathrm{f}) = [f_1, f_2, \cdots, f_{N_\mathrm{T}}]^\mathrm{T}$, points towards the direction $(\theta_\mathrm{f}, \phi_\mathrm{f})$, while the receive beamforming, denoted by $\mathbf{w}(\theta_\mathrm{w}, \phi_\mathrm{w}) = [w_1, w_2, \cdots, w_{N_\mathrm{R}}]^\mathrm{T}$, points towards the direction $(\theta_\mathrm{w}, \phi_\mathrm{w})$.

Firstly, let us consider the transmitter. Based on Figure 2.5, the signal at the input of the antenna array steered to the direction $(\theta_\mathrm{f}, \phi_\mathrm{f})$ is given by

$$\mathbf{x}(t) = \mathbf{f}(\theta_\mathrm{f}, \phi_\mathrm{f}) s(t) \in \mathbb{C}^{N_\mathrm{T}}. \tag{2.13}$$

Consequently, taking the array steering vector into account, the superposition signal in the far-field of the array, known as plane-wave, measured at an angle of $(\theta_\mathrm{T}, \phi_\mathrm{T})$ is given by

$$\begin{aligned} \widetilde{x}(t) &= \sqrt{N_\mathrm{T}} \mathbf{a}_\mathrm{T}(\theta_\mathrm{T}, \phi_\mathrm{T})^\mathrm{H} \mathbf{x}(t). \\ &= \sqrt{N_\mathrm{T}} \mathbf{a}_\mathrm{T}(\theta_\mathrm{T}, \phi_\mathrm{T})^\mathrm{H} \mathbf{f}(\theta_\mathrm{f}, \phi_\mathrm{f}) s(t). \end{aligned} \tag{2.14}$$

$\widetilde{x}(t)$ arrives at the receiver after some propagation delay, τ. Thus, ignoring the path gain and the receiver noise, for the time-being, the signal received via the direction $(\theta_{\mathrm{R}}, \phi_{\mathrm{R}})$ at the output of the receive array is modeled by

$$\begin{aligned}\mathbf{r}_0(t) &= \sqrt{N_{\mathrm{R}}}\mathbf{a}_{\mathrm{R}}(\theta_{\mathrm{R}}, \phi_{\mathrm{R}})\widetilde{x}(t-\tau), \\ &= \sqrt{N_{\mathrm{T}}N_{\mathrm{R}}}\mathbf{a}_{\mathrm{R}}(\theta_{\mathrm{R}}, \phi_{\mathrm{R}})\mathbf{a}_{\mathrm{T}}(\theta_{\mathrm{T}}, \phi_{\mathrm{T}})^{\mathrm{H}}\mathbf{f}(\theta_{\mathrm{f}}, \phi_{\mathrm{f}})s(t-\tau). \end{aligned} \tag{2.15}$$

Adding the channel gain, β, and the receiver noise, $\mathbf{n}(t)$ to the model yields,

$$\mathbf{r}(t) = \sqrt{N_{\mathrm{T}}N_{\mathrm{R}}}\beta\mathbf{a}_{\mathrm{R}}(\theta_{\mathrm{R}}, \phi_{\mathrm{R}})\mathbf{a}_{\mathrm{T}}(\theta_{\mathrm{T}}, \phi_{\mathrm{T}})^{\mathrm{H}}\mathbf{f}(\theta_{\mathrm{f}}, \phi_{\mathrm{f}})s(t-\tau) + \mathbf{n}(t) \in \mathbb{C}^{N_{\mathrm{R}}}. \tag{2.16}$$

Defining $\mathbf{H}_{\mathrm{s}} \triangleq \sqrt{N_{\mathrm{T}}N_{\mathrm{R}}}\beta\mathbf{a}_{\mathrm{R}}(\theta_{\mathrm{R}}, \phi_{\mathrm{R}})\mathbf{a}_{\mathrm{T}}(\theta_{\mathrm{T}}, \phi_{\mathrm{T}})^{\mathrm{H}}$. Subsequently, the signal processed by a receive beamformer pointing towards $(\theta_{\mathrm{w}}, \phi_{\mathrm{w}})$ is then given by

$$\begin{aligned}\mathbf{y}_{\mathrm{s}}(t) &= \mathbf{w}^{\mathrm{H}}(\theta_{\mathrm{w}}, \phi_{\mathrm{w}})\mathbf{r}(t), \\ &= \mathbf{w}^{\mathrm{H}}(\theta_{\mathrm{w}}, \phi_{\mathrm{w}})\mathbf{H}_{\mathrm{s}}\mathbf{f}(\theta_{\mathrm{f}}, \phi_{\mathrm{f}})s(t-\tau) + \mathbf{w}^{\mathrm{H}}(\theta_{\mathrm{w}}, \phi_{\mathrm{w}})\mathbf{n}(t) \in \mathbb{C}^{N_{\mathrm{R}}}. \end{aligned} \tag{2.17}$$

Finally, with similar steps, we can extend the single-path single-beam model in (2.17) to N_{B} beams and M paths. The resulting receive signal is then given by

$$\mathbf{y}(t) = \mathbf{W}^{\mathrm{H}}\sum_{m=1}^{M}\mathbf{H}_m\mathbf{F}\mathbf{s}(t-\tau_m) + \mathbf{W}^{\mathrm{H}}\mathbf{n}(t) \in \mathbb{C}^{N_{\mathrm{B}}}, \tag{2.18}$$

where

- $\mathbf{W} \triangleq [\mathbf{w}(\theta_{\mathrm{w},1}, \phi_{\mathrm{w},1}), \mathbf{w}(\theta_{\mathrm{w},2}, \phi_{\mathrm{w},2}), \cdots, \mathbf{w}(\theta_{\mathrm{w},\mathrm{N_B}}, \phi_{\mathrm{w},\mathrm{N_B}})]$, is the receive beamforming matrix, stacking the receive beamformers. The receive angles are dropped for concise presentation.
- $\mathbf{F} \triangleq [\mathbf{f}(\theta_{\mathrm{f},1}, \phi_{\mathrm{f},1}), \mathbf{f}(\theta_{\mathrm{f},2}, \phi_{\mathrm{f},2}), \cdots, \mathbf{f}(\theta_{\mathrm{f},\mathrm{N_B}}, \phi_{\mathrm{f},\mathrm{N_B}})]$, is the transmit beamforming matrix, stacking transmit beamformers. The transmit angles are dropped for concise presentation too.
- $\mathbf{H}_m = \sqrt{N_{\mathrm{T}}N_{\mathrm{R}}}\beta_m\mathbf{a}_{\mathrm{R}}(\theta_{\mathrm{R},m}, \phi_{\mathrm{R},m})\mathbf{a}_{\mathrm{T}}(\theta_{\mathrm{T},m}, \phi_{\mathrm{T},m})^{\mathrm{H}}$, the channel excluding the propagation delay, where β_m is the m^{th} path gain, $(\theta_{\mathrm{R},m}, \phi_{\mathrm{R},m})$ is the m^{th} DOA, and $(\theta_{\mathrm{T},m}, \phi_{\mathrm{T},m})$ is the m^{th} DOD.

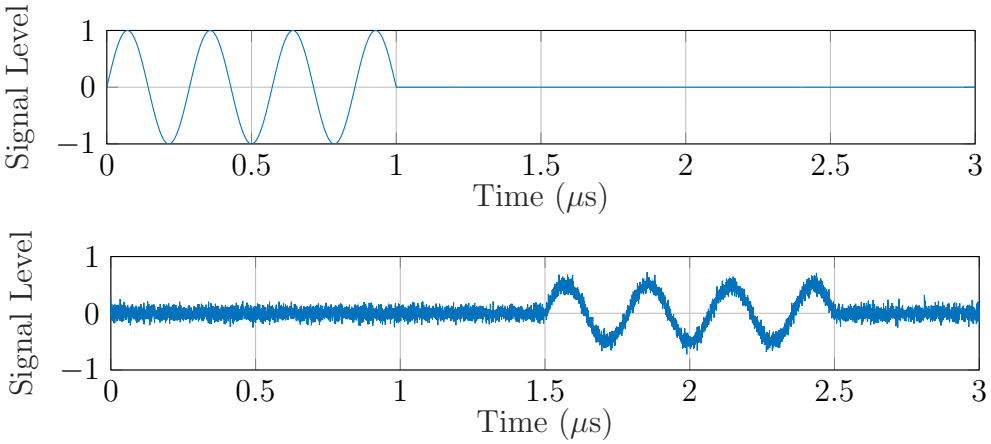

Figure 2.6: Transmitted (top) and reflected (bottom) radar pulse. The latter is contaminated by measurement noise and channel impairments.

- $\mathbf{s}(t) \triangleq [s_1(t), s_2(t), \cdots, s_M(t)]$.
- τ_m is the m^{th} TOA.

2.2 Introduction to Classical Estimation Theory

Inferring the values of unknown deterministic parameters from noisy measurements is the subject of classical[1] estimation theory. It has been widely applied in engineering problems, particularly in communication and signal processing [81–83]. As an introductory example, consider the classical ranging problem using a radar system [81]. The radar transmits a pulse of known properties similar to that in Figure 2.6, which is then reflected back to the radar system by the subject. The radar then calculates the round trip time, 2τ, from which the range can be simply obtained as τ/c, where c is the speed of the signal. Note that the determination of τ is based on a reflected signal that has been subject to deformation including the path and reflection losses, as well as the receiver noise. Therefore, the range estimate is prone to errors depending on the severity of these factors.

[1]Estimating a random unknown parameter is the subject of Bayesian estimation, which is outside the scope of this thesis.

2.2.1 Measurement Model

Consider the problem of estimating a vector of N_{v} parameters, $\boldsymbol{\varphi} \triangleq [\varphi_1, \varphi_2, \cdots, \varphi_{N_{\mathrm{v}}}]^{\mathrm{T}}$, using N_{R} observation channels, $\mathbf{r}(t) \triangleq [r_1(t), r_2(t), \cdots, r_{N_{\mathrm{R}}}(t)]^{\mathrm{T}}$, such that

$$\mathbf{r}(t) = \boldsymbol{\mu}_{\varphi}(t) + \mathbf{n}(t), \qquad 0 \leq t \leq T_{\mathrm{o}}. \tag{2.19}$$

In (2.19), $\boldsymbol{\mu}_{\varphi}(t)$ is a deterministic vector function of the unknown parameter vector, $\mathbf{n}(t) \sim \mathcal{CN}(\mathbf{0}, \boldsymbol{\Sigma}_{\mathrm{n}})$ is the measurement noise vector, $\boldsymbol{\Sigma}_{\mathbf{n}}$ is the noise covariance matrix, and T_{o} is the observation interval.

The estimator of $\boldsymbol{\varphi}$ is given by some vector function $\mathbf{g}(.)$ as $\widehat{\boldsymbol{\varphi}} = \mathbf{g}\left(\mathbf{r}(t)\right)$. Note that $\mathbf{r}(t)$ is observed in the presence of noise. Therefore, $\widehat{\boldsymbol{\varphi}}$ is a random vector, and $\mathbf{r}(t)$ is a random process whose distribution depends on the noise probability density function (PDF). In most estimation theory applications, the measurements are generally modeled by Gaussian processes such that the PDF of $\mathbf{r}$ as a function of $\boldsymbol{\varphi}$ is

$$f_{\mathrm{r}}(\mathbf{r}; \boldsymbol{\varphi}) = \frac{1}{\det(2\pi\boldsymbol{\Sigma}_{\mathrm{n}})^{\frac{1}{2}}} \mathrm{e}^{-\frac{1}{2}(\boldsymbol{\mu}_{\varphi}-\mathbf{r})^{\mathrm{H}}\boldsymbol{\Sigma}_{\mathrm{n}}^{-1}(\boldsymbol{\mu}_{\varphi}-\mathbf{r})}, \tag{2.20}$$

Recall that it is very common to assume that observations are contaminated by zero-mean and independent and identically distributed Gaussian noise, in which case $\boldsymbol{\Sigma}_{\mathbf{n}} = N_0\mathbf{I}_{N_{\mathrm{R}}}$, where N_0 is the noise power spectral density (PSD), and $\mathbf{I}_{N_{\mathrm{R}}}$ is the N_{R}-dimensional identity matrix.

Based on this PDF, the issue becomes: how can we design a "good" estimator, $\widehat{\boldsymbol{\varphi}}$? And, what is a "good" estimator? In the following, we answer these questions.

2.2.2 Estimation Performance

As an optimality criterion to assess the estimator performance, we start by the estimator mean-square error (MSE) denoted by ρ, and defined as,

$$\rho(\boldsymbol{\varphi}) \triangleq \mathbb{E}\left\{(\widehat{\boldsymbol{\varphi}} - \boldsymbol{\varphi})^2\right\} = \begin{bmatrix} \mathbb{E}\left\{(\widehat{\varphi}_1 - \varphi_1)^2\right\} \\ \vdots \\ \mathbb{E}\left\{(\widehat{\varphi}_{N_{\mathrm{v}}} - \varphi_{N_{\mathrm{v}}})^2\right\} \end{bmatrix}, \tag{2.21}$$

where $\mathbb{E}\{\cdot\}$ is the expectation operator. Without loss of generality, consider the MSE of φ_1, and write [81] as

$$\rho(\varphi_1) = \mathbb{E}\left\{(\widehat{\varphi}_1 - \varphi_1)^2\right\}, \tag{2.22a}$$

$$= \mathbb{E}\Big\{ (\widehat{\varphi}_1 - \mathbb{E}\{\widehat{\varphi}_1\} + \mathbb{E}\{\widehat{\varphi}_1\} - \varphi_1)^2 \Big\}, \tag{2.22b}$$

$$= \mathbb{E}\Big\{ (\widehat{\varphi}_1 - \mathbb{E}\{\widehat{\varphi}_1\})^2 \Big\} + (\mathbb{E}\{\widehat{\varphi}_1\} - \varphi_1)^2 . \tag{2.22c}$$

This means that the estimator error has two components: a variance, $\sigma^2_{\varphi_1} \triangleq \mathbb{E}\left\{(\widehat{\varphi}_1 - \mathbb{E}\{\widehat{\varphi}_1\})^2\right\}$, and a bias, $b_{\varphi_1} \triangleq (\mathbb{E}\{\widehat{\varphi}_1\} - \varphi_1)^2$. Any good estimator should provide an estimate of the variable that is equal to the said variable on the average. Such an estimator is called *unbiased estimator*, and is characterized by

$$\varphi_1 = \mathbb{E}\{\widehat{\varphi}_1\} \qquad \Rightarrow \qquad b_{\varphi_1} = 0. \tag{2.23}$$

Consequently, in the absence of estimation bias, the best estimator is the one that provides the least variance. This minimum variance is known as Cramér-Rao lower bound (CRLB), and the estimator that attains the CRLB is called *minimum variance unbiased estimator* (MVUE). Unfortunately, the MVUE does not always exist, or may not be practically possible [81]. Moreover, a closed-form procedure to compute the MVUE estimator does not exist. The computation of CRLB is discussed in more details in the following section.

2.2.3 Cramér-Rao lower bound (CRLB)

In the context of parameter estimation, CLRB is a useful tool that serves as a feasibility study on whether a given technology can meet some performance requirement or not. Being a lower bound, it can also be used to benchmark the performance of new estimators. Moreover, it can be used in investigating the impact of different system parameters on the overall performance of an estimator. Finally, CRLB may provide means to compute a MVUE. The use of CRLB in benchmarking is applied in Chapter 3, while its use for feasibility studies, and investigating system parameters impact is applied in Chapters 4, 5, and 6.

Assuming that the PDF $f_{\mathrm{r}}(\mathbf{r};\boldsymbol{\varphi})$ satisfies the regularity condition

$$\mathbb{E}\left\{\frac{\partial \ln f_{\mathrm{r}}(\mathbf{r};\boldsymbol{\varphi})}{\partial \boldsymbol{\varphi}}\right\} = \mathbf{0}_{N_{\mathrm{v}}}, \tag{2.24}$$

then the variance of any unbiased estimator of $\boldsymbol{\varphi}$, is computed from the information inequality given by [81, 83]

$$\begin{bmatrix} \sigma^2_{\varphi_1} \\ \vdots \\ \sigma^2_{\varphi_{N_{\mathrm{v}}}} \end{bmatrix} \geq \mathrm{diag}\left(\mathbf{J}_{\boldsymbol{\varphi}}^{-1}\right), \tag{2.25}$$

where $\mathbf{J}_{\boldsymbol{\varphi}}$ is the *Fisher Information Matrix* (FIM), whose elements are given by

$$[\mathbf{J}_{\boldsymbol{\varphi}}]_{u,v} \triangleq \mathbb{E}\left\{\frac{\partial \ln f_{\mathrm{r}}(\mathbf{r};\boldsymbol{\varphi})}{\partial \varphi_u}\frac{\partial \ln f_{\mathrm{r}}(\mathbf{r};\boldsymbol{\varphi})}{\partial \varphi_v}\right\}, \qquad 1 \leq u, v \leq N_{\mathrm{v}} \tag{2.26}$$

The CRLB is then related to the FIM by

$$\mathrm{CRLB}(\boldsymbol{\varphi}) \triangleq \begin{bmatrix} \mathrm{CRLB}(\varphi_1) \\ \vdots \\ \mathrm{CRLB}(\varphi_{N_{\mathrm{v}}}) \end{bmatrix} = \mathrm{diag}\left(\mathbf{J}_{\boldsymbol{\varphi}}^{-1}\right). \tag{2.27}$$

We now consider the most used case of Gaussian distribution. It is easy to see from (2.20) that the regularity condition is satisfied, and that the CRLB is defined for the Gaussian PDFs. For the vector Gaussian PDF given in (2.20), using (2.26), it can be shown the FIM entries are given by [81–83]

$$[\mathbf{J}_{\boldsymbol{\varphi}}]_{u,v} \triangleq \int_0^{T_{\mathrm{o}}} \Re\left\{\frac{\partial \boldsymbol{\mu}^{\mathrm{H}}_{\boldsymbol{\varphi}}(t)}{\partial \varphi_u}{\boldsymbol{\Sigma}_{\mathbf{n}}}^{-1}\frac{\partial \boldsymbol{\mu}_{\boldsymbol{\varphi}}(t)}{\partial \varphi_v}\right\}\mathrm{d}t, \qquad 1 \leq u, v \leq N_{\mathrm{v}} \tag{2.28}$$

For the widely-used case of i.i.d Gaussian noise,

$$[\mathbf{J}_{\boldsymbol{\varphi}}]_{u,v} \triangleq \frac{1}{N_0}\int_0^{T_{\mathrm{o}}} \Re\left\{\frac{\partial \boldsymbol{\mu}^{\mathrm{H}}_{\boldsymbol{\varphi}}(t)}{\partial \varphi_u}\frac{\partial \boldsymbol{\mu}_{\boldsymbol{\varphi}}(t)}{\partial \varphi_v}\right\}\mathrm{d}t, \qquad 1 \leq u, v \leq N_{\mathrm{v}} \tag{2.29}$$

Finally, note that if the measurements are discrete-time, the FIM is defined as

$$[\mathbf{J}_{\boldsymbol{\varphi}}]_{u,v} \triangleq \frac{1}{\sigma_{\mathrm{n}}^2} \sum_{n=0}^{N_{\mathrm{s}}} \Re \left\{ \frac{\partial \boldsymbol{\mu}_{\boldsymbol{\varphi}}^{\mathrm{H}}[n]}{\partial \varphi_u} \frac{\partial \boldsymbol{\mu}_{\boldsymbol{\varphi}}[n]}{\partial \varphi_v} \right\}, \qquad 1 \leq u, v \leq N_{\mathrm{v}} \tag{2.30}$$

where σ_{n}^2 is the observation noise variance. An illustrative example is now provided.

Example 2.1 *Consider a signal $s(t)$ impinging on an N_{R}-element SLA from two different paths via directions ϕ_1, and ϕ_2, so that the received signal is modeled by*

$$\mathbf{r}(t) = \sqrt{N_{\mathrm{R}}} \Big(\mathbf{a}_{\mathrm{R}}(\phi_1) + \mathbf{a}_{\mathrm{R}}(\phi_2) \Big) s(t) + \mathbf{n}(t), \qquad 0 \leq t \leq T_{\mathrm{o}},$$

where $\mathbf{a}_{\mathrm{R}}(\phi_m), m = 1, 2$, is as defined in (2.10), and $\mathbf{n}(t)$ is a zero-mean random Gaussian process with $\boldsymbol{\Sigma}_{\mathrm{n}} = N_0 \mathbf{I}_{N_{\mathrm{R}}}$. Derive the CRLB of $\boldsymbol{\varphi} = [\phi_1, \phi_2]^{\mathrm{T}}$.

Solution

From the observation model in (2.19), we take $\boldsymbol{\mu}_{\boldsymbol{\varphi}}(t) = \sqrt{N_{\mathrm{R}}} \Big(\mathbf{a}_{\mathrm{R}}(\phi_1) + \mathbf{a}_{\mathrm{R}}(\phi_2) \Big) s(t)$, then we apply (2.29), to calculate the FIM from which the CRLB can be obtained. Towards that, the array response vector of a SLA (ULA with half-wavelength inter-element separation) in the direction ϕ_m is given by

$$\mathbf{a}_{\mathrm{R}}(\phi_m) = \frac{1}{\sqrt{N_{\mathrm{R}}}} \, \mathrm{e}^{-j\pi \cos \phi_m \widetilde{\mathbf{x}}_{\mathrm{R}}}, \tag{2.31}$$

where the antenna location vector is $\widetilde{\mathbf{x}}_{\mathrm{R}}$ given in (2.7). Thus,

$$\frac{\partial \boldsymbol{\mu}_{\boldsymbol{\varphi}}(t)}{\partial \phi_m} = j\pi \sqrt{N_{\mathrm{R}}} \sin \phi_m \, \mathrm{diag}(\widetilde{\mathbf{x}}_{\mathrm{R}}) \mathbf{a}_{\mathrm{R}}(\phi_m) s(t). \tag{2.32}$$

Starting with the diagonal elements of FIM,

$$[\mathbf{J}_{\boldsymbol{\varphi}}]_{1,1} \triangleq \frac{1}{N_0} \int_0^{T_{\mathrm{o}}} \Re \left\{ \frac{\partial \boldsymbol{\mu}_{\boldsymbol{\varphi}}^{\mathrm{H}}(t)}{\partial \phi_1} \frac{\partial \boldsymbol{\mu}_{\boldsymbol{\varphi}}(t)}{\partial \phi_1} \right\} \mathrm{d}t, \tag{2.33a}$$

$$= \frac{\pi^2 N_{\mathrm{R}} \sin \phi_1^2}{N_0} \int_0^{T_{\mathrm{o}}} \Re \left\{ s^*(t) \mathbf{a}_{\mathrm{R}}^{\mathrm{H}}(\phi_1) \, \mathrm{diag}^2(\widetilde{\mathbf{x}}_{\mathrm{R}}) \mathbf{a}_{\mathrm{R}}(\phi_1) s(t) \right\} \mathrm{d}t, \tag{2.33b}$$

$$= \frac{\pi^2 N_{\mathrm{R}} \sin \phi_1^2}{N_0} \underbrace{\mathbf{a}_{\mathrm{R}}^{\mathrm{H}}(\phi_1) \, \mathrm{diag}^2(\widetilde{\mathbf{x}}_{\mathrm{R}}) \mathbf{a}_{\mathrm{R}}(\phi_1)}_{= \frac{1}{N_{\mathrm{R}}} \widetilde{\mathbf{x}}_{\mathrm{R}}^{\mathrm{T}} \widetilde{\mathbf{x}}_{\mathrm{R}}} \underbrace{\int_0^{T_{\mathrm{o}}} \Re \left\{ s^*(t) s(t) \right\} \mathrm{d}t}_{\triangleq R_0}. \tag{2.33c}$$

Note that it is straight-forward to see that $\widetilde{\mathbf{x}}_{\mathrm{R}}^{\mathrm{T}}\widetilde{\mathbf{x}}_{\mathrm{R}} = N_{\mathrm{R}}(N_{\mathrm{R}}^2-1)/12$. Thus,

$$[\mathbf{J}_{\boldsymbol{\varphi}}]_{1,1} = \frac{\pi^2}{12N_0} N_{\mathrm{R}}(N_{\mathrm{R}}^2-1) R_0 \sin\phi_1^2. \tag{2.34}$$

Similarly, we can show that

$$[\mathbf{J}_{\boldsymbol{\varphi}}]_{2,2} = \frac{\pi^2}{12N_0} N_{\mathrm{R}}(N_{\mathrm{R}}^2-1) R_0 \sin\phi_2^2. \tag{2.35}$$

Considering the off-diagonal elements, using similar steps, then

$$[\mathbf{J}_{\boldsymbol{\varphi}}]_{1,2} = [\mathbf{J}_{\boldsymbol{\varphi}}]_{2,1} \triangleq \frac{1}{N_0}\int_0^{T_{\mathrm{o}}} \Re\left\{ \frac{\partial \boldsymbol{\mu}_{\boldsymbol{\varphi}}^{\mathrm{H}}(t)}{\partial\phi_1} \frac{\partial \boldsymbol{\mu}_{\boldsymbol{\varphi}}(t)}{\partial\phi_2} \right\} \mathrm{d}t, \tag{2.36a}$$

$$= \frac{\pi^2}{N_0} N_{\mathrm{R}} R_0 \sin\phi_1 \sin\phi_2 \Re\{\mathbf{a}_{\mathrm{R}}^{\mathrm{H}}(\phi_1)\,\mathrm{diag}^2(\widetilde{\mathbf{d}})\mathbf{a}_{\mathrm{R}}(\phi_2)\}, \tag{2.36b}$$

$$= \frac{2\pi^2}{N_0} R_0 \sin\phi_1 \sin\phi_2 \sum_{n=1}^{(N_{\mathrm{R}}-1)/2} n^2 \cos\left(\pi(\cos\phi_1 - \cos\phi_2)\right), \tag{2.36c}$$

$$= \frac{2\pi^2}{N_0} \chi_{12} R_0 \sin\phi_1 \sin\phi_2 \tag{2.36d}$$

where $\chi_{12} \triangleq \sum_{n=1}^{\frac{N_{\mathrm{R}}-1}{2}} n^2 \cos\left(\pi(\cos\phi_1 - \cos\phi_2)\right)$. Since $\mathbf{J}_{\boldsymbol{\varphi}}$ is 2×2, then

$$\mathbf{J}_{\boldsymbol{\varphi}}^{-1} = \frac{1}{\det(\mathbf{J}_{\boldsymbol{\varphi}})} \begin{bmatrix} [\mathbf{J}_{\boldsymbol{\varphi}}]_{2,2} & -[\mathbf{J}_{\boldsymbol{\varphi}}]_{1,2} \\ -[\mathbf{J}_{\boldsymbol{\varphi}}]_{1,2} & [\mathbf{J}_{\boldsymbol{\varphi}}]_{1,1} \end{bmatrix} \tag{2.37}$$

Finally, from (2.27),

$$\mathrm{CRLB}(\phi_1) = \frac{[\mathbf{J}_{\boldsymbol{\varphi}}]_{2,2}}{\det(\mathbf{J}_{\boldsymbol{\varphi}})}, \tag{2.38a}$$

$$\mathrm{CRLB}(\phi_2) = \frac{[\mathbf{J}_{\boldsymbol{\varphi}}]_{1,1}}{\det(\mathbf{J}_{\boldsymbol{\varphi}})}, \tag{2.38b}$$

2.2.4 Transformation of Parameters

In many applications, the parameters of interest are functions of the unknown parameters observed. For example, estimating the signal-to-noise ratio is obviously

a function of the noise power and signal power, which are estimated separately. When multilateration or multiangulation is involved, the position estimation is also a function of TOAs, DOAs or both. Therefore, in this subsection we review the concept of parameter transformation.

Consider the problem when we are interested in the unknown parameter vector $\boldsymbol{\vartheta} \triangleq [\vartheta_1, \cdots, \vartheta_{N_\mathrm{p}}]^\mathrm{T}$, which is a function of the unknown parameter vector $\boldsymbol{\varphi}$, defined earlier. In other words, we have N_p unknowns that are functions of N_v unknowns. In many cases, it may be easier to obtain the FIM of $\boldsymbol{\varphi}$ and transform it to an FIM of $\boldsymbol{\vartheta}$ instead of computing the latter directly from the PDF of the observations. In that case, the FIM of $\boldsymbol{\vartheta}$ is given by [81, 83]

$$\mathbf{J}_{\boldsymbol{\vartheta}} = \boldsymbol{\Upsilon} \mathbf{J}_{\boldsymbol{\varphi}} \boldsymbol{\Upsilon}^\mathrm{T}, \tag{2.39}$$

where $\boldsymbol{\Upsilon}$ is the transformation matrix given by

$$\boldsymbol{\Upsilon} \triangleq \frac{\partial \boldsymbol{\varphi}^\mathrm{T}}{\partial \boldsymbol{\vartheta}} = \begin{bmatrix} \frac{\partial \varphi_1}{\partial \vartheta_1} & \frac{\partial \varphi_2}{\partial \vartheta_1} & \cdots & \frac{\partial \varphi_{N_\mathrm{v}}}{\partial \vartheta_1} \\ \frac{\partial \varphi_1}{\partial \vartheta_2} & \ddots & \ddots & \frac{\partial \varphi_{N_\mathrm{v}}}{\partial \vartheta_2} \\ \vdots & \ddots & \ddots & \vdots \\ \frac{\partial \varphi_1}{\partial \vartheta_{N_\mathrm{p}}} & \cdots & \cdots & \frac{\partial \varphi_{N_\mathrm{v}}}{\partial \vartheta_{N_\mathrm{p}}} \end{bmatrix}. \tag{2.40}$$

We now demonstrate the transformation of parameters through the following simple example.

Example 2.2 *Assume that instead of the DOAs in Example 2.1, we are interested in $\boldsymbol{\vartheta}$ such that $\vartheta_1 = \varphi_1 + \varphi_2$, and $\vartheta_2 = 3\varphi_1 - \varphi_2$. What is CRLB($\boldsymbol{\vartheta}$)?*

Solution

Firstly, we note that $\mathrm{CRLB}(\boldsymbol{\vartheta}) = \mathrm{diag}(\mathbf{J}_{\boldsymbol{\vartheta}}^{-1})$, and that $\mathbf{J}_{\boldsymbol{\vartheta}}$ can be computed from (2.39). Since $\mathbf{J}_{\boldsymbol{\varphi}}$ is derived in Example 2.1, we need to compute $\boldsymbol{\Upsilon}$. Therefore, from the given relationships, we can equivalently write

$$\varphi_1 = \frac{1}{4}(\vartheta_1 + \vartheta_2), \qquad \varphi_2 = \frac{1}{4}(3\vartheta_1 - \vartheta_2). \tag{2.41}$$

Consequently, it follows that

$$\boldsymbol{\Upsilon} = \frac{1}{4}\begin{bmatrix} 1 & 3 \\ 1 & -1 \end{bmatrix}. \tag{2.42}$$

Therefore, from (2.34), (2.35), and (2.36), it can be shown that

$$\mathbf{J}_{\boldsymbol{\vartheta}} = \frac{\pi^2}{16N_0}\begin{bmatrix} 1 & 3 \\ 1 & -1 \end{bmatrix}\begin{bmatrix} \frac{N_{\mathrm{R}}}{12}(N_{\mathrm{R}}^2-1)\sin^2\varphi_1 & \chi_{12}\sin\varphi_1\sin\varphi_2 \\ \chi_{12}\sin\varphi_1\sin\varphi_2 & \frac{N_{\mathrm{R}}}{12}(N_{\mathrm{R}}^2-1)\sin^2\varphi_2 \end{bmatrix}\begin{bmatrix} 1 & 1 \\ 3 & -1 \end{bmatrix}, \tag{2.43}$$

2.2.5 Equivalent Fisher Information Matrix (EFIM)

Although FIM helps us understand the interaction between different parameters, sometimes we need to focus on a subset of the unknown parameters and study it isolatedly. In that context, we can use the concept of equivalent FIM (EFIM) of that parameter for our investigation [84, 85].

Definition 2.1 *Given a parameter vector* $\boldsymbol{\varphi} \triangleq [\boldsymbol{\varphi}_1^{\mathrm{T}}, \boldsymbol{\varphi}_2^{\mathrm{T}}]^{\mathrm{T}}$ *with corresponding FIM*

$$\mathbf{J}_{\boldsymbol{\varphi}} = \begin{bmatrix} \mathbf{J}_{11} & \mathbf{J}_{12} \\ \mathbf{J}_{12}^{\mathrm{T}} & \mathbf{J}_{22} \end{bmatrix}, \tag{2.44}$$

Then, the EFIM of $\boldsymbol{\varphi}_1$ *is given by*

$$\mathbf{J}_{\boldsymbol{\varphi}_1}^{\mathrm{e}} = \mathbf{J}_{11} - \mathbf{J}_{12}\mathbf{J}_{22}^{-1}\mathbf{J}_{12}^{\mathrm{T}}. \tag{2.45}$$

The form in (2.45) is the well-known Schur's Complement. The first term of (2.45) is the information content related to $\boldsymbol{\varphi}_1$, in the absence of $\boldsymbol{\varphi}_2$. Moreover, based on the fact that information is always positive, it is interesting to see that the second term in (2.45) is negative. This means that when we need to estimate another parameter jointly with $\boldsymbol{\varphi}_1$, the net information at the estimator is reduced.

Example 2.3 *Write the expressions in* (2.38) *in terms of the EFIM.*

Solution

We start by writing the determinant as:

$$\det(\mathbf{J}_{\boldsymbol{\varphi}}) = [\mathbf{J}_{\boldsymbol{\varphi}}]_{1,1}[\mathbf{J}_{\boldsymbol{\varphi}}]_{2,2} - [\mathbf{J}_{\boldsymbol{\varphi}}]_{1,2}^2. \tag{2.46}$$

Consequently, it is straight forward to see that

$$\mathrm{CRLB}(\phi_1) = \frac{[\mathbf{J}_{\boldsymbol{\varphi}}]_{2,2}}{[\mathbf{J}_{\boldsymbol{\varphi}}]_{1,1}[\mathbf{J}_{\boldsymbol{\varphi}}]_{2,2} - [\mathbf{J}_{\boldsymbol{\varphi}}]_{1,2}^2} = \frac{1}{[\mathbf{J}_{\boldsymbol{\varphi}}]_{1,1} - [\mathbf{J}_{\boldsymbol{\varphi}}]_{2,2}^{-1}[\mathbf{J}_{\boldsymbol{\varphi}}]_{1,2}^2} = \frac{1}{[\mathbf{J}_{\boldsymbol{\varphi}}]_{1,1}^{\mathrm{e}}}, \tag{2.47a}$$

$$\mathrm{CRLB}(\phi_2) = \frac{[\mathbf{J}_{\boldsymbol{\varphi}}]_{1,1}}{[\mathbf{J}_{\boldsymbol{\varphi}}]_{1,1}[\mathbf{J}_{\boldsymbol{\varphi}}]_{2,2} - [\mathbf{J}_{\boldsymbol{\varphi}}]_{1,2}^2} = \frac{1}{[\mathbf{J}_{\boldsymbol{\varphi}}]_{2,2} - [\mathbf{J}_{\boldsymbol{\varphi}}]_{1,1}^{-1}[\mathbf{J}_{\boldsymbol{\varphi}}]_{1,2}^2} = \frac{1}{[\mathbf{J}_{\boldsymbol{\varphi}}]_{2,2}^{\mathrm{e}}}. \tag{2.47b}$$

We can conclude from (2.47) that the CRLB of a parameter, can be computed directly from its EFIM, without inverting the big FIM, hence the name, equivalent.

2.3 Summary

In this Chapter, we covered concepts from array signal processing and the classical estimation theory. We briefly described the concepts of array manifold vectors and analog beamforming, from which we provided a step-by-step explanation of the directional channel model used in mmWave systems. Subsequently, we provided a short introduction on estimators performance assessment via CRLB and FIM. We also introduced two important tools that are used in Chapters 4, 5 and 6, which are parameter transformation of FIM, and the equivalent FIM. Different relevant examples are given to help the reader understand the different notions studied. We note that this Chapter provides only the background necessary to understand the thesis content. However, we provide highlights to guide the reader to other resources, should more comprehensive background be necessary.

Chapter 3

Mobile Localization under LOS/NLOS Conditions in Conventional Networks

Overview: *The presence of NLOS link between a BS and UE in a cellular network, is a major issue that limits the performance of the majority of TOA localization methods. Due to blocking obstacles, a signal travels a longer distance to reach the other end of the communication link. Thus, the additional distance introduced by the presence of NLOS link is modeled by a positive measurement bias. In contrast to most of relevant works that are either search-based or iterative, in this Chapter, we propose a two-stage closed-form estimator to localize a UE by three BSs. We use a distance-dependent bias model to derive a range estimator as a first step. We then use trilateration to find an estimate of the UE position. To assess the performance of our technique, we derive the mean square error of the estimator and evaluate numerically the CRLB as a benchmark. We investigate the performance of the proposed method under mixed LOS/NLOS scenarios in four environments, ranging from bad urban environment to rural environment. The provided Monte-Carlo simulations show that our technique performs on average close to the CRLB.*

3.1 Introduction

Over the past two decades, the estimation of a mobile user location has attracted a considerable research focus due to its vital role in different wireless networks applications, such as cellular networks, wireless local area networks, and wireless sensor networks. Location-aware services are on a growing demand in cellular networks field, especially with the introduction of E-911 [9], which allows the authorities to locate the caller and provide emergency services efficiently. This would require a very accurate location estimation capability.

UE localization has been extensively studied under LOS conditions, over the last few decades (See for example, [52,86–88]). However, one major issue that limits the performance of many available methods is the presence of a NLOS link between the UE and the BS, i.e., when an obstacle or more interrupt the direct path between a UE and a BS. One of the most popular localization methods is estimating the range between the two ends by multiplying the signal speed by the TOA [41]. In the LOS case, the measured location is only contaminated by Gaussian measurement noise, while in the NLOS case a measurement *bias* is added up on the measured range and its corresponding noise. Since the presence of obstacles between the UE and BS will force the signal from one end to be reflected on these obstacles before finding its way to the other end, the measured range will always be greater than the actual distance. Therefore, the distance bias under NLOS is always *positive*.

Researchers in this field considered the problem in different approaches. These approaches can be broadly classified into five categories:

1. Identify-and-localize [43–47]: In this category, the link status is statistically identified as being LOS or NLOS. Based on this identification, localization is performed by either incorporating the NLOS links, or discarding them.

2. Mathematical programming: The idea is to formulate the UE localization problem as a constraint optimization problem and solve it by techniques such as linear programming [50], linear quadratic programming [51], the interior point method [52], and sequential quadratic programming [53].

3. Least-squares (LS) solution: These include LS [54] and weighted LS [1, 55] search-based techniques.

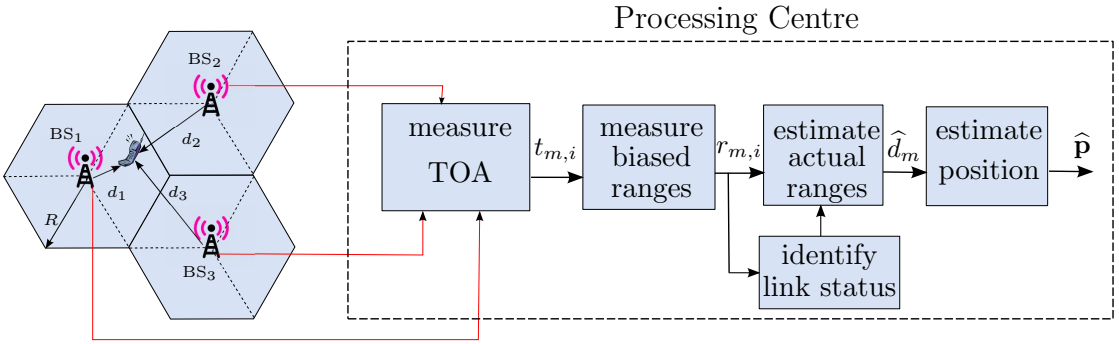

Figure 3.1: The proposed localization technique block diagram. BS_1 is the host base station, while BS_2 and BS_3 are the neighboring BSs. Note that every cell is divided into 3 sectors. R is the cell radius.

4. Robust estimation techniques: These methods try to suppress the effect of NLOS outliers on the measured ranges. To do this, they use estimators such as Huber estimator [89, 90] and least median of squares [91]. On the other hand, [92] and [93] implement robust methods to mitigate the NLOS effect by estimating the measurement bias probability distributions and the position, iteratively.

5. Hybrid methods: Techniques in this category mix TOA with other localization methods such as DOA [94] and RSS [95].

Most of relevant previous TOA-based works are either search-based or iterative. On the contrary, in this chapter we contribute to the first category by proposing a closed-from two-step localization technique for cellular networks. This technique first estimates the range between the UE and three BSs; the hosting BS and two neighboring cells BSs, by an asymptotically unbiased estimator. Subsequently, it estimates the user location using trilateration. In most of the identify-and-localize works, the measurement bias is considered either constant or a random process of a Gaussian [96], exponential [43] or uniform distribution [50] with *given* parameters. On the contrary, we consider the bias model proposed in [97] and adopted in the European standard COST 259 [98–100]. This model is more realistic in that it suggests that the bias follows a conditionally exponential distribution whose parameter is a function of the distance between the BS and UE, the median rms delay-spread, and the shadowing. Although the model in [97] is used to generate

simulation data in [55, 89], and [101], it was not incorporated in the respective localization algorithm. In our work herein, we use this bias model knowledge to derive an asymptotically unbiased estimator that finds approximate values of the range between the UE and all the three BSs. To achieve this, a processing center first collects TOA measurements and uses them to obtain range estimates and identify the link status, as shown in Figure 3.1. Once all the three ranges are estimated, they are used to define three circles. The closest three intersection points of these circles are used to define a triangle whose centroid is taken as the user location estimate. In case where two circles do not overlap, the center of the gap between them is taken as a triangle vertex. To assess the performance of our localization method, we investigate its performance in the four environments classified in [97] as: Bad urban, urban, suburban, and rural.

The contributions and merits of this chapter can be summarized as

- In contrast to [55, 89], and [101], we use a range-dependent bias model [97] to derive a TOA-based closed-form range estimator that is asymptotically unbiased. Subsequently, we use trilateration to obtain an estimator of the UE location in a closed-form.

- The MSE of the range estimator is derived and compared to the CRLB, which we evaluate numerically[1]. The range PDF for the three BS is derived herein, and is used to determine the average CRLB.

- Finally, extensive Monte-Carlo simulations are carried out to assess the performance of the proposed localization technique in the four environments mentioned above, using the performance measures defined in Section 3.5. The results show that the proposed localization technique performs on average close to the CRLB.

The rest of the chapter is organized as follows: Section 3.2 presents the problem formulation and sets the assumptions of this work. Subsequently, Section 3.3, describes in detail the range estimator and shows its unbiased behavior, while Section 3.4 explains the trilateration procedure of estimating the user location.

[1]We resort to numerical computation due to the difficulties in evaluating it analytically. These difficulties are discussed in Section 3.5.

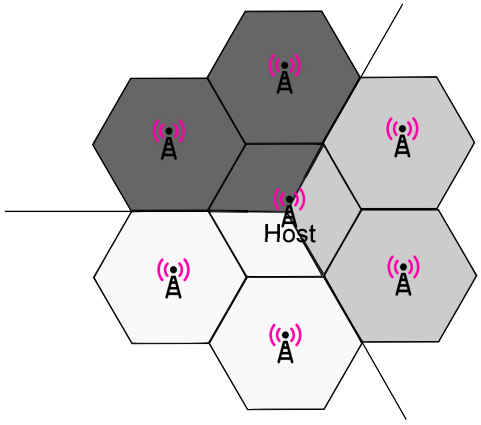

Figure 3.2: BS selection is based on the sector of the host BS that the mobile is in. Three scenarios are possible as illustrated: White, light grey and dark grey.

Section 3.5 discusses the CRLB and the difficulties of obtaining it analytically. It also lists the PDF of the range and defines the performance measure we use for our technique assessment. The numerical results of the Monte-Carlo simulation are given in Section 3.6. A thorough discussion of the results is also included in that section. Finally, the conclusions are presented in Section 3.7.

3.2 Problem Formulation

In this section, we formulate the problem under consideration. Firstly, we present the assumptions of our work, before discussing the signal model.

3.2.1 Assumptions

This work is based on the following assumptions:

- TOA measurements are readily available at the processing center, and were obtained by the TOA method used by the air interface i.e., wireless standard. The ℓ^{th} TOA measurement, τ_ℓ, is used to calculate the ℓ^{th} range, $r_\ell = \tau_\ell c$, where $c = 3 \times 10^8$ m/s is the speed of the signal.

- As shown in Figure 3.2, we consider a cellular network with regular hexagonal

cells. Each cell is divided into three sectors[2]. The user position is uniformly distributed in the cell, and the sector in which the user exists is assumed to be known. This can be identified using hand-over information available at the processing center, as used in [89]. The sector boundaries are used to select the three BSs to perform localization. In other words, considering the host cell in Figure 3.2, when the UE is in a particular sector, the BSs in the cells shaded with the corresponding color are selected to perform the localization. As a result from the hexagonal pattern, BSs locations are also assumed to be given. The backhaul link between BSs and processing center is assumed to be error-free.

- Similar to [55] and [89], the measurement bias due to NLOS is modeled as an exponential random process conditional to a zero-mean log-normal random process. These distributions are described by the nature of the environment as detailed in [97]. Consecutive bias samples are considered independent and identically distributed (i.i.d). On the other hand, the measurement noise is assumed to be i.i.d zero-mean Gaussian process, and independent of the measurement bias.

- The parameters specifying the environment surrounding the UE are considered known and fixed during the measurements acquisition phase. The status of each UE-BS link whether LOS or NLOS is assumed to stay unchanged during the measurements acquisition phase.

3.2.2 Signal Model

Based on the above assumptions the i^{th} range measurement at the m^{th} BS can be written as

$$r_{m,i} = d_m + n_{m,i} + b_{m,i}, \quad i = 1, 2, ...N_{\text{s}}, \ m = 1, 2, 3. \tag{3.1}$$

[2]A sector is a partial area of a cell that is served by a directional antenna, usually with beamwidth of 60° or 120° [102].

where N_s is the sample size. The actual distance between the UE and the m^{th} BS, positioned at $\mathbf{p} = [p_x, p_y]^\mathrm{T}$ and $\mathbf{p}_m = [p_{x,m}, p_{y,m}]^\mathrm{T}$, respectively is given by

$$d_m = \|\mathbf{p} - \mathbf{p}_m\| = \sqrt{(p_x - p_{x,m})^2 + (p_y - p_{y,m})^2}. \tag{3.2}$$

Here, d_m is an unknown variable that is considered constant over the N_s measurements. $n_{m,i}$ denotes the measurement noise and is modeled as a zero-mean Gaussian random variable, i.e., $n_{m,i} \sim \mathcal{N}(0, \sigma_\mathrm{n}^2)$. The measurement bias, which is always non-negative, is denoted by $b_{m,i}$. In fact, $b_{m,i} = 0$ in the case of a LOS link between UE and the BS. On the other hand, $b_{m,i}$ is a positive random variable under NLOS conditions. This is due to the fact that a signal reflected by obstacles will travel a longer distance compared to a LOS signal. According to [97], the stochastic distribution of $b_{m,i}$ is given by

$$f_{B_m}(b_{m,i}) = \begin{cases} 0, & \text{LOS}, \\ \int_{0^+}^{\infty} f_{B_m|Z_m}(b_{m,i}|z_m) f_{Z_m}(z_m) dz_m, & \text{NLOS}, \end{cases} \tag{3.3}$$

where,

$$f_{Z_m}(z_m) = \frac{1}{z_m \sigma_z \sqrt{2\pi}} e^{-\frac{(\ln z_m)^2}{2\sigma_z^2}}, \tag{3.4}$$

is the PDF of Z_m, the lognormal random variable representing the shadowing that affects the signal from the UE to the m^{th} BS, σ_z is measured in nepers ($\sigma_z'[\mathrm{dB}] = \sigma_z \frac{20}{\ln 10}$), and

$$f_{B_m|Z,}(b_{m,i}|z_m) = \frac{1}{\kappa_m} e^{-\frac{b_{m,i}}{\kappa_m}}. \tag{3.5}$$

The parameter κ_m is given by

$$\kappa_m = c\tau_{rms} = cT\sqrt{d_m} z_m, \tag{3.6}$$

where τ_{rms} is the *rms* delay-spread within the UE environment, and T is the median value of τ_{rms} obtained at a distance of 1 km from the BS.

Depending of the severity of T, we focus on four environments: bad urban, urban, suburban and rural environments [97]. Furthermore, we investigate mixed LOS/NLOS scenarios, where the status of a link is detected at the processing center.

Based on the assumptions and system model discussed above, our objective is to estimate the UE position, $\mathbf{p}$ in the vicinity of three BS located at $\mathbf{p}_m \in \mathbb{R}^2$, and covering three hexagonal cells of radius R.

3.3 Closed-Form NLOS Range Estimation

In this section, we propose a two-stage location estimator to address the problem described in Section 3.2. Firstly, we present an asymptotically unbiased range estimator to estimate $\widehat{d}_m$. Secondly, we use these range estimates to find an estimate position of the UE, using trilateration.

3.3.1 Range Estimator

We aim on using the first-order statistics of r_m in the range estimation. The classical approach to compute the PDF of the random variable, R_m, would be to obtain the $f_{B_m}(b_{m,i})$ in (3.3) in a closed-form and convolve it with $f_{N_m}(n_{m,i})$. However, evaluating $f_{B_m}(b_{m,i})$ is extremely intractable when considering the integration of the product of (3.4) and (3.5). In addition, as far as the derivation of our estimator is concerned, we need to know the mean of R_m, while there is no need to know the complete distribution of R_m. Thus, we resort to computing $\mathbb{E}_{R_m}[r_{m,i}]$ relying on the law of total expectation and the independence between N_m and B_m. The steps (3.7)–(3.9b) are used to obtain the expectation of R_m under NLOS conditions, which then can be *estimated* by the sample mean in (3.10b).

Taking the conditional expectation of (3.1) w.r.t. $B_m|Z_m$

$$\begin{aligned}\mathbb{E}_{B_m|Z_m}\left\{r_{m,i}\right\} &= d_m + n_{m,i} + \mathbb{E}_{B_m|Z_m}\left\{b_{m,i}|z_m\right\}, \\ &= d_m + n_{m,i} + cT\sqrt{d_m}z_m, \end{aligned} \tag{3.7}$$

where (3.7) follows from the exponential PDF in (3.5). Taking the expectation of

(3.7) w.r.t Z_m, and applying the law of total expectation [103]

$$\mathbb{E}_{Z_m}\left\{\mathbb{E}_{B_m|Z_m}\{r_{m,i}\}\right\} = \mathbb{E}_{B_m}\left\{r_{m,i}\right\} = d_m + n_{m,i} + cT\sqrt{d_m}\mu_z, \tag{3.8}$$

where $\mu_z = e^{\frac{\sigma_z^2}{2}}$ is the mean of the log-normal distribution given in (3.4).

Taking the expectation of (3.8) with respect to N_m

$$\mathbb{E}_{N_m}\left\{\mathbb{E}_{B_m}\{r_{m,i}\}\right\} = \mathbb{E}_{B_m,N_m}\{r_{m,i}\}, \tag{3.9a}$$

$$= \mathbb{E}_{R_m}\{r_{m,i}\} = d_m + cT\sqrt{d_m}\mu_z. \tag{3.9b}$$

Note that (3.9a) follows from the assumption that the measurement noise and the bias are independent, while (3.9b) uses the assumption that the noise is zero-mean. It should be remarked that (3.9b) represents the theoretical mean of the collected measurement, which requires infinite number of samples to be computed. Thus, assuming ergodicity, we use the sample mean, given by

$$\widehat{\mathbb{E}}_{R_m}\{r_{m,i}\} \triangleq \overline{r}_m = \frac{1}{N_\mathrm{s}}\sum_{i=1}^{N_\mathrm{s}} r_{m,i}, \tag{3.10a}$$

$$= d_m + \frac{1}{N_\mathrm{s}}\sum_{i=1}^{N_\mathrm{s}} b_{m,i}. \tag{3.10b}$$

instead, as a suitable estimate to the mean in (3.9b). This estimator is known to be the best mean estimator as shown in [81].

Based on the sample mean of R_m, we now proceed to derive the closed-form range estimator. Using (3.9b), and (3.10a), we can write

$$\widehat{d}_m + cT\mu_z\sqrt{\widehat{d}_m} - \overline{r}_m = 0. \tag{3.11}$$

Equation (3.11) can be seen as a quadratic equation of $\sqrt{\widehat{d}_m} \geq 0$, which can be solved to obtain

$$\sqrt{\widehat{d}_m} = \frac{-cT\mu_z + \sqrt{(cT\mu_z)^2 + 4\overline{r}_m}}{2}. \tag{3.12}$$

Defining the parameter $\overline{T} \triangleq cT\mu_z$, we write

$$\widehat{d}_m = \begin{cases} \frac{1}{2}\left(\overline{T}^2 - \overline{T}\sqrt{\overline{T}^2 + 4\overline{r}_m}\right) + \overline{r}_m, & \text{NLOS}, \\ \overline{r}_m, & \text{LOS}, \end{cases} \tag{3.13}$$

Note that when $\overline{T} = 0$, the NLOS estimator reduces to the LOS estimator. Moreover, note that since d_m and $b_{m,i}$ are positive, $\overline{r}_m$ is positive. As a result, $\sqrt{\overline{T}^2 + 4\overline{r}_m}$ is always real.

Proposition 3.1 *The proposed range estimator under NLOS in (3.13) is asymptotically unbiased.*

Proof

Using the assumption of zero-mean noise, and substituting (3.10b) in (3.13)

$$\widehat{d}_m - d_m = \frac{1}{2}\left(\overline{T}^2 - \overline{T}\sqrt{\overline{T}^2 + 4d_m + \frac{4}{N_\mathrm{s}}\sum_{i=1}^{N_\mathrm{s}} b_{m,i}}\right) + \frac{1}{N_\mathrm{s}}\sum_{i=1}^{N_\mathrm{s}} b_{m,i}. \tag{3.14}$$

Taking the expectation[3] of (3.14)

$$\mathbb{E}\{\widehat{d}_m\} - d_m = \frac{1}{2}\mathbb{E}\left\{\overline{T}^2 - \overline{T}\sqrt{\overline{T}^2 + 4d_m + \frac{4}{N_\mathrm{s}}\sum_{i=1}^{N_\mathrm{s}} b_{m,i}}\right\} + \frac{1}{N_\mathrm{s}}\sum_{i=1}^{N_\mathrm{s}} \mathbb{E}\{b_{m,i}\}. \tag{3.15}$$

If N_s is large enough, then

$$\frac{1}{N_\mathrm{s}}\sum_{i=1}^{N_\mathrm{s}} b_{m,i} \to \mathbb{E}\{b_{m,i}\} = \mathbb{E}_z\{\kappa_m\} = \overline{T}\sqrt{d_m}, \tag{3.16}$$

which implies that

$$\mathbb{E}\{\widehat{d}_m\} - d_m \to \frac{1}{2}\left(\overline{T}^2 - \overline{T}\sqrt{\overline{T}^2 + 4d_m + 4D\sqrt{d_m}}\right) + \overline{T}\sqrt{d_m}. \tag{3.17}$$

[3]Dropping the subscript from the expectation operator means that the expectation is taken with respect to the random variable between brackets.

By completing the square, and conducting straight-forward simplification, it can be shown that

$$\mathbb{E}\{\widehat{d}_m\} - d_m \to 0, \tag{3.18}$$

which means that the proposed range estimator is asymptotically unbiased. ■

It should be stressed that the notions of *measurement bias* and the *estimator bias* are completely distinct from each other. The measurement bias is inherent to the environment and is caused by the signal traveling a further distance in the case of NLOS. However, the estimator bias is the difference between the average of the estimated parameter and the actual value of this parameter. See (2.22c).This is an estimator property and is not related to the environment. For an unbiased estimator, this difference is zero [81]. See (2.22c).

3.3.2 Range Estimator Error Analysis

Since the proposed range estimator in (3.13) was shown in 3.1 to be asymptotically unbiased, the estimator error variance, $\sigma^2_{d_m}$, and mean-squared error (MSE), $\rho^2_{d_m}$, are equal [81]. In other words

$$\sigma^2_{d_m} = \mathbb{E}\{(\widehat{d}_m - d_m)^2\} = \mathbb{E}\{\widehat{d}^2_m\} - d^2_m = \rho^2_{d_m}. \tag{3.19}$$

As a performance metric, we now compute $\rho^2_{d_m}$. Substituting (3.13) in (3.19) and simplifying the result,

$$\rho^2_{d_m} = \frac{\overline{T}^4}{2} + 2\overline{T}^2\mathbb{E}\left\{\overline{r}_m\right\} + \mathbb{E}\left\{\overline{r}^2_m\right\} - \frac{\overline{T}}{2}\mathbb{E}\left\{\left(\overline{T}^2 + 2\overline{r}\right)\sqrt{\overline{T}^2 + 4\overline{r}_m}\right\} - d^2_m. \tag{3.20}$$

We now calculate the individual terms of (3.20). From (3.10b) and (3.16), respectively, we have

$$2\overline{T}^2\mathbb{E}\left\{\overline{r}_m\right\} = 2d_m\overline{T}^2 + 2\overline{T}^3\sqrt{d_m}. \tag{3.21}$$

$$\mathbb{E}\left\{\overline{r}^2_m\right\} = \mathbb{E}\left\{\left(d_m + \frac{1}{N_\mathrm{s}}\sum_{i=1}^{N_\mathrm{s}} n_{m,i} + \frac{1}{N_\mathrm{s}}\sum_{i=1}^{N_\mathrm{s}} b_{m,i}\right)^2\right\}, \tag{3.22}$$

$$
\begin{aligned}
&= d_m^2 + \frac{1}{N_\mathrm{s}^2}\mathbb{E}\left\{\Big(\sum_{i=1}^{N_\mathrm{s}} n_{m,i}\Big)^2\right\} + \frac{1}{N_\mathrm{s}^2}\mathbb{E}\left\{\Big(\sum_{i=1}^{N_\mathrm{s}} b_{m,i}\Big)^2\right\} \\
&\quad + \frac{2d_m}{N_\mathrm{s}}\sum_{i=1}^{N_\mathrm{s}}\mathbb{E}\left\{b_{m,i}\right\}, \qquad (3.23) \\
&= d_m^2 + \frac{1}{N_\mathrm{s}^2}\mathbb{E}\left\{\sum_{i=1}^{N_\mathrm{s}} n_{m,i}^2\right\} + \frac{1}{N_\mathrm{s}^2}\mathbb{E}\left\{\sum_{i=1}^{N_\mathrm{s}} b_{m,i}^2 + 2\sum_{i=1}^{N_\mathrm{s}}\sum_{j=i+1}^{N_\mathrm{s}} b_{m,i}b_{m,j}\right\} + 2d_m\overline{T}\sqrt{d_m}, \\
&= d_m^2 + \frac{\sigma_\mathrm{n}^2}{N_\mathrm{s}} + \frac{\mathbb{E}\left\{b_{m,i}^2\right\}}{N_\mathrm{s}} + \frac{(N_\mathrm{s}-1)\mathbb{E}^2\left\{b_{m,i}\right\}}{N_\mathrm{s}} + 2d_m\overline{T}\sqrt{d_m}, \\
&= d_m^2 + 2d_m\overline{T}\sqrt{d_m} + \frac{\sigma_\mathrm{n}^2+\sigma_\mathrm{b}^2}{N_\mathrm{s}} + \mathbb{E}^2\left\{b_{m,i}\right\}, \\
&= d_m^2 + \overline{T}^2 d_m + 2d_m\overline{T}\sqrt{d_m} + \frac{\sigma_\mathrm{n}^2+\sigma_\mathrm{b}^2}{N_\mathrm{s}}. \qquad (3.24)
\end{aligned}
$$

Note that the terms $\frac{2d_m}{N_\mathrm{s}}\sum_{i=1}^{N_\mathrm{s}}\mathbb{E}\left\{n_{m,i}\right\}$ and $\frac{1}{N_\mathrm{s}^2}\sum_{i=1}^{N_\mathrm{s}}\mathbb{E}\left\{n_{m,i}\right\}\sum_{i=1}^{N_\mathrm{s}}\mathbb{E}\left\{b_{m,i}\right\}$ vanish in (3.23) since the noise is zero-mean. Here, σ_b^2 is the measurement bias variance calculated by

$$
\begin{aligned}
\sigma_\mathrm{b}^2 &= \mathbb{E}\left\{b_{m,i}^2\right\} - \mathbb{E}^2\left\{b_{m,i}\right\}, \\
&= \mathbb{E}_Z\left\{\mathbb{E}_{B|Z}\left\{b_{m,i}^2|z_m\right\}\right\} - \mathbb{E}_Z^2\left\{\mathbb{E}_{B|Z}\left\{b_{m,i}|z_m\right\}\right\}, \\
&= \mathbb{E}_Z\left\{\sigma_{B|Z}^2 + \mathbb{E}_{B|Z}^2\left\{b_{m,i}|z_m\right\}\right\} - \mathbb{E}_z^2\left\{\mathbb{E}_{B|Z}\left\{b_{m,i}|z_m\right\}\right\}, \\
&= \mathbb{E}_Z\left\{c^2T^2d_mz_m^2 + c^2T^2d_mz_m^2\right\} - (cT\sqrt{d_m}\mu_z)^2 = \overline{T}^2 d_m(2\mu_z^2-1). \qquad (3.25)
\end{aligned}
$$

Furthermore, using (3.10b) and (3.16), we can write

$$
\begin{aligned}
\mathbb{E}\left\{\left(\overline{T}^2+2\overline{r}\right)\sqrt{\overline{T}^2+4\overline{r}_m}\right\} &= \left(\overline{T}^2+2d_m+2\overline{T}\sqrt{d_m}\right)\sqrt{\overline{T}^2+4d_m+4\overline{T}\sqrt{d_m}}, \\
&= \left(\overline{T}^2+2d_m+2\overline{T}\sqrt{d_m}\right)\left(\overline{T}+2\sqrt{d_m}\right), \\
&= \overline{T}^3 + 4\overline{T}^2\sqrt{d_m} + 6\overline{T}d_m + 4d_m\sqrt{d_m}. \qquad (3.26)
\end{aligned}
$$

Finally, substituting (3.21), (3.24) and (3.26) into (3.20) yields

$$
\rho_{d_m}^2 = \frac{1}{N_\mathrm{s}}\overline{T}^2(2\mu_z^2-1)d_m + \frac{1}{N_\mathrm{s}}\sigma_\mathrm{n}^2, \qquad N_\mathrm{s} \gg 1. \qquad (3.27)
$$

In summary, the asymptotic MSE is given by

$$\rho_{d_m}^2 = \begin{cases} \frac{\overline{T}^2(2\mu_z^2-1)d_m+\sigma_{\mathrm{n}}^2}{N_{\mathrm{s}}}, & \text{NLOS}, \\ \frac{\sigma_{\mathrm{n}}^2}{N_{\mathrm{s}}}, & \text{LOS}, \end{cases} \tag{3.28}$$

Note that in the case of LOS, i.e., $\overline{T} = 0$, $\rho_{d_m}^2$ reduces to the well-known CRLB of measurements contaminated by additive white Gaussian noise, $\sigma_{\mathrm{n}}^2/N_{\mathrm{s}}$ [81].

3.4 Localization Based on Range Estimates

After estimating the range between every BS and the UE, we proceed to estimate the UE location by, first, drawing circles with the estimated ranges, $\widehat{d}_m$, as radii. Then, we find the number of intersecting circles, denoted by $C \geq 0$, and the points of intersection of these circles. Two circles i, j are overlapping if

$$\widehat{d}_i + \widehat{d}_j > \|\mathbf{p}_i - \mathbf{p}_j\|. \tag{3.29}$$

Subsequently, we define a triangle and estimate the UE location as its centroid. However, since our distance estimator is asymptotically unbiased. i.e., $\mathbb{E}[\widehat{d}_m] \to d_m$, for some measurements, the distance will be under-estimated $\widehat{d}_m < d_m$, while for the other measurements, it will be over-estimated, $\widehat{d}_m > d_m$. However, on the long run the average estimated distance, $\mathbb{E}[\widehat{d}_m]$, approaches the actual distance, d_m. These two cases are depicted in Figure 3.3, depending on which the triangle is defined:

1. Case 1: Three intersecting circles ($C = 3$)
   In this case, the triangle vertices are defined by the three intersection points bounding the intersection area, as shown in Figure 3.3.(a). The three triangle vertices are given by

$$\mathbf{v}_1 = \arg \min_{\mathbf{u} \in \{\mathbf{c}_{12}^{(1)}, \mathbf{c}_{12}^{(2)}\}} \|\mathbf{u} - \mathbf{p}_3\|, \tag{3.30}$$

$$\mathbf{v}_2 = \arg \min_{\mathbf{u} \in \{\mathbf{c}_{23}^{(1)}, \mathbf{c}_{23}^{(2)}\}} \|\mathbf{u} - \mathbf{p}_1\|, \tag{3.31}$$

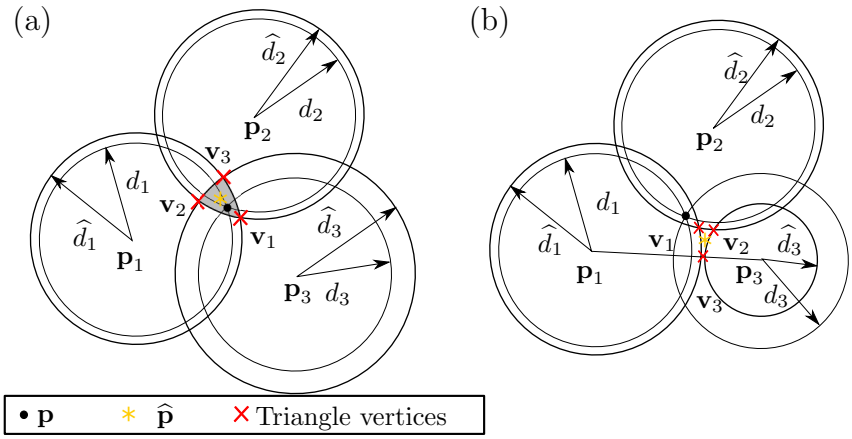

Figure 3.3: Effect of range estimation error on location estimation (a) $C = 3$ and (b) $C = 2$.

$$\mathbf{v}_3 = \arg \min_{\mathbf{u} \in \{\mathbf{c}_{31}^{(1)}, \mathbf{c}_{31}^{(2)}\}} \|\mathbf{u} - \mathbf{p}_2\|, \tag{3.32}$$

where $\mathbf{c}_{ij}^{(1)}, \mathbf{c}_{ij}^{(2)} \in \mathbb{R}^2$ are the two intersection points of the circles i and j.

2. Case 2: Less than three intersecting circles ($C < 3$)
   Because less than three circles overlap, three intersection points are partially available. To decide on triangle vertices, the circles are investigated in pairs. Since any two intersecting circles will have two intersection points, we define a triangle vertex by the intersection point closer to the third circle (non-intersecting), similar to (3.30) – (3.32). For the non-overlapping circles, we define the triangle vertex as the point in the gap center between the two circles. For the example illustrated in Figure 3.3.(b), two circles overlap, but a third point is needed for trilateration. Thus, we select the mid-gap point as a reasonable heuristic approach.

$$\mathbf{v}_3 = \mathbf{p}_1 + (\widehat{d}_1 + 0.5g)\frac{\mathbf{p}_3 - \mathbf{p}_1}{\|\mathbf{p}_3 - \mathbf{p}_1\|}, \tag{3.33}$$

   where $g = (\widehat{d}_1 + \widehat{d}_3) - \|\mathbf{p}_3 - \mathbf{p}_1\|$, is the gap between the two circles. To see why this approach is taken, consider Figure 3.3.(b). Circle 1 and circle 3 do

not overlap. This means that $\widehat{d_1}$, $\widehat{d_3}$, or both are under-estimated. However, we have no additional information to weigh among the three possibilities. For this reason, we choose the mid-gap point as a trilateration point.

After obtaining the triangle vertices, $\mathbf{v}_1, \mathbf{v}_2$ and $\mathbf{v}_3$, the UE location is estimated by

$$\widehat{\mathbf{p}} = \frac{1}{3}(\mathbf{v}_1 + \mathbf{v}_2 + \mathbf{v}_3). \tag{3.34}$$

3.5 Cramér-Rao Lower Bound

Discussed in Chapter 2, CRLB is one of the most important performance benchmark for an estimator. In our problem, the CRLB of d_m in (3.1) is defined by [81]

$$\text{CRLB}(d_m) = \frac{-1}{\mathbb{E}\left[\frac{\partial^2 \ln f(\mathbf{r}_m; d_m)}{\partial^2 d_m}\right]}, \tag{3.35}$$

where $\mathbf{r}_m = [r_{m,1}, r_{m,2}, ..., r_{m,N_\text{s}}]^T$. Note that in the classical case of LOS, this bound is given by $\sigma_\text{n}^2/N_\text{s}$ [81]. Although there has been some works on CRLB for NLOS localization, e.g., [54] and [93], none of these works addressed the problem formulated in Section 3.2. Therefore, in this section, we focus on NLOS CRLB.

To start with, we need the joint probability distribution $f(\mathbf{r}_m; d_m)$. However, since $r_{m,1}, r_{m,2}, ..., r_{m,N_\text{s}}$ are i.i.d, we can write

$$f(\mathbf{r}_m; d_m) = \prod_{i=1}^{N_\text{s}} f(r_{m,i}; d_m) = f^{N_\text{s}}(r_{m,1}; d_m), \tag{3.36}$$

where the first equality follows from the independence assumption, and the second equality follows from the identical distribution assumption. Without loss of generality, we choose PDF pf the first sample, $r_{m,1}$. We make the following remarks,

- $r_{m,1} = (d_m + n_{m,1}) + b_{m,1}$, so to evaluate $f(r_{m,1}; d_m)$, we would require the joint probability $f_{B,N+D}(b, n + d_m)$.
- From (3.1), $b_{m,1}$ and $d_m + n_{m,1}$ are not independent since $b_{m,1}$ is a function

Algorithm 1 Numerical Evaluation of CRLB in (3.35), using MATLAB

Input $N_{\rm s}, \sigma_{\rm n}, \sigma_{\rm z}, R, T, c, N_{\rm b}, I_{\rm r}, I_{\rm crlb}$.
initialize $\mathrm{CRLB}(d_m) = 0, \forall d_m$
for $k = 1 : I_{\rm crlb}$ **do**
  for $d_m = 1 : 2R$ **do**
    initialize $\widehat{f}(r; d_m) = 0$
    Generate z_m
    for $i = 1 : I_{\rm r}$ **do**
      Generate $N_{\rm b}$ instances of $b_{m,i}$, and $n_{m,i}$,
      Calculate the corresponding $N_{\rm b}$ instances of $r_{m,i} = d_m + b_{m,i} + n_{m,i}$,
      Obtain the Kernel Density Estimate,$\widehat{f}(r_i; d_m)$, using a a normal kernel function [104].
      $\widehat{f}(r; d_m) = \widehat{f}(r; d_m) + \widehat{f}(r_i; d_m)$
    end for
    $\widehat{f}(r; d_m) = \widehat{f}(r; d_m)/I_{\rm r}$
  end for
  for $j = 1 : N_{\rm b}$ **do**
    $g(j, d_m) = \frac{\partial^2}{\partial d_m^2} \ln \widehat{f}(j; d_m)$, where the second derivative is obtained by the MATLAB function `diff(.,2)`
  end for
  $\mathrm{CRLB}(d_m) = \mathrm{CRLB}(d_m) + \frac{-1}{N_{\rm s} \sum_j g(j,d_m) \widehat{f}(j;d_m)}$
end for
$\mathrm{CRLB}(d_m) = \mathrm{CRLB}(d_m)/I_{\rm crlb}$.

of d_m. Therefore, their joint distribution cannot be simply obtained by the convolution of the marginal distribution, $f_B(b)$ and d_m-shifted $f_N(n)$.

- Even if they were independent, the integral in (3.3) is very hard to evaluate from (3.4) and (3.5).

For these reasons, we proceed to evaluate the CRLB numerically as listed in Algorithm 1.

The CRLB procedure in Algorithm 1 gives a performance measure for individual range estimators. However, to evaluate the overall localization performance, we need to define some performance measures that take into account the average performance over the three cells. But before that, we need to evaluate the PDF of the range, $f_D(d_m)$, for $m = 1, 2, 3$. As derived in Appendix A, for the hosting cell

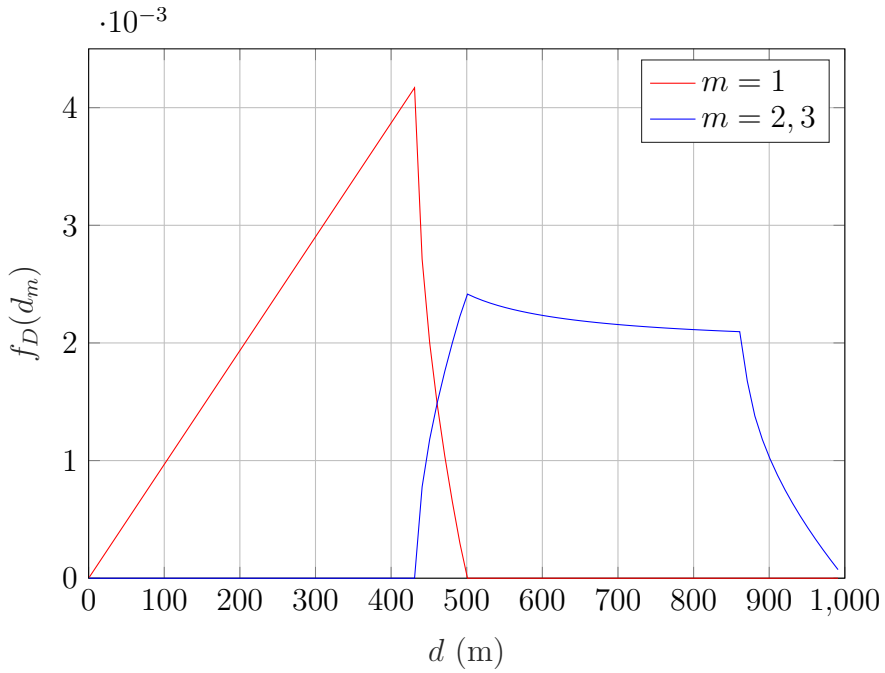

Figure 3.4: PDF of the UE range from the m^{th} BS, $m = 1$, 2 and 3. R = 500 m.

$(m = 1)$, this distribution is given by

$$f_D(d_m) = \begin{cases} \frac{4\pi d_m}{3\sqrt{3}R^2}, & 0 \leq d_m < \frac{\sqrt{3}R}{2}, \\ \frac{8d_m}{\sqrt{3}R^2}\left[\frac{\pi}{6} - \cos^{-1}\left(\frac{\sqrt{3}R}{2d_m}\right)\right], & \frac{\sqrt{3}}{2}R \leq d_m < R. \end{cases} \tag{3.37}$$

For the two neighboring cells $(m = 2, 3)$, this distribution is given by

$$f_D(d_m) = \begin{cases} \frac{4d_m}{\sqrt{3}R^2}\cos^{-1}\left(\frac{\sqrt{3}R}{2d_m}\right), & \frac{\sqrt{3}R}{2} \leq d_m < R \\ \frac{2d_m}{\sqrt{3}R^2}\sin^{-1}\left(\frac{\sqrt{3}R}{2d_m}\right), & R \leq d_m < \sqrt{3}R \\ \frac{2d_m}{\sqrt{3}R^2}\left[\sin^{-1}\left(\frac{\sqrt{3}R}{d_m}\right) - \frac{\pi}{3}\right], & \sqrt{3}R \leq d_m < 2R \end{cases} \tag{3.38}$$

Figure 3.4 shows the plots of (3.37) and (3.38) for a cell with radius of 500 m.

To measure the performance averaged over the three cells, we define the following measures:

- Average CRLB over three cells:

$$\widetilde{\sigma}^2_{\mathrm{CRLB}} = \widetilde{\sigma}^2_{\mathrm{CRLB|LOS}} Pr(\mathrm{LOS}) + \widetilde{\sigma}^2_{\mathrm{CRLB|NLOS}} Pr(\mathrm{NLOS}). \tag{3.39}$$

where $Pr(\mathrm{LOS})$ and $Pr(\mathrm{NLOS})$ are the probabilities of the link being LOS or NLOS, respectively, and are assumed to be given *a priori*. The exact values of these two probabilities depend on several factors, such as the environment, the location and being indoor or outdoor. $\widetilde{\sigma}^2_{\mathrm{CRLB|LOS}} = \sigma^2_{\mathrm{n}}/N_{\mathrm{s}}$, while

$$\widetilde{\sigma}^2_{\mathrm{CRLB|NLOS}} = \frac{1}{3}\sum_{m=1}^{3}\Big[\int_{d_m} \mathrm{CRLB}(d_m) f_D(d_m)\mathrm{d}d_m\Big]. \tag{3.40}$$

under the assumption that d_m are mutually independent, $m = 1, 2, 3$.

- Average Range Estimation MSE :
  When the link status is perfectly known at the processing center, the average range estimation MSE is denoted by

$$\widetilde{\rho}^2_{\mathrm{d_e|k}} = \left(\frac{\rho^2_{d_1} + \rho^2_{d_2} + \rho^2_{d_3}}{3}\Big|\text{link status known}\right). \tag{3.41}$$

  On the other hand, when the link status is estimated by a decision rule, the average range estimation MSE is denoted by

$$\widetilde{\rho}^2_{\mathrm{d_e|i}} = \left(\frac{\rho^2_{d_1} + \rho^2_{d_2} + \rho^2_{d_3}}{3}\Big|\text{link status identified}\right). \tag{3.42}$$

- Location Estimation MSE:
  Depending on the link status knowledge, this MSE is denoted by

$$\widetilde{\rho}^2_{\mathrm{p_e|k}} = \mathbb{E}\Big[\|\mathbf{p} - \widehat{\mathbf{p}}\|^2\Big|\text{link status known}\Big],$$
$$\widetilde{\rho}^2_{\mathrm{p_e|i}} = \mathbb{E}\Big[\|\mathbf{p} - \widehat{\mathbf{p}}\|^2\Big|\text{link status identified}\Big].$$

Table 3.1: Median RMS Delay Spread For The Considered Environments

Environment	T (μs)
Bad Urban	1.0
Urban	0.4
Suburban	0.3
Rural	0.1

3.6 Numerical Results and Discussion

To investigate the performance of the proposed algorithm, we perform extensive Monte-Carlo simulations. We also present the results for the numerical computation of the CRLB in this section, but before that, we start by describing the simulation setup.

3.6.1 Simulation Setup

The measured range samples are generated according to the model discussed in Section 3.2. The model parameters we use here are chosen to match the recommended values in [97]. In this regard, the measurement noise is generated as a zero-mean Gaussian process with $\sigma_n = 60$ m. Moreover, the lognormal shadowing, Z_m, conditioning the measurement bias parameters is specified by σ'_z =4 dB, while the values of T for the four environments under interest are given in Table 3.1.

In our simulations, we consider a seven regular hexagonal cells served by BSs located at $(0, 0)$, $(1.5R, \sqrt{3}/2R)$, $(1.5R, -\sqrt{3}/2R)$, $(0, -\sqrt{3}R)$, $(-1.5R, -\sqrt{3}/2R)$, $(-1.5R, \sqrt{3}/2R)$, and $(0, \sqrt{3}R)$, where $R = 500$ m, as shown in Figure 3.2. The user, located in the first cell, is localized by three BSs that are defined by the sector boundaries, as described in Section 3.2.1. The model in [105] was used to generate user locations uniformly distributed over a regular hexagon.

For the link status identification, we use the single BS decision-theoretic method proposed in [96]. By recalling that $\sigma^2_{\bar{r}} = \sigma^2_{\mathrm{n}} + \sigma^2_{\mathrm{b}} = \sigma^2_{\mathrm{n}} + \overline{T}^2 d_m(2\mu^2_z - 1)$, a decision

rule that can be used to identify the link status is

$$\sigma_{\overline{r}}^2 \underset{\text{LOS}}{\overset{\text{NLOS}}{\gtrless}} \eta\sigma_{\text{n}}^2, \tag{3.43}$$

where $\sigma_{\overline{r}}^2$ is the recorded sample variance and $\eta > 1$ is a decision threshold that depends on the environment and the cell being either a UE host or a neighbor cell. In our simulations, a link status is modeled as an equally-probable Bernoulli random variable.

For location estimation performance comparison, we use a Weighted-LS technique similar to [1]

$$\widehat{\mathbf{p}}_{\text{LS},i} = \arg\min_{\widehat{\mathbf{p}}} \sum_{m=1}^{3} \frac{\left(r_{m,i} - \|\widehat{\mathbf{p}} - \mathbf{p}_m\|\right)^2}{\alpha_m}, \tag{3.44}$$

where

$$\alpha_m = \begin{cases} \sigma_n^2, & \text{LOS}, \\ \sigma_n^2 + \overline{T}^2(2\mu_z^2 - 1)\|\widehat{\mathbf{p}} - \mathbf{p}_m\|, & \text{NLOS}. \end{cases} \tag{3.45}$$

Subsequently, the location estimates taken as

$$\widehat{\mathbf{p}} = \sum_{i=1}^{N_{\text{s}}} \widehat{\mathbf{p}}_{\text{LS},i}. \tag{3.46}$$

3.6.2 Range Estimation

Considering the range estimation stage only, the CRLB of the NLOS range estimator is given in Figure 3.5. Since CRLB increases with d_m, we can see that the farther the UE from the BS, the harder it is to get a lower error estimate. Also, we can infer that CRLB is a function of the environment, in that it becomes worse for environments with higher delay spread. Recall that $0 \leq d_1 \leq R$, while $\sqrt{3}R/2 \leq d_2, d_3 \leq 2R$, which means d_1 is generally better estimated than d_2 and d_3. Finally, note that the four CRLB curves approach $\sigma_{\text{n}}^2/N_{\text{s}} = 36$ m^2 when $d_m \to 0$. This is because the bias term in (3.1) vanishes and only noise is present, which

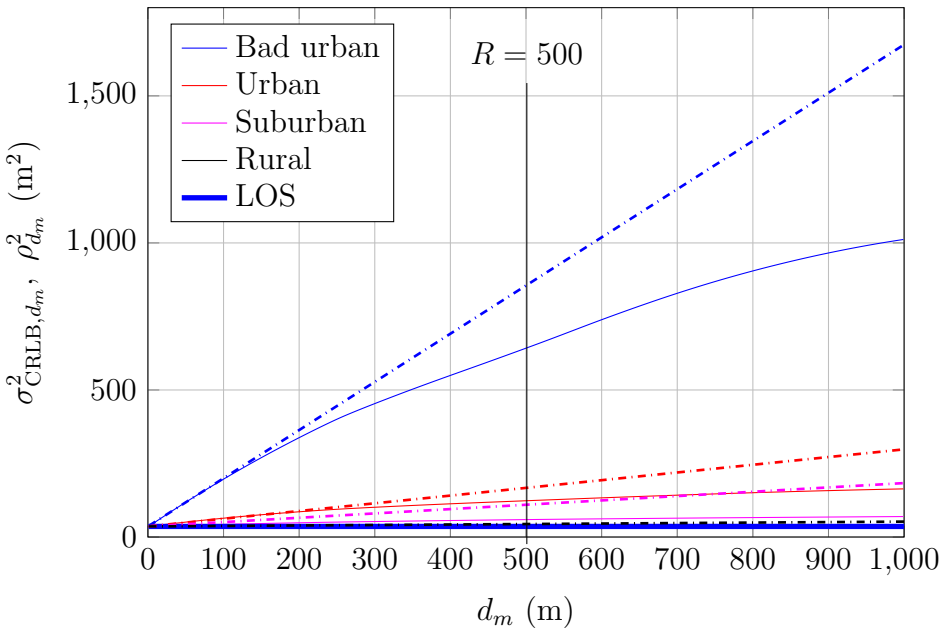

Figure 3.5: CRLB of the range estimator performance in terms of d_m (solid) compared to the range estimation error variance $\rho^2_{d_m}$ (dash-dot), for N_s=100, R=500 m. $0 \leq d_1 < R$, and $\frac{\sqrt{3}}{2}R \leq d_2, d_3 < 2R$

leads the bound to become similar to that of the LOS case. Moreover, Figure 3.5 shows that $\rho^2_{d_m}$ of the proposed distance estimator performs closely to the CRLB for lower d_m values, but diverges as the distance between the UE and BS increases.

We now present the results for the range estimation under mixed LOS/NLOS conditions with the statuses of the links are assumed to be known. Figure 3.6 shows how the selection of the data size N_s affects the range RMSE, measured by $\widetilde{\rho}_{\mathrm{de|k}}$, for the four user environments. The range RMSE decays as N_s increases, which is sensible because the range estimator requires averaging the recorded range sample, and this average is better approximated with larger history. We can also infer from this figure that the range estimation accuracy is generally inversely proportional to the value of T that specifies the environment. Note that, from (3.6), larger T implies higher delay spread, measurement bias mean, and measurement bias variance.

Figure 3.7 illustrates the identification error effect on the range estimation.

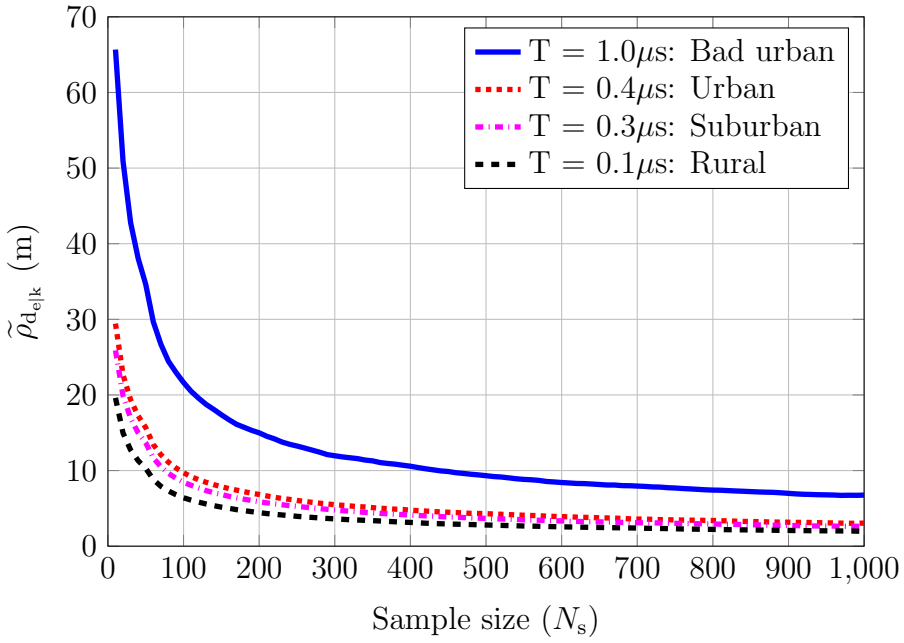

Figure 3.6: Average range RMSE as a function of N_s when link statuses are known, obtained by averaging over 1000 user location.

The identification error is the error made in the link status identification block. An identification error occurs when the actual link is LOS, while it was identified as NLOS, or vise versa. The effect of this error is quantified by the difference between $\widetilde{\rho}_{\mathrm{d_e|k}}$ and $\widetilde{\rho}_{\mathrm{d_e|i}}$. In this figure we can see that the identification error has a minor effect on the three environments with higher T, when $N_\mathrm{s} \geq 100$. However, the identification error is substantial in rural areas. For example, at $N_\mathrm{s} = 200$ the identification error is around 4.8 m. To see why, recall that the identification approach we are using from [96] and defined in (3.43), relies on the gap between the sample variance, $\sigma_{\overline{r}}^2 = \overline{T}^2 d_m(2\mu_z^2 - 1) + \sigma_n^2$, and the noise variance, σ_n^2. Consequently, the larger this gap is, the more accurate the decision. So, we compute $\sigma_{\overline{r}}^2$ for the four environments and compare it to σ_n^2, as shown in Table 3.2. It is evident that $\sigma_{\overline{r}}^2$ in the rural case is relatively close to the value of σ_n^2, in contrast to the other three environments, where $\sigma_{\overline{r}}^2$ is more pronounced and comparable to the noise variance. This means that the decision rule from [96] can easily identify link status for the bad urban, urban and suburban environments, while making larger identification errors in the case of rural environment. With this said, it should be stressed that

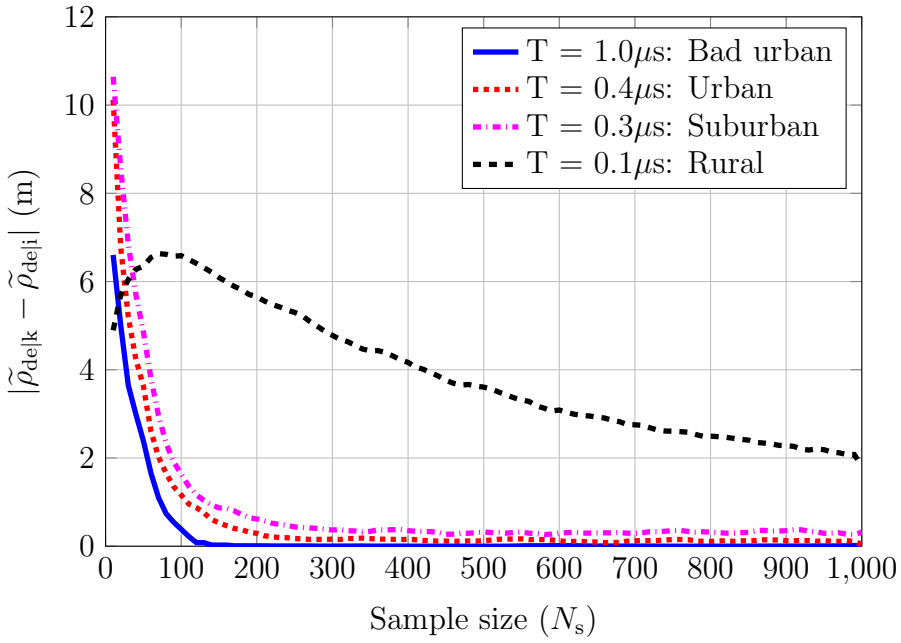

Figure 3.7: Identification error effect on range estimation as a function of N_{s} obtained by averaging over 1000 user location.

Table 3.2: Sample Variance and Noise Variance for Different Environments

Environment	$\sigma_{\overline{r}}^2 = \overline{T}^2 d_m(2\mu_z^2 - 1) + \sigma_n^2$	σ_n^2
Bad Urban	48577	3600
Urban	10796	3600
Suburban	7648	3600
Rural	4050	3600

we do not address the identification problem in this Chapter, but used this method from [96] as-is.

Although higher N_{s} can reduce the distance error (Figure 3.6 and Figure 3.7), this would require more calculations and storage capability at the processing center, i.e., higher complexity. For this reason, we select $N_{\mathrm{s}} = 100$ as a suitable trade-off for the subsequent results in this section.

To have a deeper look, we now compare the range estimation using different setups in Figure 3.8. In the legend, $\widetilde{\rho}_{\mathrm{LOS}}$ indicates that the results were obtained by

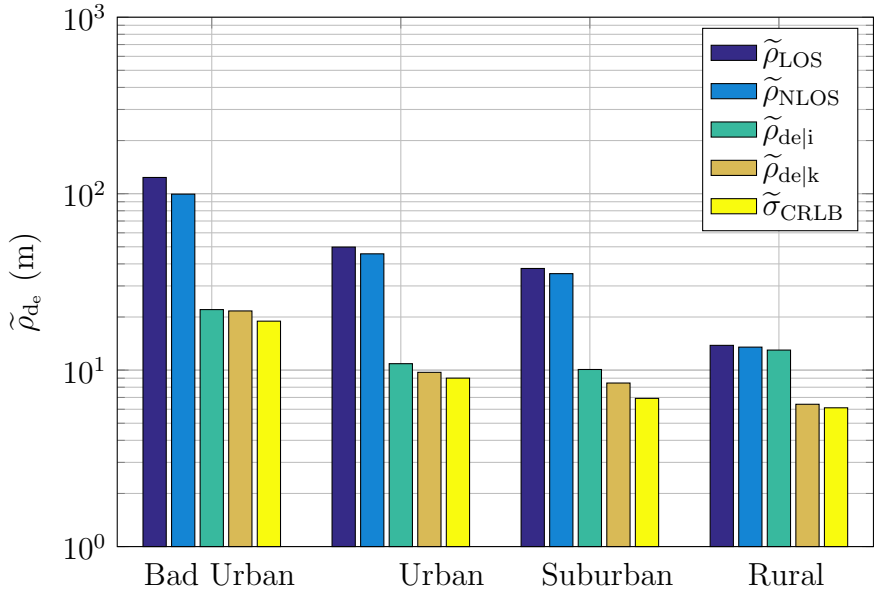

Figure 3.8: Average RMSE of range error in different setups compared to average CRLB, obtained by averaging over 1000 user location with $N_{\mathrm{s}} = 100$.

the averaging estimator that assumes that all the links are LOS [81], i.e., ignoring the existence of NLOS paths. On the contrary, $\widetilde{\rho}_{\mathrm{NLOS}}$ is obtained by the estimator in (3.13) that assumes that all the paths are NLOS, i.e., assumes measurement bias exists in all paths. $\widetilde{\rho}_{\mathrm{de|i}}$, $\widetilde{\rho}_{\mathrm{de|k}}$, and $\widetilde{\sigma}_{\mathrm{CRLB}}$ are the square roots of the quantities defined in (3.42), (3.41), and (3.39), respectively.

It can be concluded from Figure 3.8 that, when link identification is implemented, the proposed estimator performs close to $\widetilde{\sigma}_{\mathrm{CRLB}}$ with difference of 3.1 m, 1.9 m, 3.2 m, and 6.5 m in the bad urban, urban, suburban, and rural environments, respectively. Smaller gaps occur when the link status is perfectly known at the processing center, with the performance of the proposed technique approach the CRLB for the suburban and rural areas. Also, notice that the error upper-bound is well above the proposed estimator error. On an absolute measure, the proposed estimator provides range estimates with $\widetilde{\rho}_{\mathrm{de|i}}$ of: 21.4 m, 10.9 m, 10.1 m, and 13.0 m in the four environments, respectively.

Table 3.3: The Percentage of The Number of Overlaps, C with N_{s}=100.

Environment	$C=3$	$C=2$	$C=1$
Bad Urban	75.00	24.40	0.60
Urban	80.17	19.53	0.30
Suburban	81.29	18.46	0.24
Rural	80.30	19.36	0.34

3.6.3 Location Estimation

After discussing the range estimation accuracy in Section 3.6.2 as a first step, we now discuss the results of the location estimation as a second step.

Firstly, we present the frequency of the number of overlaps used for trilateration[4] in Table 3.3. These values were obtained during the simulations campaign by counting the number of overlaps in each simulation iteration, and dividing the total number of occurrences by the number of iterations, which is 10^5. As can be noticed, in the great majority of experiments, 3 overlaps are used to obtain a triangle centroid. On the other hand, 2 overlaps occur with lower probability, while 1 overlap occurs with a negligible percentage. Note that this table is obtained when the link statuses are unknown.

Figure 3.9 illustrates the location estimation accuracy in terms of $\widetilde{\rho}_{\mathrm{p_e|k}}$ for the four environments. Observations similar to Figure 3.6 can be seen in Figure 3.9. Particularly, notice that any increase of recorded data size beyond $N_{\mathrm{s}} = 200$, offers a minor enhancement relative to the additional required complexity. For example, we would get 50% RMSE enhancement when the data size is 5 times larger.

We now benchmark the location estimation error, when the status is either known or identified at the processing center, with the cases when all the links are assumed to be either LOS or NLOS. This comparison is illustrated in Figure 3.10, for N_{s} =100. Remarkably, the proposed method, isolated from identification error, performs well below the NLOS and LOS estimation cases with RMSE of 25.1 m, 14.6 m, 13.0 m, and 10.3 m, in the four environments respectively. Furthermore, when the case of $\widetilde{\rho}_{\mathrm{p_e|i}}$ is considered, we get RMSE of 25.4 m, 15.7 m, 14.6 m,

[4]Measured as a percentage of the total number of experiments.

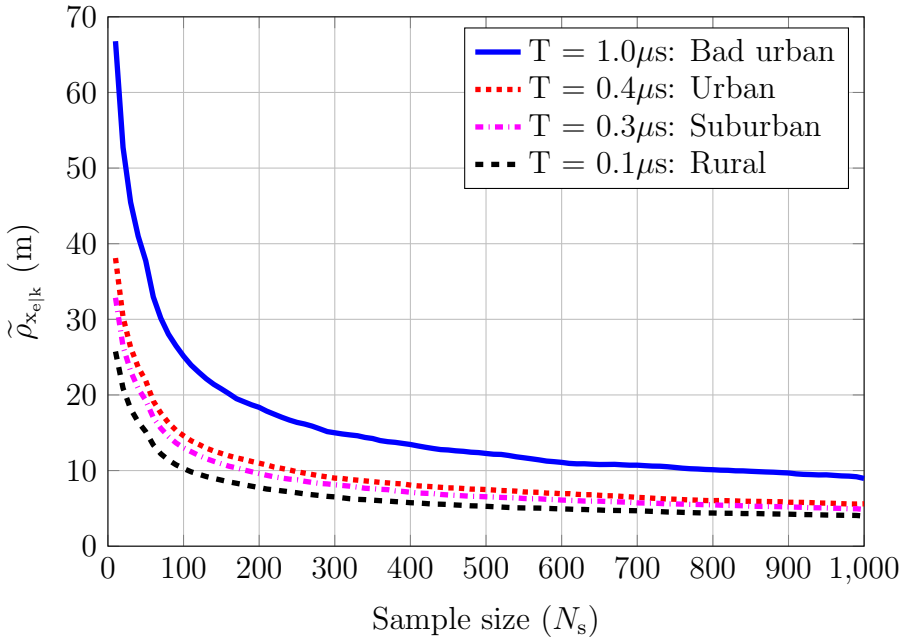

Figure 3.9: Average RMSE of location estimation error as a function of N_s, obtained by averaging over 1000 user location, with link status known.

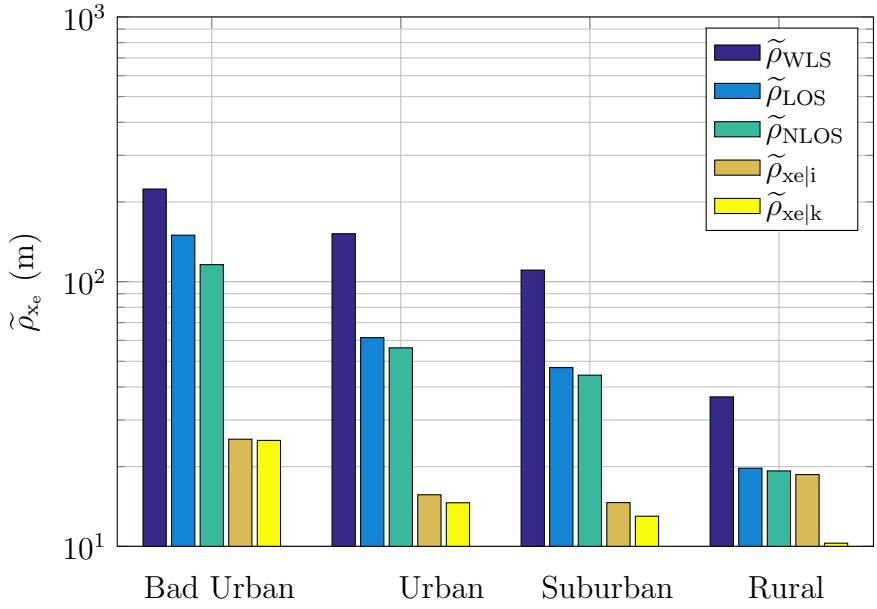

Figure 3.10: Average RMSE of location error in different setups obtained by averaging over 1000 user location with $N_\mathrm{s} = 100$, compared to the WLS method [1].

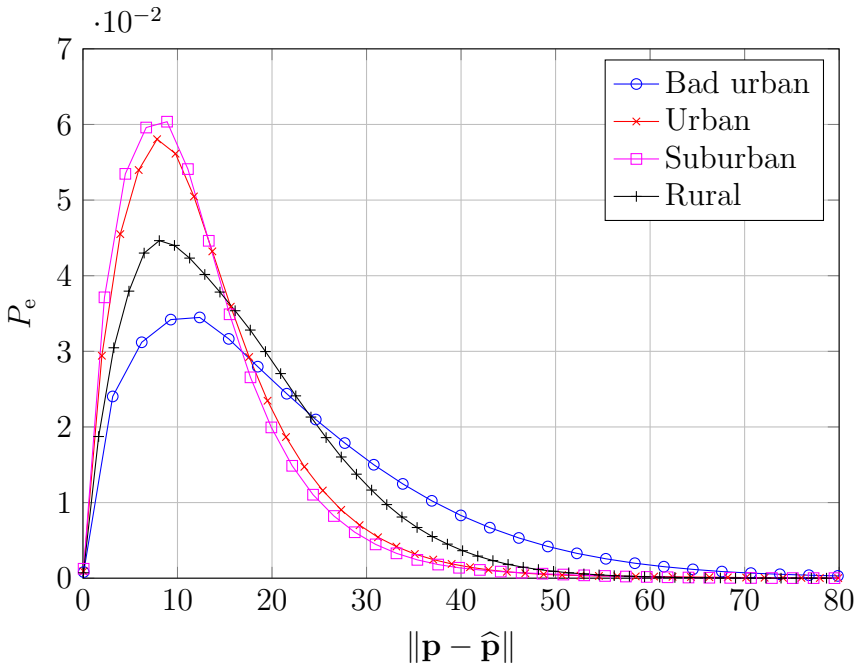

Figure 3.11: PDF of the location error with N_s =100, obtained by averaging over 1000 user locations, with link status identified.

and 18.7 m, respectively. Since the error of a stage propagates to the subsequent stage, it should be highlighted that the $\widetilde{\rho}_{\mathrm{pe|i}}$ effect in Figure 3.10 comprises three error components, namely: identification error, range estimation error and location estimation error.

Finally, note that the proposed approach outperforms the WLS approach, denoted by $\widetilde{\rho}_{\mathrm{WLS}}$ and outlined in (3.44)-(3.45), by a large margin. This is because our approach takes into account the bias distribution function, in contrast to the one in [1]. Also note that due to the bias being non-Gaussian, the numerator of (3.44) is non-Gaussian. Moreover, WLS requires a higher number of BS for an accurate estimate. These two reasons cause WLS to have a greater estimation error than the other considered approaches in Figure 3.10.

To get a better insight on the nature of location error, Figure 3.11 illustrates the approximate error distributions for the four environments obtained during the simulations with identification. Again, note that this this error is the total error due to identification error, ranging error, and localization error. It can be seen

Table 3.4: Localization Error Central Tendency Measures, N_s=100

Measure	Bad Urban	Urban	Suburban	Rural
Mean (m)	20.79	13.07	12.28	15.93
Median (m)	17.42	11.15	10.44	14.01
Mode (m)	10.97	8.14	7.90	8.16

that most of the error is concentrated at very low values. Table 3.4 describes this quantitatively. Since the bad urban environment has the highest median rms delay-spread, T, among all the investigated environments, it exhibits the worst performance in the considered scenarios.

3.7 Conclusions

In this chapter, we have presented a two-stage closed-form NLOS mobile localization technique that is based on TOA estimation at the closest three BSs. A key feature in our work is that it solves the NLOS UE localization in closed-form, in contrast to most of works that are either search-based or iterative. We have used a distance-dependent bias model to derive an asymptotically unbiased estimator in order to estimate the distance between each of the BS and the UE, at the first stage. Subsequently, the intersection points of the circles, defined by radii equal to the estimated distances, are used to define a triangle whose centroid is taken as the user location estimate. In addition, we have derived the MSE of the proposed range estimator, and obtained the CRLB numerically to benchmark the performance of the distance estimators. Furthermore, we have derived the PDF of the distance between the three BS and the UE. The simulations presented herein demonstrate that with a cell radius of 500 m, our localization method is accurate with an average position error ranging between 12–21 meters depending on the environment. It is worth mentioning that in a rural environment, a more efficient identification rule is needed. The focus of this chapter has been on localization using 3 BSs. We did not addressed the identification issue, neither did we address the case where more BSs are involved in the localization. These are left for future work. Another

potential venue for investigation in the context of this Chapter is the application of linearised solution of the TOA equations to obtain an estimate of the user location, instead of taking the centroid of the intersection area. Moreover, since the performance of the proposed technique in this Chapter is model-dependent, it is meaningful to consider model mismatch analysis and simulation for future work. Finally, we note that, even though the proposed technique performs closely with the CRLB, the average error obtained is in the order of several meters, which implies that location-aware communications have limited applications in conventional cellular networks.

Publications Resulted from This Chapter

- **Z. Abu-Shaban**, X. Zhou, T. Abhayapala, "A Novel TOA-based Mobile Localization Technique under Mixed LOS/NLOS Conditions for Cellular Networks," *IEEE Transactions on Vehicular Technology*, vol. 65, no. 11, pp. 8841-8853, Nov 2016.

Chapter 4

Beamforming for Initial Access in 5G mmWave Networks

Overview: *The utilization of the millimeter-wave frequency band in 5G is a highly-debated current topic. MmWave MIMO systems will use arrays with large number of antennas at the transmitter and the receiver, implemented on a relatively small area. With the inherent high directivity of these arrays, the initial access to the network (IA) will be challenge in 5G mmWave, since using omni-directional transmission is not feasible due to the high propagation loss. Therefore, algorithms to help the UE find the BS and establish a communication link should be carefully designed. Towards that, we examine two beamforming schemes, namely, random-phase beamforming (RPBF) and directional beamforming (DBF), under the line-of-sight channel model. Since the step following IA would be channel estimation, we compare RPBF and DBF with respect to the the CRLB of jointly estimating the channel parameters: DOA, DOD, TOA, and the complex channel gain. The results show that the application of RPBF is more appropriate in the considered scenario because it attains a lower CRLB with fewer beams compared to DBF.*

4.1 Introduction

One of the enabling technologies of the fifth generation of mobile networks (5G) is the millimeter-wave technology (mmWave) that operates at a carrier frequency

in the range of 30–300 GHz [62–65, 106]. MmWave allows packing high number of antennas in a relatively small area due to their small wavelengths – from 1 mm to 1 cm. In addition, the massively available spectrum of mmWave would easily enable transmission with extremely high data rates [62]. Although 5G localization research is still in its infancy, these two reasons reinforce the role that the mmWave technology can play in 5G localization.

Due to the special characteristics of the mmWave channel, directional transmission with large-size arrays, at both the transmitter and the receiver, is going to be utilized [64]. However, when initiating a communication link, this high directionality is an issue for a user equipment (UE) trying to find the base station (BS), or vice-versa, especially that omni-directional transmission with antenna arrays is a challenge by itself [107, 108].

The mmWave initial access (IA) techniques with analog beamforming were reviewed in [72]. The three approaches compared therein include two direction-based methods, namely exhaustive search and iterative search. The third method is a GPS-assisted algorithm. The disadvantage of these approaches is mainly the delay of finding the proper transmission direction through scanning the area of interest.

Our approach in this thesis to consider the transmission of several beams simultaneously rather than scanning. The main advantage of such approach is that it reduces the search time significantly with respect to the exhaustive search and iterative search methods. This is particularly important in mmWave systems as the 5G network will be designed for low-latency applications [61]. In contrast to the directional beamforming, we focus on random beamforming. The concept of random beamforming is not new per-se. Randomly-directional beamforming is a method of opportunistic beamforming that was investigated for mmWave receivers in [109,110]. Under this scheme, the BS generates narrow beams with random directions and select the user with the highest SNR. On the other hand, optimization-based random beamforming in [108] optimizes the beamforming weights so that the resulting beam pattern is omni-directional. The work therein focused on conventional multiple-input-multiple-output (MIMO) systems in the microwave band. Despite the advantage of omni-directional coverage in the AI phase, the cost function is complex and, for a high number of antennas, it is only solvable numerically.

Another random beamforming investigated under conventional MIMO is the unitary beamforming, whereby the beamforming matrix is obtained by the singular value decomposition of the channel matrix, e.g., see [111]. This is not applicable in an IA scenario since the channel is unknown at that phase. Analog beamforming in mmWave is implemented using phase-shifters only. Therefore, we limit our beamforming to be unit-magnitude variable phase.

In this Chapter, we look into the IA problem for a LOS mmWave channel and investigate a random beamforming scheme, referred to as *random-phase beamforming* (RPBF). Under this scheme, the beamforming vector is generated as a vector of complex exponentials with i.i.d. random phases. This scheme is used in [112] to initiate an iterative beamforming scheme which assumes full channel knowledge, and in [113], which assumes the DOD to be known. However, these two assumptions are not used in our work. We compare the RPBF with *directional beamforming* (DBF) scheme. Since the step following a successful initial access would be the channel estimation, it is meaningful to compare the performance of these two schemes in terms of the CRLB of the channel parameters: DOA, DOD, TOA, and the complex channel gain. The CRLB of a LOS mmWave channel parameters were previously studied in [114]. Therein, the CRLBs were provided as a function of the Fisher information matrix (FIM), whose entries were given by high level expressions and are valid for ULA . The current Chapter presents the closed-form CRLB expressions of the mmWave parameter using ULA, simpler than those obtained in [114]. Although mmWave may apply different array geometries, ULA is the standard array structure that is usually used to get initial insights. Finally, we investigate and assess the RPBF and DBF in terms of the CRLBs, as a function of the number of transmit antennas, receive antennas and transmit beams.

While we focus on the IA herein, in subsequent Chapters, we focus on localization performance and synchronization issues, beyond the initial access phase.

4.2 Problem Formulation

Consider the scenario illustrated in Figure 4.1, where the receiver and the transmitter are equipped with arrays of N_{R} and N_{T} antennas, respectively. Without loss of generality, we consider the uplink and assume that the BS and UE are located in the

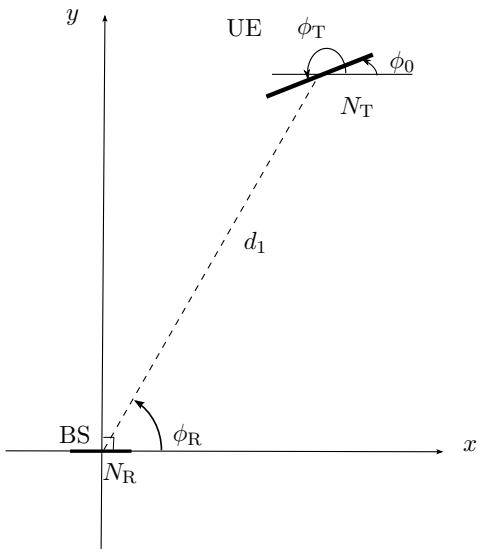

Figure 4.1: A schematic diagram of the considered scenario. d_1 is the transmitter-receiver separation distance.

same plane. Consequently, we consider a 2D approach. Moreover, similar to [114], we assume that the UE and BS communicate via a LOS path only. We leave the investigation of the NLOS where communication is carried out via scatterers and reflectors to Chapter 5. Furthermore, we assume that the transmit antenna array is rotated by an unknown orientation angle ϕ_0. Finally, we assume that the arrays are narrow-band, i.e., the signal traverses the antenna arrays apertures, both at the transmitter and the receiver, within a fraction of a symbol duration. That is $A_{\max} \ll cT_{\mathrm{s}}$, where $A_{\max}$ is the maximum array aperture.

As described in Section 2.1.3, and based on the above assumptions, the channel matrix is modeled by

$$\mathbf{H} \triangleq \sqrt{N_{\mathrm{R}}N_{\mathrm{T}}}\beta\mathbf{a}_{\mathrm{R}}(\phi_{\mathrm{R}})\mathbf{a}_{\mathrm{T}}^{\mathrm{H}}(\phi_{\mathrm{T}}) \in \mathbb{C}^{N_{\mathrm{R}}\times N_{\mathrm{T}}}, \tag{4.1}$$

where $\beta = \beta_{\mathrm{R}} + j\beta_{\mathrm{I}} \in \mathbb{C}$ is the complex channel gain, ϕ_{R} is the DOA, and ϕ_{T} is the DOD. Under mmWave channel, DOD depends on the orientation angle and both are crucial in beamforming, since the knowledge of the direction of departure and the orientation angle would enable more efficient beamforming. From Section 2.1.1, for a receiver equipped with a ULA of N_{R} elements placed along the x-axis

with d inter-element spacing, the array response vector is given by

$$\mathbf{a}_{\mathrm{R}}(\phi_{\mathrm{R}}) = \frac{1}{\sqrt{N_{\mathrm{R}}}} \mathrm{e}^{-j\frac{2\pi d}{\lambda}\cos\phi_{\mathrm{R}}\mathbf{x}_{\mathrm{R}}} \qquad \in \mathbb{C}^{N_{\mathrm{R}}}, \tag{4.2}$$

where $\mathbf{x}_{\mathrm{R}}$ is as defined in (2.9). Similarly, by using the subscript T, the transmitter array steering vector is given by

$$\mathbf{a}_{\mathrm{T}}(\phi_{\mathrm{T}}) = \frac{1}{\sqrt{N_{\mathrm{T}}}} \mathrm{e}^{-j\frac{2\pi d}{\lambda}\cos\phi_{\mathrm{T}}\mathbf{x}_{\mathrm{T}}} \qquad \in \mathbb{C}^{N_{\mathrm{T}}}. \tag{4.3}$$

For notation simplicity, we drop the angle parameter from $\mathbf{a}_{\mathrm{R}}(\phi_{\mathrm{R}})$ and $\mathbf{a}_{\mathrm{T}}(\phi_{\mathrm{T}})$. These two vectors are normalized so that $\|\mathbf{a}_{\mathrm{R}}\|^2 = \|\mathbf{a}_{\mathrm{T}}\|^2 = 1$. Thus, the received signal at the analog output of the array at a time instant t, can be written as

$$\begin{aligned} \mathbf{r}(t) &\triangleq [r_1(t), r_2(t), ..., r_{N_{\mathrm{R}}}(t)]^{\mathrm{T}}, \quad \in \mathbb{C}^{N_{\mathrm{R}}}, t \in [0, T_{\mathrm{o}}], \\ &= \mathbf{H}\mathbf{x}(t-\tau) + \mathbf{n}(t). \end{aligned} \tag{4.4}$$

where $T_{\mathrm{o}} \approx N_{\mathrm{s}}T_{\mathrm{s}}$ is the observation time and N_{s} is the number of pilot symbols. Moreover, $\tau \in \mathbb{R}^+$ is the propagation delay of the transmitted signal, i.e., TOA, and is related to the transmitter-receiver distance , by $\tau = d_1/c$. Furthermore, $\mathbf{n}(t) \triangleq [n_1(t), n_2(t), ..., n_{N_{\mathrm{T}}}(t)]^{\mathrm{T}} \in \mathbb{C}^{N_{\mathrm{R}}}$ denotes zero-mean additive white Gaussian noise processes with spectral density (PSD) N_0. Furthermore, $\mathbf{x}(t) \triangleq [x_1(t), x_2(t), ..., x_{N_{\mathrm{T}}}(t)]^{\mathrm{T}} \in \mathbb{C}^{N_{\mathrm{T}}}$ is the single-carrier transmitted signal vector at the output of a beamforming matrix $\mathbf{F} \triangleq [\mathbf{f}_1, \mathbf{f}_2, ...\mathbf{f}_{N_{\mathrm{B}}}]$ such that $\mathbf{x}(t) = \sqrt{E_{\mathrm{t}}}\mathbf{F}\mathbf{s}(t)$ and $\mathbf{s}(t) \triangleq [s_1(t), s_2(t), ..., s_{N_{\mathrm{B}}}(t)]^{\mathrm{T}}$, where N_{B} is the number of transmitted beams and E_{t} is the transmitted energy per symbol. Moreover,

$$s_\ell(t) = \sum_{k=0}^{N_{\mathrm{s}}-1} a_{\ell,k}\, p(t - kT_{\mathrm{s}}), \qquad \ell = 1, ..., N_{\mathrm{B}} \tag{4.5}$$

where $a_{\ell,k}$ is the k^{th} pilot symbol transmitted over the ℓ^{th} beam, and $p(t)$ is a unit-energy pulse with a PSD $|P(f)|^2$ and a bandwidth W. To keep the transmitted power fixed, regardless of the number of antennas, N_{T}, we normalize $\mathbf{F}$ such that $\mathrm{Tr}\left(\mathbf{F}^{\mathrm{H}}\mathbf{F}\right) = 1$, and $\mathbf{s}(t)\mathbf{s}^{\mathrm{H}}(t) = \mathbf{I}_{N_{\mathrm{B}}}$. Matrix $\mathbf{F}$ is modeled in two ways: directional and random. These models and the differences between them are discussed in detail

in the sequel of Section 4.3.

Our aim is to investigate the impact of the two beamforming schemes on the estimation lower bounds of the channel parameters, $\boldsymbol{\varphi} = [\phi_{\mathrm{R}}, \phi_{\mathrm{T}}, \beta_{\mathrm{R}}, \beta_{\mathrm{I}}, \tau]^{\mathrm{T}}$ based on the observed signal, $\mathbf{r}(t)$.

4.3 Beamforming: Random-Phase and Directional

In this section, we formally define the two beamforming schemes considered here. The impact of these two schemes on the joint estimation of the channel parameters is investigated in subsequent sections. The first scheme we consider is DBF, which spatially steers the transmission beams towards the azimuth angles $\phi_{\mathrm{B},\ell}$ such that

$$\mathbf{f}_\ell \triangleq \frac{1}{\sqrt{N_{\mathrm{B}}}}\mathbf{a}_{\mathrm{T}}(\phi_{\mathrm{B},\ell}), \qquad 1 \leq \ell \leq N_{\mathrm{B}} \tag{4.6}$$

where $\mathbf{a}_{\mathrm{T}}(\phi_{\mathrm{B},\ell})$ has the same structure as (4.3).

On the other hand, the RPBF generates beams with uniformly distributed random phases such that

$$\mathbf{f}_\ell \triangleq \frac{1}{\sqrt{N_{\mathrm{T}}N_{\mathrm{B}}}}[\mathrm{e}^{j\vartheta_{\ell,1}}, ..., \mathrm{e}^{j\vartheta_{\ell,N_{\mathrm{T}}}}]^{\mathrm{T}}, \tag{4.7}$$

where $\vartheta_{\ell,n} \sim \mathcal{U}(-\pi, \pi)$. Recall that analog beamforming is implemented solely using phase shifter. Thus, RPBF and DBF have unit-magnitude weights. Although, practical phase shifters generate quantized phases, recently, phase shifters for mmWave with 3.5° (≈ 0.06 rad) phase resolution were proposed [115, 116].

Note that in (4.7) the phase is random, in contrast to the scheme in [109, 110], which have a structure similar to (4.6), but with a random direction. Moreover, note that both (4.6) and (4.7) have $\|\mathbf{f}_\ell\|^2 = \frac{1}{N_{\mathrm{B}}}$. This implies that increasing the number of beams, will linearly scale down the power per beam to preserve the constant transmitted power condition.

A good advantage of (4.7) is that the generated beams are not too narrow compared to those of DBF as shown in Figure 4.2. Thus, RPBF exhibits a better spatial coverage, which is an essential feature when the initial direction of transmission is unknown.

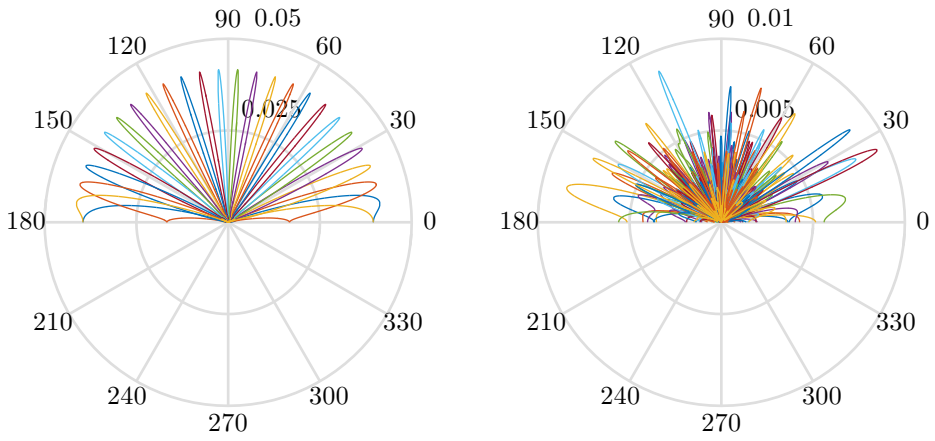

Figure 4.2: Beam patterns generated using DBF (left) and RPBF (right) with $N_{\mathrm{T}} = 32$ and $N_{\mathrm{B}} = 24$. For directional beamforming, $\phi_{\mathrm{B},\ell} = 7.2°\ell$.

4.4 Cramér-Rao Lower Bound

As discussed in Section 2.2.3, a widely used performance measure in the estimation theory is the CRLB [81]. CRLB provides a lower bound on the variance of an unbiased estimator of a given parameter. In this Chapter, we use the CRLB to compare the best performance of RPBF and DBF in the scenario described in Section 4.2 in terms of the CRLBs of channel parameters

The CRLB of estimating $\boldsymbol{\varphi}$ for an array with arbitrary geometry is derived in Appendix C.2. Subsequently, for the case of ULA, we show in Appendix C.3.2 that the CRLBs for jointly estimating $\phi_{\mathrm{R}}, \phi_{\mathrm{T}}, \beta$ and τ are given by (4.8). Note that since $\beta = \beta_{\mathrm{R}} + j\beta_{\mathrm{I}}$, we provide $\mathrm{CRLB}(\beta) = \mathrm{CRLB}(\beta_{\mathrm{R}}) + j\,\mathrm{CRLB}(\beta_{\mathrm{I}})$.

$$\mathrm{CRLB}(\phi_{\mathrm{R}}) = \frac{12}{\gamma_0 |\beta|^2 N_{\mathrm{R}}^3 N_{\mathrm{T}} [\mathbf{Q}]_{1,1}} \left(\frac{\lambda}{2\pi d \sin \phi_{\mathrm{R}}} \right)^2, \tag{4.8a}$$

$$\mathrm{CRLB}(\phi_{\mathrm{T}}) = \frac{[\mathbf{Q}]_{1,1}}{\gamma_0 |\beta|^2 N_{\mathrm{R}} N_{\mathrm{T}} \det(\mathbf{Q})} \left(\frac{\lambda}{2\pi d \sin \phi_{\mathrm{T}}} \right)^2, \tag{4.8b}$$

$$\mathrm{CRLB}(\beta) = \frac{1}{\gamma_0 N_{\mathrm{R}} N_{\mathrm{T}} [\mathbf{Q}]_{1,1}} \left(1 + \frac{[\mathbf{Q}]_{1,1} [\mathbf{Q}]_{2,2}}{\det(\mathbf{Q})} \right), \tag{4.8c}$$

$$\mathrm{CRLB}(\tau) = \frac{1}{4\pi^2\gamma_0|\beta|^2 N_\mathrm{R} N_\mathrm{T} W_\mathrm{eff}^2 [\mathbf{Q}]_{1,1}}. \tag{4.8d}$$

where

$$\gamma_0 = \frac{N_\mathrm{s} E_\mathrm{t}}{N_0}, \tag{4.9a}$$

$$W_\mathrm{eff}^2 \triangleq \int_{-\infty}^{\infty} \left(\frac{\partial p(t)}{\partial \tau}\right)^2 dt = \int_{\frac{-W}{2}}^{\frac{W}{2}} f^2 |P(f)|^2 \mathrm{d}f, \tag{4.9b}$$

$$\mathbf{Q} \triangleq \begin{bmatrix} \mathbf{a}_\mathrm{T}^\mathrm{H}\mathbf{F}\mathbf{F}^\mathrm{H}\mathbf{a}_\mathrm{T} & \mathbf{a}_\mathrm{T}^\mathrm{H}\mathbf{X}_\mathrm{T}\mathbf{F}\mathbf{F}^\mathrm{H}\mathbf{a}_\mathrm{T} \\ \mathbf{a}_\mathrm{T}^\mathrm{H}\mathbf{X}_\mathrm{T}\mathbf{F}\mathbf{F}^\mathrm{H}\mathbf{a}_\mathrm{T} & \mathbf{a}_\mathrm{T}^\mathrm{H}\mathbf{X}_\mathrm{T}\mathbf{F}\mathbf{F}^\mathrm{H}\mathbf{X}_\mathrm{T}\mathbf{a}_\mathrm{T} \end{bmatrix}. \tag{4.9c}$$

$$\mathbf{X}_\mathrm{T} = \mathrm{diag}(\mathbf{x}_\mathrm{T}) \tag{4.9d}$$

Note that γ_0 denotes the transmitted SNR, and that (4.9b) follows from Parseval's theorem. W_eff is called the *effective bandwidth*. Note that directly from (4.8), it is easy to see that the CRLBs of channel parameters improve with N_R, namely $\mathrm{CRLB}(\phi_R) \propto \frac{1}{N_\mathrm{R}^3}$, while $\mathrm{CRLB}(\phi_T), \mathrm{CRLB}(\beta)$, and $\mathrm{CRLB}(d_1) \propto \frac{1}{N_\mathrm{R}}$. However, the relationships of these bounds with respect to N_T, are not as obvious. Therefore, in the following, we analyze the expressions (4.8) for both DBF and RPBF with respect to N_T.

4.4.1 DBF Analysis

Define $\varpi_\ell \triangleq \frac{2\pi d}{\lambda}\big(\cos\phi_\mathrm{T} - \cos\phi_{\mathrm{B},\ell}\big)$. Then, for DBF, it can be shown that

$$[\mathbf{Q}]_{1,1} = \frac{1}{N_\mathrm{T}^2 N_\mathrm{B}} \sum_{\ell=1}^{N_\mathrm{B}} \frac{1-\cos N_\mathrm{T}\varpi_\ell}{1-\cos\varpi_\ell}, \tag{4.10a}$$

$$[\mathbf{Q}]_{2,2} = \frac{1}{2N_\mathrm{T}^2 N_\mathrm{B}} \sum_{\ell=1}^{N_\mathrm{B}} \frac{N_\mathrm{T}^2 - N_\mathrm{T}}{1-\cos\varpi_\ell} + \frac{1+\cos N_\mathrm{T}\varpi_\ell}{(1-\cos\varpi_\ell)^2}, \tag{4.10b}$$

$$\Re\{[\mathbf{Q}]_{1,2}\} = \frac{(N_\mathrm{T}-1)}{2}[\mathbf{Q}]_{1,1}, \tag{4.10c}$$

$$\Im\{[\mathbf{Q}]_{1,2}\} = \frac{1}{N_\mathrm{T}^2 N_\mathrm{B}} \sum_{\ell=1}^{N_\mathrm{B}} \frac{(1-\cos N_\mathrm{T}\varpi_\ell)\sin\varpi_\ell - N_\mathrm{T}(1-\cos\varpi_\ell)\sin N_\mathrm{T}\varpi_\ell}{(1-\cos\varpi_\ell)^2}. \tag{4.10d}$$

Note that (4.10) imply that the performance of DBF is highly governed by the difference between ϕ_{T} and $\phi_{\mathrm{B},\ell}$. Ideally, the difference should be zero to achieve the lowest CRLB. Moreover, carefully inspecting (4.10), one can notice the averaging over N_{B}. Thus, after a certain value of N_{B}, increasing N_{B} has a little effect on the CRLBs, and a performance floor is reached.

Since N_{T} and N_{B} will be typically very large, it is meaningful to analyze the limiting behavior of the elements and determinant of $\mathbf{Q}$ with N_{T}. Focusing on the relationship between the DBF CRLB and N_{T}, we can see that there are two components in (4.10); a short-term harmonic component represented by $\cos(N_{\mathrm{T}}\varpi_\ell)$ and a long-time trend represented by a polynomial of N_{T}. Focusing on the long-term trend, it can be noticed that $[\mathbf{Q}]_{1,1} \sim \mathcal{O}(\frac{1}{N_{\mathrm{T}}^2})$, $[\mathbf{Q}]_{2,2}$ is constant, the real and imaginary parts of $[\mathbf{Q}]_{1,2} \sim \mathcal{O}(\frac{1}{N_{\mathrm{T}}})$, and finally, $\det(\mathbf{Q}) \sim \mathcal{O}(\frac{1}{N_{\mathrm{T}}^2})$. Consequently, from (4.8), we can deduce that, under DBF,

$$\mathrm{CRLB}(\phi_{\mathrm{R}}) \sim \mathcal{O}(N_{\mathrm{T}}), \tag{4.11a}$$

$$\mathrm{CRLB}(\phi_{\mathrm{T}}) \sim \mathcal{O}(\frac{1}{N_{\mathrm{T}}}), \tag{4.11b}$$

$$\mathrm{CRLB}(\beta) \sim \mathcal{O}(N_{\mathrm{T}}), \tag{4.11c}$$

$$\mathrm{CRLB}(\tau) \sim \mathcal{O}(N_{\mathrm{T}}). \tag{4.11d}$$

Due to the fixed transmit power constraint, higher N_{T} leads to narrower beams and higher received power in a certain direction as implied by (4.6). If that direction mismatches ϕ_{T}, the CRLBs of $\phi_{\mathrm{R}}, \beta,$ and τ tend to worsen when N_{T} increases.

4.4.2 RPBF Analysis

For the RPBF case, since both N_{T} and N_{B} are typically high in mmWave systems, we resort to the law of large numbers to compute the average CRLB. We calculate $\mathbb{E}\{[\mathbf{Q}]_{1,1}\}$, $\mathbb{E}\{[\mathbf{Q}]_{2,2}\}$, and $\mathbb{E}\{\det(\mathbf{Q})\}$, to obtain the limiting behavior of (4.8) as

$$\mathbb{E}\{[\mathbf{Q}]_{1,1}\} = \mathbf{a}_{\mathrm{T}}^{\mathrm{H}}\mathbb{E}\{\mathbf{F}\mathbf{F}^{\mathrm{H}}\}\mathbf{a}_{\mathrm{T}} = \frac{\mathbf{a}_{\mathrm{T}}^{\mathrm{H}}\mathbf{a}_{\mathrm{T}}}{N_{\mathrm{T}}} = \frac{1}{N_{\mathrm{T}}}, \tag{4.12a}$$

$$\mathbb{E}\{[\mathbf{Q}]_{2,2}\} = \frac{\mathbf{a}_{\mathrm{T}}^{\mathrm{H}}\mathbf{X}_{\mathrm{T}}^2\mathbf{a}_{\mathrm{T}}}{N_{\mathrm{T}}} = \frac{1}{N_{\mathrm{T}}^2}\sum_{i=0}^{N_{\mathrm{T}}-1}\left(i - \frac{N_{\mathrm{T}}-1}{2}\right)^2 = \frac{N_{\mathrm{T}}^2-1}{12N_{\mathrm{T}}}, \tag{4.12b}$$

Table 4.1: Scaling Effect on CRLBs For High N_{T} And N_{B}.

	N_{R}	N_{T} (RPBF)	N_{T} (DBF)	N_{B}
CRLB(ϕ_{R})	$\frac{1}{N_{\mathrm{R}}^3}$	constant	$\mathcal{O}\left(N_{\mathrm{T}}\right)$	constant
CRLB(ϕ_{T})	$\frac{1}{N_{\mathrm{R}}}$	$\mathcal{O}\left(\frac{1}{N_{\mathrm{T}}^2}\right)$	$\mathcal{O}\left(\frac{1}{N_{\mathrm{T}}}\right)$	constant
CRLB(β)	$\frac{1}{N_{\mathrm{R}}}$	constant	$\mathcal{O}\left(N_{\mathrm{T}}\right)$	constant
CRLB(τ)	$\frac{1}{N_{\mathrm{R}}}$	constant	$\mathcal{O}\left(N_{\mathrm{T}}\right)$	constant

$$\mathbb{E}\{[\mathbf{Q}]_{1,2}\} = \frac{\mathbf{a}_{\mathrm{T}}^{\mathrm{H}}\mathbf{X}_{\mathrm{T}}\mathbf{a}_{\mathrm{T}}}{N_{\mathrm{T}}} = \frac{1}{N_{\mathrm{T}}^2}\sum_{i=0}^{N_{\mathrm{T}}-1}\left(i - \frac{N_{\mathrm{T}}-1}{2}\right) = 0, \tag{4.12c}$$

$$\mathbb{E}\{\det(\mathbf{Q})\} = \frac{N_{\mathrm{T}}^2 - 1}{12N_{\mathrm{T}}^2} \to \frac{1}{12}. \tag{4.12d}$$

The results in (4.12) in conjugation with (4.8) imply that CRLB(ϕ_{T}) $\sim \mathcal{O}(1/N_{\mathrm{T}}^2)$, while CRLB($\phi_{\mathrm{R}}$), CRLB($\beta$), and CRLB($\tau$) are constant in N_{T} and N_{B}. In contrast to DBF, increased N_{T} does not decrease the spatial coverage. Thus, higher N_{T} does not affect the received power in average, and the CRLBs of $\phi_{\mathrm{R}}, \beta,$ and τ stay constant. Table 4.1 summarizes the scaling factors of DBF and RPBF with respect to N_{T} and N_{R}.

4.5 Simulation and Numerical Results

With reference to the scenario illustrated in Figure 4.1, we consider a receiver equipped with a ULA lying in the x-axis with $d = \lambda/2$, and covering a spatial field $(0, \pi)$. The transmitter, operating at $f = 38$ GHz, is assumed to be tilted with an orientation angle ϕ_0 measured from the positive x-axis. Without loss of generality, we select $\phi_0 = 0$. The DODs and DOAs are measured counter-clockwise from x-axis in line with the standard polar coordinates. The BS is assumed to be located at the origin, while the UE is located at $\mathbf{p} = (5, 25)$ m. This leads to the angles $\phi_{\mathrm{R}} = 78.7°$, $\phi_{\mathrm{T}} = 191.3°$. Similar to [117], the complex channel gain is computed using the free-space propagation model, leading to $\beta = \beta_{\mathrm{R}} + j\beta_{\mathrm{I}} = -(56.5 + j53.7) \times 10^{-3}$. Moreover, we consider $p(t)$ to be a unit-energy ideal pulse

given by

$$p(t) = \frac{1}{\sqrt{W}} \operatorname{sinc}(Wt). \tag{4.13}$$

Consequently, it follows from Parseval's theorem that $W_{\text{eff}}^2 = W^2/3$, where $W = R_b/2b$, and R_b is the bit rate, and b is the number of bits per symbol. We present the results for 1 Gbps bit rate and 16 QAM transmission, i.e., $W = 125$ MHz. To improve the results presentation, we provide the CRLB(τ) in terms of CRLB(d_1) = c^2 CRLB(τ). It should be noted that using the values above, the SNR at the given location can be calculated to be 30.7 dB, which is high enough to guarantee the tightness of the CRLB of the parameters.

For DBF, the directions are chosen to be equally spaced to cover the region $(0, \pi)$, i.e., $\phi_{\text{B},\ell} = \frac{\pi\ell}{N_{\text{B}}+1}, 1 \leq \ell \leq N_{\text{B}}$. Finally, in the following results, when referring to RPBF, CRLB means the average CRLB. RPBF plots are obtained by Monte-Carlo simulation averaged over 1000 iteration.

4.5.1 Effect of N_{B} on the CRLBs of Channel Parameters

Figure 4.3 illustrates the CRLBs of the channel parameters as a function of N_{B} with $N_{\text{T}} = 32$ and $N_{\text{R}} = 64$. It can be seen that, using RPBF, the CRLB floor is reached at $N_{\text{B}} = 18$. Also, note that for $N_{\text{B}} < 10$ the average CRLBs of ϕ_{R} and d_1 are less sensitive to N_{B} compared to those of ϕ_{T}, and β. On the other hand, the CRLB under DBF is non-monotonic. Thus, N_{B} should be carefully chosen for optimum estimation. However, since in the initial access phase the transmitter has no information on the direction of transmission, an optimal beam is not guaranteed.

Comparing RPBF with DBF in Figure 4.3, it can be inferred that the RPBF scheme attains a lower floor at a low N_{B} than the DBF, except when the latter happens to have a beam close to the receiver direction. To see why the CRLB floors, notice the averaging effect in (4.10), and the independence of N_{B} in (4.12). Intuitively, recall that with a fixed N_{R} the receiver beam-width about ϕ_{R} is fixed. Now, consider the RPBF case shown in Figure 4.2. When N_{B} is small, there is a limited chance that a random transmit beam will cover ϕ_{R} with a suitable gain, but

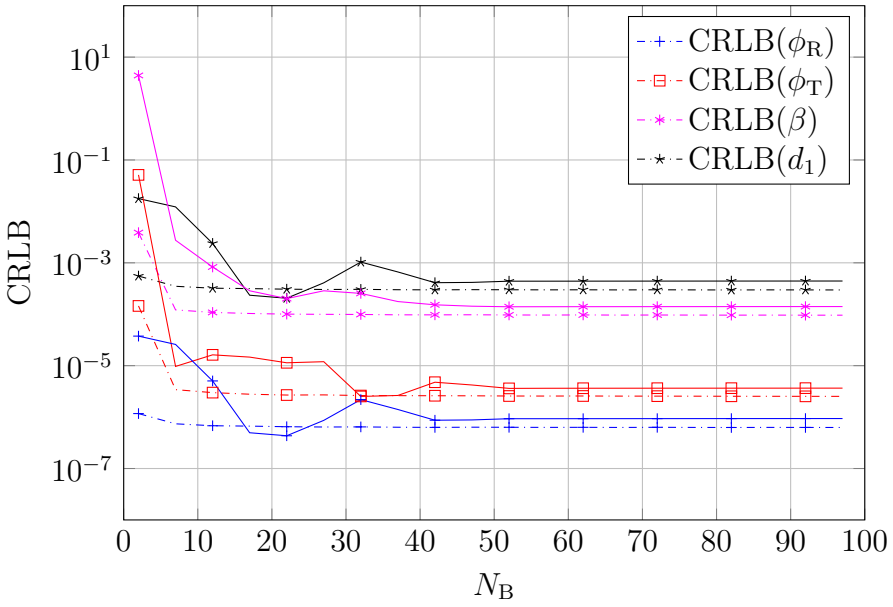

Figure 4.3: CRLB of the channel parameters w.r.t N_{B} using RPBF (dashed line) and DBF (solid line) with $N_{\mathrm{R}} = 64, N_{\mathrm{T}} = 32$. Directional beams are equally spaced over $(0,\pi)$

as N_{B} goes up, this chance enhances and the CRLB starts to decrease. As N_{B} grows significantly, the resultant beams becomes almost omni-directional and, regardless of how high N_{B} is, the CRLB becomes fixed. On the other hand, consider the DBF case in Figure 4.2, where beams have a comb-like shape and the CRLB mainly depends on the difference between the transmit beams and the DOD. As N_{B} grows higher, more transmit beams fall within the vicinity of the DOA. However, since $\|\mathbf{f}_\ell\|^2 = 1/N_{\mathrm{B}}$, the received power stays fixed, and the CRLB floor is reached.

4.5.2 Effect of N_{R} on the CRLBs of Channel Parameters

The CRLBs of the channel parameters as function of N_{R} are provided in Figure 4.4. In both schemes, CRLBs of ϕ_{T}, β, and τ decrease as $1/N_{\mathrm{R}}$. On the other hand, CRLB of ϕ_{R} decreases by three orders of magnitude, when N_{R} increases by one order of magnitude. This is in line with the theoretical expressions in (4.8). Finally, as is the case with respect to N_{T}, these results confirm the conclusion made using Figure 4.3 that RPBF provides better bounds than DBF does when N_{B} is fixed.

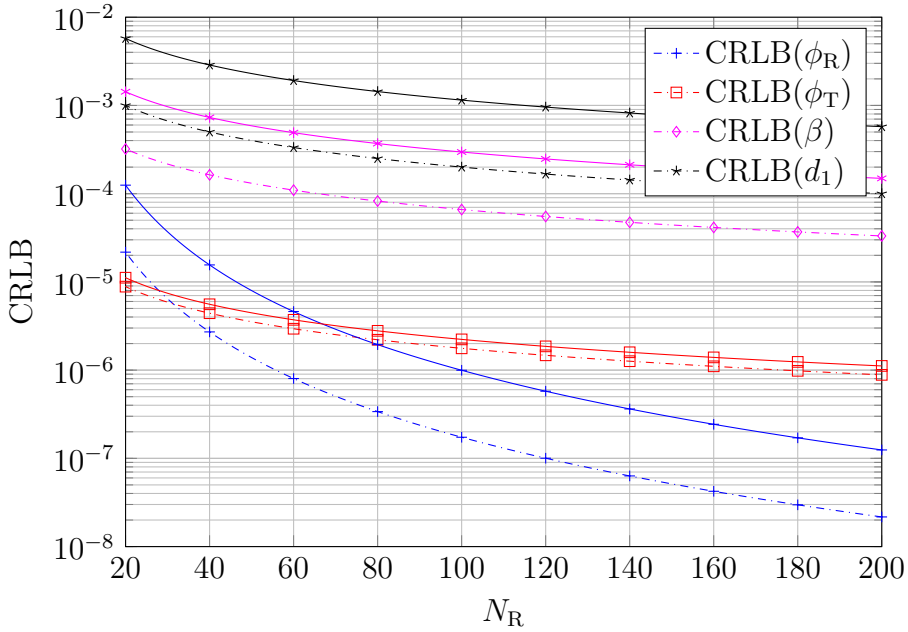

Figure 4.4: CRLB w.r.t N_R using RPBF (dashed line) and DBF (solid line) with $N_B = 18, N_T = 32$. Directional beams are equally spaced over $(0,\pi)$

4.5.3 Effect of N_T on the CRLB

Figure 4.5 illustrates the results of investigating the CRLB in terms of N_T. Considering DBF, it is hard to draw any conclusion for scaling factors in terms of N_T due to the high non-linearity observed and represented by (4.10). However, there is an average trend that can be seen, as discussed in Section 4.4, whereby CRLB(ϕ_T) decreases with $1/N_T^2$ while the other CRLBs increase with N_T. As for RPBF, it can be seen from Figure 4.5 that only the estimation of ϕ_T improves when increasing N_T. Note that due to the power normalization discussed in Section 4.2, the CRLBs of β and ϕ_R are not affected by an increased N_T.

4.5.4 Summary of Results

From Figures 4.3 – 4.5, it can be inferred that RPBF outperforms DBF in terms of the CRLBs of the channel parameters, except in some cases shown in Figure 4.3, where a few N_B choices can result in a better DBF performance. Note that in these cases a beam or more are close enough to the receiver direction, hence the

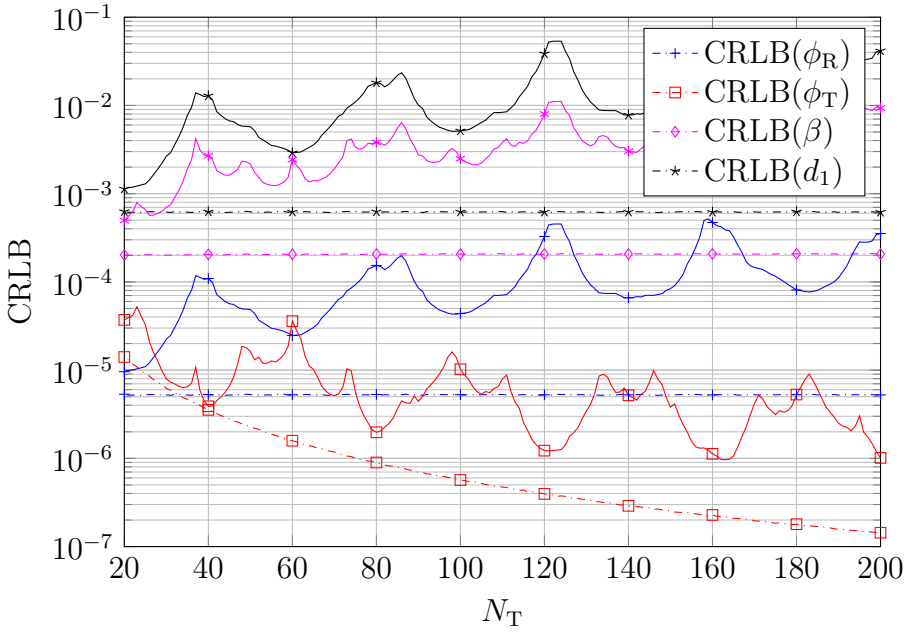

Figure 4.5: CRLB w.r.t N_{T} using RPBF (dashed line) and DBF (solid line) with $N_{\mathrm{B}} = 18, N_{\mathrm{R}} = 32$. Directional beams are equally spaced over $(0,\pi)$

better CRLB. However, since at the IA stage the receiver location is unknown, a careful choice of N_{B} cannot be made for DBF. As a result, RPBF is more reliable in this case during AI phase.

4.6 Conclusion

In this Chapter, we have studied the impact of two beamforming schemes on the CRLBs of the channel parameter: DOA, DOD, TOA, and complex channel gain. RPBF has shown better CRLB floor at a smaller number of beams than DBF. Thus, as shown by the numerical results, it would be favorable to use RPBF in the initial access phase. Table 4.1 summarizes the scaling factors of CRLB in terms of $N_{\mathrm{R}}, N_{\mathrm{T}}$ and N_{B}. In the next Chapter, we consider 3D mmWave channels with multi-path propagation and carry out an analytical investigation on the localization bounds in 5G for both, uplink and downlink.

Publications Resulted from This Chapter

- **Z. Abu-Shaban**,H. Wymeersch, X. Zhou, G. Seco-Granados, T. Abhayapala "Random-Phase Beamforming for Initial Access in the Millimeter-Wave Cellular Networks" in *2016 IEEE Global Communications Conf. (GLOBECOM)*, Washington, DC, pp. 1-6, Dec 2016.

Chapter 5

Uplink and Downlink 3D Localization Error Bounds in 5G mmWave Systems

Overview: *Location-aware communication systems are expected to play a pivotal part in the next generation of mobile communication networks. Therefore, there is a need to understand the localization limits in these networks, particularly, using mmWave. Towards that, we address the uplink and downlink localization limits in terms of 3D position and orientation error bounds for mmWave multipath channels. We also carry out a detailed analysis of the dependence of the bounds on different system parameters. Our key findings indicate that the uplink and downlink behave differently in two distinct ways. First of all, the error bounds have different scaling factors with respect to the number of antennas in the uplink and downlink. Secondly, uplink localization is sensitive to the orientation angle of the UE, whereas downlink is not. Moreover, in the considered outdoor scenarios, the non-line-of-sight paths generally improve localization when a line-of-sight path exists. Finally, our numerical results show that mmWave systems are capable of localizing a UE with sub-meter position error, and sub-degree orientation error.*

5.1 Introduction

Having considered the initial network access problem in the previous Chapter, we now focus on UE localization in mmWave location-aided systems.

Location-aided systems are expected to have a wide range of applications in 5G mmWave communication [26], whether for vehicular communications [118], assisted living applications [68], or to support the communication robustness and effectiveness in different aspects such as resource allocation [119], beamforming [33, 71], and pilot assignment [34]. Therefore, the study of positioning in 5G mmWave systems becomes especially imperative. Due to the use of directional beamforming in mmWave, in addition to the UE position also the UE *orientation* plays an important role in location-aided systems.

Conventionally position information is obtained by GPS, though this has several limitations. Most importantly, GPS suffers from degraded performance in outdoor rich-scattering scenarios and urban canyons, and may fail to provide a position fix for indoor scenarios. Even in good conditions, GPS positioning accuracy ranges between 1–5 meters. To address these limitations, there has been intense research on competing radio-based localization technologies. To understand the fundamental behavior of any technology, the CRLB or related bounds can be used. As discussed in Section 2.2.3, the CRLB provides a lower bound on the variance of an unbiased estimator of a certain parameter. The square-root of the CRLB of the position and the orientation are termed the position error bound (PEB), and the orientation error bound (OEB), respectively. PEB and OEB can be computed indirectly by transforming the bounds of the channel parameters, namely: DOA, DOD, and TOA.

For conventional MIMO systems, the bounds of the 2D channel parameters are derived in [120], based on received digital signals and uniform linear arrays (ULA), while bounds are derived in [121] based on 3D channel matrix with no transmit beamforming. It was found that having more transmit and receive antennas is beneficial for estimating the DOA and DOD. In both [120, 121] beamforming was not considered. The bounds on the channel parameters can be transformed into PEB and OEB as in [84,122–124] that considered 2D cooperative wideband localization, highlighting the benefit of large bandwidths.

MmWave communication combines large antenna arrays with large bandwidths, and should be promising for localization, then. In [125], PEB and OEB for 2D mmWave downlink localization using ULA are reported, while [126] considers 2D uplink multi-anchor localization. Furthermore, for indoor scenarios, PEB and OEB are analyzed in [127] for 3D mmWave uplink localization with a single beam whose direction is assumed to be known. Although multipath channels are considered in [125–127], the difference between the uplink and downlink for 3D and 2D with large number of antennas and analog transmit beamforming is yet to be investigated.

In this Chapter, we consider 3D mmWave localization problem for both the uplink and downlink under multipath conditions, and derive and analyze the PEB and OEB using multi-beam directional beamforming with arbitrary array geometry. By their nature, these bounds are theoretical, and serve as benchmarks to assess location estimation techniques, as well as being a feasibility study to see how well the location and orientation can be potentially estimated. We derive these bounds by transforming the Fisher information matrix (FIM) of the channel parameters into the FIM of location parameters. We stress that although the FIM of the channel parameters is structured similarly in the uplink and downlink, this is untrue for the location parameters FIM, which is obtained by transforming the FIM of the channel parameters. Using procedure similar to the one introduced in Section 2.2.4, this transformation is different in the uplink and downlink, and leads to different PEB and OEB. The contributions of this Chapter are summarized as follows:

- Based on the low-scattering sparse nature of the mmWave channel and the resulting geometrical model, we show that, under some conditions, the multipath parameter estimation can be reduced to a problem of multiple single-path estimation. We refer to this reduction as the *approximate approach*. These conditions are highly relevant in mmWave due to channel sparsity, high number of receive and transmit antennas, and the very large bandwidth.

- We derive the single-path CRLB of the channel parameters in a closed-form for arbitrary geometry, and show how these bounds are related to the PEB and OEB bounds. We also propose closed-form expressions of PEB and OEB for 3D and 2D LOS localization. Although our derivation is for an arbitrary array geometry, we specify the results for URA and ULA.

- We derive the PEB and OEB for general uplink and downlink localization, based on *exact* and approximate approaches, and show the asymmetry between uplink and downlink via both analytical scaling results and numerical simulations with a URA.

The rest of this Chapter is organized as follows. Section 5.2 presents the problem statement. Then, in Section 5.3, we derive the FIM of the channel parameters in a general setup of arbitrary arrays for 3D localization.The transformation of the channel parameters FIM into PEB and OEB is detailed in Section 5.4. The simulation results and the related insights are provided in Section 5.5. Finally, the conclusions are reported in Section 5.6.

5.2 Problem Formulation

5.2.1 System Geometry

By extending the 2D system geometry considered in Chapter 4, to the general case of 3D, we consider a BS equipped with an array of N_{BS} antennas arranged in an arbitrary but known geometry whose centroid, i.e., geometric center, is located at the origin ($\mathbf{O}$), and orientation angle is $\mathbf{o}_{\text{BS}} = [0, 0]^{\text{T}}$. On the other hand, the centroid of the UE is located at an unknown position $\mathbf{p} = [p_x, p_y, p_z]^{\text{T}}$ and equipped with a second array of N_{UE} antennas arranged in an arbitrary but known geometry with an unknown orientation $\mathbf{o} = [\theta_0, \phi_0]^{\text{T}}$, aligning the UE with the rotated axes x', y' and z'. An example with URAs is depicted in Figure 5.1. ϕ_0 is defined as the rotation around the z-axis, while θ_0 is defined as the rotation around the $-x'$-axis. Thus, the UE array elements locations is obtained using a rotation matrix $\mathbf{R}(\theta_0, \phi_0)$ derived in (5.35). Considering two orientation angles is highly relevant in applications such as vehicular communication and robotics, where the UE turns left and right, or goes up or down hills, without rotating the vehicle axis. We further assume that there are $M \geq 1$ paths between BS and UE, where the first path is LOS, while with the other $M - 1$ paths are associated with clusters located at $\mathbf{q}_m = [q_{m,x}, q_{m,y}, q_{m,z}]^{\text{T}}$, $2 \leq m \leq M$. These clusters can reflectors or scatterers. Due to the mmWave propagation characteristics, the number of paths is small [62] and correspond to single-bounce reflections [117, 125]. In fact, it

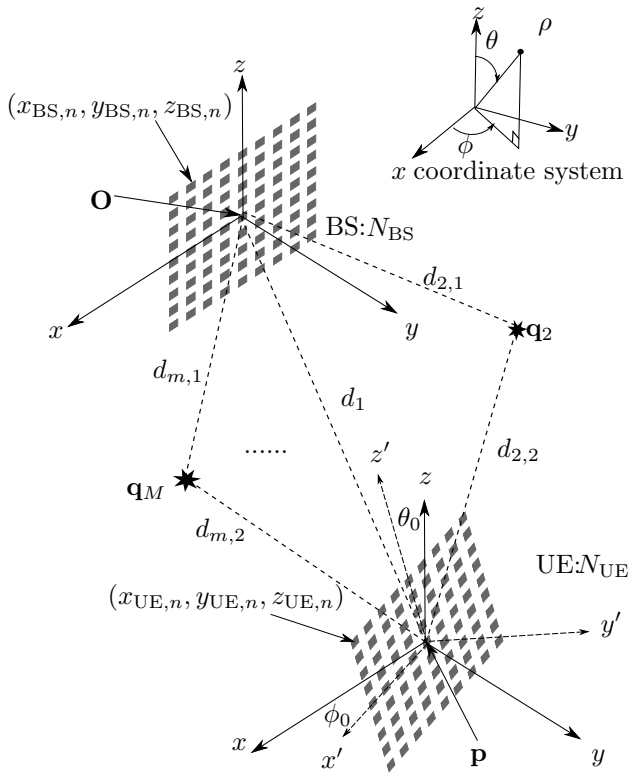

Figure 5.1: An example scenario composed of a URA of $N_{\mathrm{UE}} = N_{\mathrm{BS}} = 81$ antennas, and M paths. We use the spherical coordinate system highlighted in the top right corner. The axes rotated by orientation angles (θ_0, ϕ_0) are labeled x', y', z'.

was experimentally observed in [66] that the average value of M under mmWave propagation in an urban environment in New York City is 2 to 3 paths with a maximum of 4 paths present during measurement. This consequently resulted in modeling M by a Poisson mass function whose average is 1.8 and 1.9 at 28 GHz, and 73 GHz, respectively. Thus, the channel can be considered spatially sparse, and the parameters of different paths are assumed to be distinct, i.e., we assume unique DOAs, DODs, and TOA.

5.2.2 Channel Model

Denote the m^{th} DOD and DOA by $(\theta_{\mathrm{T},m}, \phi_{\mathrm{T},m})$ and $(\theta_{\mathrm{R},m}, \phi_{\mathrm{R},m}), 1 \leq m \leq M$, respectively, where the related unit-norm array response vectors are given by [58]

$$\mathbf{a}_{\mathrm{T},m}(\theta_{\mathrm{T},m}, \phi_{\mathrm{T},m}) \triangleq \frac{1}{\sqrt{N_{\mathrm{T}}}} e^{-j\boldsymbol{\Delta}_{\mathrm{T}}^{\mathrm{T}}\mathbf{k}(\theta_{\mathrm{T},m}, \phi_{\mathrm{T},m})}, \qquad \in \mathbb{C}^{N_{\mathrm{T}}} \tag{5.1}$$

$$\mathbf{a}_{\mathrm{R},m}(\theta_{\mathrm{R},m},\phi_{\mathrm{R},m}) \triangleq \frac{1}{\sqrt{N_{\mathrm{R}}}} e^{-j\boldsymbol{\Delta}_{\mathrm{R}}^{\mathrm{T}}\mathbf{k}(\theta_{\mathrm{R},m},\phi_{\mathrm{R},m})}, \qquad \in \mathbb{C}^{N_{\mathrm{R}}} \tag{5.2}$$

where $\mathbf{k}(\theta,\phi), \lambda$, and $\boldsymbol{\Delta}_{\mathrm{R}} \in \mathbb{R}^{3\times N_{\mathrm{R}}}$, are as defined in Section 2.1.1, while N_{R} is the number of receiving antennas. N_{T}, and $\boldsymbol{\Delta}_{\mathrm{T}}$ are defined similarly[1]. We drop the angle parameters from the notation of $\mathbf{a}_{\mathrm{T},m}$, and $\mathbf{a}_{\mathrm{R},m}$.

Assuming synchronization[2], and denoting the TOA of the m^{th} path by τ_m, the channel can be expressed[3] as

$$\mathbf{H}(t) = \sum_{m=1}^{M} \mathbf{H}_m \delta(t-\tau_m), \tag{5.3}$$

From Figure 5.1, $\tau_m = d_m/c$, where $d_m = d_{m,1} + d_{m,2}$, for $m > 1$ and

$$\mathbf{H}_m \triangleq \sqrt{N_{\mathrm{R}}N_{\mathrm{T}}}\beta_m \mathbf{a}_{\mathrm{R},m}\mathbf{a}_{\mathrm{T},m}^{\mathrm{H}} \in \mathbb{C}^{N_{\mathrm{R}}\times N_{\mathrm{T}}}, \tag{5.4}$$

where β_m is the complex gain of the m^{th} path. Finally, we define the following

$$\begin{aligned} \boldsymbol{\theta}_{\mathrm{R}} &\triangleq [\theta_{\mathrm{R},1},\theta_{\mathrm{R},2},...,\theta_{\mathrm{R},M}]^{\mathrm{T}}, & \boldsymbol{\phi}_{\mathrm{R}} &\triangleq [\phi_{\mathrm{R},1},\phi_{\mathrm{R},2},...,\phi_{\mathrm{R},M}]^{\mathrm{T}}, \\ \boldsymbol{\theta}_{\mathrm{T}} &\triangleq [\theta_{\mathrm{T},1},\theta_{\mathrm{T},2},...,\theta_{\mathrm{T},M}]^{\mathrm{T}}, & \boldsymbol{\phi}_{\mathrm{T}} &\triangleq [\phi_{\mathrm{T},1},\phi_{\mathrm{T},2},...,\phi_{\mathrm{T},M}]^{\mathrm{T}}, \\ \boldsymbol{\beta} &\triangleq [\beta_1,\beta_2,...,\beta_M]^{\mathrm{T}}, & \boldsymbol{\tau} &\triangleq [\tau_1,\tau_2,...,\tau_M]^{\mathrm{T}}. \end{aligned}$$

5.2.3 Transceiver Model

The transmitter sends a signal $\mathbf{x}(t) = \sqrt{E_{\mathrm{t}}}\mathbf{F}\mathbf{s}(t)$, as defined in (4.4). Here, we only consider directional beamforming such that $\mathbf{F} \triangleq [\mathbf{f}_1,\mathbf{f}_2,...\mathbf{f}_{N_{\mathrm{B}}}]$, where

$$\mathbf{f}_\ell = \frac{1}{\sqrt{N_{\mathrm{B}}}}\mathbf{a}_{\mathrm{T},\ell}(\theta_\ell,\phi_\ell), \quad 1 \le \ell \le N_{\mathrm{B}} \tag{5.5}$$

[1]The subscripts T and R refer to the transmit and receive sides, respectively, regardless of using the uplink or downlink. On the other hand, when the notation is unique to the base station or the user equipment, we use the subscript BS and UE.

[2]We rely on the commonly used synchronization assumption e.g., [68], [120], [84,122–124], [126], to gain fundamental understanding. We, however, realize that in practice synchronization errors must be accounted for in protocols and algorithms. This can be done by, e.g., a two-way protocol or a joint localization and synchronization approach, which is addressed in Chapter 6.

[3]We use a narrow-band array model, so that $A_{\max} \ll c/W$, where $A_{\max}$ is maximum array aperture, c is speed of light, and W is the system bandwidth [58].

The received signal observed at the input of the receive beamformer is given by

$$\mathbf{r}(t) \triangleq \sum_{m=1}^{M} \sqrt{E_{\mathrm{t}}}\mathbf{H}_m\mathbf{F}\mathbf{s}(t-\tau_m) + \mathbf{n}(t), \quad t \in [0, T_{\mathrm{o}}], \tag{5.6}$$

where $\mathbf{n}(t) \triangleq [n_1(t), n_2(t), ..., n_{N_{\mathrm{R}}}(t)]^{\mathrm{T}} \in \mathbb{C}^{N_{\mathrm{R}}}$ is zero-mean white Gaussian noise with PSD N_0. Similar to [128, 129], we assume that a low-noise amplifier and a passband filter are attached to each receive antenna. While this may seem a restrictive assumption, it will allow us to derive the PEB and OEB, which are fundamental lower bounds irrespective of the type of processing performed at the receiver, such as receive beamforming.

5.2.4 3D Localization Problem

Our objective is to derive the UE PEB and OEB, based on the observed signal, $\mathbf{r}(t)$, for both the uplink and downlink. We achieve this in two steps: firstly, we derive bounds on the channel parameters, namely, direction of arrival, $(\boldsymbol{\theta}_{\mathrm{R}}, \boldsymbol{\phi}_{\mathrm{R}})$, direction of departure, $(\boldsymbol{\theta}_{\mathrm{T}}, \boldsymbol{\phi}_{\mathrm{T}})$, time of arrival $\boldsymbol{\tau}$, and paths gains, $\boldsymbol{\beta}$. Secondly, we transform these bounds into the position domain.

5.3 FIM of The Channel Parameters

We first derive exact expressions for the entries of the FIM. Then, we determine the conditions under which the individual paths can be considered orthogonal. Subsequently, we provide closed-form expressions of the CRLB for the single-path case for 3D and 2D localization.

5.3.1 Exact Expression

Let us define the parameter vector

$$\boldsymbol{\varphi} \triangleq [\boldsymbol{\theta}_{\mathrm{R}}^{\mathrm{T}}, \boldsymbol{\theta}_{\mathrm{T}}^{\mathrm{T}}, \boldsymbol{\phi}_{\mathrm{R}}^{\mathrm{T}}, \boldsymbol{\phi}_{\mathrm{T}}^{\mathrm{T}}, \boldsymbol{\tau}^{\mathrm{T}}, \boldsymbol{\beta}_{\mathrm{R}}^{\mathrm{T}}, \boldsymbol{\beta}_{\mathrm{I}}^{\mathrm{T}}]^{\mathrm{T}}, \tag{5.7}$$

where $\boldsymbol{\beta}_{\mathrm{R}} \triangleq \Re\{\boldsymbol{\beta}\}$, and $\boldsymbol{\beta}_{\mathrm{I}} \triangleq \Im\{\boldsymbol{\beta}\}$ are the real and imaginary parts of $\boldsymbol{\beta}$, respectively, and denote the u^{th} element in $\boldsymbol{\varphi}$ by φ_u. Then, the corresponding FIM, partitioned into $M \times M$ submatrices, is structured as

$$\mathbf{J}_{\boldsymbol{\varphi}} \triangleq \begin{bmatrix} \mathbf{J}_{\boldsymbol{\theta}_{\mathrm{R}}\boldsymbol{\theta}_{\mathrm{R}}} & \mathbf{J}_{\boldsymbol{\theta}_{\mathrm{R}}\boldsymbol{\theta}_{\mathrm{T}}} & \cdots & \mathbf{J}_{\boldsymbol{\theta}_{\mathrm{R}}\boldsymbol{\beta}_{\mathrm{I}}} \\ \mathbf{J}^{\mathrm{T}}_{\boldsymbol{\theta}_{\mathrm{R}}\boldsymbol{\theta}_{\mathrm{T}}} & \ddots & \cdots & \vdots \\ \vdots & \cdots & \ddots & \vdots \\ \mathbf{J}^{\mathrm{T}}_{\boldsymbol{\theta}_{\mathrm{R}}\boldsymbol{\tau}} & \cdots & \cdots & \mathbf{J}_{\boldsymbol{\beta}_{\mathrm{I}}\boldsymbol{\beta}_{\mathrm{I}}} \end{bmatrix}, \tag{5.8}$$

where, due to the additive white Gaussian noise [81],

$$[\mathbf{J}_{\boldsymbol{\varphi}}]_{u,v} \triangleq \frac{1}{N_0} \int_0^{T_{\mathrm{o}}} \Re\left\{ \frac{\partial \boldsymbol{\mu}^{\mathrm{H}}_{\boldsymbol{\varphi}}(t)}{\partial \varphi_u} \frac{\partial \boldsymbol{\mu}_{\boldsymbol{\varphi}}(t)}{\partial \varphi_v} \right\} \mathrm{d}t, \tag{5.9}$$

where $\boldsymbol{\mu}_{\boldsymbol{\varphi}}(t)$ is the noiseless part of received signal in (5.6).

$$\boldsymbol{\mu}_{\boldsymbol{\varphi}}(t) \triangleq \sqrt{N_{\mathrm{R}} N_{\mathrm{T}} E_{\mathrm{t}}} \sum_{m=1}^{M} \beta_m \mathbf{a}_{\mathrm{R},m} \mathbf{a}^{\mathrm{H}}_{\mathrm{T},m} \mathbf{F} \mathbf{s}(t - \tau_m). \tag{5.10}$$

We now introduce the following matrices to simplify the notation

$$\mathbf{B} \triangleq \mathrm{diag}(\boldsymbol{\beta}) \tag{5.11a}$$

$$\mathbf{A}_{\mathrm{R}} \triangleq [\mathbf{a}_{\mathrm{R},1}, \mathbf{a}_{\mathrm{R},2}, ..., \mathbf{a}_{M}], \tag{5.11b}$$

$$\widetilde{\mathbf{K}}_{\mathrm{R},m} \triangleq \mathrm{diag}\left(\frac{\partial}{\partial \theta_{\mathrm{R},m}} \boldsymbol{\Delta}^{\mathrm{T}}_{\mathrm{R}} \mathbf{k}(\theta_{\mathrm{R},m}, \phi_{\mathrm{R},m}) \right), \tag{5.11c}$$

$$\widetilde{\mathbf{P}}_{\mathrm{R},m} \triangleq \mathrm{diag}\left(\frac{\partial}{\partial \phi_{\mathrm{R},m}} \boldsymbol{\Delta}^{\mathrm{T}}_{\mathrm{R}} \mathbf{k}(\theta_{\mathrm{R},m}, \phi_{\mathrm{R},m}) \right), \tag{5.11d}$$

$$\mathbf{K}_{\mathrm{R}} \triangleq [\widetilde{\mathbf{K}}_{\mathrm{R},1} \mathbf{a}_{\mathrm{R},1}, \widetilde{\mathbf{K}}_{\mathrm{R},2} \mathbf{a}_{\mathrm{R},2}, ..., \widetilde{\mathbf{K}}_{\mathrm{R},N_{\mathrm{R}}} \mathbf{a}_{\mathrm{R},N_{\mathrm{R}}}], \tag{5.11e}$$

$$\mathbf{P}_{\mathrm{R}} \triangleq [\widetilde{\mathbf{P}}_{\mathrm{R},1} \mathbf{a}_{\mathrm{R},1}, \widetilde{\mathbf{P}}_{\mathrm{R},2} \mathbf{a}_{\mathrm{R},2}, ..., \widetilde{\mathbf{P}}_{\mathrm{R},N_{\mathrm{R}}} \mathbf{a}_{\mathrm{R},N_{\mathrm{R}}}], \tag{5.11f}$$

with similar expressions obtained by replacing "R" with "T". It is shown in Appendix B that each submatrix in (5.8) is of the form

$$\mathbf{J}_{\mathbf{x},\mathbf{x}'} = \Re\left\{ (\text{RX factor}) \odot (\text{TX factor}) \odot (\text{signal factor}) \right\}, \tag{5.12}$$

where $\odot$ denotes the Hadamard product, the RX factor relates to the receiver array, the TX factor relates to the transmitter array and beamforming, and the signal factor relates to the pilot signals. The RX factor is a product of the matrices $\{\mathbf{A}_{\mathrm{R}}\mathbf{B}, \mathbf{K}_{\mathrm{R}}\mathbf{B}, \mathbf{P}_{\mathrm{R}}\mathbf{B}\}$, while the TX part is a product of similar matrices $\{\mathbf{F}^{\mathrm{H}}\mathbf{A}_{\mathrm{T}}, \mathbf{F}^{\mathrm{H}}\mathbf{K}_{\mathrm{T}}, \mathbf{F}^{\mathrm{H}}\mathbf{P}_{\mathrm{T}}\}$, associated with the transmitter as well as $\mathbf{F}$. Under the assumption of i.i.d. symbols, the signal factor depends on

$$[\mathbf{R}_i]_{uv} \triangleq \int_{-W/2}^{W/2} (2\pi f)^i |P(f)|^2 e^{-j2\pi f \Delta\tau_{uv}} \mathrm{d}f, \tag{5.13}$$

in which $\Delta\tau_{uv} \triangleq \tau_v - \tau_u$, $i \in \{0, 1, 2\}$. The signal factor in (5.13) represents the correlation between different paths obtained in the frequency domain using Parseval's theorem. See (B.8), (B.11) and (B.12).

For instance, defining the signal-to-noise ratio (SNR) as

$$\gamma \triangleq \frac{N_{\mathrm{R}} N_{\mathrm{T}} N_{\mathrm{s}} E_{\mathrm{t}}}{N_0}, \tag{5.14}$$

it can be verified that

$$\mathbf{J}_{\boldsymbol{\theta}_{\mathrm{R}}\boldsymbol{\theta}_{\mathrm{R}}} = \gamma \Re\left\{ (\mathbf{B}^{\mathrm{H}}\mathbf{K}_{\mathrm{R}}^{\mathrm{H}}\mathbf{K}_{\mathrm{R}}\mathbf{B}) \odot (\mathbf{A}_{\mathrm{T}}^{\mathrm{H}}\mathbf{F}\mathbf{F}^{\mathrm{H}}\mathbf{A}_{\mathrm{T}})^{\mathrm{T}} \odot \mathbf{R}_0 \right\}, \tag{5.15}$$

The rest of the FIM entries in (5.8) are listed in Appendix B, and all exhibit the structure in (5.12). Observe that the FIMs in (5.8) scale linearly with SNR, which means that the CRLB decreases as SNR increases.

5.3.2 Approximate FIM of the Channel Parameters

The exact FIMs presented in Section 5.3.1 provide the exact CRLB of the channel parameters. However, under some circumstances, it is possible to simplify this computation by reducing the submatrices of the FIMs to either diagonal or zero matrices, by exploiting the structure in (5.12). Inspired by [130], we start by introducing the following definition.

Definition 5.1 *Given a square matrix $\mathbf{A}(\kappa)$ that can be decomposed into a diagonal matrix $\mathbf{D}(\kappa) \neq \mathbf{0}$ plus a hollow matrix $\mathbf{E}(\kappa) \neq \mathbf{0}$, then $\mathbf{A}(\kappa) = \mathbf{D}(\kappa) + \mathbf{E}(\kappa)$ is*

almost diagonal (AD) for any parameter κ if

$$\lim_{\kappa\to\infty} \delta(\mathbf{A},\kappa) \triangleq \lim_{\kappa\to\infty} \frac{\|\mathbf{E}(\kappa)\|_{\mathrm{F}}}{\|\mathbf{D}(\kappa)\|_{\mathrm{F}}} = 0. \tag{5.16}$$

We now use Definition 5.1 to inspect the factors in (5.12), and understand the behavior under typical mmWave conditions, i.e., large transmit and receive arrays and large system bandwidth.

- *Factor 1 – Receiver Side:* For a large number of receive antennas, the power received from a direction $(\theta_{\mathrm{R},u},\phi_{\mathrm{R},u})$ via a steering vector in the direction $(\theta_{\mathrm{R},v},\phi_{\mathrm{R},v})$ is very small, i.e., $\|\mathbf{a}_{\mathrm{R},u}^{\mathrm{H}}\mathbf{a}_{\mathrm{R},v}\| \ll \|\mathbf{a}_{\mathrm{R},u}\|^2$, $u\neq v$, when the DOAs of the different paths are distinct. Thus, $\lim_{N_{\mathrm{R}}\to\infty}\delta(\mathbf{A}_{\mathrm{R}}^{\mathrm{H}}\mathbf{A}_{\mathrm{R}},N_{\mathrm{R}})=0$. Similarly, considering the exponential form of $\mathbf{a}_{\mathrm{R},m}$ and that $\widetilde{\mathbf{K}}_{\mathrm{R},m},\widetilde{\mathbf{P}}_{\mathrm{R},m}$ are diagonal,

$$\lim_{N_{\mathrm{R}}\to\infty}\delta(\mathbf{K}_R^{\mathrm{H}}\mathbf{K}_{\mathrm{R}},N_{\mathrm{R}}) = \lim_{N_{\mathrm{R}}\to\infty}\delta(\mathbf{P}_R^{\mathrm{H}}\mathbf{P}_{\mathrm{R}},N_{\mathrm{R}}), \tag{5.17a}$$

$$= \lim_{N_{\mathrm{R}}\to\infty}\delta(\mathbf{K}_{\mathrm{R}}^{\mathrm{H}}\mathbf{P}_{\mathrm{R}},N_{\mathrm{R}}) = 0. \tag{5.17b}$$

  On the other hand, using the facts that the BS centroid is at the origin, then for uplink $\mathrm{Tr}(\widetilde{\mathbf{K}}_{\mathrm{R},m}) = \sum_{n=0}^{N_{\mathrm{R}}}\frac{\partial}{\partial\theta_{\mathrm{R}}}\boldsymbol{\Delta}_{\mathrm{R}}^{\mathrm{T}}\mathbf{k} = \left(\sum_{n=0}^{N_{\mathrm{R}}}\boldsymbol{\Delta}_{\mathrm{R}}^{\mathrm{T}}\right)\frac{\partial}{\partial\theta_{\mathrm{R}}}\mathbf{k} = 0$, and similarly, $\mathrm{Tr}(\widetilde{\mathbf{P}}_{\mathrm{R},m})=0$, and that the UE centroid is at $\mathbf{p}$, then for downlink $\mathrm{Tr}(\widetilde{\mathbf{K}}_{\mathrm{R},m}) = \mathbf{p}^{\mathrm{T}}\frac{\partial}{\partial\theta_m}\mathbf{k}$, $\mathrm{Tr}(\widetilde{\mathbf{P}}_{\mathrm{R},m}) = \mathbf{p}^{\mathrm{T}}\frac{\partial}{\partial\phi_m}\mathbf{k}$. Moreover, Noting that $[\mathbf{K}_{\mathrm{R}}^{\mathrm{H}}\mathbf{A}_{\mathrm{R}}]_{m,m} = \mathrm{Tr}(\widetilde{\mathbf{K}}_{\mathrm{R},m})/N_{\mathrm{R}}$, then, for both uplink or downlink,

$$\lim_{N_{\mathrm{R}}\to\infty}\mathbf{K}_{\mathrm{R}}^{\mathrm{H}}\mathbf{A}_{\mathrm{R}} = \lim_{N_{\mathrm{R}}\to\infty}\mathbf{P}_{\mathrm{R}}^{\mathrm{H}}\mathbf{A}_{\mathrm{R}} = \mathbf{0}_{M\times M}. \tag{5.18}$$

  where $\mathbf{0}_{M\times M}$ is an $M\times M$ matrix of zeros.

- *Factor 2 – Transmitter Side:* The transmitter side contributes to the FIM in (5.15) by $\mathbf{A}_{\mathrm{T}}^{\mathrm{H}}\mathbf{F}\mathbf{F}^{\mathrm{H}}\mathbf{A}_{\mathrm{T}}$. Recalling that $[\mathbf{A}_{\mathrm{T}}^{\mathrm{H}}\mathbf{F}\mathbf{F}^{\mathrm{H}}\mathbf{A}_{\mathrm{T}}]_{u,v} = \mathbf{a}_{\mathrm{T},u}^{\mathrm{H}}\mathbf{F}\mathbf{F}^{\mathrm{H}}\mathbf{a}_{\mathrm{T},v}$, the right-hand side term can be interpreted as the spatial cross-correlation between the u^{th} and the v^{th} DODs. So, considering directional beamforming, as N_{T} increases, the beams become narrower, leading to

$$\lim_{N_{\mathrm{T}}\to\infty}\mathbf{a}_{\mathrm{T},u}^{\mathrm{H}}\mathbf{F}\mathbf{F}^{\mathrm{H}}\mathbf{a}_{\mathrm{T},v} \approx 0 \qquad u\neq v. \tag{5.19}$$

Moreover, for extremely narrow beams, the likelihood of covering the v^{th} DOD is almost zero,

$$\lim_{N_{\text{T}}\to\infty} \mathbf{a}_{\text{T},v}^{\text{H}} \mathbf{F}\mathbf{F}^{\text{H}} \mathbf{a}_{\text{T},v} = \lim_{N_{\text{T}}\to\infty} \|\mathbf{F}^{\text{H}} \mathbf{a}_{\text{T},v}\|^2 \approx 0. \tag{5.20}$$

In this extreme case, $\mathbf{A}_{\text{T}}^{\text{H}} \mathbf{F}\mathbf{F}^{\text{H}} \mathbf{A}_{\text{T}} \approx \mathbf{0}$, which implies the whole FIM is zero. However, since (5.19) approaches 0 faster than (5.20), the transmission over directional beamforming should be restricted to $N_{\text{T}} < \infty$. That said, there are cases where (5.20) does not hold and $\mathbf{A}_{\text{T}}^{\text{H}} \mathbf{F}\mathbf{F}^{\text{H}} \mathbf{A}_{\text{T}}$ is AD, e.g., when using random beamforming. By inspection, a similar statement can be made for $(\mathbf{P}_{\text{T}}^{\text{H}} \mathbf{F}\mathbf{F}^{\text{H}} \mathbf{P}_{\text{T}})^{\text{T}}$, $(\mathbf{K}_{\text{T}}^{\text{H}} \mathbf{F}\mathbf{F}^{\text{H}} \mathbf{K}_{\text{T}})^{\text{T}}$, and $(\mathbf{P}_{\text{T}}^{\text{H}} \mathbf{F}\mathbf{F}^{\text{H}} \mathbf{K}_{\text{T}})^{\text{T}}$.

- *Factor 3: Multipath Cross-Correlation*: It can be shown that the cross-correlation functions in (5.13) are even in $\Delta\tau_{uv}$ for $i = 0, 2$ and have maxima on their diagonals. These maxima are constant with values 1 and $4\pi^2 W_{\text{eff}}^2$, respectively, where W_{eff}^2 is as defined in (4.9b). Moreover,

$$\lim_{W\to\infty} \delta(\mathbf{R}_0, W) = 0, \tag{5.21a}$$

$$\lim_{W\to\infty} \delta(\mathbf{R}_2, W) = 0. \tag{5.21b}$$

Regarding $\mathbf{R}_1$, we note that for any W, $\text{diag}(\mathbf{R}_1) = \mathbf{0}_M$ so that $\mathbf{R}_1$ is a hollow matrix, with $\lim_{W\to\infty} \mathbf{R}_1 = \mathbf{0}_{M\times M}$. So, in effect, the paths overlapping in time is negligible, which is consistent with [131] and [132].

In combination, given the Hadamard product structure of (5.12), we find that under typical mmWave conditions, due to the combined effect of large values of N_{R}, and W, some submatrices of the FIM in (5.8) are AD, while the others are almost zero as shown in Figure 5.2 (left). This effect relates to the fact that paths can be resolved in either direction of arrival or delay domain, both of which reinforce each other in mmWave. In other words, it is sufficient to have $N_{\text{R}} \to \infty$ or $W \to \infty$ in order for the paths to be orthogonal. However, as it is customary to have a very large antenna array at the base station, it is reasonable to assume that paths are always orthogonal. Re-ordering the parameters, grouping them path by path, we obtain the block diagonal FIM in Figure 5.2 (right).

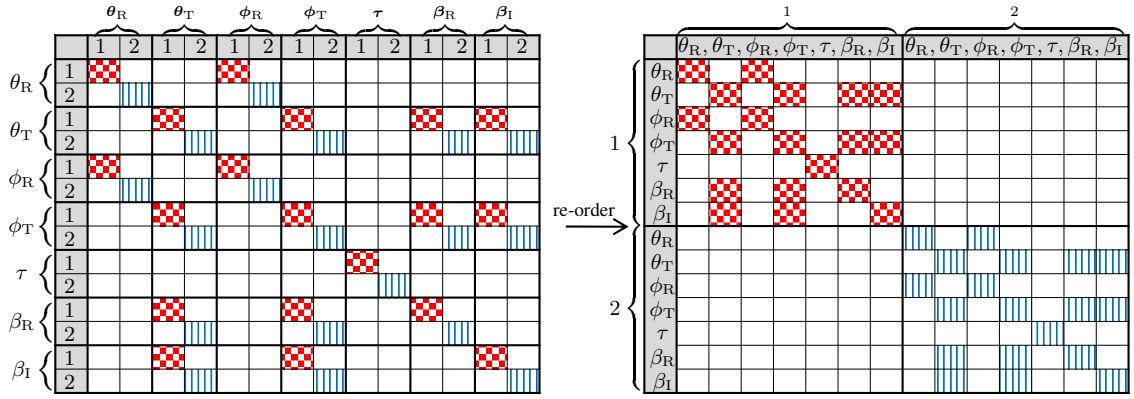

Figure 5.2: An example on the approximate FIM in (5.8) with $M = 2$. The red and blue cells represent the non-zero entries of the FIM and correspond to $m = 1, 2$, respectively. Re-ordering the FIM on the left yields the FIMs in (5.37).

5.3.3 FIM of Single-Path mmWave Channel Parameters

Focusing on the FIM of the m^{th} path, it is interesting to note that after obtaining the FIM in Figure 5.2 (right), it becomes evident that the estimation of τ_m is independent of any other parameter. This follows from the fact that, for the m^{th} path, $\Delta\tau_{mm} = 0$ and $[\mathbf{R}_1]_{m,m} = 0$. Moreover, note that the estimation of $\theta_{\text{R},m}$ and $\phi_{\text{R},m}$ is independent of the other parameters, unlike $\theta_{\text{T},m}$ and $\phi_{\text{T},m}$ which depend on β_m. This is because we use transmit beamforming only, hence power gain has two components: channel gain and antenna directional gain.

We now use the notion of the equivalent FIM (EFIM) from [84], and reviewed in Chapter 2, to isolate the effect of the nuisance parameter β. EFIM is a measure of the information corresponding to a certain unknown parameter, taking into account the uncertainties of the other unknown parameters.

Given the block-diagonal structure of the approximate FIM, it becomes meaningful to study paths separately. Thus, considering β as a nuisance parameter, we focus on a single path, with the parameters of interest being $\boldsymbol{\varphi}_{\text{ch}} \triangleq [\theta_{\text{R}}, \theta_{\text{T}}, \phi_{\text{R}}, \phi_{\text{T}}, \tau]^{\text{T}}$, and write the EFIM of the DOA, DOD, and TOA, from Appendix C, as follows

$$\mathbf{J}^{\text{e}}_{\boldsymbol{\varphi}_{\text{ch}}} = \begin{bmatrix} \mathbf{J}^{\text{e}}_{\boldsymbol{\theta},\boldsymbol{\phi}} & \mathbf{0}_4 \\ \mathbf{0}_4^{\text{T}} & \gamma|\beta|^2 4\pi^2 G W_{\text{eff}}^2 \end{bmatrix}, \tag{5.22}$$

where

$$\mathbf{J}^{\mathrm{e}}_{\boldsymbol{\theta},\boldsymbol{\phi}} = \gamma|\beta|^2 \begin{bmatrix} R_\theta G & 0 & X_{\theta,\phi} G & 0 \\ 0 & \frac{L_\theta}{G} & 0 & \frac{Y_{\theta,\phi}}{G} \\ X_{\theta,\phi} G & 0 & R_\phi G & 0 \\ 0 & \frac{Y_{\theta,\phi}}{G} & 0 & \frac{L_\phi}{G} \end{bmatrix}, \tag{5.23}$$

in which

$$\begin{aligned} R_\theta &\triangleq \mathbf{a}_{\mathrm{R}}^{\mathrm{H}} \widetilde{\mathbf{K}}_{\mathrm{R}}^2 \mathbf{a}_{\mathrm{R}}, & L_\theta &\triangleq G T_\theta - |V_\theta|^2, & G &\triangleq \mathbf{a}_{\mathrm{T}}^{\mathrm{H}} \mathbf{F}\mathbf{F}^{\mathrm{H}} \mathbf{a}_{\mathrm{T}}, \\ R_\phi &\triangleq \mathbf{a}_{\mathrm{R}}^{\mathrm{H}} \widetilde{\mathbf{P}}_{\mathrm{R}}^2 \mathbf{a}_{\mathrm{R}}, & L_\phi &\triangleq G T_\phi - |V_\phi|^2, & X_{\theta,\phi} &\triangleq \mathbf{a}_{\mathrm{R}}^{\mathrm{H}} \widetilde{\mathbf{K}}_{\mathrm{R}} \widetilde{\mathbf{P}}_{\mathrm{R}} \mathbf{a}_{\mathrm{R}}, \\ V_\theta &\triangleq \mathbf{a}_{\mathrm{T}}^{\mathrm{H}} \widetilde{\mathbf{K}}_{\mathrm{T}} \mathbf{F}\mathbf{F}^{\mathrm{H}} \mathbf{a}_{\mathrm{T}}, & T_\theta &\triangleq \mathbf{a}_{\mathrm{T}}^{\mathrm{H}} \widetilde{\mathbf{K}}_{\mathrm{T}} \mathbf{F}\mathbf{F}^{\mathrm{H}} \widetilde{\mathbf{K}}_{\mathrm{T}} \mathbf{a}_{\mathrm{T}}, & Y_{\theta,\phi} &\triangleq G Y'_{\theta,\phi} - \Re\{V_\phi V_\theta^*\}, \\ V_\phi &\triangleq \mathbf{a}_{\mathrm{T}}^{\mathrm{H}} \widetilde{\mathbf{P}}_{\mathrm{T}} \mathbf{F}\mathbf{F}^{\mathrm{H}} \mathbf{a}_{\mathrm{T}}. & T_\phi &\triangleq \mathbf{a}_{\mathrm{T}}^{\mathrm{H}} \widetilde{\mathbf{P}}_{\mathrm{T}} \mathbf{F}\mathbf{F}^{\mathrm{H}} \widetilde{\mathbf{P}}_{\mathrm{T}} \mathbf{a}_{\mathrm{T}}, & Y'_{\theta,\phi} &\triangleq \Re\{\mathbf{a}_{\mathrm{T}}^{\mathrm{H}} \widetilde{\mathbf{P}}_{\mathrm{T}} \mathbf{F}\mathbf{F}^{\mathrm{H}} \widetilde{\mathbf{K}}_{\mathrm{T}} \mathbf{a}_{\mathrm{T}}\}, \end{aligned}$$

Note that G denotes the transmit array gain in a direction θ_{T}, while $R_\theta, R_\phi, T_\theta$, and T_ϕ are the information contents related to the spatial aspects of the received signal and correspond to θ_{R}, ϕ_{R}, θ_{T}, and ϕ_{T}, excluding the SNR, i.e., the integrands in (5.9). Similarly, $V_\theta, V_\phi, X_{\theta,\phi}$, and $Y'_{\theta,\phi}$ respectively represent the mutual spatial information between θ_{T} and β, ϕ_{T} and β, θ_{R} and ϕ_{R}, and θ_{T} and ϕ_{T}. Consequently, L_θ and L_ϕ represent the *equivalent* Fisher spatial information of θ_{T} and ϕ_{T}, respectively, after removing the dependence on β. Finally, $Y_{\theta,\phi}$ denotes the equivalent mutual information of θ_{T} and ϕ_{T}, after removing the dependence on β.

The CRLB of the channel parameters for arbitrary array geometries is provided below.

Proposition 5.1 *Based on the FIM in (5.22), the CRLBs of the DOA, DOD and TOA are given by*

$$\mathrm{CRLB}\,(\theta_{\mathrm{R}}) = \frac{1}{\gamma|\beta|^2\, G\left(R_\theta - \frac{X_{\theta,\phi}^2}{R_\phi}\right)} = \frac{R_\phi}{\gamma\zeta_1|\beta|^2 G}, \tag{5.24a}$$

$$\mathrm{CRLB}\,(\phi_{\mathrm{R}}) = \frac{1}{\gamma|\beta|^2\, G\left(R_\phi - \frac{X_{\theta,\phi}^2}{R_\theta}\right)} = \frac{R_\theta}{\gamma\zeta_1|\beta|^2 G}, \tag{5.24b}$$

$$\mathrm{CRLB}\,(\theta_{\mathrm{T}}) = \frac{G}{\gamma|\beta|^2\left(L_\theta - \frac{Y_{\theta,\phi}^2}{L_\phi}\right)} = \frac{G L_\phi}{\gamma\zeta_2|\beta|^2}, \tag{5.24c}$$

$$\text{CRLB}\left(\phi_{\text{T}}\right)= \frac{G}{\gamma|\beta|^2\left(L_\phi - \frac{Y_{\theta,\phi}^2}{L_\theta}\right)} = \frac{GL_\theta}{\gamma\zeta_2|\beta|^2}, \tag{5.24d}$$

$$\text{CRLB}(\tau) = \frac{1}{(4\pi^2 W_{\text{eff}}^2)(\gamma|\beta|^2 G)}. \tag{5.24e}$$

where $\zeta_1 = R_\theta R_\phi - X_{\theta,\phi}^2$, *and* $\zeta_2 = L_\theta L_\phi - Y_{\theta,\phi}^2$.

Proof

See Appendix C.1.

Note that the CRLBs in (5.24) consist of two components: Firstly, there is an SNR component represented by $\gamma|\beta|^2\, G$ for the receiver angles, and by $G/(\gamma|\beta|^2)$ for the transmitter angles. This component is inversely proportional to the CRLBs, which means with higher SNR, the CRLBs of the channel parameters decrease. Secondly, there is a spatial information part in the parentheses containing the equivalent information after removing the dependence on the other parameter.

Proposition 5.2 *For 2D localization, when the UE and BS are located in the xy-plane,* $\theta_{\text{R}} = \theta_{\text{T}} = \pi/2$

$$\text{CRLB}(\phi_{\text{R}}) = \frac{1}{\gamma|\beta|^2 R_\phi G}, \tag{5.25a}$$

$$\text{CRLB}(\phi_{\text{T}}) = \frac{G}{\gamma|\beta|^2 L_\phi}, \tag{5.25b}$$

while $\text{CRLB}(\tau)$ *is unchanged.*

Proof

See Appendix C.2.

Recall that $\theta_{\text{R}} = \theta_{\text{T}}$ are known and can be removed from $\boldsymbol{\varphi}_{\text{ch}}$, leading to (5.25). Moreover, Note that these expressions can be viewed as special cases of Proposition 5.1, by ignoring the terms relating to the coupling between θ and ϕ. Appendix C.3 provides details on the computation of the FIM and CRLB for URA and ULA as special cases.

5.4 FIM of the Location Parameters

In the preceding sections, we have seen how the FIM of the multipath channel parameters can be approximated by multiple single-path FIMs. We have also derived the single-path FIM for different settings. In this section, we derive the PEB and the OEB by applying a transformation [81] to the EFIM of DOA, DOD, and TOA, computed from (5.8), to obtain the exact FIM of position and orientation. We also transform $\mathbf{J}_{\boldsymbol{\varphi}_{\text{ch}}}$, defined in (5.22), to obtain the approximate one.

5.4.1 PEB and OEB: Exact Approach

General Formulation

Before proceeding further, we state the following theorem.

Theorem 5.1 (Equivalence Theorem) *The FIM of position and orientation obtained by transforming the EFIM of the directions of arrival and departure, and the time of arrival is equivalent to the EFIM of position and orientation obtained by direct transformation of the FIM of the directions of arrival, departure, time of arrival and other nuisance parameter.*

Proof
See Appendix D.1.

This means that instead of transforming the FIM of all the channel parameters (useful and nuisance), and then computing the EFIM of $\mathbf{p}$ and $\mathbf{o}$, we can simplify that by only transforming the EFIM of the useful channel parameters (DOAs, DODs, TOAs).

In this section, we derive the PEB and OEB based on the EFIM of the multipath channel parameters of interest $\boldsymbol{\varphi}_{\text{CH}} \triangleq [\boldsymbol{\theta}^{\text{T}}, \boldsymbol{\phi}^{\text{T}}, \boldsymbol{\tau}^{\text{T}}]^{\text{T}}$. We do so by first transforming $\mathbf{J}^{\text{e}}_{\boldsymbol{\varphi}_{\text{CH}}}$ to a FIM of the location parameters $\boldsymbol{\varphi}_{\text{L}} \triangleq [\mathbf{o}^{\text{T}}, \mathbf{p}^{\text{T}}, \mathbf{q}^{\text{T}}]^{\text{T}}$, where

$$\boldsymbol{\theta} \triangleq \left[\boldsymbol{\theta}_{\text{R}}^{\text{T}}, \boldsymbol{\theta}_{\text{T}}^{\text{T}}\right]^{\text{T}}, \tag{5.26a}$$

$$\boldsymbol{\phi} \triangleq \left[\boldsymbol{\phi}_{\text{R}}^{\text{T}}, \boldsymbol{\phi}_{\text{T}}^{\text{T}}\right]^{\text{T}}, \tag{5.26b}$$

$$\mathbf{q} \triangleq \left[\mathbf{q}_2^{\text{T}}, \mathbf{q}_3^{\text{T}}, \cdots, \mathbf{q}_M^{\text{T}}\right]^{\text{T}}. \tag{5.26c}$$

Towards that, we write

$$\mathbf{J}_{\boldsymbol{\varphi}_{\mathrm{L}}} \triangleq \boldsymbol{\Upsilon}\mathbf{J}^{\mathrm{e}}_{\boldsymbol{\varphi}_{\mathrm{CH}}}\boldsymbol{\Upsilon}^{\mathrm{T}} \triangleq \begin{bmatrix} \mathbf{J}_{\mathbf{op}} & \mathbf{J}_{\mathbf{op,q}} \\ \mathbf{J}^{\mathrm{T}}_{\mathbf{op,q}} & \mathbf{J}_{\mathbf{q}} \end{bmatrix}, \tag{5.27}$$

where $\mathbf{J}_{\mathbf{op}} \in \mathbb{R}^{5\times 5}$, $\mathbf{J}_{\mathbf{q}} \in \mathbb{R}^{3(M-1)\times 3(M-1)}$ and

$$\boldsymbol{\Upsilon} = \frac{\partial \boldsymbol{\varphi}^{\mathrm{T}}_{\mathrm{CH}}}{\partial \boldsymbol{\varphi}_{\mathrm{L}}} = \begin{bmatrix} \frac{\partial \boldsymbol{\theta}^{\mathrm{T}}}{\partial \mathbf{o}} & \frac{\partial \boldsymbol{\phi}^{\mathrm{T}}}{\partial \mathbf{o}} & \frac{\partial \boldsymbol{\tau}^{\mathrm{T}}}{\partial \mathbf{o}} \\ \frac{\partial \boldsymbol{\theta}^{\mathrm{T}}}{\partial \mathbf{p}} & \frac{\partial \boldsymbol{\phi}^{\mathrm{T}}}{\partial \mathbf{p}} & \frac{\partial \boldsymbol{\tau}^{\mathrm{T}}}{\partial \mathbf{p}} \\ \frac{\partial \boldsymbol{\theta}^{\mathrm{T}}}{\partial \mathbf{q}} & \frac{\partial \boldsymbol{\phi}^{\mathrm{T}}}{\partial \mathbf{q}} & \frac{\partial \boldsymbol{\tau}^{\mathrm{T}}}{\partial \mathbf{q}} \end{bmatrix}. \tag{5.28}$$

Consequently, the EFIM of $\mathbf{p}$ and $\mathbf{o}$ is found via Schur's complement as

$$\mathbf{J}^{\mathrm{e}}_{\mathbf{o,p}} = \mathbf{J}_{\mathbf{op}} - \mathbf{J}_{\mathbf{op,q}}\mathbf{J}^{-1}_{\mathbf{q}}\mathbf{J}^{\mathrm{T}}_{\mathbf{op,q}}. \tag{5.29}$$

Finally, the PEB and OEB are given by the square roots of the squared-PEB (SPEB) and squared-OEB (SOEB) defined in the following.

Definition 5.2 *For the equivalent Fisher information matrix of the position and the orientation, $\mathbf{J}^{\mathrm{e}}_{\mathbf{o,p}} \in \mathbb{R}^{5\times 5}$, the SOEB and SPEB are defined as:*

$$\mathrm{SOEB} = \left[(\mathbf{J}^{\mathrm{e}}_{\mathbf{o,p}})^{-1}\right]_{1,1} + \left[(\mathbf{J}^{\mathrm{e}}_{\mathbf{o,p}})^{-1}\right]_{2,2}, \tag{5.30a}$$

$$\mathrm{SPEB} = \left[(\mathbf{J}^{\mathrm{e}}_{\mathbf{o,p}})^{-1}\right]_{3,3} + \left[(\mathbf{J}^{\mathrm{e}}_{\mathbf{o,p}})^{-1}\right]_{4,4} + \left[(\mathbf{J}^{\mathrm{e}}_{\mathbf{o,p}})^{-1}\right]_{5,5}. \tag{5.30b}$$

Transformation for Uplink and Downlink

The relationships governing the UE position and orientation with the BS and UE angles are different. Therefore, unlike $\mathbf{J}_{\boldsymbol{\varphi}}$, the structure of $\boldsymbol{\Upsilon}$ and, effectively, $\mathbf{J}^{\mathrm{e}}_{\mathbf{o,p}}$, depends on whether the uplink or downlink is used for signal transmission. For this reason, we switch to the explicit notation with the subscripts BS and UE,

$$\boldsymbol{\theta} = \begin{cases} \left[\boldsymbol{\theta}^{\mathrm{T}}_{\mathrm{BS}}, \boldsymbol{\theta}^{\mathrm{T}}_{\mathrm{UE}}\right]^{\mathrm{T}}, & \text{uplink} \\ \left[\boldsymbol{\theta}^{\mathrm{T}}_{\mathrm{UE}}, \boldsymbol{\theta}^{\mathrm{T}}_{\mathrm{BS}}\right]^{\mathrm{T}}, & \text{downlink} \end{cases}, \tag{5.31a}$$

$$\boldsymbol{\phi} = \begin{cases} \left[\boldsymbol{\phi}^{\mathrm{T}}_{\mathrm{BS}}, \boldsymbol{\phi}^{\mathrm{T}}_{\mathrm{UE}}\right]^{\mathrm{T}}, & \text{uplink} \\ \left[\boldsymbol{\phi}^{\mathrm{T}}_{\mathrm{UE}}, \boldsymbol{\phi}^{\mathrm{T}}_{\mathrm{BS}}\right]^{\mathrm{T}}, & \text{downlink.} \end{cases} \tag{5.31b}$$

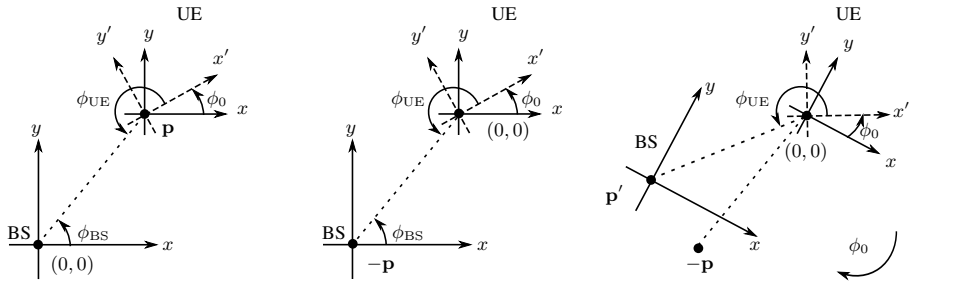

Original coordinate system | Step 1: Shift the origin to $\mathbf{p}$ | Step 2: Rotate the coordinate system by $-\phi_0$

Figure 5.3: Two-step derivation of the UE angle in 2D. It is easy to see that $\phi_{\text{UE}} = \tan^{-1}\left(p'_y/p'_x\right)$, where $\mathbf{p}' = -\mathbf{R}_z(-\phi_0)\mathbf{p}$.

where $\boldsymbol{\phi}_{\text{BS}}$ and $\boldsymbol{\theta}_{\text{BS}}$ denote the vectors of the azimuth and elevation angles at the BS, and $\boldsymbol{\phi}_{\text{UE}}$ and $\boldsymbol{\theta}_{\text{UE}}$ are the azimuth and elevation angles at the UE.

Starting with LOS and using the spherical coordinates, it can be seen from Fig. 5.1 that

$$\theta_{\text{BS},1} = \cos^{-1}\left(p_z/\|\mathbf{p}\|\right), \tag{5.32a}$$

$$\phi_{\text{BS},1} = \tan^{-1}\left(p_y/p_x\right), \tag{5.32b}$$

$$\tau_1 = \|\mathbf{p}\|/c. \tag{5.32c}$$

However, the relationship of the UE angles with the position and orientation angles are not as obvious. Therefore, we resort to the two-step procedure illustrated in Fig. 5.3 for 2D, but easily extensible to 3D. In the first step, we shift the coordinate system origin to the UE, hence, the BS is shifted to $-\mathbf{p}$. In the second step, the coordinate system is rotated in the negative direction of the orientation angle (ϕ_0). Consequently, the BS location is also rotated, and the UE angles are then taken as the spherical coordinates of the new BS location. Mathematically, this location is given by $\mathbf{p}' = -\mathbf{R}_z(-\phi_0)\mathbf{p} = -\mathbf{R}_z^{-1}(\phi_0)\mathbf{p}$, where $\mathbf{R}_z(\phi_0)$ is the rotation matrix in the direction ϕ_0 around the z-axis. Generalizing this result to the 3D case yields,

$$\mathbf{p}' = -\mathbf{R}^{-1}(\theta_0, \phi_0)\mathbf{p}. \tag{5.33}$$

Consequently, defining $\mathbf{p}' \triangleq [p'_x, p'_y, p'_z]^{\text{T}}$ and noting that $\|\mathbf{p}\| = \|\mathbf{p}'\|$, we write

$$\theta_{\text{UE},1} = \cos^{-1}\left(p'_z/\|\mathbf{p}\|\right), \tag{5.34a}$$

$$\phi_{\mathrm{UE},1} = \tan^{-1}\left(p'_y/p'_x\right). \tag{5.34b}$$

With the right-hand rule in mind, the rotation considered in this paper (See Fig. 5.1) is a rotation by ϕ_0 around the z-axis, followed by another rotation by θ_0 around the *negative* x'-axis. Thus, the rotation matrix is given by [133]

$$\begin{aligned}\mathbf{R}(\theta_0,\phi_0) &= \mathbf{R}_z(\phi_0)\mathbf{R}_{-x'}(\theta_0),\\ &= \begin{bmatrix}\cos\phi_0 & -\sin\phi_0\cos\theta_0 & -\sin\phi_0\sin\theta_0\\ \sin\phi_0 & \cos\phi_0\cos\theta_0 & \cos\phi_0\sin\theta_0\\ 0 & -\sin\theta_0 & \cos\theta_0\end{bmatrix}.\end{aligned} \tag{5.35}$$

Note that $\mathbf{R}(\theta_0,\phi_0)$ is orthogonal and hence satisfies $\mathbf{R}^{-1}(\theta_0,\phi_0) = \mathbf{R}^{\mathrm{T}}(\theta_0,\phi_0)$.

Next, considering the NLOS paths ($2 \le m \le M$) and using the same procedure, the following relations can be obtained

$$\theta_{\mathrm{UE},m} = \cos^{-1}\left(w'_{m,z}/\|\mathbf{w}_m\|\right), \tag{5.36a}$$
$$\phi_{\mathrm{UE},m} = \tan^{-1}\left(w'_{m,y}/w'_{m,x}\right), \tag{5.36b}$$
$$\theta_{\mathrm{BS},m} = \cos^{-1}\left(q_{m,z}/\|\mathbf{q}_m\|\right), \tag{5.36c}$$
$$\phi_{\mathrm{BS},m} = \tan^{-1}\left(q_{m,y}/q_{m,x}\right), \tag{5.36d}$$
$$\tau_m = \left(\|\mathbf{q}_m\| + \|\mathbf{w}_m\|\right)/c, \tag{5.36e}$$
$$\mathbf{w}_m = \mathbf{p} - \mathbf{q}_m, \tag{5.36f}$$

where $\mathbf{w}'_m \triangleq [w'_{m,x}, w'_{m,y}, w'_{m,z}]^{\mathrm{T}} = -\mathbf{R}^{\mathrm{T}}(\theta_0,\phi_0)\mathbf{w}_m$. Based on (5.32), (5.34), and (5.36), the non-zero elements of $\boldsymbol{\Upsilon}$ are listed in Appendix E.

5.4.2 PEB and OEB: Approximate Approach

In Section 5.3.2, it was concluded that, under certain conditions, the multiple paths arriving at the receiver can be treated as non-interfering paths carrying independent information. Thus, we can write the total EFIM of position and orientation as a sum of the individual EFIMs obtained by transforming the FIM of useful channel parameters (DOAs, DODs,TOAs), and apply Theorem 5.1 in the following proposition.

Proposition 5.3 *Define the vector of useful channel parameters of the m^{th} path by $\boldsymbol{\varphi}_{\text{ch}}^{(m)} \triangleq [\theta_{\text{R},m}, \theta_{\text{T},m}, \phi_{\text{R},m}, \phi_{\text{T},m}, \tau_m]^{\text{T}}$, and let $\mathbf{J}_{\boldsymbol{\varphi}_s}^{(m)}$ be the FIM of all the parameters of m^{th} path, such that $\boldsymbol{\varphi}_s{}^{(m)} \triangleq [\theta_{\text{R},m}, \theta_{\text{T},m}, \phi_{\text{R},m}, \phi_{\text{T},m}, \tau_m, \beta_{\text{R},m}, \beta_{\text{I},m}]$. Then we write*

$$\mathbf{J}_{\boldsymbol{\varphi}_s}^{(m)} \triangleq \begin{bmatrix} \mathbf{J}_{\text{ch}}^{(m)} & \mathbf{J}_{\text{ch},\beta}^{(m)} \\ \mathbf{J}_{\text{ch},\beta}^{(m)\text{T}} & \mathbf{J}_{\beta\beta}^{(m)} \end{bmatrix}, \tag{5.37}$$

where $\mathbf{J}_{\text{ch}}^{(m)} \in \mathbb{R}^{5\times5}$ is the FIM of $\boldsymbol{\varphi}_{\text{ch}}^{(m)}$, $\mathbf{J}_{\beta\beta}^{(m)} \in \mathbb{R}^{2\times2}$ is the FIM of $\beta_{\text{R},m}$ and $\beta_{\text{I},m}$, and $\mathbf{J}_{\text{ch},\beta}^{(m)} \in \mathbb{R}^{5\times2}$ is the mutual information matrix of $\boldsymbol{\varphi}_{\text{ch}}^{(m)}$ and β. Moreover, denote the EFIM of the m^{th} DOA, DOD, and TOA by

$$\mathbf{J}_{\text{ch}}^{(\text{e},m)} = \mathbf{J}_{\text{ch}}^{(m)} - \mathbf{J}_{\text{ch},\beta}^{(m)} \left(\mathbf{J}_{\beta\beta}^{(m)}\right)^{-1} \mathbf{J}_{\text{ch},\beta}^{(m)\text{T}}, \tag{5.38}$$

and the corresponding transformation matrix in block form by

$$\boldsymbol{\Upsilon}_m \triangleq \begin{cases} \overline{\boldsymbol{\Upsilon}}_1, & m = 1 \\ \begin{bmatrix} \overline{\boldsymbol{\Upsilon}}_m^{\text{T}} & \overline{\overline{\boldsymbol{\Upsilon}}}_m^{\text{T}} \end{bmatrix}^{\text{T}}, & 2 \le m \le M \end{cases} \tag{5.39}$$

where $\overline{\boldsymbol{\Upsilon}}_m$ is the 5×5 matrix relating to $\mathbf{o}$ and $\mathbf{p}$, and $\overline{\overline{\boldsymbol{\Upsilon}}}_m$ is the 3×5 matrix relating to $\mathbf{q}_m$. Then, the approximate EFIM of $\mathbf{o}$ and $\mathbf{p}$ is given by

$$\widetilde{\mathbf{J}}_{\mathbf{o},\mathbf{p}}^{\text{e}} \triangleq \sum_{m=1}^{M} \mathbf{J}_{\mathbf{o},\mathbf{p}}^{(m)}, \tag{5.40}$$

$$= \sum_{m=1}^{M} \overline{\boldsymbol{\Upsilon}}_m \mathbf{J}_{\text{ch}}^{(m)} \overline{\boldsymbol{\Upsilon}}_m^{\text{T}} - \underbrace{\sum_{m=1}^{M} \overline{\boldsymbol{\Upsilon}}_m \mathbf{J}_{\text{ch},\beta}^{(m)} \left(\mathbf{J}_{\beta\beta}^{(m)}\right)^{-1} \mathbf{J}_{\text{ch},\beta}^{(m)\text{T}} \overline{\boldsymbol{\Upsilon}}_m^{\text{T}}}_{\text{path gains uncertainty}}$$

$$- \underbrace{\sum_{m=2}^{M} \overline{\boldsymbol{\Upsilon}}_m \mathbf{J}_{\text{ch}}^{(\text{e},m)} \overline{\overline{\boldsymbol{\Upsilon}}}_m^{\text{T}} \left(\overline{\overline{\boldsymbol{\Upsilon}}} \mathbf{J}_{\text{ch}}^{(\text{e},m)} \overline{\overline{\boldsymbol{\Upsilon}}}^{\text{T}}\right)^{-1} \overline{\overline{\boldsymbol{\Upsilon}}}_m \mathbf{J}_{\text{ch}}^{(\text{e},m)} \overline{\boldsymbol{\Upsilon}}_m^{\text{T}}}_{\text{clusters locations uncertainty}}. \tag{5.41}$$

Proof

See Appendix D.2.

We make the following remarks from (5.41). Firstly, due to the additive nature of

the EFIM, the FIM of the useful localization information (TOA, DOA, DOD) of the M paths accumulate positively to construct the first term. On the other hand, the channel gain, β_m, is a nuisance unknown parameter which needs to be estimated despite not being useful for localization. Not knowing β_m decreases the amount of available information as highlighted by the negative second term comprising $\mathbf{J}^{(m)}_{\text{ch},\beta}$, the mutual information relating β with TOA, DOA, and DOD. Finally, since $m = 1$ is assumed to be a LOS path, the third term is defined starting from $m = 2$. This term is also negative to represent the loss of information due to not knowing the clusters' locations, $\mathbf{q}_m$.

5.4.3 Closed-Form Expressions for LOS: 3D and 2D

Although it is hard to derive closed-form solutions of the general case of PEB and OEB, here we present expressions for the LOS case ($M = 1$).

Proposition 5.4 *For the localization problem set in Section 5.2, in the existence of a LOS path only, the 3D localization SPEB and SOEB of a UE located at* $\mathbf{p}$ *with an orientation angle* $\mathbf{o}$ *are given by*

$$\begin{aligned}\text{SPEB} =& \|\mathbf{p}\|^2 \,\text{CRLB}(\theta_{\text{BS}}) + \|\mathbf{p}\|^2 \sin^2\theta_{\text{BS}} \,\text{CRLB}(\phi_{\text{BS}}) + c^2 \,\text{CRLB}(\tau), \qquad (5.42a)\\ \text{SOEB} =& b_1 \,\text{CRLB}(\theta_{\text{BS}}) + b_2 \,\text{CRLB}(\phi_{\text{BS}}) + b_3\sigma^2_{\theta_{\text{BS}}\phi_{\text{BS}}} \\ &+ b_4 \,\text{CRLB}(\theta_{\text{UE}}) + b_5 \,\text{CRLB}(\phi_{\text{UE}}) + b_6\sigma^2_{\theta_{\text{UE}}\phi_{\text{UE}}}. \qquad (5.42b)\end{aligned}$$

where $\sigma^2_{\theta_{\text{BS}}\phi_{\text{BS}}}$ *and* $\sigma^2_{\theta_{\text{UE}}\phi_{\text{UE}}}$ *are covariance terms arising from the mutual information of the angles in the subscript, and* $b_1, ..., b_6$ *are as given in* (F.13).

Proof

See Appendix F.

In light of (5.42), it can be seen that SPEB depends on the BS angles rather than the UE angles. In other words, SPEB depends on CRLB(DOA) in the uplink, and CRLB(DOD) in the downlink, which have different expressions in (5.24). Thus, SPEB is asymmetric in these two cases. On the other hand, SOEB depends on both UE angles and BS angles, albeit with different weights in the uplink and downlink. As a result, although the SOEB expression in (5.42) is valid for both

Table 5.1: Scaling Factors of CRLBs of the Channel Parameters, PEB and OEB

	URA	ULA
CRLB(θ_{R})	N_{R}^{-2}	N/A
CRLB(θ_{T})	N_{R}^{-1}	N/A
CRLB(ϕ_{R})	N_{R}^{-2}	N_{R}^{-3}
CRLB(ϕ_{T})	N_{R}^{-1}	N_{R}^{-1}
CRLB(τ)	N_{R}^{-1}	N_{R}^{-1}
SPEB (DL)	N_{R}^{-1}	N_{R}^{-1}
SPEB (UL)	$N_{\mathrm{R}}^{-1} + N_{\mathrm{R}}^{-2}$	$N_{\mathrm{R}}^{-1} + N_{\mathrm{R}}^{-3}$
SOEB	$N_{\mathrm{R}}^{-1} + N_{\mathrm{R}}^{-2}$	$N_{\mathrm{R}}^{-1} + N_{\mathrm{R}}^{-3}$

uplink and downlink, SOEB is asymmetric in general. Finally, for the 2D special case, it can be shown that, discarding the terms related to the elevation angles, SOEB $= \mathrm{CRLB}(\phi_{\mathrm{BS}}) + \mathrm{CRLB}(\phi_{\mathrm{UE}})$ and SPEB $= c^2\,\mathrm{CRLB}(\tau) + \|\mathbf{p}\|^2\,\mathrm{CRLB}(\phi_{\mathrm{BS}})$.

These results can be used to determine scaling laws. For instance, evaluating (5.24) and (5.42) as a function of N_{R}, the scaling factors in Table 5.1 are obtained. Similarly the scaling factors for ULA are obtained in Chapter 4. We see that URAs and ULAs have different scaling, in that for CRLB(ϕ_{R}) scales with $1/N_{\mathrm{R}}^2$ for URAs, but with $1/N_{\mathrm{R}}^3$ for ULAs. This can be explained by noting that these scaling factor consist of two multiplicative components: SNR improvement that scales with $1/N_{\mathrm{R}}$ for both geometries, and a spatial resolution that depends on the squared number of antennas in the x-axis direction, that is $1/N_{\mathrm{R}}^2$ for ULA, and $1/(\sqrt{N_{\mathrm{R}}})^2$ for URA.

To obtain scaling laws for SPEB and SOEB, we highlight that while the expressions in (5.42) are valid for both uplink and downlink, the values of the CRLBs in the expressions are different in these two cases (see (5.24)). The CRLB(DOA) and CRLB(DOD) have different scaling laws and thus SPEB will scale differently in the uplink and downlink. However, since $b_1, ..., b_6$ do not depend on the number of antennas, the scaling factors of SOEB is unchanged in both cases.

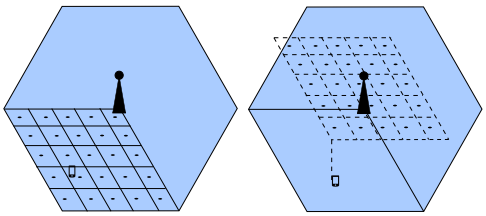

Figure 5.4: A cell sectorized into three sectors, each served by 25 beams directed towards a grid on the ground in the downlink (left) and towards a virtual grid in uplink (right). The grid has the same orientation as the UE.

5.5 Numerical Results and Discussion

5.5.1 Simulation Environment

Although the theoretical results are valid for any arbitrary array geometry, we focus on URAs, as an example of 3D localization. Particularly, we consider a scenario where a BS with standard square array is located in the xz-plane centered at the *origin* with $\sqrt{N_{\text{BS}}} \times \sqrt{N_{\text{BS}}}$ antenna elements and a height of $h_{\text{BS}} = 10$ meters. The UE, operating at $f = 38$ GHz, is equipped with a square array which have $\sqrt{N_{\text{UE}}} \times \sqrt{N_{\text{UE}}}$ antenna elements, and assumed to be tilted by an orientation angle of 0° or 10° in both azimuth and elevation. We investigate the performance over a flat 120° sector of a sectorized cell with a radius of 50 meters as shown in Figure 5.4. The UE is assumed to be located anywhere in this sector, which lies in the plane $z = -h_{\text{BS}} = -10$ meters. Moreover, we consider the ideal sinc pulse defined in (4.13) so that $W_{\text{eff}}^2 = W^2/3$, where $W = 125$ MHz, $E_{\text{t}}/T_{\text{s}} = 0$ dBm, $N_0 = -170$ dBm/Hz, and $N_{\text{s}} = 16$ pilot symbols. The LOS SNR at any location in the sector is given by $\text{SNR[dB]} = 144.24 + 20\log_{10}|\beta| + 20\log_{10}\|\mathbf{a}_T\mathbf{F}\|$, with 95% of the locations having an SNR of at least 30 dB. We utilize the directional beamforming scheme defined in (5.5). In the downlink case, the directions of the beams are fixed and chosen such that the beams centers are equispaced on the ground. On the other hand, in the uplink, the centers of beams are fixed and equispaced on a virtual sector containing the BS. Initially, when the UE has zero orientation, i.e, lying in the xz-plane and facing the BS (See Figure 5.1), this virtual sector lies in the horizontal plane $z = 0$ meters. The beamforming angles

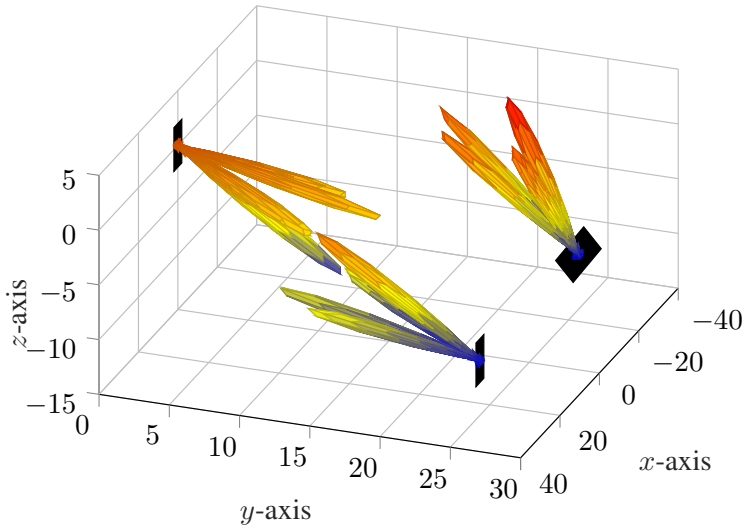

Figure 5.5: An example on beamforming configuration with 4 beams. The rightmost device has orientation angles of 30°, while the other two have 0°.

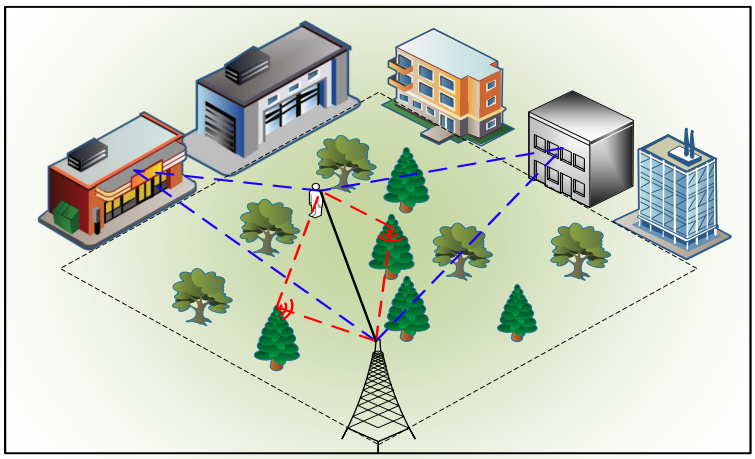

Figure 5.6: A scenario with LOS (black), 2 reflectors (blue) and 2 scatterers (red).

are measured with respect to the UE array plane. Thus, when the orientation of the UE is non-zero, the virtual plane is rotated by the same orientation angles. Figure 5.4 depicts the sector layout with $N_{\mathrm{B}} = 25$ for both downlink and uplink. Figure 5.5 provides an example beamforming configuration, where the BS is located at $(0, 0, 0)$, with beams pointing downwards. A UE is located at $(25, 25, -10)$ with zero orientation angles, and another UE is located at $(-25, 25, -10)$ with orientation angles $\mathbf{o} = [30°, 30°]^{\mathrm{T}}$. The black rectangles denote the array frame

of reference of the device. Note that the first UE has reversed beam direction compared to BS, while the second UE has beam directions reversed and rotated by $[30°, 30°]^{\mathrm{T}}$, so that the beams direction remains constant with respect to the frame of reference.

The environment comprises scatterers and reflectors, with scatterers distributed arbitrarily in the 3D space, and reflectors placed close to the sector edge, as shown in the example scenario in Figure 5.6. We use 5 reflectors placed at the edge of the sector, not to obscure the area behind them if placed otherwise. We also use 15 scatterers distributed arbitrarily in the volume formed by the sector as base, and the BS as height. We only consider the clusters that contribute by a power greater than 10% of the LOS power. As shown in Figure 5.7, it is seen that this configuration leads to a maximum number of paths $M = 6$ at any location in the studied sector, which is similar to the probability mass function in [66]. Accordingly, the complex channel gain of the m^{th} path is modeled by $\beta_m = |\beta_m| e^{j\vartheta_m}$ such that

$$|\beta_m|^2 = \frac{\lambda^2}{(4\pi)^2} \begin{cases} 1/d_1^2 & \text{LOS} \\ \Gamma_{\mathrm{R}}/(d_{1,m} + d_{2,m})^2 & \text{reflector} \\ \sigma_{\mathrm{RCS}}^2/(4\pi(d_{m,1}d_{m,2})^2) & \text{scatterer,} \end{cases} \tag{5.43}$$

where $\vartheta_1 = 2\pi d_1/\lambda$ and $\vartheta_m = 2\pi(d_{m,1} + d_{m,2})/\lambda$ for $m > 1$, while $\sigma_{\mathrm{RCS}}^2 = 50$ m^2, and $\Gamma_{\mathrm{R}} = 0.7$ are the radar cross section, and the reflection coefficient, respectively. Although our derivations are valid for any path loss model, we use the model in (5.43) and the corresponding parameters values to get comparative insights into the role of reflectors and scatterers on the performance bounds. This may not be the typical case in reality where scatterers are characterized by the roughness of the surfaces, which would lead to random path loss, and consequently, random PEB and OEB. The locations of reflectors are computed using the virtual transmitter method [134], shown in Figure 5.8

We consider 5 scenarios, for each of which we evaluate the PEB and OEB:

1. *LOS*: Free space propagation only, without NLOS paths.
2. *LOS+R*: A LOS path and $M - 1$ reflected NLOS paths.
3. *LOS+S*: A LOS path and $M - 1$ scattered NLOS paths.

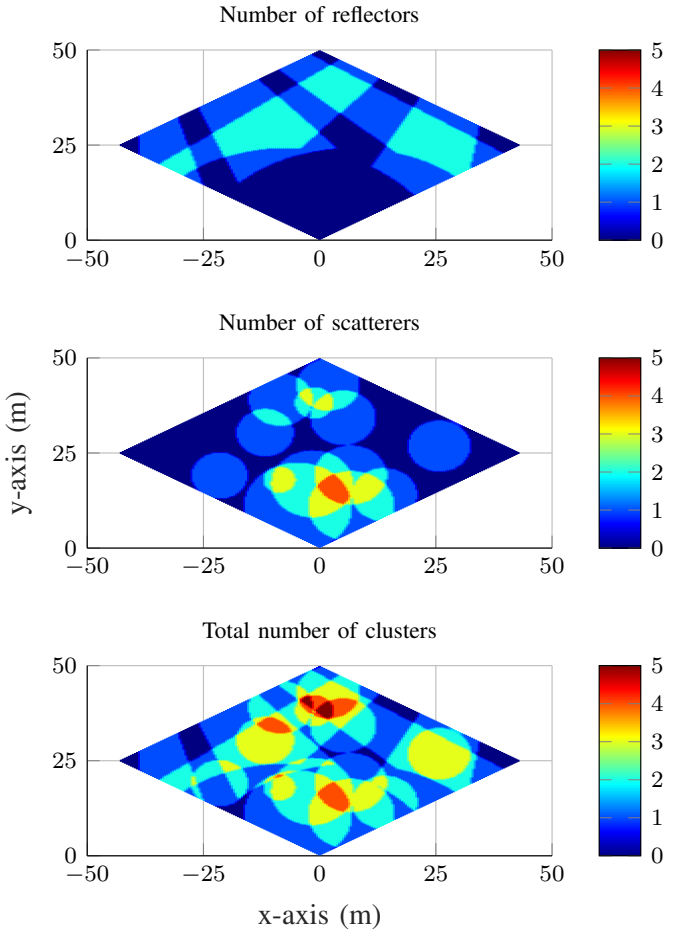

Figure 5.7: The number of reflectors (top), clusters (middle), and clusters (bottom) as function of the UE location.

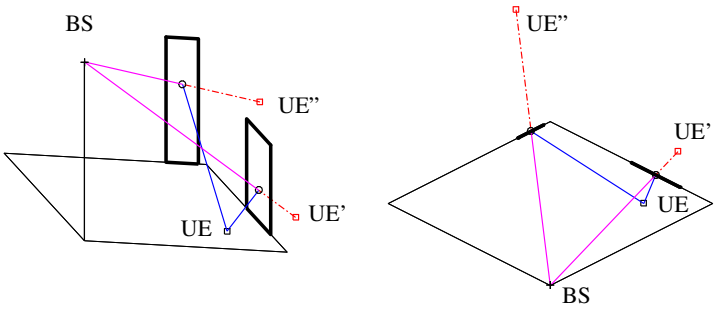

Figure 5.8: The virtual transmitter method in 3D (left) and its top view (right).

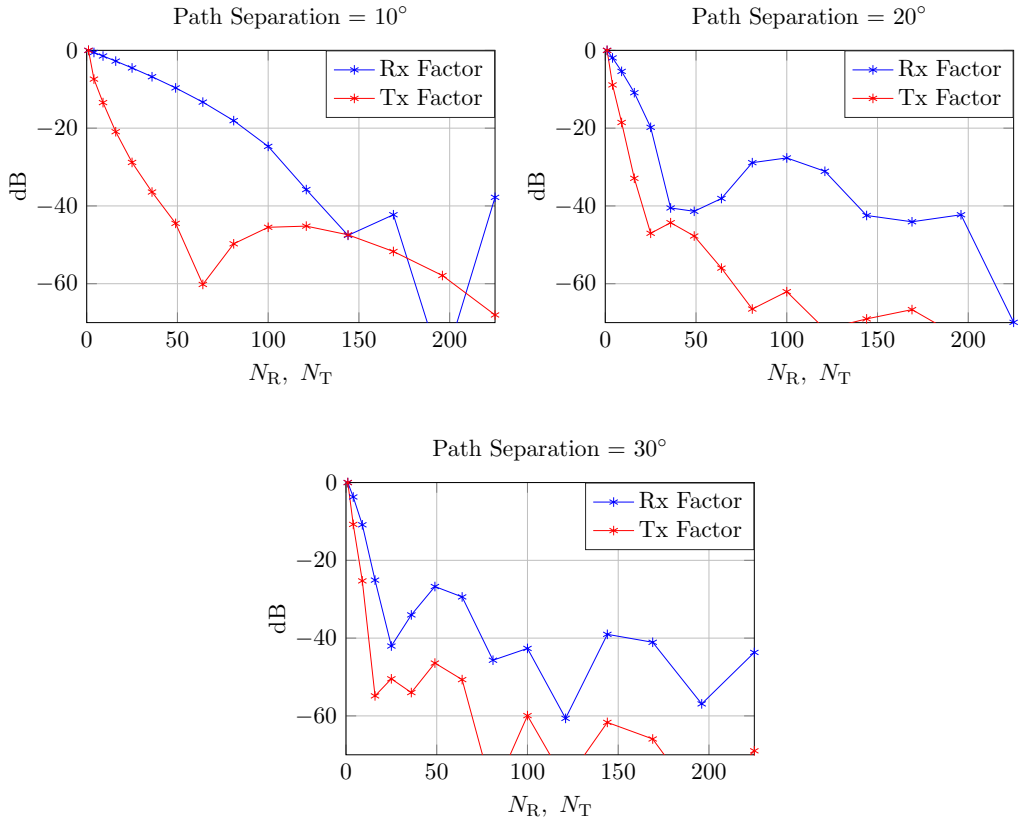

Figure 5.9: Receiver and Transmitter factors w.r.t. N_R and N_T for URA with different path separation angles. The separation angle is the angle difference between the azimuth and elevation angles of the two paths.

4. *LOS+C*: A LOS path and a mix of both scattered and reflected NLOS paths.

5. *NLOS*: The LOS path is blocked, so only scattered and reflected NLOS paths exist.

All the following results are obtained with $N_B = 25$, $N_T = N_R = 144$, unless otherwise stated. We choose equal array sizes at the UE and BS to make the comparison of uplink and downlink localization fair by having a symmetric channel setup. However, it is understood that more complexity is allowed at the BS and its array can grow to larger sizes such as that in [135] to have up to 10,000 antennas, which will improve the localization bounds presented herein, subject to the number of beams used.

5.5.2 Tx and Rx Factors of the Approximate FIM

We now investigate numerically the trend of the RX and TX factors in (5.12) with respect to N_{R} and N_{T} and the path separation angles, as shown in Figure 5.9. Each subfigure is obtained for a different separation angle, that is the azimuth and elevation angle difference between two paths. It can be seen that with a separation of 10°, $N_{\mathrm{R}} = 100$ and $N_{\mathrm{T}} = 16$, the corresponding factor drops below -20 dB (1% of the maximum). On the other hand, for higher separation angles, the two factors drop below -20 dB with less number of antennas. Finally, note that the approximate FIM is obtained by a combined effect of these two factors, plus the signal factor. Therefore, if $N_{\mathrm{R}} \geq 100$ or $N_{\mathrm{T}} \geq 16$, the total FIM will be almost diagonal.

5.5.3 Downlink PEB and OEB

Figure 5.10 shows the downlink PEB and OEB as a function of the UE location for the LOS case with the BS located at $(0, 0)$. With $N_{\mathrm{T}} = N_{\mathrm{R}} = 144$, and $N_{\mathrm{B}} = 25$, the maximum PEB in the sector is 40 cm, while the maximum OEB is 1° in the LOS scenario. Note that from (5.42), the PEB increases with $\|\mathbf{p}\|$. This explains the dark area around the corners. Moreover, the closer the UE to the BS, i.e., as $\theta_{\mathrm{BS}} \to \pi$, singularities appear in the FIM, and the OEB tends to worsen, hence the dark areas around the BS. Scatterers and reflectors are introduced in the 3D space, so that a maximum of 5 clusters contribute at any given location. Based on that, Figure 5.11 shows the PEB and OEB for the LOS+C case. Although incorporating NLOS clusters in the localization does not lower the maximum bound value, it improves the bounds at those locations where the clusters' signal are received. In the illustrated example, the clusters mainly affect the top and center areas of the sector. Finally, note the singularity dots in the central area of the PEB and OEB (LOS+C). These dots occur because at these locations, the scatterer blocks the LOS, violating the unique parameters assumption, and causing singularities in the FIM.

To obtain a more concise quantitative assessment of the performance, we collect all the PEB and OEB values across the space and visualize them in a cumulative distribution function (CDF). Subsequently, Figure 5.12 shows PEB obtained for

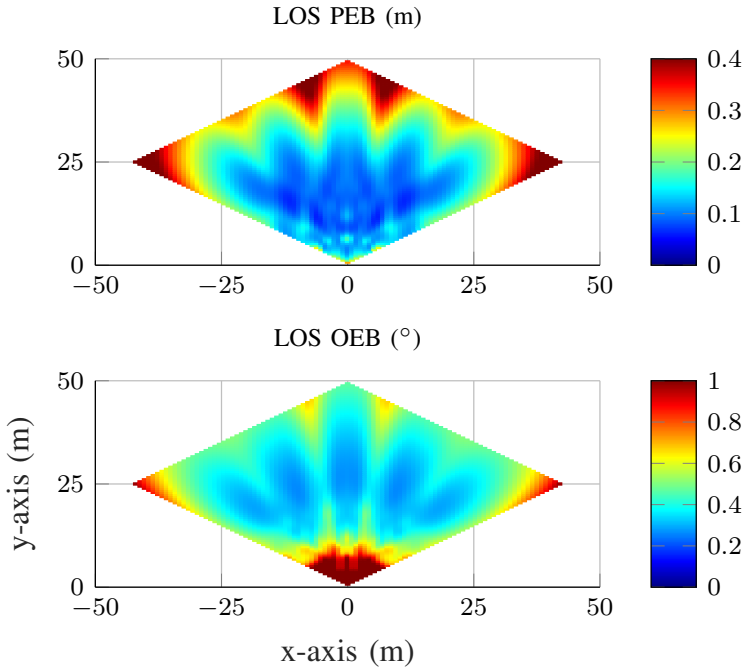

Figure 5.10: PEB and OEB for downlink LOS. The black dots denote the centers of beams, $N_{\mathrm{B}} = 25$, $N_{\mathrm{R}} = N_{\mathrm{T}} = 144$.

all 5 considered scenarios. The PEB obtained from the approximate approach, is also shown in the figure. We observe the following: overall, scatterers and/or reflectors improve the localization performance, compared to the LOS-only scenario, despite the fact that more parameters need to be estimated. Scatterers are mainly useful in providing rather low PEB improvement for many locations, while reflectors can provide modest PEB improvement for fewer locations. When scatterers and reflectors are combined, we see both phenomena. It is also apparent that the approximate approaches closely follow the exact PEB and OEB and that the approximation always leads to a slightly lower PEB and OEB, due to the independent paths assumption, under this approach. Note that at a 90% CDF, the PEB values for LOS, LOS+R, LOS+S, LOS+C are 0.23 m, 0.21 m, 0.19 m and 0.18 m, respectively. Moreover, note that the NLOS scenario is unreliable, with a PEB of 0.5 m at a 13% CDF, and reaches 90% CDF at a value that is irrelevant in mmWave localization. OEB curves (not shown) look similar to those in Figure 5.12, with 90% CDF ranging between 0.42° and 0.5° when a LOS exists. Finally, we obtained

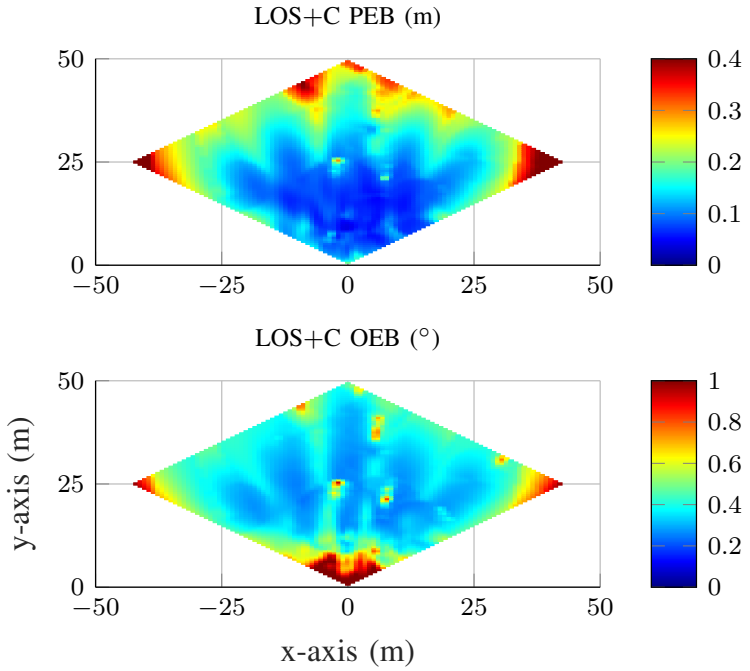

Figure 5.11: PEB and OEB for downlink LOS+C. The black dots denote the centers of beams, $N_{\mathrm{B}} = 25$, $N_{\mathrm{R}} = N_{\mathrm{T}} = 144$.

similar qualitative results with $N_{\mathrm{R}} = 25$, but with PEB and OEB of $45 - 55$ cm and $1.77° - 1.84°$, at 90% CDF respectively, when a LOS exists.

5.5.4 The Selection of N_{B}

In this section, we evaluate the impact of the number of beams on downlink localization. Considering directional beamforming and a given number of transmit antennas, i.e., a fixed beamwidth, the selection of N_{B} becomes a trade-off between hardware complexity and the coverage area up to a certain value of N_{B}, where more beams do not necessarily assist the localization. This relationship is highlighted in Figure 5.13 for PEB values across the space, at a CDF of 90% (similar results hold for the OEB, not shown). It can be seen that at a small N_{B}, the bounds are high, but as N_{B} increases, the bounds start to decrease due better coverage. However, as N_{B} continues to increase, the bounds reach a floor and adding more beams only adds more complexity while providing negligible improvement. To see why, recall that the total transmitted power over the sector is fixed. So, starting

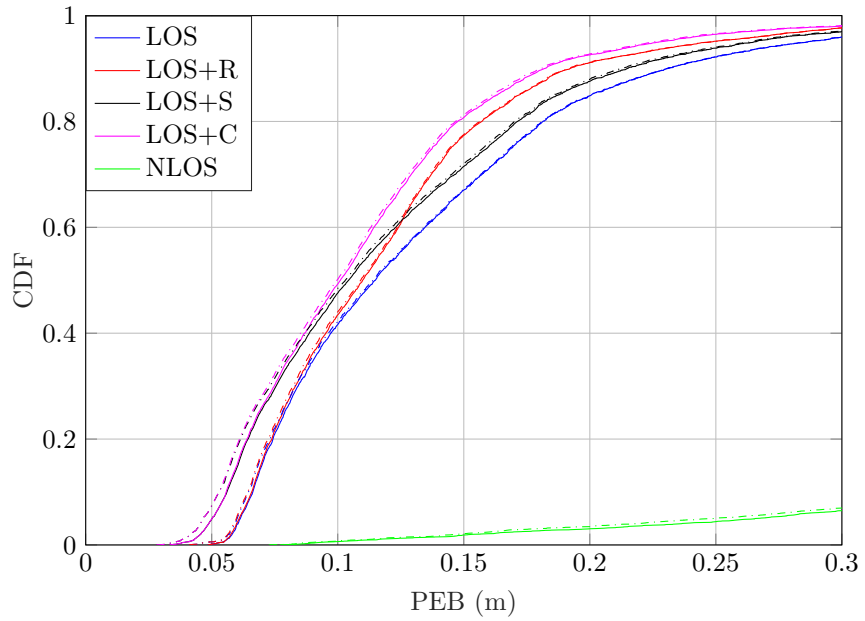

Figure 5.12: The CDF of downlink PEB for different scenarios using the exact (solid) and approximate (dashed) FIM approaches.

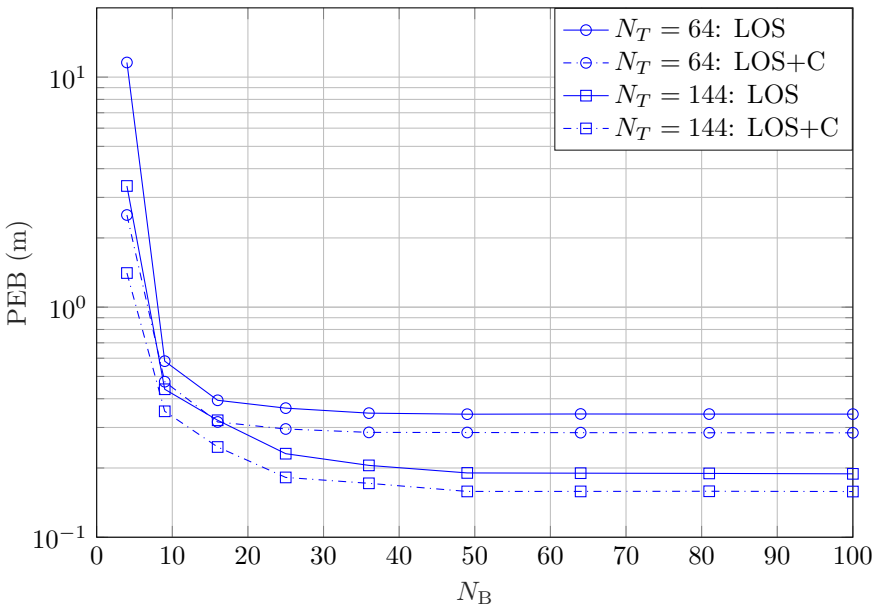

Figure 5.13: Effect of N_{B} on the exact downlink PEB with $N_{\mathrm{R}} = 144, N_{\mathrm{T}} \in \{64, 144\}$, for LOS and LOS+C, at CDF = 0.9.

with a small N_{B} and increasing it gradually improves the coverage, while reducing the power per beam. Eventually, beams start to overlap, but this does not improve the performance because the power impinging on a certain area remains approximately constant. This means that N_{B} should be selected as a function of the beamwidth. For instance, considering $N_{\mathrm{T}} \in \{64, 144\}$, beams with $N_{\mathrm{T}} = 64$ are wider than $N_{\mathrm{T}} = 144$, and thus wider beams provide better coverage for a fixed value of N_{B}. This is why, in this case, it is sufficient to have 16 beams for $N_{\mathrm{T}} = 64$, compared to 25 beams in the case of $N_{\mathrm{T}} = 144$. Finally, note that this trade-off does not depend on whether clusters exist or not.This means that N_{B} should be selected as a function of the beamwidth, which is in turn a function of N_{T}. For instance, considering $N_{\mathrm{T}} \in \{64, 144\}$, beams with $N_{\mathrm{T}} = 64$ are wider[4] than $N_{\mathrm{T}} = 144$. Therefore, smaller N_{B} is required to provide full area coverage when $N_{\mathrm{T}} = 64$. More specifically, it is sufficient to have 16 beams when $N_{\mathrm{T}} = 64$, compared to 25 beams in the case of $N_{\mathrm{T}} = 144$. However, it should be noted that while a higher N_{T} provides narrower beams and necessitates more beams for coverage, it provides higher array gain, i.e., higher SNR due to scaling with γ, hence, lower PEB and OEB. This conclusion manifests in Fig. 5.13, in that the use of 144 antennas attains a lower floor than 64 antennas.

5.5.5 Downlink vs. Uplink Comparison

We now compare uplink and downlink in terms of the following parameters: (i) UE orientation; (ii) number of transmit antennas; (iii) number of receive antennas. We recall that in the downlink, the position and orientation of the transmitter (BS) are known, while in the uplink, (UE transmitter) they are unknown.

UE Orientation impact on PEB and OEB

Considering Figure 5.14, the CDF of PEB is shown for uplink and downlink with two different UE orientation angles. Recall that in the downlink, the UE is a receiver, where no beamforming is assumed. In that sense, and for the sake of

[4]From [58], a URA is considered as two ULAs in orthogonal directions. The half-power beamwidth in each direction is given by $\mathrm{HPBW} = 2\sin^{-1}\left(\frac{0.891}{N_{\mathrm{T}}}\right)$. Thus, high N_{T} leads to small HPBW.

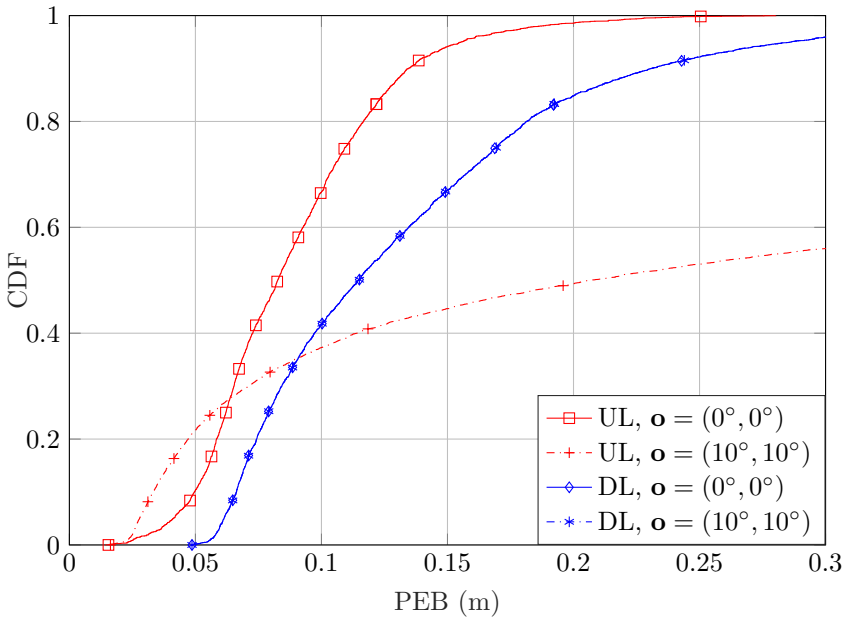

Figure 5.14: CDF of the PEB over the entire sector, for uplink and downlink, with different orientation angles.

computing the bounds regardless of the processing at the receiver, we assume that the receiver is equipped with isotropic antenna elements. Therefore, the *downlink PEB* is independent of the UE orientation, the downlink PEB is identical in both 0° and 10° orientation cases. On the contrary, the *uplink PEB* is highly dependent on the UE orientation: beamforming from the UE is performed in fixed directions in the UE's frame of reference. Depending on the UE location, beams may miss the BS. With 10° orientation, this happens more frequently, thus degrading the PEB. Finally, although in this example the uplink with 0° orientation is better than the downlink in Figure 5.14, this is not alway the case. In fact, this depends on the choice of N_{R}, as will be demonstrated.

For the OEB in Figure 5.15, downlink curves again coincide, with the uplink OEB for 0° yielding similar performance. This is due to OEB being a function of DOA and DOD, which are interchangeable when UE and BS have the same orientation. However, when the UE orientation is 10°, OEB is again degraded, similar to the PEB. Note that to improve the presentation, Figures 5.14 and 5.15 are truncated to show the relevant values of PEB and OEB, respectively.

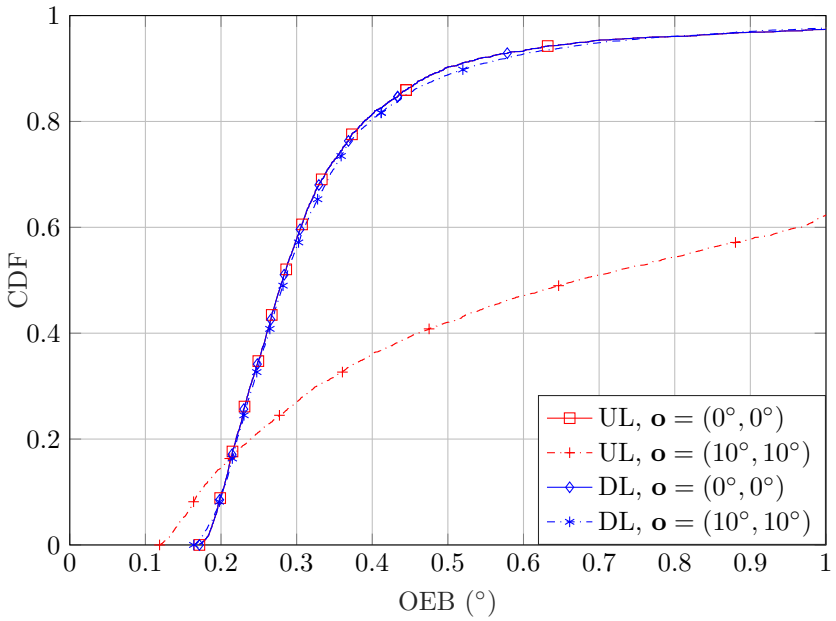

Figure 5.15: CDF of the OEB over the entire sector, for uplink and downlink, with different orientation angles.

Effect of N_{R} and N_{T}

Figure 5.16 shows the scaling effect of the PEB at 90% CDF for LOS, which in line with Table 5.1, implies that uplink and downlink have different scaling exponents. This leads the two lines to cross at some value. So, regarding PEB, choosing N_{R} on either side of this crossing point dictates the outperforming scheme, uplink or downlink. Specifically, for very large number of receive antennas, uplink PEB becomes far better than downlink PEB. With reference to Table 5.1 and (**??**), downlink PEB $\propto \frac{1}{\sqrt{N_{\mathrm{R}}}}$, while uplink PEB $\propto \sqrt{\frac{c_1}{N_{\mathrm{R}}} + \frac{c_2}{N_{\mathrm{R}}^2}}$, for some constants c_1, and c_2 that depend on location, bandwidth, and path gain. For the uplink case, the first term corresponds to CRLB(TOA), while the second term corresponds to CRLB(DOA), from Figure 5.16, it can be inferred that CRLB(TOA) is much smaller than CRLB(DOA) yielding uplink PEB $\propto \frac{1}{N_{\mathrm{R}}}$, which decays faster than PEB $\propto \frac{1}{\sqrt{N_{\mathrm{R}}}}$. This also means that the estimation of the UE location is limited by the estimation of the angles rather than the range.

From Table 5.1, however, the OEB scaling is different than PEB. This is confirmed by the results of the OEB at 90% CDF for LOS shown in Figure 5.17. It

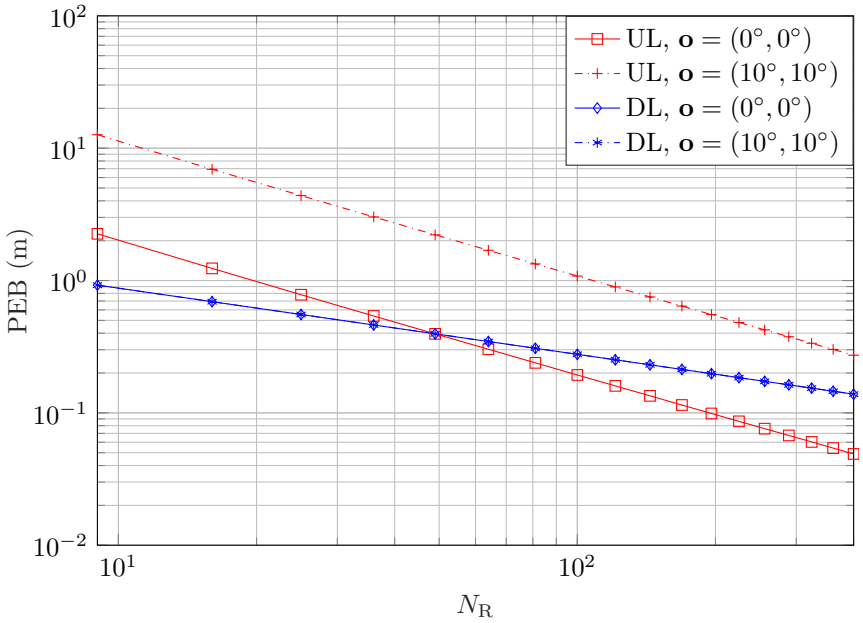

Figure 5.16: Scaling of the PEB w.r.t N_{R} for uplink and downlink LOS scenarios, at CDF = 0.9, with different orientation angles.

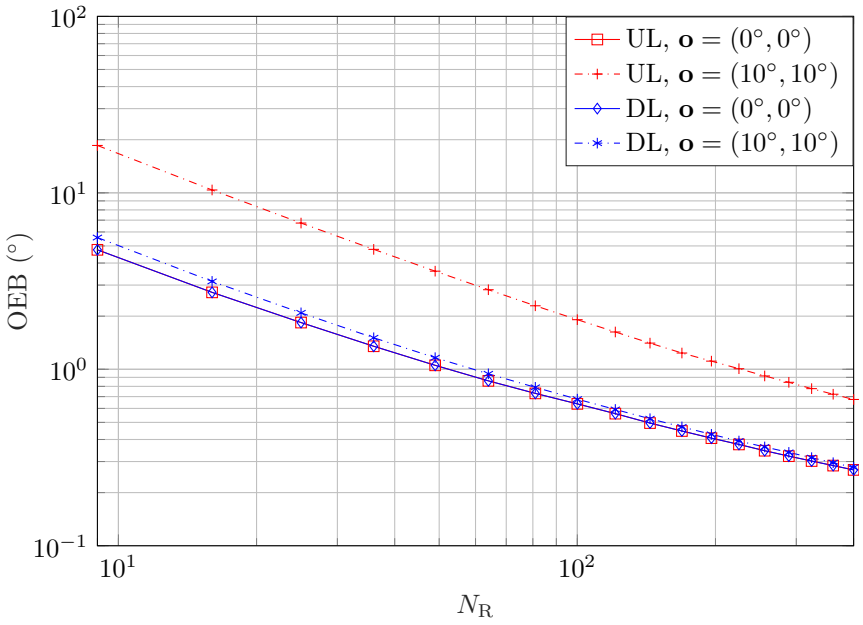

Figure 5.17: Scaling of the OEB w.r.t N_{R} for uplink and downlink LOS scenarios, at CDF = 0.9, with different orientation angles.

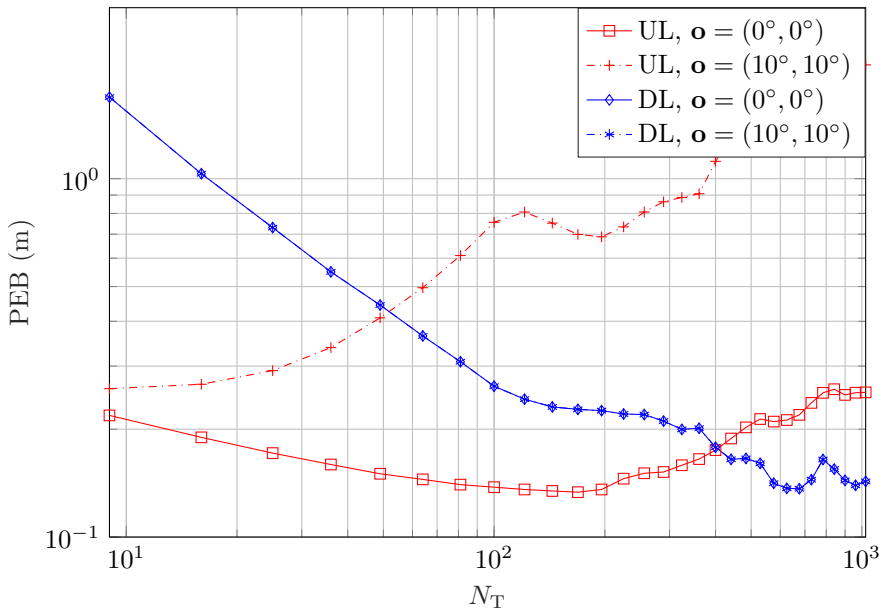

Figure 5.18: Scaling of the PEB w.r.t N_{T} for uplink and downlink LOS scenarios, at CDF = 0.9, with different orientation angles.

can be seen that for relatively large N_{R}, OEB scales of $1/\sqrt{N_{\mathrm{R}}}$, while for small N_{R}, it scales of $1/N_{\mathrm{R}}$, in both uplink and downlink.

Finally, we discuss the effect of N_{T} on the PEB shown in Figure 5.18 (similar OEB results are observed, not shown). Both PEB and OEB scale non-linearly with N_{T}. Small N_{T} results in bad performance due to less spatial resolution and lower SNR. As N_{T} increases, the SNR increases but the beamwidth decreases. At a certain point, the beams become too narrow and bounds start to worsen. Both uplink and downlink suffer from this effect, but it is more severe in the uplink.

5.5.6 Summary of Results

Focusing on outdoor scenarios, our simulations of the approximate approach under mmWave assumptions showed that when $N_{\mathrm{R}} = 100$ and $N_{\mathrm{T}} = 16$, the paths are resolvable in the space domains, and the multipath components can be considered orthogonal. Moreover, our investigations implied that NLOS clusters improve the localization when a LOS path exists. Particularly, we observed that reflectors provide modest PEB improvement for some locations, while scatterers provide small

PEB decrease for more locations. Our analysis of the impact of the N_{B} and N_{T} showed that although smaller N_{T} provide better coverage due to the wider beams, larger N_{T} provides higher SNR, leading to lower PEB and OEB. We also observed that PEB and OEB are more sensitive to the orientation angle in the uplink than in the downlink. Finally, we showed that under mmWave assumptions, PEB < 1 meters and OEB $< 1^{\circ}$ are feasible for BS-UE separation of up to 50 m.

5.6 Conclusions

In this Chapter, we considered mmWave localization performance limits in terms of PEB and OEB, for uplink and downlink localization with arbitrary array geometries in multipath environments. We obtained these bounds by transforming the FIM of the channel parameters that was shown to be composed of three factors related to the receiver side, the transmitter side, and the transmitted signals. Our investigations of an approximate approach under mmWave assumptions showed that if the number of antennas at the receiver is very high, or if the bandwidth is very large, the paths are resolvable in either the time or space domains, and the multipath components can be considered orthogonal. Consequently, the total FIM is the sum of the FIM of individual paths. We also derived closed-form expressions for single-path PEB and OEB, and showed that OEB is a function of the CRLB of the DOA and DOD, while PEB is a function of the CRLB of the TOA and the CRLB of the BS angles (DOD in the downlink, and DOA in the uplink).

Focusing on outdoor scenarios, our simulations show that the NLOS clusters improve the localization when a LOS path exists. Particularly, we observed that reflectors provide modest PEB improvement for some locations, while scatterers provide small PEB decrease for more locations. We analyzed the impact of the number of beams, and the number of transmit and receive antennas. Although having many receive antennas is more beneficial in uplink localization than in downlink localization, the former is generally harder since transmit beamforming at UE may point towards directions not useful for localization. Finally, we observed that PEB and OEB are more sensitive to the orientation angle in the uplink than in the downlink.

Publications Resulted from This Chapter

- **Z. Abu-Shaban**, X. Zhou, T. Abhayapala, G. Seco-Granados, H. Wymeersch, "Error Bounds for Uplink and Downlink 3D Localization in 5G mmWave Systems," Accepted in *IEEE Transactions on Wireless Communication*, April 2018.

- **Z. Abu-Shaban**, X. Zhou, T. Abhayapala, G. Seco-Granados, H. Wymeersch "Location and Orientation Estimation Performance with Uplink and Downlink 5G mmWave Multipath Signals" in the proceedings of *IEEE Wireless Communications and Networking Conf. (WCNC)*, Barcelona, Spain, April 2018.

Chapter 6

Two-Way Localization Bounds for 5G mmWave Systems

Overview: *In Chapter 5, we have seen that 5G mmWave localization is promising with error being in the order centimeters. An assumption usually made in the investigation of localization methods is that the UE and BS are synchronized. This was also the case in Chapter 5. However, in reality communications systems are not finely synchronized to a level useful for localization. Therefore, in this Chapter we investigate two-way localization protocols that alleviate the need for high-level of synchronization. Namely, we consider a distributed localization protocol (DLP), whereby the BS and UE exchange signals in two rounds of transmission and then localization is achieved using the signal received in the second round. On the other hand, we consider a centralized localization protocol (CLP), whereby localization is achieved using the signals received after the two rounds of transmission, where the first signal is assumed to be fed-back to the first device without error. We derive the PEB and OEB applying beamforming at both ends, and compare them to the traditional one-way localization (OWL). Our results show that CLP outperforms DLP by a significant margin, and that DLP barely outperforms OWL because mmWave localization is mainly limited by angular rather than temporal estimation. Our simulations also show that it is more beneficial to have more antennas at the BS than at the UE.*

6.1 Introduction

Recently, the accuracy of single-anchor localization for 5G mmWave systems has been studied in several papers in terms of position (PEB) and orientation error bounds (OEB). In [125], the UE PEB and OEB of 2D localization were investigated using ULAs in 5G mmWave systems. Moreover, [127] and our work in Chapter 5 derived, with different approaches, the PEB and OEB for mmWave 3D localization using arrays with arbitrary geometry. The results in [125, 127, 136] showed a 5G mmWave localization performance with error in the order of centimeters. However, one important, yet usually overlooked, requirement for localization is the synchronization of BS and UE. For example, [125] and our work in Chapter 5 assume that the BS and UE are perfectly synchronized, while [127] assumes coarse synchronization, and includes a residual synchronization error in their model.

Inspired by two-way ranging methods [36, 137, 138], where the time-of-flight is utilized to estimated the range, in this Chapter, we focus on cooperative two-way localization (TWL). We study the PEB and OEB under line-of-sight (LOS) communication with two TWL protocols that account for timing bias between the clocks of the BS and UE. Higher order artifacts such as clock drift and skew are not addressed herein, but can be estimated using the so-called three-way ranging [36] or multi-way ranging [139, 140]. Under TWL, a device transmits a known signal to a receiver, which responds by transmitting another known signal. Upon receiving the latter signal, the first device can estimate the range between the two devices with reference to its local clock. Since this clock was originally used to transmit the first signal, it will alleviates the need for fine time synchronization. In the first protocol, referred to as *Distributed Localization Protocol (DLP),* a device initiates the localization process. Then, a second device estimates the TOA with reference to its local clock and, after a pre-agreed interval, transmits back another signal. Subsequently, localization is carried out using the signal received back at the first device. On the contrary, in the second protocol, referred to as *Centralized Localization Protocol (CLP),* the BS and UE are assumed to be *coarsely* synchronized, so that the two transmission rounds take place in non-overlapping time frames. Under coarse synchronization, the clocks will still have residual bias. Moreover, the pre-agreed waiting interval is taken with reference to the clock of the first de-

vice, and localization is achieved using the signals received at both devices. In this context, the signal received at the second device is assumed to be fed-back to the first device via an error-free link. Note that TWL can be either uplink or downlink, depending on the device where localization is executed. Finally, the contributions of this Chapter are summarized as follows

- We investigate the DLP and CLP for LOS 5G mmWave signals, as a means of alleviating the fine synchronization requirement of 5G localization.
- We derive the FIMs of the position and orientation of the two protocols using 5G mmWave signals, with the timing bias between the BS and UE as a nuisance parameter.
- Unlike [125, 127, 136], we consider multi-direction receive beamforming, and account for the spatially correlated noise resulting from this beamforming.
- Based on the derived FIMs, we evaluate the PEB and OEB numerically for different protocols, and investigate the impact of the number of antennas at BS and UE, as well as the bandwidth.

The rest of the Chapter is organized as follows. In Section 6.2, we provide the system model and highlight the underlying assumptions, while in Section 6.3, we present the DLP and CLP in detail. In Section 6.4, we derive the PEB and OEB for the two protocols, first by calculating the channel parameter FIM, then applying a transformation of variables. In Section 6.5, we provide the numerical results and the discussion, while in Section 6.6, we draw the conclusions.

6.2 Channel Model and Beamforming

Based on the system geometry detailed in Section 5.2.1, we consider two-way localization protocols in which either BS or UE initiates the protocol. Thus, we denote the device initiating the protocol by D_1 and the responding device by D_2.
Notes on notation: In the following, all parameters related to D_1 are denoted by the subscript "1", while those related to D_2 are denoted by the subscript "2". Moreover, the superscripts "f" and "b" are used to relate the parameters to the

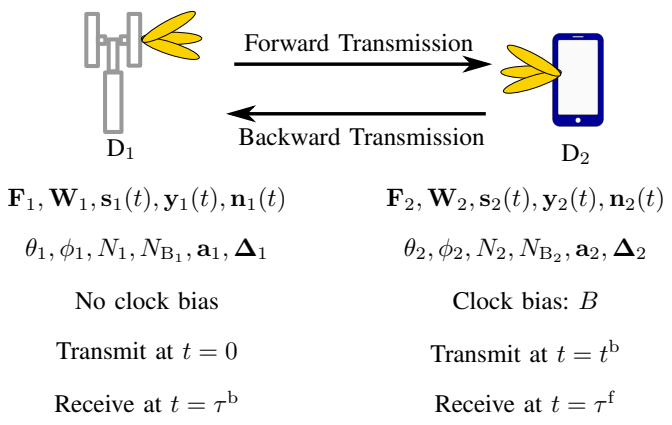

Figure 6.1: Summary of parameters at D_1 and D_2. Although D_1 and D_2 in the figure are BS and UE, this assignment can be reversed.

forward and backward transmissions, respectively. Finally, unless otherwise stated, all the provided times are with respect to the clock of D_1, which is considered a global clock. See Fig. 6.1

Forward Channel

The *forward* signal, transmitted from D_1 at time $t = 0$, and received at D_2 at time $t = \tau^{\mathrm{f}}$, undergoes a forward channel given by

$$\mathbf{H}^{\mathrm{f}}(\beta, \boldsymbol{\vartheta}) \triangleq \mathbf{H}_{\mathrm{s}}^{\mathrm{f}}(\beta, \boldsymbol{\vartheta})\delta(t - \tau^{\mathrm{f}}), \in \mathbb{C}^{N_2 \times N_1} \tag{6.1}$$

where $\delta(t)$ is the Dirac delta function, and $\mathbf{H}_{\mathrm{s}}^{\mathrm{f}}(\beta, \boldsymbol{\vartheta})$ is the channel part corresponding the spatial channel parameters, such that

$$\mathbf{H}_{\mathrm{s}}^{\mathrm{f}}(\beta, \boldsymbol{\vartheta}) \triangleq \sqrt{N_1 N_2}\beta \mathbf{a}_2(\theta_2, \phi_2)\mathbf{a}_1^{\mathrm{H}}(\theta_1, \phi_1), \tag{6.2}$$

where β is the complex LOS path gain, N_1 and N_2 are the number of antennas at D_1 and D_2, respectively, while

$$\boldsymbol{\vartheta} \triangleq [\theta_1, \phi_1, \theta_2, \phi_2]^{\mathrm{T}}, \tag{6.3}$$

and (θ_2, ϕ_2) and (θ_1, ϕ_1) are the forward DOAs and DODs at D_2 and D_1, respectively. Finally, $\mathbf{a}_2$ and $\mathbf{a}_1$ are the response vectors at D_2 and D_1, respectively, given

by

$$\mathbf{a}_1(\theta_1,\phi_1) \triangleq \frac{1}{\sqrt{N_1}} e^{-j\boldsymbol{\Delta}_1^{\mathrm{T}}\mathbf{k}(\theta_1,\phi_1)}, \qquad \in \mathbb{C}^{N_1} \tag{6.4}$$

$$\mathbf{a}_2(\theta_2,\phi_2) \triangleq \frac{1}{\sqrt{N_2}} e^{-j\boldsymbol{\Delta}_2^{\mathrm{T}}\mathbf{k}(\theta_2,\phi_2)}, \qquad \in \mathbb{C}^{N_2} \tag{6.5}$$

where $\mathbf{k}(\theta,\phi)$ is the wavenumber vector, $\boldsymbol{\Delta}_1 \in \mathbb{C}^{3\times N_1}$ is a matrix whose columns contain the 3D Cartesian coordinates of the array elements of D_1 in meters, and $\boldsymbol{\Delta}_2 \in \mathbb{C}^{3\times N_2}$ is defined similarly for D_2. For presentation purposes, we drop the angle parameters from the notation of $\mathbf{a}_1$ and $\mathbf{a}_2$.

The signal transmitted from D_1 is modeled by $\sqrt{E_{\mathrm{t}}}\mathbf{F}_1\mathbf{s}_1(t)$, where E_{t} is the transmitted energy per symbol, and

$$\mathbf{F}_1 \triangleq [\mathbf{f}_{1,1}, \mathbf{f}_{1,2}, ...\mathbf{f}_{1,N_{\mathrm{B}_1}}]. \tag{6.6}$$

is a D_1 transmit beamforming matrix, $\mathbf{f}_{1,b}, 1 \le b \le N_{\mathrm{B}_1}$ is the b^{th} transmit beam, and N_{B_1} is the number of transmit beams. The pilot signal $\mathbf{s}_1(t) \triangleq [s_{1,1}(t), s_{1,2}(t), ..., s_{1,N_{\mathrm{B}_1}}(t)]^{\mathrm{T}}$ is written as

$$s_{1,b}(t) = \sum_{\ell=0}^{N_{\mathrm{s}}-1} a_{1,\ell}^{(b)} p(t-\ell T_{\mathrm{s}}),\ 1 \le b \le N_{\mathrm{B}_1}, \tag{6.7}$$

where $a_{1,\ell}^{(b)}$ are known unit-energy pilot symbols transmitted over the b^{th} beam from D_1. Similarly, define the receive beamforming matrix at D_2 as

$$\mathbf{W}_2 \triangleq [\mathbf{w}_{2,1}, \mathbf{w}_{2,2}, ...\mathbf{w}_{2,N_{\mathrm{B}_2}}], \tag{6.8}$$

where $\mathbf{w}_{2,k}, 1 \le k \le N_{\mathrm{B}_2}$ is a D_2 receive beam, and N_{B_2} is the number of receive beams.

Backward Channel

Similarly, the backward channel from D_2 to D_1 is defined as

$$\mathbf{H}^{\mathrm{b}}(\beta,\boldsymbol{\vartheta}) \triangleq \mathbf{H}_{\mathrm{s}}^{\mathrm{b}}(\beta,\boldsymbol{\vartheta})\delta(t-\tau^{\mathrm{b}}) \in \mathbb{C}^{N_1\times N_2}, \tag{6.9}$$

where

$$\mathbf{H}_{\mathrm{s}}^{\mathrm{b}}(\beta, \boldsymbol{\vartheta}) \triangleq \sqrt{N_1 N_2}\beta \mathbf{a}_1(\theta_1, \phi_1)\mathbf{a}_2^{\mathrm{H}}(\theta_2, \phi_2), \tag{6.10}$$

where τ^{b} denotes the local TOA at D_2, (θ_2, ϕ_2) and (θ_1, ϕ_1) are the backward DODs and DOAs at D_2 and D_1, respectively. We assume that both transmissions occur within the coherence time, so that the channel gain remains unchanged.

In the backward transmission, D_2 transmits via a beamforming matrix, $\mathbf{F}_2$ containing N_{B_2} beams, while D_1 receives via a beamforming matrix, $\mathbf{W}_1$ containing N_{B_1} beams. Both $\mathbf{F}_2$ and $\mathbf{W}_1$ are defined similar to $\mathbf{W}_2$ and $\mathbf{F}_1$, respectively, but with possibly different beam directions.

Our objective is to derive the performance bounds of estimating $\mathbf{p}$ and $\mathbf{o}$, via TOA, DOA, and DOD, in the presence of the unknown nuisance parameters: timing offset between the BS and UE clocks, B, and the unknown path gain, β. This will be done for the DLP and CLP protocols described below.

6.3 Two-Way Localization Protocols

In this section, we define two different two-way localization protocols with the aid of Fig. 6.2.

6.3.1 General Operation

In our formulation, we assume that D_1 has *no timing bias*, while D_2 has a *clock bias* with respect to the clock at D_1, denoted by B. We also denote the nominal TOA by $\tau = \|\mathbf{p}\|/c$, where c is the speed of light.

1. **Forward Transmission** is initiated by D_1 at time $t = 0$, and received at D_2 at local time

$$t = \tau^{\mathrm{f}} = B + \tau. \tag{6.11}$$

The received signal after beamforming at D_2 is given by

$$\mathbf{y}_2(t) = \sqrt{E_{\mathrm{t}}}\mathbf{W}_2^{\mathrm{H}}\mathbf{H}_{\mathrm{s}}^{\mathrm{f}}(\beta, \boldsymbol{\vartheta})\mathbf{F}_1\mathbf{s}_1(t - \tau^{\mathrm{f}}) + \mathbf{n}_2(t), \tag{6.12}$$

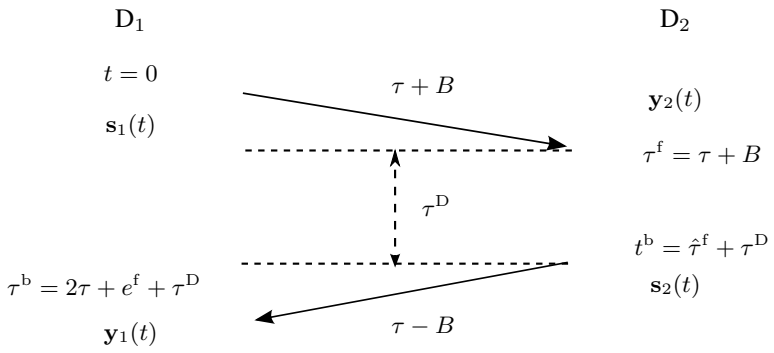

(a) Distributed Localization Protocol

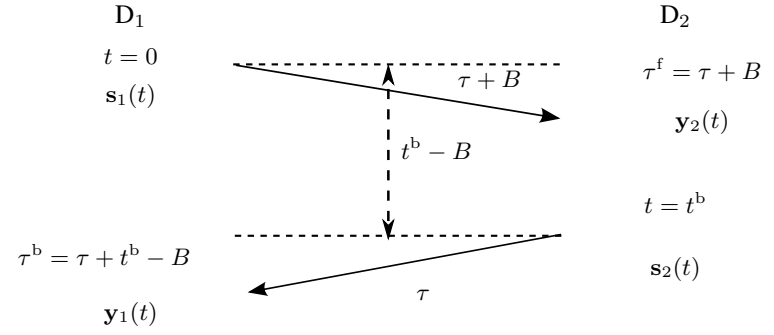

(b) Centralized Localization Protocol

Figure 6.2: The timeline of the studied TWL protocols .

We determine the FIM of $\left[\boldsymbol{\vartheta}^{\mathrm{T}}, \beta_{\mathrm{R}}, \beta_{\mathrm{I}}, \tau^{\mathrm{f}}\right]^{\mathrm{T}}$ based on $\mathbf{y}_2(t)$, and denote the equivalent FIM (EFIM) of τ^{f} by $J_{\tau^{\mathrm{f}}}$.

2. **Backward Transmission** is initiated by D_2 at time $t = t^{\mathrm{b}}$, and received at D_1 at local (which is in the case of D_1 is also global) time

$$t = \tau^{\mathrm{b}} = t^{\mathrm{b}} + \tau - B. \tag{6.13}$$

The received signal after beamforming at D_1 is

$$\mathbf{y}_1(t) = \sqrt{E_{\mathrm{t}}}\mathbf{W}_1^{\mathrm{H}}\mathbf{H}_{\mathrm{s}}^{\mathrm{b}}(\beta, \boldsymbol{\vartheta})\mathbf{F}_2\mathbf{s}_2(t - \tau^{\mathrm{b}}) + \mathbf{n}_1(t) \tag{6.14}$$

Based on $\mathbf{y}_1(t)$, we determine the FIM of $\left[\boldsymbol{\vartheta}^{\mathrm{T}}, \beta_{\mathrm{R}}, \beta_{\mathrm{I}}, \tau^{\mathrm{b}}\right]^{\mathrm{T}}$ and EFIM of τ^{b}, denoted by $J_{\tau^{\mathrm{b}}}$.

We introduce the following estimation error notation

$$e^{\mathrm{f}} \triangleq \widehat{\tau}^{\mathrm{f}} - \tau^{\mathrm{f}}, \qquad \text{and} \qquad e^{\mathrm{b}} \triangleq \widehat{\tau}^{\mathrm{b}} - \tau^{\mathrm{b}}, \quad \text{such that} \tag{6.15}$$

$$\mathbb{E}\{\left(e^{\mathrm{f}}\right)^2\} \geq J_{\tau^{\mathrm{f}}}^{-1}, \qquad \mathbb{E}\{\left(e^{\mathrm{b}}\right)^2\} \geq J_{\tau^{\mathrm{b}}}^{-1}. \tag{6.16}$$

Note that, since the received signals are observed at the beamformer output, $\mathbf{n}_2(t)$ and $\mathbf{n}_1(t)$ in (6.12) and (6.14) are zero-mean additive *spatially-correlated* Gaussian processes. Therefore, the corresponding auto-covariance matrices are $\mathbf{R}_{\mathrm{n}2} = N_0\mathbf{W}_2^{\mathrm{H}}\mathbf{W}_2$, and $\mathbf{R}_{\mathrm{n}1} = N_0\mathbf{W}_1^{\mathrm{H}}\mathbf{W}_1$. N_0 is assumed identical at BS and UE.

The main difference between DLP and CLP is how each protocol coordinates the response message from D_2. In the following, we describe each of these protocols.

6.3.2 Distributed Localization Protocol (DLP)

After a pre-agreed delay τ^{D}, measured from the time $\mathbf{y}_2(t)$ is received, D_2 sends back a signal $\mathbf{s}_2(t)$ at $t^{\mathrm{b}} = \widehat{\tau}^{\mathrm{f}} + \tau^{\mathrm{D}}$. See Fig. 6.2(a). Subsequently, D_1 receives the signal $\mathbf{y}_1(t)$ at

$$\tau^{\mathrm{b}} = \widehat{\tau}^{\mathrm{f}} + \tau^{\mathrm{D}} + \tau - B = 2\tau + e^{\mathrm{f}} + \tau^{\mathrm{D}}. \tag{6.17}$$

Finally, based on $\mathbf{y}_1(t)$, D_1 estimates $\widehat{\tau}^{\mathrm{b}}$ and eventually determines $\mathbf{p}$, and $\mathbf{o}$. Note that B in the forward and backward transmissions cancel out, and need not be estimated at D_2.

6.3.3 Centralized Localization Protocol (CLP)

We assume that D_1 and D_2 are *coarsely* synchronized to avoid overlapping transmissions. At this level of synchronization, there is still some residual clock bias, typically, in the order of hundreds of microseconds. In light of Fig. 6.2.(b), in CLP, t^{b} is a pre-agreed time with reference to the clock of D_2 ($t_{\mathrm{b}} - B$ with reference to the clock of D_1), known to both D_1 and D_2. Upon receiving the signal of D_1, D_2 sends back a signal $\mathbf{s}_2(t)$ at $t = t^{\mathrm{b}}$, which is received at D_1 at τ^{b} given in (6.13). In parallel to that, D_1 also receives $\mathbf{y}_2(t)$ via an error-free feedback link that can possibly be established using a microwave channel. Finally, based on $\mathbf{y}_1(t)$ and the

fed-back $\mathbf{y}_2(t)$, D_1 estimates $\mathbf{p}$, and $\mathbf{o}$.

Under CLP, we determine the FIM of $\left[\boldsymbol{\vartheta}^{\mathrm{T}}, \beta_{\mathrm{R}}, \beta_{\mathrm{I}}, \tau, B\right]^{\mathrm{T}}$ based on both $\mathbf{y}_1(t)$ and $\mathbf{y}_2(t)$. Since the transmissions occur over non-overlapping interval, they provide independent information. We use this fact to sum up the FIMs of the forward and backward directions in the following section.

6.4 Derivation of Two-Way PEB and OEB

The PEB and OEB can be computed from the EFIM of position and orientation, obtained by the transformation of channel parameters; DOA, DOD, and TOA. Therefore, for both DLP and CLP, we start by computing the FIM of the channel parameters before deriving the corresponding PEB and OEB using a parameter transformation procedure similar to that used in Chapter 5.

6.4.1 PEB and OEB for DLP

To compute the PEB and OEB, it is sufficient to obtain the EFIM of position and orientation, and then use Definition 5.2.

FIM of Channel Parameters

In light of (6.10), (6.14), and (6.17), the vector of the unknowns under DLP is

$$\boldsymbol{\varphi}_{\mathrm{D}} \triangleq \left[\boldsymbol{\vartheta}^{\mathrm{T}}, \beta_{\mathrm{R}}, \beta_{\mathrm{I}}, \tau\right]^{\mathrm{T}}. \tag{6.18}$$

Consequently, the FIM of $\boldsymbol{\varphi}_{\mathrm{D}}$ is defined as

$$\mathbf{J}_{\boldsymbol{\varphi}_{\mathrm{D}}} \triangleq \begin{bmatrix} \mathbf{J}^{\mathrm{b}}_{\mathrm{SS}} & \mathbf{0}_6 \\ \mathbf{0}_6^{\mathrm{T}} & J_{\tau\tau} \end{bmatrix}, \tag{6.19}$$

where,

$$\mathbf{J}^{\mathrm{b}}_{\mathrm{SS}} = \begin{bmatrix} \mathbf{J}^{\mathrm{b}}_{\boldsymbol{\vartheta}\boldsymbol{\vartheta}} & \mathbf{J}^{\mathrm{b}}_{\boldsymbol{\vartheta}\beta} \\ \left(\mathbf{J}^{\mathrm{b}}_{\boldsymbol{\vartheta}\beta}\right)^{\mathrm{T}} & J^{\mathrm{b}}_{\beta_{\mathrm{R}}\beta_{\mathrm{R}}}\mathbf{I}_2 \end{bmatrix}, \tag{6.20}$$

is the FIM corresponding to the spatial part of $\mathbf{J}_{\boldsymbol{\varphi}_{\mathrm{D}}}$, such that

$$\mathbf{J}^{\mathrm{b}}_{\boldsymbol{\vartheta}\boldsymbol{\vartheta}} \triangleq \begin{bmatrix} J^{\mathrm{b}}_{\theta_1\theta_1} & J^{\mathrm{b}}_{\theta_1\phi_1} & J^{\mathrm{b}}_{\theta_1\theta_2} & J^{\mathrm{b}}_{\theta_1\phi_2} \\ J^{\mathrm{b}}_{\theta_1\phi_1} & J^{\mathrm{b}}_{\phi_1\phi_1} & J^{\mathrm{b}}_{\phi_1\theta_2} & J^{\mathrm{b}}_{\phi_1\phi_2} \\ J^{\mathrm{b}}_{\theta_1\theta_2} & J^{\mathrm{b}}_{\phi_1\theta_2} & J^{\mathrm{b}}_{\theta_2\theta_2} & J^{\mathrm{b}}_{\theta_2\phi_2} \\ J^{\mathrm{b}}_{\theta_1\phi_2} & J^{\mathrm{b}}_{\phi_1\phi_2} & J^{\mathrm{b}}_{\theta_2\phi_2} & J^{\mathrm{b}}_{\phi_2\phi_2} \end{bmatrix}, \tag{6.21}$$

and

$$\mathbf{J}_{\boldsymbol{\vartheta}\beta} \triangleq \begin{bmatrix} J^{\mathrm{b}}_{\theta_1\beta_{\mathrm{R}}} & J^{\mathrm{b}}_{\theta_1\beta_{\mathrm{I}}} \\ J^{\mathrm{b}}_{\phi_1\beta_{\mathrm{R}}} & J^{\mathrm{b}}_{\phi_1\beta_{\mathrm{I}}} \\ J^{\mathrm{b}}_{\theta_2\beta_{\mathrm{R}}} & J^{\mathrm{b}}_{\theta_2\beta_{\mathrm{I}}} \\ J^{\mathrm{b}}_{\phi_2\beta_{\mathrm{R}}} & J^{\mathrm{b}}_{\phi_2\beta_{\mathrm{I}}} \end{bmatrix}. \tag{6.22}$$

Note that the mutual information between the temporal and spatial parts in (6.19) is zero based on realistic mmWave assumptions of large number of antennas at the transmitter and receiver, large bandwidth and spatially sparse channel. Moreover, note that, in (6.20), we used the fact that $J^{\mathrm{b}}_{\beta_{\mathrm{R}}\beta_{\mathrm{R}}} = J^{\mathrm{b}}_{\beta_{\mathrm{I}}\beta_{\mathrm{I}}}$.

While we can determine $J_{\tau^{\mathrm{f}}}$ based on $\mathbf{y}_2(t)$, the FIM of $\left[\boldsymbol{\vartheta}^{\mathrm{T}}, \beta_{\mathrm{R}}, \beta_{\mathrm{I}}, \tau^{\mathrm{b}}\right]^{\mathrm{T}}$ is based on $\mathbf{y}_1(t)$. To obtain the FIM of $\boldsymbol{\varphi}_{\mathrm{D}}$ that includes τ rather than τ^{b}, we apply the fact that the delays are not dependent on any of the other parameters proven in Chapter 5. Towards that, recall that $\widehat{\tau}^{\mathrm{b}} = 2\tau + e^{\mathrm{f}} + e^{\mathrm{b}} + \tau^{\mathrm{D}}$, and define

$$\tau' \triangleq \frac{\widehat{\tau}^{\mathrm{b}} - \tau^{\mathrm{D}}}{2} = \tau + \frac{e^{\mathrm{f}} + e^{\mathrm{b}}}{2}. \tag{6.23}$$

Consequently, using (6.16) yields

$$\mathbb{E}\Big\{ \left(\tau' - \tau\right)^2 \Big\} \geq \frac{1}{4}\left(J^{-1}_{\tau^{\mathrm{f}}} + J^{-1}_{\tau^{\mathrm{b}}}\right), \tag{6.24}$$

that is,

$$J_{\tau\tau} = 4\left(J^{-1}_{\tau^{\mathrm{f}}} + J^{-1}_{\tau^{\mathrm{b}}}\right)^{-1}. \tag{6.25}$$

The value of $J_{\tau\tau}$ as well as the entries of (6.20) are listed in (G.6) and (G.7), derived in Appendix G.

FIM of Location Parameters

To obtain the FIM of the location parameters (position and orientation), we need the EFIM of $\boldsymbol{\vartheta}$ and τ. Since the temporal and spatial parts in (6.19) are independent, the EFIM of DOD and DOA is obtained from (6.20) by Schur's complement

$$\mathbf{J}^{\mathrm{e,b}}_{\boldsymbol{\vartheta}\boldsymbol{\vartheta}} = \mathbf{J}^{\mathrm{b}}_{\boldsymbol{\vartheta}\boldsymbol{\vartheta}} - \frac{1}{J^{\mathrm{b}}_{\beta_{\mathrm{R}}\beta_{\mathrm{R}}}} \mathbf{J}^{\mathrm{b}}_{\boldsymbol{\vartheta}\beta} \left(\mathbf{J}^{\mathrm{b}}_{\boldsymbol{\vartheta}\beta}\right)^{\mathrm{T}}. \tag{6.26}$$

Consequently, the EFIM of $\boldsymbol{\vartheta}$ and τ is given by

$$\mathbf{J}^{\mathrm{e,b}}_{\boldsymbol{\vartheta}\tau} = \begin{bmatrix} \mathbf{J}^{\mathrm{e,b}}_{\boldsymbol{\vartheta}\boldsymbol{\vartheta}} & \mathbf{0}_4 \\ \mathbf{0}_4^{\mathrm{T}} & J_{\tau\tau} \end{bmatrix}. \tag{6.27}$$

Applying a parameter transformation to (6.27), we obtain the EFIM of $\mathbf{o}$ and $\mathbf{p}$

$$\mathbf{J}^{\mathrm{e,b}}_{\mathbf{o},\mathbf{p}} = \boldsymbol{\Upsilon}^{\mathrm{b}} \mathbf{J}^{\mathrm{e,b}}_{\boldsymbol{\vartheta}\tau} \left(\boldsymbol{\Upsilon}^{\mathrm{b}}\right)^{\mathrm{T}}, \tag{6.28}$$

where

$$\boldsymbol{\Upsilon}^{\mathrm{b}} \triangleq \left[\begin{array}{cccc:c} \frac{\partial\theta_1}{\partial\mathbf{o}} & \frac{\partial\phi_1}{\partial\mathbf{o}} & \frac{\partial\theta_2}{\partial\mathbf{o}} & \frac{\partial\phi_2}{\partial\mathbf{o}} & \frac{\partial\tau}{\partial\mathbf{o}} \\ \frac{\partial\theta_1}{\partial\mathbf{p}} & \frac{\partial\phi_1}{\partial\mathbf{p}} & \frac{\partial\theta_2}{\partial\mathbf{p}} & \frac{\partial\phi_2}{\partial\mathbf{p}} & \frac{\partial\tau}{\partial\mathbf{p}} \end{array}\right] = \left[\begin{array}{c:c} \boldsymbol{\Upsilon}^{\mathrm{b}}_{\mathrm{s}} & \boldsymbol{\Upsilon}_{\tau} \end{array}\right]. \tag{6.29}$$

Note that while

$$\boldsymbol{\Upsilon}_{\tau} = \left[\mathbf{0}_2^{\mathrm{T}} \quad \frac{\mathbf{p}^{\mathrm{T}}}{c\|\mathbf{p}\|}\right]^{\mathrm{T}}, \tag{6.30}$$

for both the uplink and downlink, $\boldsymbol{\Upsilon}^{\mathrm{b}}_{\mathrm{s}}$ is defined differently. From Chapter 5

$$\boldsymbol{\Upsilon}^{\mathrm{b}}_{\mathrm{s}}|_{\mathrm{UL}} = \begin{bmatrix} 0 & 0 & -\frac{p'_y}{a'} & -\frac{p'_x p'_z}{a'^2} \\ 0 & 0 & \frac{p'_x \sin\theta_0}{a'} & \frac{-p'^2_x \cos\theta_0 + g p'_y}{a'^2} \\ \frac{\dot{\mathbf{p}}_\theta}{\|\mathbf{p}\| a} & \frac{[-p_y, p_x, 0]^{\mathrm{T}}}{a^2} & \frac{\mathbf{r}_3 + \frac{p'_z}{\|\mathbf{p}\|}\mathbf{p}}{a'} & \frac{(\mathbf{r}_2\mathbf{r}_1^{\mathrm{T}} - \mathbf{r}_1\mathbf{r}_2^{\mathrm{T}})\mathbf{p}}{a'^2} \end{bmatrix}, \tag{6.31}$$

$$\boldsymbol{\Upsilon}^{\mathrm{b}}_{\mathrm{s}}|_{\mathrm{DL}} = \begin{bmatrix} -\frac{p'_y}{a'} & -\frac{p'_x p'_z}{a'^2} & 0 & 0 \\ \frac{p'_x \sin\theta_0}{a'} & \frac{-p'^2_x \cos\theta_0 + g p'_y}{a'^2} & 0 & 0 \\ \frac{\mathbf{r}_3 + \frac{p'_z}{\|\mathbf{p}\|}\mathbf{p}}{a'} & \frac{(\mathbf{r}_2\mathbf{r}_1^{\mathrm{T}} - \mathbf{r}_1\mathbf{r}_2^{\mathrm{T}})\mathbf{p}}{a'^2} & \frac{\dot{\mathbf{p}}_\theta}{\|\mathbf{p}\| a} & \frac{[-p_y, p_x, 0]^{\mathrm{T}}}{a^2} \end{bmatrix}, \tag{6.32}$$

where $g \triangleq p_y \cos\phi_0 - p_x \sin\phi_0$, $\dot{\mathbf{p}}_\theta \triangleq [p_x p_z, p_y p_z, -a^2]^{\mathrm{T}}$, $a \triangleq \sqrt{p_x^2 + p_y^2}$, $a' \triangleq \sqrt{p_x'^2 + p_y'^2}$, $[p_x', p_y', p_z']^{\mathrm{T}} \triangleq \mathbf{R}\mathbf{p}$, and $\mathbf{R} \triangleq [\mathbf{r}_1, \mathbf{r}_2, \mathbf{r}_3]$ is the rotation matrix as defined in (5.35).

Subsequently, for DLP, we can isolate the spatial and temporal parts and write,

$$\mathbf{J}_{\mathbf{o},\mathbf{p}}^{\mathrm{e,b}} = \underbrace{\boldsymbol{\Upsilon}_{\mathrm{s}}^{\mathrm{b}} \mathbf{J}_{\boldsymbol{\vartheta}\boldsymbol{\vartheta}}^{\mathrm{e,b}} \left(\boldsymbol{\Upsilon}_{\mathrm{s}}^{\mathrm{b}}\right)^{\mathrm{T}}}_{\text{Spatial Part}} + \underbrace{J_{\tau\tau} \boldsymbol{\Upsilon}_{\tau} \boldsymbol{\Upsilon}_{\tau}^{\mathrm{T}}}_{\text{Temporal Part}} . \tag{6.33}$$

6.4.2 PEB and OEB for CLP

FIM of Channel Parameters

Unlike DLP, in CLP we have to retrieve B, as can be inferred from (6.11) and (6.13). Therefore, we define the vector of unknown parameters as

$$\boldsymbol{\varphi}_{\mathrm{C}} \triangleq \left[\boldsymbol{\vartheta}^{\mathrm{T}}, \beta_{\mathrm{R}}, \beta_{\mathrm{I}}, \tau, B\right]^{\mathrm{T}} . \tag{6.34}$$

Since D_2 transmission time is independent of the TOA of $\mathbf{y}_2(t)$, and the transmission in the two ways occurs in a non-overlapping time slots, the forward and backward transmissions can be considered independent, and we can write

$$\begin{aligned} \mathbf{J}_{\boldsymbol{\varphi}_{\mathrm{C}}} &= \mathbf{J}_{\boldsymbol{\varphi}_{\mathrm{C}}}^{\mathrm{f}} + \mathbf{J}_{\boldsymbol{\varphi}_{\mathrm{C}}}^{\mathrm{b}}, \\ &= \begin{bmatrix} \mathbf{J}_{\mathrm{SS}}^{\mathrm{f}} & \mathbf{0}_{6\times 2} \\ \mathbf{0}_{2\times 6} & \mathbf{J}_{\mathrm{TT}}^{\mathrm{f}} \end{bmatrix} + \begin{bmatrix} \mathbf{J}_{\mathrm{SS}}^{\mathrm{b}} & \mathbf{0}_{6\times 2} \\ \mathbf{0}_{2\times 6} & \mathbf{J}_{\mathrm{TT}}^{\mathrm{b}} \end{bmatrix} . \end{aligned} \tag{6.35}$$

where the superscripts "f", "b" indicate that the FIM is of the channel parameters from forward and backward transmission, respectively. Note that while $\mathbf{J}_{\mathrm{SS}}^{\mathrm{b}}$ in (6.20) can be directly obtained from (G.6), $\mathbf{J}_{\mathrm{SS}}^{\mathrm{f}}$ is obtained by swapping the subscripts "1" and "2" of the right-hand side of (G.6) in Appendix G.

Moreover, $\mathbf{J}_{\mathrm{TT}}^{\mathrm{f}}$ and $\mathbf{J}_{\mathrm{TT}}^{\mathrm{b}} \in \mathbb{R}^{2\times 2}$ are the FIMs of the temporal parameters, τ and B, in the forward and backward transmission, respectively, such that

$$\mathbf{J}_{\mathrm{TT}}^{\mathrm{f}} \triangleq \begin{bmatrix} J_{\tau\tau}^{\mathrm{f}} & J_{\tau B}^{\mathrm{f}} \\ J_{\tau B}^{\mathrm{f}} & J_{BB}^{\mathrm{f}} \end{bmatrix} \tag{6.36}$$

and $\mathbf{J}_{\mathrm{TT}}^{\mathrm{b}}$ is defined similarly with matching superscripts.

To obtain $\mathbf{J}_{\mathrm{TT}}^{\mathrm{f}}$ and $\mathbf{J}_{\mathrm{TT}}^{\mathrm{b}}$, we use transformation of variables. From (6.11)

$$\mathbf{J}_{\mathrm{TT}}^{\mathrm{f}} = \begin{bmatrix} \frac{\partial \tau^{\mathrm{f}}}{\partial \tau} \\ \frac{\partial \tau^{\mathrm{f}}}{\partial B} \end{bmatrix} J_{\tau^{\mathrm{f}}} \begin{bmatrix} \frac{\partial \tau^{\mathrm{f}}}{\partial \tau} & \frac{\partial \tau^{\mathrm{f}}}{\partial B} \end{bmatrix} = J_{\tau^{\mathrm{f}}} \begin{bmatrix} 1 & 1 \\ 1 & 1 \end{bmatrix}. \tag{6.37}$$

Similarly, from (6.13)

$$\mathbf{J}_{\mathrm{TT}}^{\mathrm{b}} = \begin{bmatrix} \frac{\partial \tau^{\mathrm{b}}}{\partial \tau} \\ \frac{\partial \tau^{\mathrm{b}}}{\partial B} \end{bmatrix} J_{\tau^{\mathrm{b}}} \begin{bmatrix} \frac{\partial \tau^{\mathrm{b}}}{\partial \tau} & \frac{\partial \tau^{\mathrm{b}}}{\partial B} \end{bmatrix} = J_{\tau^{\mathrm{b}}} \begin{bmatrix} 1 & -1 \\ -1 & 1 \end{bmatrix}. \tag{6.38}$$

Note that although both $\mathbf{J}_{\mathrm{TT}}^{\mathrm{f}}$ and $\mathbf{J}_{\mathrm{TT}}^{\mathrm{b}}$ are rank-deficient[1], their sum is full-rank, and is given by

$$\mathbf{J}_{\mathrm{TT}}^{\mathrm{f}} + \mathbf{J}_{\mathrm{TT}}^{\mathrm{b}} = \begin{bmatrix} J_{\tau^{\mathrm{b}}} + J_{\tau^{\mathrm{f}}} & J_{\tau^{\mathrm{f}}} - J_{\tau^{\mathrm{b}}} \\ J_{\tau^{\mathrm{f}}} - J_{\tau^{\mathrm{b}}} & J_{\tau^{\mathrm{b}}} + J_{\tau^{\mathrm{f}}} \end{bmatrix}. \tag{6.39}$$

Consequently, the EFIM of τ is obtained from (6.39) by Schur's complement as

$$\begin{aligned} J_{\tau\tau}^{\mathrm{e}} &= J_{\tau^{\mathrm{b}}} + J_{\tau^{\mathrm{f}}} - \frac{(J_{\tau^{\mathrm{b}}} - J_{\tau^{\mathrm{f}}})^2}{J_{\tau^{\mathrm{b}}} + J_{\tau^{\mathrm{f}}}}, \\ &= \frac{(J_{\tau^{\mathrm{b}}} + J_{\tau^{\mathrm{f}}})^2 - (J_{\tau^{\mathrm{b}}} - J_{\tau^{\mathrm{f}}})^2}{J_{\tau^{\mathrm{b}}} + J_{\tau^{\mathrm{f}}}}, \\ &= \frac{4 J_{\tau^{\mathrm{b}}} J_{\tau^{\mathrm{f}}}}{J_{\tau^{\mathrm{b}}} + J_{\tau^{\mathrm{f}}}}, \\ &= 4 \left(J_{\tau^{\mathrm{f}}}^{-1} + J_{\tau^{\mathrm{b}}}^{-1} \right)^{-1} \end{aligned} \tag{6.40}$$

which is equivalent to $J_{\tau\tau}$ of DLP given in (6.25).

FIM of Location Parameters

Under CLP, we transform the FIM of the channel parameters vector $\boldsymbol{\varphi}_{\mathrm{C}}$ into a FIM of the location parameters vector

$$\boldsymbol{\varphi}_{\mathrm{L}} \triangleq [\mathbf{o}^{\mathrm{T}}, \mathbf{p}^{\mathrm{T}}, \beta_R, \beta_I, B]^{\mathrm{T}}, \tag{6.41}$$

[1]Hence, τ and B cannot be estimated using only one transmission.

as follows

$$\begin{aligned}\mathbf{J}_{\boldsymbol{\varphi}_{\mathrm{L}}} &= \boldsymbol{\Upsilon}^{\mathrm{b}}\mathbf{J}_{\boldsymbol{\varphi}_{\mathrm{C}}}\left(\boldsymbol{\Upsilon}^{\mathrm{b}}\right)^{\mathrm{T}} = \boldsymbol{\Upsilon}^{\mathrm{b}}\left(\mathbf{J}^{\mathrm{f}}_{\boldsymbol{\varphi}_{\mathrm{C}}}+\mathbf{J}^{\mathrm{b}}_{\boldsymbol{\varphi}_{\mathrm{C}}}\right)\left(\boldsymbol{\Upsilon}^{\mathrm{b}}\right)^{\mathrm{T}},\\ &= \underbrace{\boldsymbol{\Upsilon}^{\mathrm{b}}\mathbf{J}^{\mathrm{f}}_{\boldsymbol{\varphi}_{\mathrm{C}}}\left(\boldsymbol{\Upsilon}^{\mathrm{b}}\right)^{\mathrm{T}}}_{\triangleq\mathbf{J}^{\mathrm{f}}_{\boldsymbol{\varphi}_{\mathrm{L}}}}+\underbrace{\boldsymbol{\Upsilon}^{\mathrm{b}}\mathbf{J}^{\mathrm{b}}_{\boldsymbol{\varphi}_{\mathrm{C}}}\left(\boldsymbol{\Upsilon}^{\mathrm{b}}\right)^{\mathrm{T}}}_{\triangleq\mathbf{J}^{\mathrm{b}}_{\boldsymbol{\varphi}_{\mathrm{L}}}},\end{aligned} \tag{6.42}$$

such that

$$\boldsymbol{\Upsilon}^{\mathrm{b}} = \frac{\partial\boldsymbol{\varphi}_{\mathrm{C}}^{\mathrm{T}}}{\partial\boldsymbol{\varphi}_{\mathrm{L}}} \triangleq \begin{bmatrix}\boldsymbol{\Upsilon}^{\mathrm{b}}_{\mathrm{s}} & \mathbf{0}_{5\times2} & \boldsymbol{\Upsilon}_{\tau} & \mathbf{0}_5\\ \mathbf{0}_{2\times4} & \mathbf{I}_2 & \mathbf{0}_2 & \mathbf{0}_2\\ \mathbf{0}_4^{\mathrm{T}} & \mathbf{0}_2^{\mathrm{T}} & 0 & 1\end{bmatrix} \tag{6.43}$$

where $\boldsymbol{\Upsilon}_{\tau}$ is the transformation vector from τ to $\mathbf{o}$ and $\mathbf{p}$ defined in (6.30) and $\boldsymbol{\Upsilon}^{\mathrm{b}}_{\mathrm{s}}$ is the transformation matrix from DOD and DOA to $\mathbf{o}$ and $\mathbf{p}$, defined in (6.31) and (6.32) for the uplink and downlink. Moreover, from (6.20) and (6.35), we write

$$\mathbf{J}^{\mathrm{b}}_{\boldsymbol{\varphi}_{\mathrm{C}}} = \left[\begin{array}{cc:c}\mathbf{J}^{\mathrm{b}}_{\boldsymbol{\vartheta}\boldsymbol{\vartheta}} & \mathbf{J}^{\mathrm{b}}_{\boldsymbol{\vartheta}\beta} & \mathbf{0}_{6\times2}\\ \left(\mathbf{J}^{\mathrm{b}}_{\boldsymbol{\vartheta}\beta}\right)^{\mathrm{T}} & \mathbf{J}^{\mathrm{b}}_{\beta\beta} & \\ \hdashline \mathbf{0}_{6\times2} & & \mathbf{J}^{\mathrm{b}}_{\mathrm{TT}}\end{array}\right]. \tag{6.44}$$

Note that $\mathbf{J}^{\mathrm{f}}_{\boldsymbol{\varphi}_{\mathrm{C}}}$ is defined similarly with matching superscripts.

Substituting $\boldsymbol{\Upsilon}^{\mathrm{b}}$, $\mathbf{J}^{\mathrm{f}}_{\boldsymbol{\varphi}_{\mathrm{C}}}$ and $\mathbf{J}^{\mathrm{b}}_{\boldsymbol{\varphi}_{\mathrm{C}}}$ into (6.42), it can be shown that $\mathbf{J}_{\boldsymbol{\varphi}_{\mathrm{L}}}$ is given by

$$\mathbf{J}_{\boldsymbol{\varphi}_{\mathrm{L}}} = \begin{bmatrix}\mathbf{J}_{\mathbf{o},\mathbf{p}} & \boldsymbol{\Upsilon}^{\mathrm{b}}_{\mathrm{s}}\left(\mathbf{J}^{\mathrm{f}}_{\boldsymbol{\vartheta}\beta}+\mathbf{J}^{\mathrm{b}}_{\boldsymbol{\vartheta}\beta}\right) & (J_{\tau^{\mathrm{f}}}-J_{\tau^{\mathrm{b}}})\boldsymbol{\Upsilon}_{\tau}\\ \left(\mathbf{J}^{\mathrm{f}}_{\boldsymbol{\vartheta}\beta}+\mathbf{J}^{\mathrm{b}}_{\boldsymbol{\vartheta}\beta}\right)\left(\boldsymbol{\Upsilon}^{\mathrm{b}}_{\mathrm{s}}\right)^{\mathrm{T}} & \mathbf{J}^{\mathrm{f}}_{\beta\beta}+\mathbf{J}^{\mathrm{b}}_{\beta\beta} & \mathbf{0}_2\\ (J_{\tau^{\mathrm{f}}}-J_{\tau^{\mathrm{b}}})\boldsymbol{\Upsilon}_{\tau}^{\mathrm{T}} & \mathbf{0}_2^{\mathrm{T}} & J_{\tau^{\mathrm{b}}}+J_{\tau^{\mathrm{f}}}\end{bmatrix}, \tag{6.45}$$

where $\mathbf{J}_{\mathbf{o},\mathbf{p}} = \boldsymbol{\Upsilon}^{\mathrm{b}}_{\mathrm{s}}\left(\mathbf{J}^{\mathrm{f}}_{\boldsymbol{\vartheta}\boldsymbol{\vartheta}}+\mathbf{J}^{\mathrm{b}}_{\boldsymbol{\vartheta}\boldsymbol{\vartheta}}\right)\left(\boldsymbol{\Upsilon}^{\mathrm{b}}_{\mathrm{s}}\right)^{\mathrm{T}} + (J_{\tau^{\mathrm{b}}}+J_{\tau^{\mathrm{f}}})\boldsymbol{\Upsilon}_{\tau}\boldsymbol{\Upsilon}_{\tau}^{\mathrm{T}}$.

Finally, taking the Schur's Complement with respect to $\mathbf{J}_{\mathbf{o},\mathbf{p}}$, and using (6.26), and (6.40), it can be shown that the EFIM of the position and orientation is

$$\begin{aligned}\mathbf{J}^{(\mathrm{e})}_{\mathbf{o},\mathbf{p}} =& \boldsymbol{\Upsilon}^{\mathrm{b}}_{\mathrm{s}}\left(\mathbf{J}^{\mathrm{f}}_{\boldsymbol{\vartheta}\boldsymbol{\vartheta}}+\mathbf{J}^{\mathrm{b}}_{\boldsymbol{\vartheta}\boldsymbol{\vartheta}}\right)\left(\boldsymbol{\Upsilon}^{\mathrm{b}}_{\mathrm{s}}\right)^{\mathrm{T}} + \left(J_{\tau^{\mathrm{b}}}+J_{\tau^{\mathrm{f}}}-\frac{(J_{\tau^{\mathrm{b}}}-J_{\tau^{\mathrm{f}}})^2}{J_{\tau^{\mathrm{b}}}+J_{\tau^{\mathrm{f}}}}\right)\boldsymbol{\Upsilon}_{\tau}\left(\boldsymbol{\Upsilon}_{\tau}\right)^{\mathrm{T}}\\ &- \boldsymbol{\Upsilon}^{\mathrm{b}}_{\mathrm{s}}\left(\mathbf{J}^{\mathrm{f}}_{\boldsymbol{\vartheta}\beta}+\mathbf{J}^{\mathrm{b}}_{\boldsymbol{\vartheta}\beta}\right)\left(\mathbf{J}^{\mathrm{f}}_{\beta\beta}+\mathbf{J}^{\mathrm{b}}_{\beta\beta}\right)^{-1}\left(\mathbf{J}^{\mathrm{f}}_{\boldsymbol{\vartheta}\beta}+\mathbf{J}^{\mathrm{b}}_{\boldsymbol{\vartheta}\beta}\right)\left(\boldsymbol{\Upsilon}^{\mathrm{b}}_{\mathrm{s}}\right)^{\mathrm{T}}.\end{aligned}$$

$$= \underbrace{\boldsymbol{\Upsilon}_{\mathrm{s}}^{\mathrm{b}} \mathbf{J}_{\boldsymbol{\vartheta}\boldsymbol{\vartheta}}^{\mathrm{e,f}} \left(\boldsymbol{\Upsilon}_{\mathrm{s}}^{\mathrm{b}}\right)^{\mathrm{T}}}_{\text{Forward Spatial Part}} + \underbrace{\boldsymbol{\Upsilon}_{\mathrm{s}}^{\mathrm{b}} \mathbf{J}_{\boldsymbol{\vartheta}\boldsymbol{\vartheta}}^{\mathrm{e,b}} \left(\boldsymbol{\Upsilon}_{\mathrm{s}}^{\mathrm{b}}\right)^{\mathrm{T}}}_{\text{Backward Spatial Part}} + \underbrace{J_{\tau\tau}^{\mathrm{e}} \boldsymbol{\Upsilon}_{\tau} \boldsymbol{\Upsilon}_{\tau}^{\mathrm{T}}}_{\text{Temporal Part}} + \underbrace{\frac{J_{\beta_{\mathrm{R}}\beta_{\mathrm{R}}}^{\mathrm{b}} J_{\beta_{\mathrm{R}}\beta_{\mathrm{R}}}^{\mathrm{f}}}{J_{\beta_{\mathrm{R}}\beta_{\mathrm{R}}}^{\mathrm{f}} + J_{\beta_{\mathrm{R}}\beta_{\mathrm{R}}}^{\mathrm{b}}} \mathbf{J}_{\mathrm{fb}} \mathbf{J}_{\mathrm{fb}}^{\mathrm{T}}}_{\text{Channel Redundant Information}} , \tag{6.46}$$

where $\mathbf{J}_{\mathrm{fb}} = \boldsymbol{\Upsilon}_{\mathrm{s}}^{\mathrm{b}} \left(\frac{\mathbf{J}_{\boldsymbol{\vartheta}\beta}^{\mathrm{f}}}{J_{\beta_{\mathrm{R}}\beta_{\mathrm{R}}}^{\mathrm{f}}} - \frac{\mathbf{J}_{\boldsymbol{\vartheta}\beta}^{\mathrm{b}}}{J_{\beta_{\mathrm{R}}\beta_{\mathrm{R}}}^{\mathrm{b}}} \right)$. In the following, we obtain some insights from this equation.

6.4.3 Comparison of DLP, CLP and OWL

It can be seen that (6.46) comprises four terms: two spatial information terms related to both the forward and backward transmissions, one term related to the temporal information, and another term, carrying mutual information relating the path gain with the DOA and DOD. Note that although we assume a single β in both transmissions, it is estimated using two different observations, $\mathbf{y}_1(t)$ and $\mathbf{y}_2(t)$. This provides more spatial information useful in localization, since the path gain, DOA and DOD are not mutually independent (See (6.20)). Moreover, this mutual information is non-zero due to having different beamformers at both ends, hence $\frac{\mathbf{J}_{\boldsymbol{\vartheta}\beta}^{\mathrm{f}}}{J_{\beta_{\mathrm{R}}\beta_{\mathrm{R}}}^{\mathrm{f}}} \neq \frac{\mathbf{J}_{\boldsymbol{\vartheta}\beta}^{\mathrm{b}}}{J_{\beta_{\mathrm{R}}\beta_{\mathrm{R}}}^{\mathrm{b}}}$.

Comparing DLP to CLP, we note that (6.33) contains only one spatial information term, related to the backward transmission, and another temporal information term. These two terms are equal to their counterparts in (6.46). Since CLP has two more terms, it provides more information on the position and orientation, and consequently lower PEB and OEB. Thus, CLP will always outperform DLP.

We now compare DLP to the one-way localization (OWL) presented in Chapter 5. Recall that for OWL, $\mathbf{J}_{\mathbf{o},\mathbf{p}}^{\mathrm{e,b}}$ has the same expression as (6.33), but with

$$J_{\tau\tau} = J_{\tau^{\mathrm{b}}}. \tag{6.47}$$

Based on that, we provide the following proposition.

Proposition 6.1 *DLP outperforms OWL if,*

$$J_{\tau^{\mathrm{f}}} > \frac{1}{3} J_{\tau^{\mathrm{b}}}.$$

Proof

Comparing DLP with OWL, it can be seen that they have equal spatial, but different temporal information. Therefore, comparing (6.25) with (6.47), for DLP to outperform OWL, we should have

$$J_{\tau^{\mathrm{b}}} < 4\left(J_{\tau^{\mathrm{f}}}^{-1} + J_{\tau^{\mathrm{b}}}^{-1}\right)^{-1} = J_{\tau^{\mathrm{b}}}\frac{4J_{\tau^{\mathrm{f}}}}{J_{\tau^{\mathrm{f}}} + J_{\tau^{\mathrm{b}}}},$$

which leads to $J_{\tau^{\mathrm{f}}} > \frac{1}{3}J_{\tau^{\mathrm{b}}}$.

This means that, when the bandwidth is equal in both directions, the forward link should have at least one third the SNR of the backward link for DLP to outperform OWL. From (G.7), it can be seen that this mainly depends on the beamforming at the transmitter and receiver. However, under the general case of non-identical bandwidth allocation, (G.7) can be used to determine the values of bandwidth and SNR that satisfy the condition in Proposition 6.1.

6.5 Simulation Results and Discussion

6.5.1 Simulation Environment

System Layout and Channel

In our numerical simulations, we investigate and compare the DLP and CLP. Since both protocols involve forward and backward transmission, we selected equal number of antennas at both the BS and the UE to make the comparison of these protocols fair. Towards that, we consider a BS and a UE both with 12×12 uniform rectangular antenna array (URA) communicating via a LOS. Moreover, we assume that the BS array is located in the xz-plane centered about the origin $[0, 0, 0]^{\mathrm{T}}$, thus has orientation angles of $[0^\circ, 0^\circ]^{\mathrm{T}}$. On the other hand, the UE moves freely within a diamond-shape 120° defined by the vertices $\{(0, 0, -10), (25\sqrt{3}, 25, -10), (0, 50, -10), (-25\sqrt{3}, 25, -10)\}$. That is, the BS height is 10 meters. We focus on two cases of orientation angles with respect to the z-axis and x-axis: $\mathbf{o} = [\theta_0, \phi_0] = [0^\circ, 0^\circ]^{\mathrm{T}}$ and $\mathbf{o} = [30^\circ, 30^\circ]^{\mathrm{T}}$ as specified in the sequel. Finally, at a distance d_1, the channel

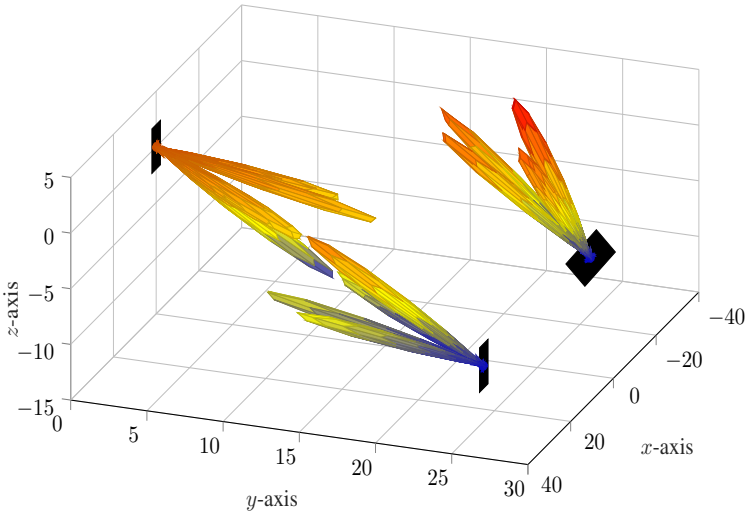

Figure 6.3: Beamforming configuration examples with 4 beams. The rightmost device has orientation angles of 30°, while the other two have 0°.

gain is modeled as

$$\beta = \frac{\lambda}{4\pi\ d_1} \exp\left(j\frac{2\pi}{\lambda}d_1\right), \tag{6.48}$$

Transmit-Receive Model

We select the mmWave frequency of $f = 38$ GHz, and bandwidth $W = 125$ MHz. We assume an ideal sinc pulse such that $W_{\text{eff}}^2 = W^2/3$. The transmitted power $E_{\text{t}}/T_{\text{s}} = 0$ dBm, and $N_0 = -170$ dBm/Hz. Furthermore, we specify the number of pilots to be $N_{\text{s}} = 64$ pilot symbols. This yields a location-dependent SNR [dB] $= 150.26 + 20\log_{10}(|\beta|\|\mathbf{a}_i\mathbf{F}_i\|\|\mathbf{a}_j\mathbf{W}_j\|)$, where $i, j \in \{1, 2\}, i \neq j$, specified depending on the communication direction being forward or backward. This provides 95% of the location with an SNR of at least 30 dB, which guarantees a tight CRLB. Similar to Chapter 5, we adopt fixed directional beamforming with $N_{\text{B}_1} = N_{\text{B}_2} = 25$ beams at the UE and BS such that

$$\mathbf{f}_{1,b} = \frac{1}{\sqrt{N_{\text{B}_1}}}\mathbf{a}_1(\theta_{1,b}^{\text{f}}, \phi_{1,b}^{\text{f}}),$$
$$\mathbf{w}_{1,b} = \frac{1}{\sqrt{N_{\text{B}_1}}}\mathbf{a}_1(\theta_{1,b}^{\text{w}}, \phi_{1,b}^{\text{w}}), \quad 1 \leq b \leq N_{\text{B}_1}$$

are D_1 transmit and receive beams pointing towards $(\theta^{\mathrm{f}}_{1,b}, \phi^{\mathrm{f}}_{1,b})$ and $(\theta^{\mathrm{w}}_{1,b}, \phi^{\mathrm{w}}_{1,b})$, respectively. The transmit and receive beamforming at D_2 can be similarly defined with subscript "2". The directions of the beams at the BS are chosen to be equispaced on the sector. On the UE, these directions are reversed to point upwards, and rotated with respect to the UE frame of reference by the same orientation angles specified in the studied experiment. This setting provides 90% of the locations with an SNR of at least 17 dB. Fig. 6.3 provides three examples on beamforming configuration: a BS at $(0, 0, 0)$, with beams pointing downwards, a UE at $(25, 25, -10)$ with zero orientation angles, and another UE at $(-25, 25, -10)$ with $\mathbf{o} = [30^\circ, 30^\circ]^{\mathrm{T}}$. The black rectangles denote the array frame of reference of the device. Note that the first UE has reversed beam direction compared to BS, while the second UE has beam directions reversed and rotated by $[30^\circ, 30^\circ]^{\mathrm{T}}$, so that the beams direction remains constant with respect to the UE local frame of reference.

Scenarios Studied

We study the PEB and OEB under DLP and CLP and compare these bounds to those obtained for OWL in Chapter 5. Each of these three protocols is studied when localization is performed in the uplink (at BS) and in the downlink (at UE).

6.5.2 PEB and OEB with 0° UE Orientation

The PEB with zero orientation angles is provided in Fig. 6.4 for all the considered protocols. First of all, to have a fair comparison, we compare the three solid curves corresponding to uplink localization, and then compare those related to downlink localization (dash-dot lines). It can be seen that DLP provides a negligible improvement over OWL. Despite that, DLP is still a better approach since it alleviates the need of high-accuracy synchronization, with the cost of UE-BS coordination. As discussed in Section 6.4.3, DLP and OWL have the same spatial component, but DLP has higher temporal information content. However, Fig. 6.4 shows almost identical results for both protocols, which means that the additional temporal information in DLP is of little importance, and thus the localization performance is limited by the angles estimation rather than the time delay. To understand this phenomenon more, we study the impact of the bandwidth on the performance

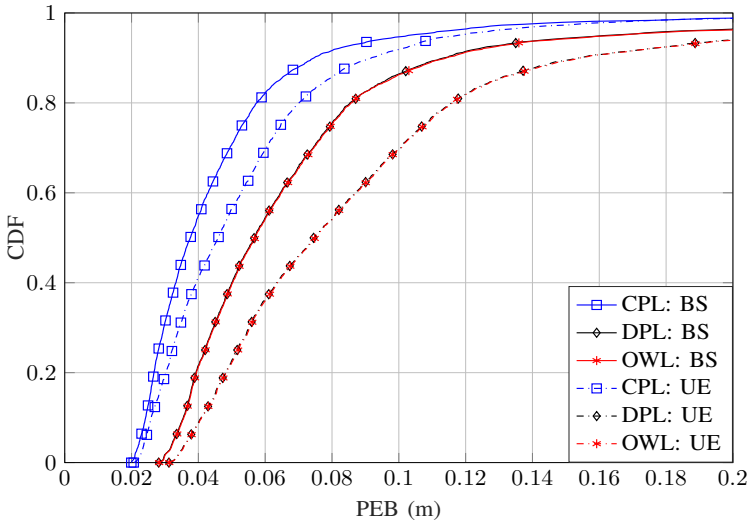

Figure 6.4: CDF of PEB with UE orientation angles of 0°, and $N_{\mathrm{UE}} = N_{\mathrm{BS}} = 144$, $N_{\mathrm{B}} = 25$.

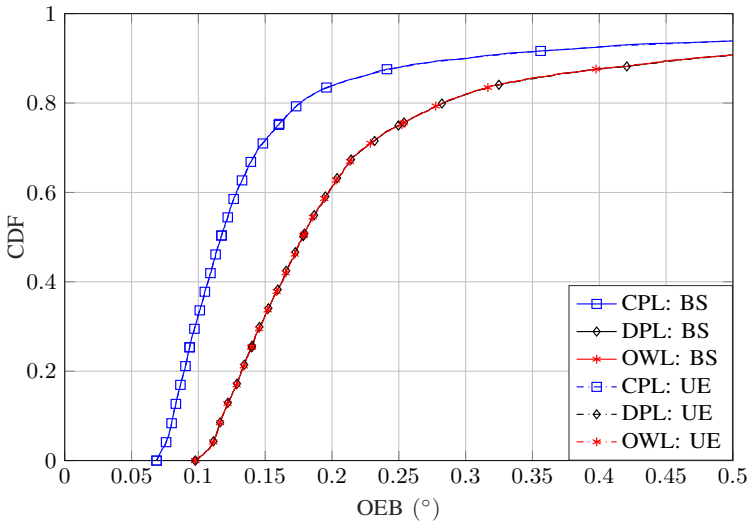

Figure 6.5: CDF of OEB with UE orientation angles of 0°, and $N_{\mathrm{UE}} = N_{\mathrm{BS}} = 144$, $N_{\mathrm{B}} = 25$.

later in Section 6.5.4. On the other hand, as expected, CLP represents the best approach among the three studied, since it attains more useful information. However, this comes with the cost of a more complex implementation due to the need for a feedback channel.

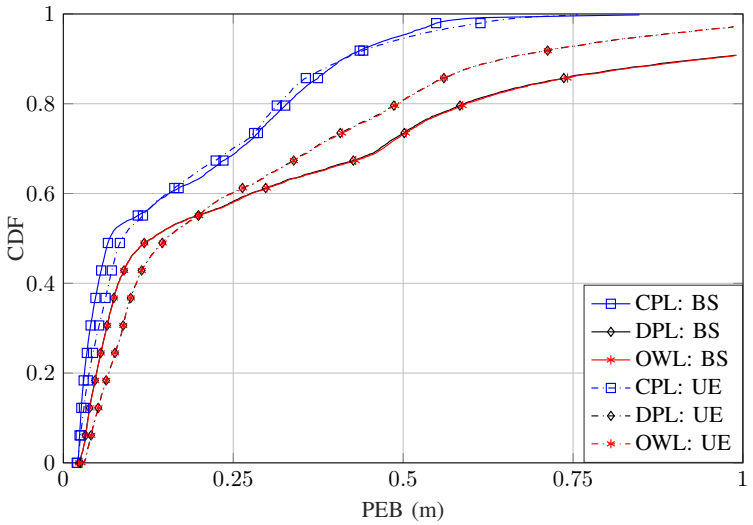

Figure 6.6: CDF of PEB with UE orientation angles of 30°, and $N_{\mathrm{UE}} = N_{\mathrm{BS}} = 144$, $N_{\mathrm{B}} = 25$.

Although similar statements can be made for downlink localization, we note that an extensive comparison between the uplink and downlink localization is discussed in Chapter 5. It was concluded that, under matched orientation between the BS and UE, the uplink PEB is lower than the downlink PEB due to 1) PEB is a function of the CRLB of the BS angles, and 2) CRLB of DOA is lower than CRLB of DOD. Therefore, when the BS angles are DOAs (uplink), the PEB will be lower.

Considering OEB with zero orientation angles in Fig. 6.5, it can be seen that DLP and OWL exhibit identical performance. Note that OEB depends on DOA and DOD, while the enhancement of DLP over OWL is in the temporal domain. Furthermore, in line with the results in Chapter 5 with zero orientation angles, the uplink and downlink OEB are the same. Therefore, the four curves of DLP and OWL with uplink and downlink localization coincide. Moreover, in terms of OEB, CLP is also better than DLP and OWL due to the fourth term in (6.46), which accounts for the coupling between the path gain and the transmission angles, providing more spatial information on the orientation angles.

6.5.3 PEB and OEB with 30° UE Orientation

The PEB with orientation angles $\mathbf{o} = [30°, 30°]^{\mathrm{T}}$ is shown in Fig. 6.6, for all the considered protocols. The overall observation from this figure, in comparison with

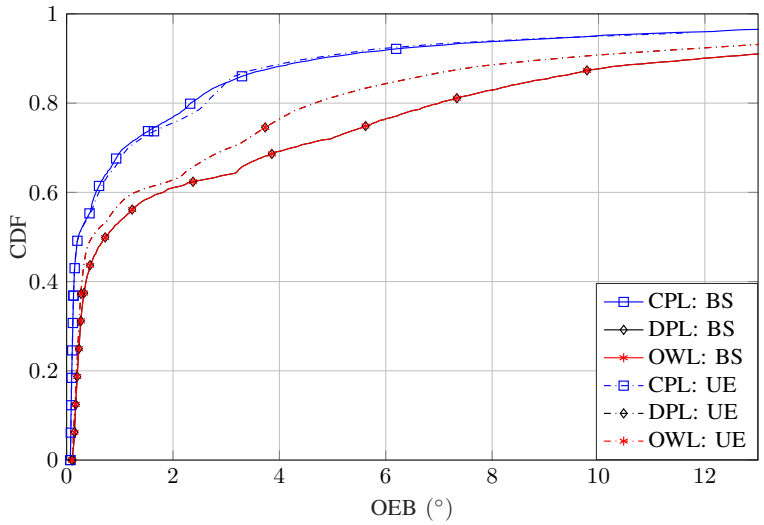

Figure 6.7: CDF of OEB with UE orientation angles of 30°, and $N_{\mathrm{UE}} = N_{\mathrm{BS}} = 144$, $N_{\mathrm{B}} = 25$.

Fig. 6.4, is that the performance worsens due to the beams being steered away, when the orientation angles are non-zero. This can result in a loss of beamforming gain that depends non-linearly on the UE location, and orientation angles. However, CLP performance is still superior to DLP and OWL. In this example, performance loss of 42 cm, 54 cm, and 80 cm were observed at a PEB CDF of 90%, under CLP, uplink DLP, and downlink DLP, respectively. On the other hand, comparing Fig. 6.7 with Fig. 6.5, it can be seen that, at a CDF of 90%, there is a OEB performance loss of 6.8°, 8.8°, and 11.5° under CLP, uplink DLP, and downlink DLP, respectively. Considering the PEB and OEB loss, it can be concluded that, among the studied approaches, CLP is the approach that is most robust to UE mis-orientation. Finally, we note that in comparison with the case of matched orientation, under 30° mis-orientation, the system can still provide sub-meter PEB, while providing significantly higher OEB. This means that orientation estimation is more challenging than position estimation.

6.5.4 Impact of the System Bandwidth on PEB

In Section 6.5.3, we concluded that the system is limited by the estimation of the angles rather than the time delay. To investigate that further, we now look closer into the impact of the bandwidth. The results shown in Fig. 6.8 indicate that as

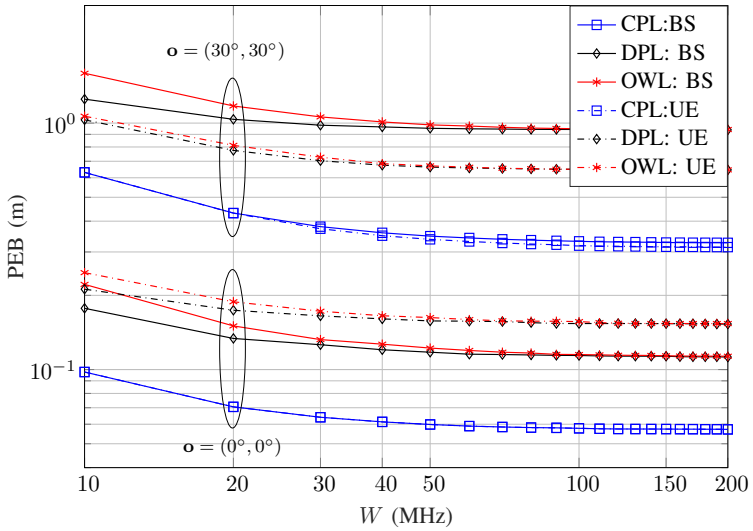

Figure 6.8: PEB at 0.9 CDF with respect to the bandwidth W.

the bandwidth increases the PEB decreases, until it reaches a floor at around 100 MHz when $\mathbf{o} = [0°, 0°]^{\mathrm{T}}$, and 60 MHz when $\mathbf{o} = [30°, 30°]^{\mathrm{T}}$. Based on these results, we make the following observations:

1. At higher bandwidths that are more relevant in mmWave, the temporal information is very high compared to the spatial information, and the performance becomes fixed with W, i.e., the systems is spatially-limited.

2. under mis-orientation, the accuracy of spatial information degrades, and the system becomes spatially-limited. Hence, the improved temporal information does not provide any benefit to the performance achieved at lower bandwidths.

3. On the contrary, for lower bandwidths, the amount of temporal information decreases and becomes comparable to the spatial information. Therefore, the weight of the temporal information in the forward transmission becomes more significant, and the difference between OWL and DLP becomes more pronounced.

6.5.5 Impact of N_{BS} and N_{UE} on PEB

We now study the effect of the number of antennas at BS and UE on the PEB under CLP and DLP. Since this number can be N_1 or N_2 depending on the device

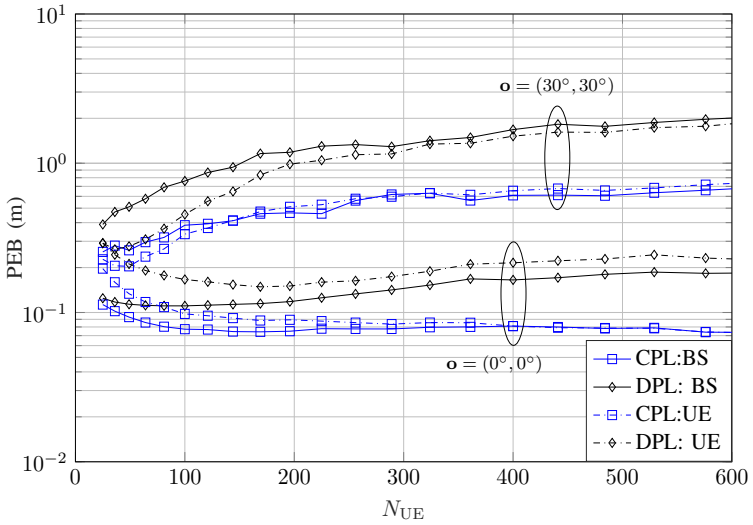

Figure 6.9: PEB at 0.9 CDF as a function of the UE number of antennas, with $N_{\mathrm{B}} = 25$, with orientation angles 0° and 30°, and $N_{\mathrm{BS}} = 144$.

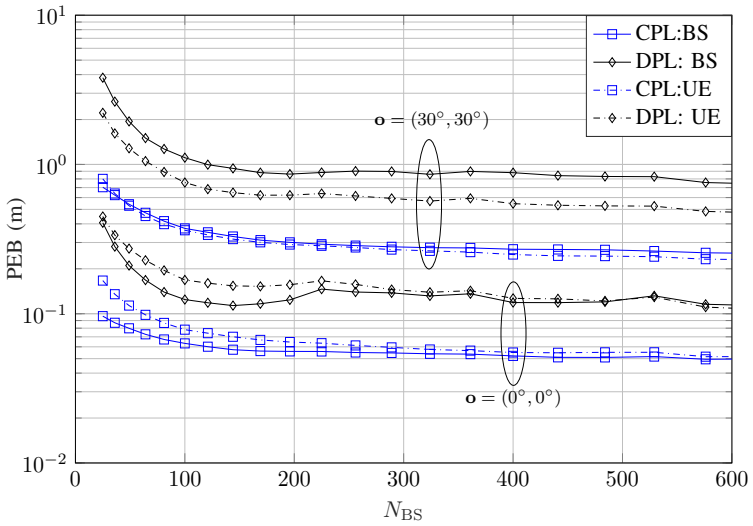

Figure 6.10: PEB at 0.9 CDF as a function of the BS number of antennas, with $N_{\mathrm{B}} = 25$, with orientation angles 0° and 30°, and $N_{\mathrm{UE}} = 144$.

role, we use N_{BS} and N_{UE} to unify the notation of the number of antennas at BS and UE, respectively.

Fig. 6.9 illustrates the effect of N_{UE} on PEB with $N_{\mathrm{B}} = 25$ and $N_{\mathrm{BS}} = 144$. It can be seen that a higher N_{UE} generally results in a worse performance. This

is because with higher N_{UE}, the UE beams become narrower, which requires more beams to cover the area. Note that with UE mis-orientation, the rate of performance deterioration is higher. It is interesting to see that this rate is almost the same for the three protocols, which means that the performance loss is mainly due to SNR loss.

On the other hand, the impact of N_{BS} is shown in Fig. 6.10 with $N_{\mathrm{B}} = 25$ and $N_{\mathrm{UE}} = 144$. It can be seen that a higher N_{BS} will slightly improve the PEB in general. Similar to the case in Fig. 6.9, it is understood that the PEB will generally increase when N_{BS} increases, albeit, at N_{BS} values well beyond those displayed in Fig. 6.10, and with a lesser magnitude than higher N_{UE}. Therefore, adding more antennas at the BS will not reduce the localization performance, as the UE antennas potentially would, at least within the studied range of array size. Finally, notice that both Figs. 6.9 and 6.10 exhibit some non-monotonic trend. This is due to the nature of directional beamforming, whereby the beamforming gain depends on the user location, number of antennas, and beams directions as detailed in Chapter 4.

6.6 Conclusions

Many publications on localization assume that the BS and UE are tightly synchronized. However, usually communication systems are not synchronized to a high-level useful for localization. Focusing on this issue, in this Chapter, we considered two protocols of two-way localization referred to *Distributed Localization Protocol* (DLP) and *Centralized Localization Protocol* (CLP). We investigated the PEB and OEB under these two protocols, where we showed mathematically that CLP outperforms DLP with a significant margin. However, this comes with the cost of requiring feedback channel, unlike DLP where no synchronization or feedback are required, although it may need dedicated hardware to trigger the response. In our derivations, we considered beamforming at the transmitter and the receiver, and accounted for the spatially-correlated receive noise. Comparing DLP to the traditional one-way localization, the enhancement observed through numerical simulations was limited. That is, the localization was angle-limited rather than delay-limited. Our numerical results also showed that it is more beneficial to have more

antennas at the BS than at the UE. Future work based on this Chapter includes considering adaptive beamforming, whereby the beams directions are modified in the second round of transmission. Moreover, multipath propagation would be a relevant extension, since scatterers may differ in the uplink and downlink, depending on the beam directions.

Publications Resulted from This Chapter

- **Z. Abu-Shaban**, H. Wymeersch, T. Abhayapala, G. Seco-Granados, "Single-Anchor Two-Way Localization Bounds for 5G mmWave Systems: Two Protocols," to be submitted to *IEEE Transactions on Wireless Communication*, May 2018.

- **Z. Abu-Shaban**, H. Wymeersch, T. Abhayapala, G. Seco-Granados, "Single-Anchor Two-Way Localization Bounds for 5G mmWave Systems," to be submitted to *2018 IEEE Global Communications Conf. (GLOBECOM Workshops)*, Abu Dhabi, UAE, Dec 2018.

Chapter 7

Conclusions and Future Research

This thesis provided applied and fundamental research results on active areas of mobile localization, with more focus on 5G mmWave localization performance. In this chapter, we draw conclusions with respect to the questions posed in this thesis (Section 1.5) and suggest possible future research directions

7.1 Conclusions

- The problem of multi-anchor localization under mixed LOS and NLOS conditions is addressed in Chapter 3. A key advantage in our work is that it solves the NLOS UE localization in a closed-form, in contrast to most of works that are either search-based or iterative. We used a distance-dependent bias model to derive an unbiased range estimator as a first step. Subsequently, we used trilateration to find an estimate of the UE position. We then performed error analysis and evaluated numerically the CRLB as a benchmark. Our approach was to identify the NLOS links and then use a statistical signal model to account for the positive range bias. Our proposed localization techniques showed performance close to the CRLB. With a cell radius of 500 m, our method is accurate with an average position error ranging between 12–21 meters depending on the environment. Finally, we note that, although the proposed method performs closely with the CRLB, the average error obtained is in the order of several meters, which implies that location-aware

communications have limited applications in conventional cellular network.

- Focusing on 2D scenarios of 5G mmWave, the initial access problem was addressed in Chapter 4. We investigated two beamforming schemes (RPBF and DBF) and compared their capabilities in terms of the channel parameters' CRLBs. Our analysis and simulation results showed that in the absence of any prior location knowledge, application of RPBF is more appropriate in the considered scenario because it attains a lower CRLBs with fewer beams compared to DBF. We also observed that in DBF, the CRLBs tend to increase with N_{T}, while under RPBF, they stay constant. An exception to this is the CRLB of DOD, which decreases with N_{T}, with varying degrees in RPBF and DBF. On the other hand, we observed that increasing N_{R} always reduced the CRLB of all parameters in both schemes. We used CRLB to compare these two schemes. However, the values of these CRLB are of little importance until location information is inferred from them, which is the topic of Chapter 5.

- Contributing to the emerging 5G mmWave networks, and focusing on the localization part of the system beyond the initial access phase, Chapter 5 investigate the position and device orientation estimation error bounds. Both uplink and downlink localization were considered. Our key findings indicate that the uplink and downlink behave differently in two distinct ways. First of all, the error bounds have different scaling factors with respect to the number of antennas in the uplink and downlink. Secondly, uplink localization is sensitive to the orientation angle of the UE, whereas downlink is not. Moreover, in the considered outdoor scenarios, the NLOS paths generally improve localization when a LOS path exists. We observed that reflectors provide modest PEB improvement for some locations, while scatterers provide small PEB decrease for more locations.

- Although having many receive antennas is more beneficial in uplink localization than in downlink localization, the former is generally harder since transmit beamforming at UE may point towards directions not useful for localization. We analyzed the impact of the N_{B}, and noticed a saturation effect appears after some value, after which adding more beams does not enhance

the performance. We also studied the impact of N_{T} and N_{R} on PEB and OEB, and concluded that increasing N_{R} always improves the performance with the cost of increased hardware and computation complexities. Finally, our numerical results showed that mmWave systems are capable of localizing a UE with sub-meter position error, and sub-degree orientation error.

- In Chapter 7 we addressed the synchronization issue of 5G mmWave systems by studying two-way localization protocols: DLP and CLP. Our studies show that mmWave localization is mainly limited by angular rather than temporal estimation. Thus, estimating the DOA and DOD is much harder than TOA, as far as localization is concerned. We investigated the PEB and OEB under these two protocols, where we showed mathematically that CLP outperforms DLP with a significant margin. However, this comes with the cost of requiring a coarse synchronization, unlike DLP where no synchronization is required. Our simulations also showed that it is more beneficial to have more antennas at the BS than at the UE. This is consistent with the results obtained in Chapter 5, although we did not consider receive beamforming in that Chapter.

The main outcome of this thesis is a fundamental understanding of how 5G mmWave technology can be an enabler for extremely accurate localization. Through theoretical performance bounds, we have developed insights as to why and when 5G localization is feasible, how 5G localization systems should be designed, and how 5G localization and 5G communication can support each other. This thesis highlights that 5G localization with mmWave technology will play a central role in communication network optimization and unlock opportunities that were not available in conventional networks.

7.2 Future Research Directions

Localization in 5G mmWave networks is still in its infancy. This thesis contributed significantly to the understanding of the factors interplay and the expected error performance. Our findings in this thesis show that 5G mmWave is much more promising than conventional networks in terms of location-aware applications.

However, there are still many problems open for investigation. These problems can be classified into five areas:

- **Beamforming:** We considered beamforming with fixed beams, but we also believe that adapting the beam directions based on the estimated user location is beneficial for both communication system optimization and localization performance. Moreover, in this thesis, we used analog beamforming with an RF-chain dedicated to each beam. Other structures include hybrid beamforming where part of the beamforming is achieved in the digital domain too. Although the mathematical relationships presented in this thesis can be easily extended to the hybrid beamforming case, more attention should be paid to the design of the beamformers. The related hardware complexity also forms a challenge in this direction.

- **Synchronization:** We addressed the time-offset clock bias in LOS scenarios, but since the 5G mmWave are angle-limited rather than delay-limited, it is worthwhile to focus on joint carrier frequency offset and clock offset in multipath environments, to avoid phase and range errors simultaneously. Moreover, higher order clock artifacts such as clock drift and skews can potentially be interesting research venues under 5G mmWave paradigm.

- **Estimators:** The broad objective of our studies was to gain an understanding and study the feasibility of 5G localization. The next natural step is to design location and orientation estimators and benchmark their performance against the PEB and OEB derived herein. We expect the estimation of DOA and DOD to be more challenging than TOA. However, the sparsity of mmWave channel poses as an opportunity that can be efficiently exploited to apply sparse signal processing techniques such as compressed sensing.

- **Location information fusion:** MmWave localization can play an integral part with already existing localization methods. Location fusion from multiple sources can lead to more available information, and eventually enhanced localization performance. Energy efficient algorithms should be developed taking into account the existing infrastructure.

- **Localization Modeling and Analysis Using Stochastic Geometry:** Since the concept of "cell" is vanishing in favor of dense base stations located in random locations. More adequate mathematical tools suitable to model new mobile networks are those based on stochastic geometry. Therefore, it is of high interest to investigate how localization techniques can be modeled and analyzed in such random configurations.

- **New application fields:** We believe that mmWave localization can be a key enabler for device-to-device, vehicle-to-vehicle communication, vehicle-to-everything networks, and the internet-of-things. A key challenge in these networks is when the device is moving, which necessitates the investigation of tracking methods similar to [29], for example. Having tens or hundreds of antennas for tracking would require very efficient computation power.

Appendix A

Derivation of The Range PDF

Assuming that the UE occupies an infinitesimal area that can be approximated by a point, the PDF in this case is given by the length of the arc, L, of radius d_m and angle θ, divided by the area of the sector, A, of radius R, where, $L = d_m\theta$ and $A = \frac{\sqrt{3}}{2}R^2$.

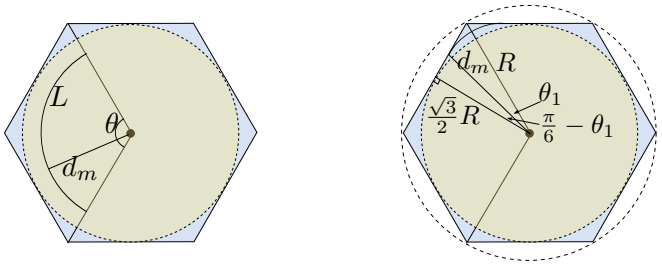

(a) $0 \leq d_m < \frac{\sqrt{3}}{2}R$. (b) $\frac{\sqrt{3}}{2}R \leq d_m < R$

Figure A.1: Geometrical setup with $m = 1$.

A.1 Hosting Cell ($m = 1$)

For the area $0 \leq d_m < \frac{\sqrt{3}}{2}R$, from Fig. A.1a, $\theta = 2\pi/3$, and

$$f_D(d_m) = \frac{L}{A} = \frac{4\pi d_m}{3\sqrt{3}R^2}, \quad 0 \leq d_m < \frac{\sqrt{3}}{2}R.$$

On the other hand, for the area $\frac{\sqrt{3}}{2}R \leq d_m < R$, from Fig. A.1b, we can write

$$\theta_1 = \frac{\pi}{6} - \cos^{-1}\left(\frac{\sqrt{3}R}{2d_m}\right).$$

From the symmetry, it can be deduced that

$$f_D(d_m) = \frac{4\theta_1 d_m}{A} = \frac{8d_m}{\sqrt{3}R^2}\left[\frac{\pi}{6} - \cos^{-1}\left(\frac{\sqrt{3}R}{2d_m}\right)\right], \quad \frac{\sqrt{3}}{2}R \leq d_m < R.$$

A.2 Neighboring Cells ($m = 2, 3$)

For the region $\frac{\sqrt{3}}{2}R \leq d_m < R$, from Fig. A.2a, the arc angle can be computed as

$$\frac{\theta}{2} = \cos^{-1}\left(\frac{\sqrt{3}R}{2d_m}\right),$$

Consequently, we can write

$$f_D(d_m) = \frac{4d_m}{\sqrt{3}R^2}\cos^{-1}\left(\frac{\sqrt{3}R}{2d_m}\right), \qquad \frac{\sqrt{3}}{2}R \leq d_m < R.$$

On the other hand, for the region $R \leq d_m < \sqrt{3}R$, from Fig. A.2b, and using the law of sine, it is easy to see that

$$\frac{\sin\theta}{R} = \frac{\sin(2\pi/3)}{d_m}, \qquad \Rightarrow \qquad \theta = \sin^{-1}\left(\frac{\sqrt{3}R}{2d_m}\right).$$

therefore,

$$f_D(d_m) = \frac{2d_m}{\sqrt{3}R^2}\sin^{-1}\left(\frac{\sqrt{3}R}{2d_m}\right), \qquad R \leq d_m < \sqrt{3}R.$$

Finally, for the region $\sqrt{3}R \leq d_m < 2R$, from Fig. A.2c, it is easy to see that

$$\sin\left(\theta + \frac{\pi}{3}\right) = \frac{\sqrt{3}R}{d_m}, \qquad \Rightarrow \qquad \theta = \sin^{-1}\left(\frac{\sqrt{3}R}{d_m}\right) - \frac{\pi}{3},$$

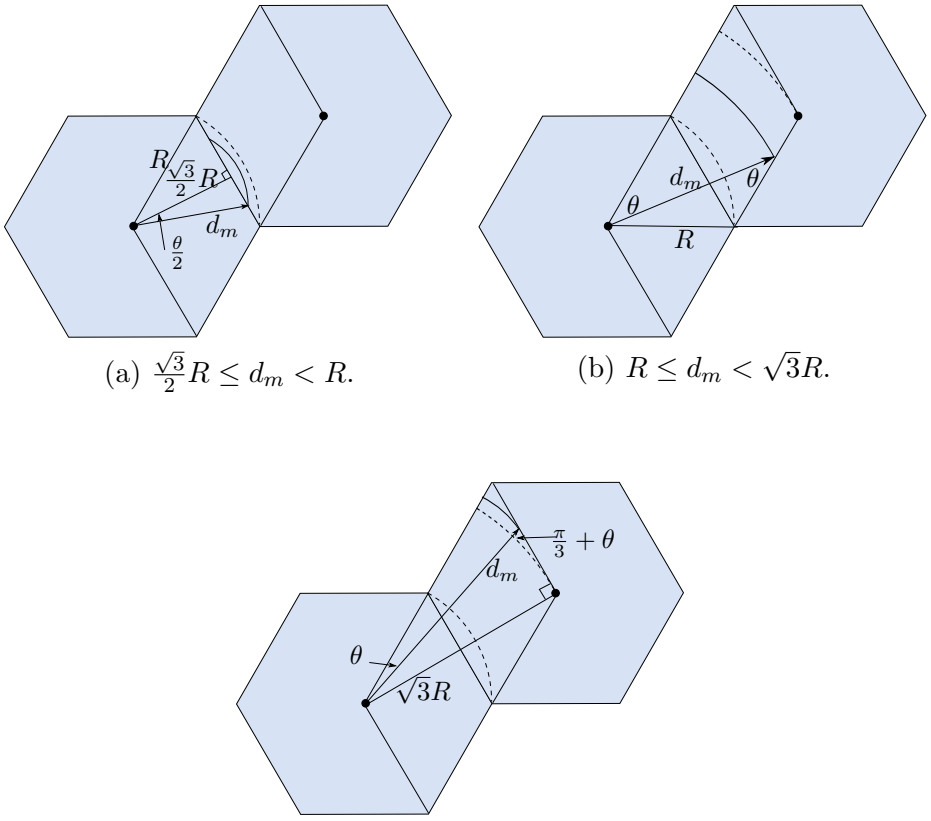

(a) $\frac{\sqrt{3}}{2}R \leq d_m < R$.

(b) $R \leq d_m < \sqrt{3}R$.

(c) $\sqrt{3}R \leq d_m < 2R$.

Figure A.2: Geometrical setup with $m = 2, 3$.

from which we write,

$$f_D(d_m) = \frac{2d_m}{\sqrt{3}R^2}\left[\sin^{-1}\left(\frac{\sqrt{3}R}{d_m}\right) - \frac{\pi}{3}\right], \qquad \sqrt{3}R \leq d_m < 2R.$$

To sup up, for $m = 1$, this distribution is given by

$$f_D(d_m) = \begin{cases} \frac{4\pi d_m}{3\sqrt{3}R^2}, & 0 \leq d_m < \frac{\sqrt{3}R}{2}, \\ \frac{8d_m}{\sqrt{3}R^2}\left[\frac{\pi}{6} - \cos^{-1}\left(\frac{\sqrt{3}R}{2d_m}\right)\right], & \frac{\sqrt{3}}{2}R \leq d_m < R. \end{cases} \tag{A.1}$$

For $m = 2$ and 3, this distribution is given by

$$f_D(d_m) = \begin{cases} \frac{4d_m}{\sqrt{3}R^2}\cos^{-1}\left(\frac{\sqrt{3}R}{2d_m}\right), & \frac{\sqrt{3}R}{2} \leq d_m < R \\ \frac{2d_m}{\sqrt{3}R^2}\sin^{-1}\left(\frac{\sqrt{3}R}{2d_m}\right), & R \leq d_m < \sqrt{3}R \\ \frac{2d_m}{\sqrt{3}R^2}\left[\sin^{-1}\left(\frac{\sqrt{3}R}{d_m}\right) - \frac{\pi}{3}\right], & \sqrt{3}R \leq d_m < 2R \end{cases} \tag{A.2}$$

Appendix B

FIM of 3D Multipath Channel Parameters with Arrays of Arbitrary Geometry

Considering the model in (5.6), define $\boldsymbol{\beta}_{\mathrm{R}} \triangleq \Re\{\boldsymbol{\beta}\}, \boldsymbol{\beta}_{\mathrm{I}} \triangleq \Im\{\boldsymbol{\beta}\}$, where $\Re\{\cdot\}$ and $\Im\{\cdot\}$ denote the real and imaginary parts, respectively. Also define the vector of unknown parameters and the measurement mean as

$$\boldsymbol{\varphi} \triangleq [\boldsymbol{\theta}_{\mathrm{R}}^{\mathrm{T}}, \boldsymbol{\theta}_{\mathrm{T}}^{\mathrm{T}}, \boldsymbol{\phi}_{\mathrm{R}}^{\mathrm{T}}, \boldsymbol{\phi}_{\mathrm{T}}^{\mathrm{T}}, \boldsymbol{\tau}^{\mathrm{T}}, \boldsymbol{\beta}_{\mathrm{R}}^{\mathrm{T}}, \boldsymbol{\beta}_{\mathrm{I}}^{\mathrm{T}}]^{\mathrm{T}}, \tag{B.1}$$

$$\boldsymbol{\mu}_{\boldsymbol{\varphi}} \triangleq \sum_{m=1}^{M} \mathbf{H}_m \mathbf{x}(t-\tau_m) = \sqrt{N_{\mathrm{R}} N_{\mathrm{T}} E_{\mathrm{t}}} \sum_{m=1}^{M} \beta_m \mathbf{a}_{\mathrm{R},m} \mathbf{a}_{\mathrm{T},m}^{\mathrm{H}} \mathbf{F}\mathbf{s}(t-\tau_m), \tag{B.2}$$

Then, for the case of measurement under additive white Gaussian noise process, the FIM of $\boldsymbol{\varphi}$ is given element-wise as [81]

$$[\mathbf{J}_{\boldsymbol{\varphi}}]_{u,v} \triangleq \frac{1}{N_0} \int_0^{T_o} \Re\left\{ \frac{\partial \boldsymbol{\mu}_{\boldsymbol{\varphi}}^{\mathrm{H}}}{\partial \varphi_u} \frac{\partial \boldsymbol{\mu}_{\boldsymbol{\varphi}}}{\partial \varphi_v} \right\} dt, \tag{B.3}$$

where φ_u is the u^{th} element in $\boldsymbol{\varphi}$. Consequently, it can be shown that

$$\frac{\partial \boldsymbol{\mu}_{\boldsymbol{\varphi}}}{\partial \theta_{\mathrm{R},m}} = -j\sqrt{N_{\mathrm{R}} N_{\mathrm{T}} E_{\mathrm{t}}} \beta_m \widetilde{\mathbf{K}}_{\mathrm{R},m} \mathbf{a}_{\mathrm{R},m} \mathbf{a}_{\mathrm{T},m}^{\mathrm{H}} \mathbf{F}\mathbf{s}(t-\tau_m), \tag{B.4a}$$

$$\frac{\partial \boldsymbol{\mu}_{\boldsymbol{\varphi}}}{\partial \theta_{\mathrm{T},m}} = j\sqrt{N_{\mathrm{R}}N_{\mathrm{T}}E_{\mathrm{t}}}\beta_m \mathbf{a}_{\mathrm{R},m}\mathbf{a}_{\mathrm{T},m}^{\mathrm{H}}\widetilde{\mathbf{K}}_{\mathrm{T},m}\mathbf{F}\mathbf{s}(t-\tau_m), \tag{B.4b}$$

$$\frac{\partial \boldsymbol{\mu}_{\boldsymbol{\varphi}}}{\partial \phi_{\mathrm{R},m}} = -j\sqrt{N_{\mathrm{R}}N_{\mathrm{T}}E_{\mathrm{t}}}\beta_m \widetilde{\mathbf{P}}_{\mathrm{R},m}\mathbf{a}_{\mathrm{R},m}\mathbf{a}_{\mathrm{T},m}^{\mathrm{H}}\mathbf{F}\mathbf{s}(t-\tau_m), \tag{B.4c}$$

$$\frac{\partial \boldsymbol{\mu}_{\boldsymbol{\varphi}}}{\partial \phi_{\mathrm{T},m}} = j\sqrt{N_{\mathrm{R}}N_{\mathrm{T}}E_{\mathrm{t}}}\beta_m \mathbf{a}_{\mathrm{R},m}\mathbf{a}_{\mathrm{T},m}^{\mathrm{H}}\widetilde{\mathbf{P}}_{\mathrm{T},m}\mathbf{F}\mathbf{s}(t-\tau_m), \tag{B.4d}$$

$$\frac{\partial \boldsymbol{\mu}_{\boldsymbol{\varphi}}}{\partial \beta_{\mathrm{R},m}} = -j\frac{\partial \boldsymbol{\mu}_{\boldsymbol{\varphi}}}{\partial \beta_{\mathrm{I},m}} = \sqrt{N_{\mathrm{R}}N_{\mathrm{T}}E_{\mathrm{t}}}\mathbf{a}_{\mathrm{R},m}\mathbf{a}_{\mathrm{T},m}^{\mathrm{H}}\mathbf{F}\mathbf{s}(t-\tau_m), \tag{B.4e}$$

$$\frac{\partial \boldsymbol{\mu}_{\boldsymbol{\varphi}}}{\partial \tau_m} = \sqrt{N_{\mathrm{R}}N_{\mathrm{T}}E_{\mathrm{t}}}\beta_m \mathbf{a}_{\mathrm{R},m}\mathbf{a}_{\mathrm{T},m}^{\mathrm{H}}\mathbf{F}\frac{\partial \mathbf{s}(t-\tau_m)}{\partial \tau_m}, \tag{B.4f}$$

where

$$\widetilde{\mathbf{K}}_{\mathrm{R},m} \triangleq \frac{2\pi d}{\lambda}\,\mathrm{diag}\left(\frac{\partial}{\partial \theta_{\mathrm{R},m}}\mathbf{k}^{\mathrm{T}}(\theta_{\mathrm{R},m},\phi_{\mathrm{R},m})\Delta_{\mathrm{R}}\right),$$
$$\widetilde{\mathbf{P}}_{\mathrm{R},m} \triangleq \frac{2\pi d}{\lambda}\,\mathrm{diag}\left(\frac{\partial}{\partial \phi_{\mathrm{R},m}}\mathbf{k}^{\mathrm{T}}(\theta_{\mathrm{R},m},\phi_{\mathrm{R},m})\Delta_{\mathrm{R}}\right),$$
$$\Delta_{\mathrm{R}} \triangleq \begin{bmatrix}\mathbf{u}_1 & \mathbf{u}_2 & ... & \mathbf{u}_{N_{\mathrm{R}}}\end{bmatrix} \triangleq \begin{bmatrix}\mathbf{x}_{\mathrm{R}} & \mathbf{y}_{\mathrm{R}} & \mathbf{z}_{\mathrm{R}}\end{bmatrix}^{\mathrm{T}}.$$

$\widetilde{\mathbf{K}}_{\mathrm{T},m}$ and $\widetilde{\mathbf{P}}_{\mathrm{T},m}$ are defined similarly by replacing the subscript R by T. Moreover, defining $\gamma \triangleq N_{\mathrm{R}}N_{\mathrm{T}}N_{\mathrm{s}}E_{\mathrm{t}}/N_0$, we partition $\mathbf{J}_{\boldsymbol{\varphi}}$ into $M \times M$ submatrices, so that

$$\mathbf{J}_{\boldsymbol{\varphi}} \triangleq \begin{bmatrix}\mathbf{J}_{\boldsymbol{\theta}_{\mathrm{R}}\boldsymbol{\theta}_{\mathrm{R}}} & \mathbf{J}_{\boldsymbol{\theta}_{\mathrm{R}}\boldsymbol{\theta}_{\mathrm{T}}} & \cdots & \mathbf{J}_{\boldsymbol{\theta}_{\mathrm{R}}\boldsymbol{\beta}_{\mathrm{I}}} \\ \mathbf{J}_{\boldsymbol{\theta}_{\mathrm{R}}\boldsymbol{\theta}_{\mathrm{T}}}^{\mathrm{T}} & \ddots & \cdots & \vdots \\ \vdots & \cdots & \ddots & \vdots \\ \mathbf{J}_{\boldsymbol{\theta}_{\mathrm{R}}\boldsymbol{\tau}}^{\mathrm{T}} & \cdots & \cdots & \mathbf{J}_{\boldsymbol{\beta}_{\mathrm{I}}\boldsymbol{\beta}_{\mathrm{I}}}\end{bmatrix}, \tag{B.6}$$

For $1 \le u, v \le M$,

$$\begin{aligned}[\mathbf{J}_{\theta_{\mathrm{R}}\theta_{\mathrm{R}}}]_{u,v} &= \frac{1}{N_0}\int_0^{T_o} \Re\left\{\frac{\partial \boldsymbol{\mu}_{\boldsymbol{\varphi}}^{\mathrm{H}}}{\partial \theta_{R,u}}\frac{\partial \boldsymbol{\mu}_{\boldsymbol{\varphi}}}{\partial \theta_{R,v}}\right\} dt, \\ &= \frac{N_{\mathrm{R}}N_{\mathrm{T}}E_{\mathrm{t}}}{N_0}\int_0^{T_o} \Re\left\{\beta_u^*\beta_v \widetilde{\mathbf{K}}_{\mathrm{R},v}\mathbf{a}_{\mathrm{R},v}\mathbf{a}_{\mathrm{T},v}^{\mathrm{H}}\mathbf{F}\mathbf{s}(t-\tau_v)\mathbf{s}^{\mathrm{H}}(t-\tau_u)\mathbf{F}^{\mathrm{H}}\mathbf{a}_{\mathrm{T},u}\mathbf{a}_{\mathrm{R},u}^{\mathrm{H}}\widetilde{\mathbf{K}}_{\mathrm{R},u}\right\}\mathrm{d}t, \\ &= \gamma\Re\left\{\beta_u^*\beta_v[\mathbf{R}_0]_{u,v}\mathbf{a}_{R,u}^{\mathrm{H}}\widetilde{\mathbf{K}}_{R,u}\widetilde{\mathbf{K}}_{R,v}\mathbf{a}_{R,v}\mathbf{a}_{T,v}^{\mathrm{H}}\mathbf{F}\mathbf{F}^{\mathrm{H}}\mathbf{a}_{T,u}\right\}\end{aligned} \tag{B.7}$$

where $\int_0^{T_o} \mathbf{s}(t-\tau_v)\mathbf{s}^{\mathrm{H}}(t-\tau_u) = N_{\mathrm{s}}[\mathbf{R}_0]_{u,v}\mathbf{I}_{N_B}$, and

$$[\mathbf{R}_0]_{u,v} \triangleq \int_0^{T_o} s_\ell(t-\tau_v)s_\ell^*(t-\tau_u)\mathrm{d}t = \int_{-W/2}^{W/2} |P(f)|^2 e^{-j2\pi f\Delta\tau_{uv}}\mathrm{d}f, \tag{B.8}$$

where $\Delta\tau_{uv} = \tau_v - \tau_u$. Note that to obtain (B.7), we used the fact that $\mathbf{a}^{\mathrm{H}}\mathbf{b}\mathbf{c}^{\mathrm{H}}\mathbf{d} = \mathbf{c}^{\mathrm{H}}\mathbf{d}\mathbf{a}^{\mathrm{H}}\mathbf{b}$, and that (B.8) follows from Parseval's theorem.

Defining the following matrices,

$$\begin{aligned}
\mathbf{K}_{\mathrm{R}} &\triangleq [\widetilde{\mathbf{K}}_{R,1}\mathbf{a}_{R,1}, \widetilde{\mathbf{K}}_{R,2}\mathbf{a}_{R,2}, ..., \widetilde{\mathbf{K}}_{R,N_{\mathrm{R}}}\mathbf{a}_{R,N_{\mathrm{R}}}],\\
\mathbf{P}_{\mathrm{R}} &\triangleq [\widetilde{\mathbf{P}}_{R,1}\mathbf{a}_{R,1}, \widetilde{\mathbf{P}}_{R,2}\mathbf{a}_{R,2}, ..., \widetilde{\mathbf{P}}_{R,N_{\mathrm{T}}}\mathbf{a}_{R,N_{\mathrm{T}}}],\\
\mathbf{A}_{\mathrm{R}} &\triangleq [\mathbf{a}_{R,1}, \mathbf{a}_{R,2}, ..., \mathbf{a}_{R,N_{\mathrm{R}}}],\\
\mathbf{B} &\triangleq \mathrm{diag}(\boldsymbol{\beta}),
\end{aligned}$$

we can rewrite (B.7) as

$$\mathbf{J}_{\theta_{\mathrm{R}}\theta_{\mathrm{R}}} = \Re\left\{(\mathbf{B}^{\mathrm{H}}\mathbf{K}_{\mathrm{R}}^{\mathrm{H}}\mathbf{K}_{\mathrm{R}}\mathbf{B}) \odot (\mathbf{A}_{\mathrm{T}}^{\mathrm{H}}\mathbf{F}\mathbf{F}^{\mathrm{H}}\mathbf{A}_{\mathrm{T}})^{\mathrm{T}} \odot \mathbf{R}_0\right\}. \tag{B.9}$$

The other sub-matrices of (B.6) can be similarly obtained as

$$\mathbf{J}_{\boldsymbol{\theta}_{\mathrm{T}}\boldsymbol{\theta}_{\mathrm{T}}} = \gamma\Re\{(\mathbf{B}^{\mathrm{H}}\mathbf{A}_{\mathrm{R}}^{\mathrm{H}}\mathbf{A}_{\mathrm{R}}\mathbf{B}) \odot (\mathbf{K}_{\mathrm{T}}^{\mathrm{H}}\mathbf{F}\mathbf{F}^{\mathrm{H}}\mathbf{K}_{\mathrm{T}})^{\mathrm{T}} \odot \mathbf{R}_0\}, \tag{B.10a}$$

$$\mathbf{J}_{\boldsymbol{\phi}_{\mathrm{R}}\boldsymbol{\phi}_{\mathrm{R}}} = \gamma\Re\{(\mathbf{B}^{\mathrm{H}}\mathbf{P}_{\mathrm{R}}^{\mathrm{H}}\mathbf{P}_{\mathrm{R}}\mathbf{B}) \odot (\mathbf{A}_{\mathrm{T}}^{\mathrm{H}}\mathbf{F}\mathbf{F}^{\mathrm{H}}\mathbf{A}_{\mathrm{T}})^{\mathrm{T}} \odot \mathbf{R}_0\}, \tag{B.10b}$$

$$\mathbf{J}_{\boldsymbol{\phi}_{\mathrm{T}}\boldsymbol{\phi}_{\mathrm{T}}} = \gamma\Re\{(\mathbf{B}^{\mathrm{H}}\mathbf{A}_{\mathrm{R}}^{\mathrm{H}}\mathbf{A}_{\mathrm{R}}\mathbf{B}) \odot (\mathbf{P}_{\mathrm{T}}^{\mathrm{H}}\mathbf{F}\mathbf{F}^{\mathrm{H}}\mathbf{P}_{\mathrm{T}})^{\mathrm{T}} \odot \mathbf{R}_0\}, \tag{B.10c}$$

$$\mathbf{J}_{\boldsymbol{\beta}_{\mathrm{R}}\boldsymbol{\beta}_{\mathrm{R}}} = \mathbf{J}_{\boldsymbol{\beta}_{\mathrm{I}}\boldsymbol{\beta}_{\mathrm{I}}} = \Re\{(\mathbf{A}_{\mathrm{R}}^{\mathrm{H}}\mathbf{A}_{\mathrm{R}}) \odot (\mathbf{A}_{\mathrm{T}}^{\mathrm{H}}\mathbf{F}\mathbf{F}^{\mathrm{H}}\mathbf{A}_{\mathrm{T}})^{\mathrm{T}} \odot \mathbf{R}_0\}, \tag{B.10d}$$

$$\mathbf{J}_{\boldsymbol{\tau}\boldsymbol{\tau}} = \gamma\Re\{(\mathbf{B}^{\mathrm{H}}\mathbf{A}_{\mathrm{R}}^{\mathrm{H}}\mathbf{A}_{\mathrm{R}}\mathbf{B}) \odot (\mathbf{A}_{\mathrm{T}}^{\mathrm{H}}\mathbf{F}\mathbf{F}^{\mathrm{H}}\mathbf{A}_{\mathrm{T}})^{\mathrm{T}} \odot \mathbf{R}_2\}, \tag{B.10e}$$

$$\mathbf{J}_{\boldsymbol{\theta}_{\mathrm{R}}\boldsymbol{\theta}_{\mathrm{T}}} = \gamma\Im\{j(\mathbf{B}^{\mathrm{H}}\mathbf{K}_{\mathrm{R}}{}^{\mathrm{H}}\mathbf{A}_{\mathrm{R}}\mathbf{B}) \odot (\mathbf{K}_{\mathrm{T}}^{\mathrm{H}}\mathbf{F}\mathbf{F}^{\mathrm{H}}\mathbf{A}_{\mathrm{T}})^{\mathrm{T}} \odot \mathbf{R}_0\}, \tag{B.10f}$$

$$\mathbf{J}_{\boldsymbol{\theta}_{\mathrm{R}}\boldsymbol{\phi}_{\mathrm{R}}} = \gamma\Re\{(\mathbf{B}^{\mathrm{H}}\mathbf{K}_{\mathrm{R}}^{\mathrm{H}}\mathbf{P}_{\mathrm{R}}\mathbf{B}) \odot (\mathbf{A}_{\mathrm{T}}^{\mathrm{H}}\mathbf{F}\mathbf{F}^{\mathrm{H}}\mathbf{A}_{\mathrm{T}})^{\mathrm{T}} \odot \mathbf{R}_0\}, \tag{B.10g}$$

$$\mathbf{J}_{\boldsymbol{\theta}_{\mathrm{R}}\boldsymbol{\phi}_{\mathrm{T}}} = \gamma\Im\{j(\mathbf{B}^{\mathrm{H}}\mathbf{K}_{\mathrm{R}}{}^{\mathrm{H}}\mathbf{A}_{\mathrm{R}}\mathbf{B}) \odot (\mathbf{P}_{\mathrm{T}}^{\mathrm{H}}\mathbf{F}\mathbf{F}^{\mathrm{H}}\mathbf{A}_{\mathrm{T}})^{\mathrm{T}} \odot \mathbf{R}_0\}, \tag{B.10h}$$

$$\mathbf{J}_{\boldsymbol{\theta}_{\mathrm{T}}\boldsymbol{\phi}_{\mathrm{R}}} = \gamma\Im\{j(\mathbf{B}^{\mathrm{H}}\mathbf{A}_{\mathrm{R}}^{\mathrm{H}}\mathbf{P}_{\mathrm{R}}\mathbf{B}) \odot (\mathbf{A}_{\mathrm{T}}^{\mathrm{H}}\mathbf{F}\mathbf{F}^{\mathrm{H}}\mathbf{K}_{\mathrm{T}})^{\mathrm{T}} \odot \mathbf{R}_0\}, \tag{B.10i}$$

$$\mathbf{J}_{\boldsymbol{\theta}_{\mathrm{T}}\boldsymbol{\phi}_{\mathrm{T}}} = \gamma\Re\{(\mathbf{B}^{\mathrm{H}}\mathbf{A}_{\mathrm{R}}^{\mathrm{H}}\mathbf{A}_{\mathrm{R}}\mathbf{B}) \odot (\mathbf{P}_{\mathrm{T}}^{\mathrm{H}}\mathbf{F}\mathbf{F}^{\mathrm{H}}\mathbf{K}_{\mathrm{T}})^{\mathrm{T}} \odot \mathbf{R}_0\}, \tag{B.10j}$$

$$\mathbf{J}_{\boldsymbol{\phi}_{\mathrm{R}}\boldsymbol{\phi}_{\mathrm{T}}} = \gamma\Im\{j(\mathbf{B}^{\mathrm{H}}\mathbf{P}_{\mathrm{R}}^{\mathrm{H}}\mathbf{A}_{\mathrm{R}}\mathbf{B}) \odot (\mathbf{P}_{\mathrm{T}}^{\mathrm{H}}\mathbf{F}\mathbf{F}^{\mathrm{H}}\mathbf{A}_{\mathrm{T}})^{\mathrm{T}} \odot \mathbf{R}_0\}, \tag{B.10k}$$

$$\mathbf{J}_{\boldsymbol{\beta}_{\mathrm{R}}\boldsymbol{\beta}_{\mathrm{I}}} = \gamma\Re\{j(\mathbf{A}_{\mathrm{R}}^{\mathrm{H}}\mathbf{A}_{\mathrm{R}}) \odot (\mathbf{A}_{\mathrm{T}}^{\mathrm{H}}\mathbf{F}\mathbf{F}^{\mathrm{H}}\mathbf{A}_{\mathrm{T}})^{\mathrm{T}} \odot \mathbf{R}_0\}, \tag{B.10l}$$

$$\mathbf{J}_{\boldsymbol{\theta}_{\mathrm{R}}\boldsymbol{\tau}} = \gamma\Re\{j(\mathbf{B}^{\mathrm{H}}\mathbf{K}_{\mathrm{R}}^{\mathrm{H}}\mathbf{A}_{\mathrm{R}}\mathbf{B}) \odot (\mathbf{A}_{\mathrm{T}}^{\mathrm{H}}\mathbf{F}\mathbf{F}^{\mathrm{H}}\mathbf{A}_{\mathrm{T}})^{\mathrm{T}} \odot \mathbf{R}_1\}, \tag{B.10m}$$

$$\mathbf{J}_{\boldsymbol{\theta}_{\mathrm{T}}\boldsymbol{\tau}} = \gamma\Im\{(\mathbf{B}^{\mathrm{H}}\mathbf{A}_{\mathrm{R}}^{\mathrm{H}}\mathbf{A}_{\mathrm{R}}\mathbf{B}) \odot (\mathbf{A}_{\mathrm{T}}^{\mathrm{H}}\mathbf{F}\mathbf{F}^{\mathrm{H}}\mathbf{K}_{\mathrm{T}})^{\mathrm{T}} \odot \mathbf{R}_1\}, \tag{B.10n}$$

$$\mathbf{J}_{\boldsymbol{\phi}_{\mathrm{R}}\boldsymbol{\tau}} = \gamma\Re\{j(\mathbf{B}^{\mathrm{H}}\mathbf{P}_{\mathrm{R}}^{\mathrm{H}}\mathbf{A}_{\mathrm{R}}\mathbf{B}) \odot (\mathbf{A}_{\mathrm{T}}^{\mathrm{H}}\mathbf{F}\mathbf{F}^{\mathrm{H}}\mathbf{A}_{\mathrm{T}})^{\mathrm{T}} \odot \mathbf{R}_1\}, \tag{B.10o}$$

$$\mathbf{J}_{\boldsymbol{\phi}_{\mathrm{T}}\boldsymbol{\tau}} = \gamma\Im\{(\mathbf{B}^{\mathrm{H}}\mathbf{A}_{\mathrm{R}}^{\mathrm{H}}\mathbf{A}_{\mathrm{R}}\mathbf{B}) \odot (\mathbf{A}_{\mathrm{T}}^{\mathrm{H}}\mathbf{F}\mathbf{F}^{\mathrm{H}}\mathbf{P}_{\mathrm{T}})^{\mathrm{T}} \odot \mathbf{R}_1\}, \tag{B.10p}$$

$$\mathbf{J}_{\boldsymbol{\theta}_{\mathrm{R}}\boldsymbol{\beta}_{\mathrm{I}}} + j\mathbf{J}_{\boldsymbol{\theta}_{\mathrm{R}}\boldsymbol{\beta}_{\mathrm{R}}} = -\gamma\ (\mathbf{B}^{\mathrm{H}}\mathbf{K}_{\mathrm{R}}^{\mathrm{H}}\mathbf{A}_{\mathrm{R}}) \odot (\mathbf{A}_{\mathrm{T}}^{\mathrm{H}}\mathbf{F}\mathbf{F}^{\mathrm{H}}\mathbf{A}_{\mathrm{T}})^{\mathrm{T}} \odot \mathbf{R}_0, \tag{B.10q}$$

$$\mathbf{J}_{\boldsymbol{\theta}_{\mathrm{T}}\boldsymbol{\beta}_{\mathrm{I}}} + j\mathbf{J}_{\boldsymbol{\theta}_{\mathrm{T}}\boldsymbol{\beta}_{\mathrm{R}}} = \gamma\ (\mathbf{B}^{\mathrm{H}}\mathbf{A}_{\mathrm{R}}^{\mathrm{H}}\mathbf{A}_{\mathrm{R}}) \odot (\mathbf{A}_{\mathrm{T}}^{\mathrm{H}}\mathbf{F}\mathbf{F}^{\mathrm{H}}\mathbf{K}_{\mathrm{T}})^{\mathrm{T}} \odot \mathbf{R}_0, \tag{B.10r}$$

$$\mathbf{J}_{\boldsymbol{\phi}_{\mathrm{R}}\boldsymbol{\beta}_{\mathrm{I}}} + j\mathbf{J}_{\boldsymbol{\phi}_{\mathrm{R}}\boldsymbol{\beta}_{\mathrm{R}}} = -\gamma\ (\mathbf{B}^{\mathrm{H}}\mathbf{P}_{\mathrm{R}}^{\mathrm{H}}\mathbf{A}_{\mathrm{R}}) \odot (\mathbf{A}_{\mathrm{T}}^{\mathrm{H}}\mathbf{F}\mathbf{F}^{\mathrm{H}}\mathbf{A}_{\mathrm{T}})^{\mathrm{T}} \odot \mathbf{R}_0, \tag{B.10s}$$

$$\mathbf{J}_{\boldsymbol{\phi}_{\mathrm{T}}\boldsymbol{\beta}_{\mathrm{I}}} + j\mathbf{J}_{\boldsymbol{\phi}_{\mathrm{T}}\boldsymbol{\beta}_{\mathrm{R}}} = \gamma\ (\mathbf{B}^{\mathrm{H}}\mathbf{A}_{\mathrm{R}}^{\mathrm{H}}\mathbf{A}_{\mathrm{R}}) \odot (\mathbf{A}_{\mathrm{T}}^{\mathrm{H}}\mathbf{F}\mathbf{F}^{\mathrm{H}}\mathbf{P}_{\mathrm{T}})^{\mathrm{T}} \odot \mathbf{R}_0, \tag{B.10t}$$

$$\mathbf{J}_{\boldsymbol{\beta}_{\mathrm{R}}\boldsymbol{\tau}} + j\mathbf{J}_{\boldsymbol{\beta}_{\mathrm{I}}\boldsymbol{\tau}} = \gamma\ (\mathbf{A}^{\mathrm{H}}\mathbf{A}_{\mathrm{R}}\mathbf{B}) \odot (\mathbf{A}_{\mathrm{T}}^{\mathrm{H}}\mathbf{F}\mathbf{F}^{\mathrm{H}}\mathbf{A}_{\mathrm{T}})^{\mathrm{T}} \odot \mathbf{R}_1, \tag{B.10u}$$

where, similar to $\mathbf{R}_0$ the elements of $\mathbf{R}_1$ and $\mathbf{R}_2$ are given by

$$\begin{aligned}[\mathbf{R}_1]_{u,v} &\triangleq \int_0^{T_o} \frac{\partial s_\ell(t-\tau_v)}{\partial \tau_v} s_\ell^*(t-\tau_u)\mathrm{d}t \\ &= \int_{-W/2}^{W/2} 2\pi f |P(f)|^2 e^{-j2\pi f \Delta\tau_{uv}}\mathrm{d}f, \end{aligned} \tag{B.11}$$

$$\begin{aligned}[\mathbf{R}_2]_{u,v} &\triangleq \int_0^{T_o} \frac{\partial s_\ell(t-\tau_v)}{\partial \tau_v} \frac{\partial s_\ell^*(t-\tau_u)}{\partial \tau_u}\mathrm{d}t \\ &= \int_{-W/2}^{W/2} (2\pi f)^2 |P(f)|^2 e^{-j2\pi f \Delta\tau_{uv}}\mathrm{d}f. \end{aligned} \tag{B.12}$$

Appendix C

FIM and CRLB of Single-Path Channel with Arrays of Arbitrary Geometry

C.1 Signle-path 3D Channels

We now consider the case of single-path channel parameters nd define the vector of unknown parameters as

$$\boldsymbol{\varphi}_s \triangleq [\theta_{\mathrm{R}}, \theta_{\mathrm{T}}, \phi_{\mathrm{R}}, \phi_{\mathrm{T}}, \beta, \tau]^T \tag{C.1}$$

Note that the subscript m is dropped from the path parameters to simplify presentation.

Without loss of generality, we start by computing LOS FIM[1]

$$J_{\varphi_{s_u}\varphi_{s_v}} \triangleq \frac{1}{N_0}\int_0^{T_o} \Re\left\{\frac{\partial \boldsymbol{\mu}_{\boldsymbol{\varphi_s}}^H}{\partial \varphi_{s_u}}\frac{\partial \boldsymbol{\mu}_{\boldsymbol{\varphi_s}}}{\partial \varphi_{s_v}}\right\} dt,$$

where φ_{s_u} is the p^{th} element in $\boldsymbol{\varphi_s}$, $1 \leq u, v \leq 7$. The easiest way to do that is to evaluate the matrices in (B.9) and (B.10) for the first path, i.e., taking the element at

[1]As far as the FIM of the channel parameters is concerned, the difference between LOS and NLOS paths is how the path loss is modeled.

$(1,1)$ position of each matrix, which leads to

$$J_{\theta_{\mathrm{R}}\theta_{\mathrm{R}}} = \gamma|\beta|^2 \mathbf{a}_{\mathrm{R}}^H \mathbf{K}_R^2 \mathbf{a}_{\mathrm{R}} \mathbf{a}_{\mathrm{T}}^H \mathbf{F}\mathbf{F}^H \mathbf{a}_{\mathrm{T}}. \tag{C.2}$$

$$J_{\theta_{\mathrm{T}}\theta_{\mathrm{T}}} = \gamma|\beta|^2 \mathbf{a}_{\mathrm{T}}^H \mathbf{K}_{\mathrm{T}} \mathbf{F}\mathbf{F}^H \mathbf{K}_{\mathrm{T}} \mathbf{a}_{\mathrm{T}}, \tag{C.3}$$

$$J_{\phi_{\mathrm{R}}\phi_{\mathrm{R}}} = \gamma|\beta|^2 \mathbf{a}_{\mathrm{R}}^H \mathbf{P}_R^2 \mathbf{a}_{\mathrm{R}} \mathbf{a}_{\mathrm{T}}^H \mathbf{F}\mathbf{F}^H \mathbf{a}_{\mathrm{T}}. \tag{C.4}$$

$$J_{\phi_{\mathrm{T}}\phi_{\mathrm{T}}} = \gamma|\beta|^2 \mathbf{a}_{\mathrm{T}}^H \mathbf{P}_{\mathrm{T}} \mathbf{F}\mathbf{F}^H \mathbf{P}_{\mathrm{T}} \mathbf{a}_{\mathrm{T}}, \tag{C.5}$$

$$J_{\beta_{\mathrm{R}}\beta_{\mathrm{R}}} = J_{\beta_{\mathrm{I}}\beta_{\mathrm{I}}} = \gamma \mathbf{a}_{\mathrm{T}}^H \mathbf{F}\mathbf{F}^H \mathbf{a}_{\mathrm{T}}, \tag{C.6}$$

$$J_{\tau\tau} = 4\gamma\pi^2|\beta|^2 W_{\mathrm{eff}}^2 \mathbf{a}_{\mathrm{T}}^H \mathbf{F}\mathbf{F}^H \mathbf{a}_{\mathrm{T}}, \tag{C.7}$$

$$J_{\theta_{\mathrm{R}}\phi_{\mathrm{R}}} = \gamma|\beta|^2 \mathbf{a}_{\mathrm{R}}^H \mathbf{K}_R \mathbf{P}_R \mathbf{a}_{\mathrm{R}} \mathbf{a}_{\mathrm{T}}^H \mathbf{F}\mathbf{F}^H \mathbf{a}_{\mathrm{T}}. \tag{C.8}$$

$$J_{\theta_{\mathrm{T}}\phi_{\mathrm{T}}} = \gamma|\beta|^2 N_0 \Re\{\mathbf{a}_{\mathrm{T}}^H \mathbf{P}_{\mathrm{T}} \mathbf{F}\ \mathbf{F}^H \mathbf{K}_{\mathrm{T}} \mathbf{a}_{\mathrm{T}}\}, \tag{C.9}$$

$$J_{\theta_{\mathrm{T}}\beta_{\mathrm{R}}} = -\gamma \Re\{j\beta^* \mathbf{a}_{\mathrm{T}}^H \mathbf{F}\mathbf{F}^H \mathbf{K}_{\mathrm{T}} \mathbf{a}_{\mathrm{T}}\}, \tag{C.10}$$

$$J_{\theta_{\mathrm{T}}\beta_{\mathrm{I}}} = \gamma \Re\{\beta^* \mathbf{a}_{\mathrm{T}}^H \mathbf{F}\mathbf{F}^H \mathbf{K}_{\mathrm{T}} \mathbf{a}_{\mathrm{T}}\}, \tag{C.11}$$

$$J_{\phi_{\mathrm{T}}\beta_{\mathrm{R}}} = -\gamma \Re\{j\beta^* \mathbf{a}_{\mathrm{T}}^H \mathbf{F}\mathbf{F}^H \mathbf{P}_{\mathrm{T}} \mathbf{a}_{\mathrm{T}}\}, \tag{C.12}$$

$$J_{\phi_{\mathrm{T}}\beta_{\mathrm{I}}} = \gamma \Re\{\beta^* \mathbf{a}_{\mathrm{T}}^H \mathbf{F}\mathbf{F}^H \mathbf{P}_{\mathrm{T}} \mathbf{a}_{\mathrm{T}}\}, \tag{C.13}$$

while the remaining elements in $\mathbf{J}_{\boldsymbol{\varphi}_s}$ are zero. Finally, the FIM of $\boldsymbol{\varphi}_s$, can be written as

$$\mathbf{J}_{\boldsymbol{\varphi}_s} \triangleq \begin{bmatrix} \mathbf{J}_{\boldsymbol{\theta},\boldsymbol{\phi},\boldsymbol{\beta}} & \mathbf{0}_6 \\ \mathbf{0}_6^T & J_{\tau\tau} \end{bmatrix}, \tag{C.14}$$

where

$$\mathbf{J}_{\boldsymbol{\theta},\boldsymbol{\phi},\boldsymbol{\beta}} \triangleq \gamma|\beta|^2 \left[\begin{array}{c:c} \mathbf{A} & \mathbf{U} \\ \hdashline \mathbf{U}^{\mathrm{T}} & \mathbf{C} \end{array}\right] \tag{C.15}$$

$$= \gamma|\beta|^2 \left[\begin{array}{cccc:cc} R_\theta G & 0 & X_{\theta,\phi} G & 0 & 0 & 0 \\ 0 & T_\theta & 0 & Y'_{\theta,\phi} & S_\theta & U_\theta \\ X_{\theta,\phi} G & 0 & R_\phi G & 0 & 0 & 0 \\ 0 & Y'_{\theta,\phi} & 0 & T_\phi & S_\phi & U_\phi \\ \hdashline 0 & S_\theta & 0 & S_\phi & \frac{G}{|\beta|^2} & 0 \\ 0 & U_\theta & 0 & U_\phi & 0 & \frac{G}{|\beta|^2} \end{array}\right], \tag{C.16}$$

where $S_\theta \triangleq -\Im\{\beta V_\theta\}/|\beta|^2, U_\theta \triangleq \Re\{\beta V_\theta\}/|\beta|^2, S_\phi \triangleq -\Im\{\beta V_\phi\}/|\beta|^2$, and $U_\phi \triangleq \Re\{\beta V_\phi\}/|\beta|^2$.

Then, we compute the CRLBs of DOA and DOD using their EFIM as

$$\mathbf{J}^{\mathrm{e}}_{\boldsymbol{\theta},\boldsymbol{\phi}} \triangleq \gamma|\beta|^2(\mathbf{A}-\mathbf{U}\mathbf{C}^{-1}\mathbf{U}^{\mathrm{T}}) = \gamma|\beta|^2 \begin{bmatrix} R_\theta G & 0 & X_{\theta,\phi}G & 0 \\ 0 & \frac{L_\theta}{G} & 0 & \frac{Y_{\theta,\phi}}{G} \\ X_{\theta,\phi}G & 0 & R_\phi G & 0 \\ 0 & \frac{Y_{\theta,\phi}}{G} & 0 & \frac{L_\phi}{G} \end{bmatrix}. \tag{C.17}$$

To simplify the inverse computation, we utilize the independence between DOA and DOD to re-order $\mathbf{J}^{\mathrm{e}}_{\boldsymbol{\theta},\boldsymbol{\phi}}$ to write (C.18), from which (5.24) follow.

$$\mathrm{CRLB}\left((\theta_{\mathrm{R}},\phi_{\mathrm{R}})\right) = \frac{1}{\gamma|\beta|^2 G}\begin{bmatrix} R_\theta & X_{\theta,\phi} \\ X_{\theta,\phi} & R_\phi \end{bmatrix}^{-1}, \tag{C.18a}$$

$$\mathrm{CRLB}\left((\theta_{\mathrm{T}},\phi_{\mathrm{T}})\right) = \frac{G}{\gamma|\beta|^2}\begin{bmatrix} L_\theta & Y_{\theta,\phi} \\ Y_{\theta,\phi} & L_\phi \end{bmatrix}^{-1}, \tag{C.18b}$$

Finally, directly from (C.14), it is easy to see that

$$\mathrm{CRLB}(\tau) = \frac{1}{4\gamma\pi^2|\beta|^2 G W^2_{\mathrm{eff}}}. \tag{C.19}$$

C.2 Signle-path 2D Channels

When the UE and BS are in xy-plane, $\theta_{\mathrm{R}} = \theta_{\mathrm{T}} = \pi/2$, and the channel is modeled by the azimuth angle only. As a result, the CRLB of the channel parameters can be obtained by inverting the relevant sub-matrix of $\mathbf{J}_{\boldsymbol{\varphi_s}}$ defined in (C.16). In other words, we seek to invert the matrix

$$\mathbf{J}_{\boldsymbol{\varphi}'_{\boldsymbol{s}}} \triangleq \gamma|\beta|^2 \begin{bmatrix} R_\phi G & 0 & 0 & 0 \\ 0 & T_\phi & S_\phi & U_\phi \\ 0 & S_\phi & \frac{G}{|\beta|^2} & 0 \\ 0 & U_\phi & 0 & \frac{G}{|\beta|^2} \end{bmatrix} \tag{C.20}$$

where $\mathbf{J}_{\boldsymbol{\varphi}'_{\boldsymbol{s}}} \triangleq [\phi_{\mathrm{R}},\phi_{\mathrm{T}},\beta_{\mathrm{R}},\beta_{\mathrm{I}}]^T$. Consequently, it is easy to see that

$$\mathrm{CRLB}(\phi_{\mathrm{R}}) = \frac{1}{\gamma|\beta|^2 R_\phi G}, \tag{C.21a}$$

$$\mathrm{CRLB}(\phi_{\mathrm{T}}) = \frac{G}{\gamma|\beta|^2 L_\phi}. \tag{C.21b}$$

Note that following from the fact that $\beta_{\rm R}$ and $\beta_{\rm I}$ are orthogonal, we can write $\text{CRLB}(\beta) = \text{CRLB}(\beta_{\rm R}) + \text{CRLB}(\beta_{\rm I})$, which is straight forward to write as

$$\begin{aligned}\text{CRLB}\left(\beta\right) &= \frac{1}{\gamma|\beta|^2}\,\text{Tr}\left((\mathbf{C}-\mathbf{U}^{\rm T}\mathbf{A}^{-1}\mathbf{U})^{-1}\right),\\ &= \frac{1}{\gamma G}\left(1+\frac{GT_\phi}{GT_\phi-|V_\phi|^2}\right),\end{aligned} \tag{C.22}$$

while $\text{CRLB}(\tau)$ is similar to that in (C.19).

C.3 Examples

C.3.1 Example – URA and 3D Channel

To compute the CRLBs, PEB or OEB for URA, in this section, we specify the parameters of (C.14) assuming that the receiver array is located in xz-plane, as described in Section 2.1.1, and the normalized element locations are given by (2.7), then assuming that $d_{\rm x} = d_{\rm z} = d$, we can write

$$\widetilde{\mathbf{K}}_{\rm R} = \frac{2\pi d}{\lambda}\,\text{diag}(\cos\theta_{\rm R}\cos\phi_{\rm R}\mathbf{x}_{\rm R} - \sin\theta_{\rm R}\mathbf{z}_{\rm R}), \tag{C.23a}$$

$$\widetilde{\mathbf{P}}_{\rm R} = -\frac{2\pi d}{\lambda}\sin\theta_{\rm R}\sin\phi_{\rm R}\,\text{diag}(\mathbf{x}_{\rm R}), \tag{C.23b}$$

Defining $\alpha \triangleq 4\pi^2 d^2/\lambda^2$, and assuming $(N_{{\rm R},z}^2-1)\approx N_{{\rm R},z}^2$ and $(N_{{\rm R},x}^2-1)\approx N_{{\rm R},x}^2$, then $\mathbf{x}_{\rm R}^{\rm T}\mathbf{x}_{\rm R} = N_{\rm R}N_{{\rm R},x}^2/12, \mathbf{z}_{\rm R}^{\rm T}\mathbf{z}_{\rm R} = N_{\rm R}N_{{\rm R},z}^2/12$. As a result, it can be verified that,

$$X_{\theta,\phi} = \frac{\text{Tr}(\widetilde{\mathbf{K}}_{\rm R}\widetilde{\mathbf{P}}_{\rm R})}{N_{\rm R}} = -\frac{\alpha}{12}\cos\theta_{\rm R}\cos\phi_{\rm R}\sin\theta_{\rm R}\sin\phi_{\rm R}N_{{\rm R},z}^2, \tag{C.24a}$$

$$R_\theta = \frac{\text{Tr}(\widetilde{\mathbf{K}}_{\rm R}^2)}{N_{\rm R}} = \frac{\alpha}{12}\big(\cos^2\theta_{\rm R}\cos^2\phi_{\rm R}N_{{\rm R},x}^2 + \sin^2\theta_{\rm R}N_{{\rm R},z}^2\big), \tag{C.24b}$$

$$R_\phi = \frac{\text{Tr}(\widetilde{\mathbf{P}}_{\rm R}^2)}{N_{\rm R}} = \frac{\alpha}{12}\sin^2\theta_{\rm R}\sin^2\phi_{\rm R}N_{{\rm R},x}^2. \tag{C.24c}$$

To compute the transmitter-side parameters, define $\mathbf{X}_{\rm T} = \text{diag}(\mathbf{x}_{\rm T})$, $\mathbf{Z}_{\rm T} = \text{diag}(\mathbf{z}_{\rm T})$, and

$$\mathbf{M} \triangleq \begin{bmatrix} \mathbf{a}_{\rm T}^{\rm H}\mathbf{F}\mathbf{F}^{\rm H}\mathbf{a}_{\rm T} & \Re\{\mathbf{a}_{\rm T}^{\rm H}\mathbf{X}_{\rm T}\mathbf{F}\mathbf{F}^{\rm H}\mathbf{Z}_{\rm T}\mathbf{a}_{\rm T}\} \\ \mathbf{a}_{\rm T}^{\rm H}\mathbf{X}_{\rm T}\mathbf{F}\mathbf{F}^{\rm H}\mathbf{a}_{\rm T} & \mathbf{a}_{\rm T}^{\rm H}\mathbf{X}_{\rm T}\mathbf{F}\mathbf{F}^{\rm H}\mathbf{X}_{\rm T}\mathbf{a}_{\rm T} \\ \mathbf{a}_{\rm T}^{\rm H}\mathbf{Z}_{\rm T}\mathbf{F}\mathbf{F}^{\rm H}\mathbf{a}_{\rm T} & \mathbf{a}_{\rm T}^{\rm H}\mathbf{Z}_{\rm T}\mathbf{F}\mathbf{F}^{\rm H}\mathbf{Z}_{\rm T}\mathbf{a}_{\rm T} \end{bmatrix}, \tag{C.25}$$

Using the same procedure by which R_θ, R_ϕ, and $X_{\theta,\phi}$ are obtained, it can be shown that

$$T_\theta = \alpha\left(\cos^2\theta_{\mathrm{T}}\cos^2\phi_{\mathrm{T}}[\mathbf{M}]_{2,2} + \sin^2\theta_{\mathrm{T}}[\mathbf{M}]_{3,2} - 2\cos\theta_{\mathrm{T}}\cos\phi_{\mathrm{T}}\sin\theta_{\mathrm{T}}[\mathbf{M}]_{1,2}\right), \quad \text{(C.26a)}$$

$$V_\theta = \sqrt{\alpha}\left(\cos\theta_{\mathrm{T}}\cos\phi_{\mathrm{T}}[\mathbf{M}]_{2,1} - \sin\theta_{\mathrm{T}}[\mathbf{M}]_{3,1}\right), \quad \text{(C.26b)}$$

$$T_\phi = \alpha\sin^2\theta_{\mathrm{T}}\sin^2\phi_{\mathrm{T}}[\mathbf{M}]_{2,2}, \quad \text{(C.26c)}$$

$$V_\phi = -\sqrt{\alpha}\sin\theta_{\mathrm{T}}\sin\phi_{\mathrm{T}}[\mathbf{M}]_{2,1}, \quad \text{(C.26d)}$$

$$Y'_{\theta,\phi} = \alpha(-\cos\theta_{\mathrm{T}}\cos\phi_{\mathrm{T}}\sin\theta_{\mathrm{T}}\sin\phi_{\mathrm{T}}[\mathbf{M}]_{2,2} + \sin^2\theta_{\mathrm{T}}\sin\phi_{\mathrm{T}}[\mathbf{M}]_{1,2}). \quad \text{(C.26e)}$$

C.3.2 Example – ULA and 2D Channel

For a ULA lying on the x-axis, $\mathbf{x}_{\mathrm{R}} = \mathbf{x}_{\mathrm{R}}^{(1)}/d$, $\mathbf{y}_{\mathrm{R}} = \mathbf{z}_{\mathrm{R}} = \mathbf{0}_{N_{\mathrm{R}}}$, and $\theta_{\mathrm{R}} = \theta_{\mathrm{T}} = \pi/2$. So,

$$R_\phi = \frac{4\pi^2\sin^2\phi_{\mathrm{R}}}{\lambda^2 N_{\mathrm{R}}}\mathbf{x}_{\mathrm{R}}^{\mathrm{T}}\mathbf{x}_{\mathrm{R}} = \frac{\alpha}{12}(N_{\mathrm{R}}^2 - 1)\sin^2\phi_{\mathrm{R}}. \quad \text{(C.27)}$$

Moreover, write $\widetilde{\mathbf{P}}_{\mathrm{T}} = -\sqrt{\alpha}\sin\phi_{\mathrm{T}}\mathbf{X}_{\mathrm{T}}$, then

$$T_\phi = \alpha\sin^2(\phi_{\mathrm{T}})(\mathbf{a}_{\mathrm{T}}^{\mathrm{H}}\mathbf{X}_{\mathrm{T}}\mathbf{F}\mathbf{F}^{\mathrm{H}}\mathbf{X}_{\mathrm{T}}\mathbf{a}_{\mathrm{T}}), \quad \text{(C.28a)}$$

$$V_\phi = -\sqrt{\alpha}\sin(\phi_{\mathrm{T}})(\mathbf{a}_{\mathrm{T}}^{\mathrm{H}}\mathbf{X}_{\mathrm{T}}\mathbf{F}\mathbf{F}^{\mathrm{H}}\mathbf{a}_{\mathrm{T}}). \quad \text{(C.28b)}$$

Substituting (C.27) and (C.28) into (C.21) and (C.22), and defining

$$\mathbf{Q} \triangleq \begin{bmatrix} \mathbf{a}_{\mathrm{T}}^{\mathrm{H}}\mathbf{F}\mathbf{F}^{\mathrm{H}}\mathbf{a}_{\mathrm{T}} & \mathbf{a}_{\mathrm{T}}^{\mathrm{H}}\mathbf{X}_{\mathrm{T}}\mathbf{F}\mathbf{F}^{\mathrm{H}}\mathbf{a}_{\mathrm{T}} \\ \mathbf{a}_{\mathrm{T}}^{\mathrm{H}}\mathbf{X}_{\mathrm{T}}\mathbf{F}\mathbf{F}^{\mathrm{H}}\mathbf{a}_{\mathrm{T}} & \mathbf{a}_{\mathrm{T}}^{\mathrm{H}}\mathbf{X}_{\mathrm{T}}\mathbf{F}\mathbf{F}^{\mathrm{H}}\mathbf{X}_{\mathrm{T}}\mathbf{a}_{\mathrm{T}} \end{bmatrix},$$

and $\gamma_0 \triangleq N_{\mathrm{s}}P_{\mathrm{s}}/N_0$, it can be shown that

$$\mathrm{CRLB}(\phi_{\mathrm{R}}) = \frac{12}{\gamma_0|\beta|^2 N_{\mathrm{R}}^3 N_{\mathrm{T}}[\mathbf{Q}]_{1,1}}\left(\frac{\lambda}{2\pi d\sin\phi_{\mathrm{R}}}\right)^2, \quad \text{(C.29a)}$$

$$\mathrm{CRLB}(\phi_{\mathrm{T}}) = \frac{[\mathbf{Q}]_{1,1}}{\gamma_0|\beta|^2 N_{\mathrm{R}}N_{\mathrm{T}}\det(\mathbf{Q})}\left(\frac{\lambda}{2\pi d\sin\phi_{\mathrm{T}}}\right)^2, \quad \text{(C.29b)}$$

$$\mathrm{CRLB}(\beta) = \frac{1}{\gamma_0 N_{\mathrm{R}}N_{\mathrm{T}}[\mathbf{Q}]_{1,1}}\left(1 + \frac{[\mathbf{Q}]_{1,1}[\mathbf{Q}]_{2,2}}{\det(\mathbf{Q})}\right), \quad \text{(C.29c)}$$

$$\mathrm{CRLB}(\tau) = \frac{1}{4\pi^2\gamma_0|\beta|^2 N_{\mathrm{R}}N_{\mathrm{T}}W_{\mathrm{eff}}^2[\mathbf{Q}]_{1,1}}. \quad \text{(C.29d)}$$

Appendix D

Proof of Theorem 5.1 and Proposition 5.2

D.1 Proof of the Equivalence Theorem

Let $\mathbf{J}_{\text{Ch}}$ be the FIM of the DOA, DOD and TOA of all the paths, and $\mathbf{J}_{\boldsymbol{\beta}\boldsymbol{\beta}}$ be the FIM of complex gains of all the paths. Then the FIM of the channel parameters is given by

$$\mathbf{J}_{\boldsymbol{\varphi}} \triangleq \begin{bmatrix} \mathbf{J}_{\text{Ch}} & \mathbf{J}_{\text{Ch},\boldsymbol{\beta}} \\ \mathbf{J}_{\text{Ch},\boldsymbol{\beta}}^{\text{T}} & \mathbf{J}_{\boldsymbol{\beta}\boldsymbol{\beta}} \end{bmatrix} \tag{D.1}$$

Furthermore, define the transformation matrix of the channel parameters $(\boldsymbol{\theta}, \boldsymbol{\phi}, \boldsymbol{\tau}, \boldsymbol{\beta})$ into position parameters, $(\mathbf{o}, \mathbf{p}, \mathbf{q}, \boldsymbol{\beta})$, as

$$\boldsymbol{\Upsilon} \triangleq \begin{bmatrix} \boldsymbol{\Upsilon}_{\text{p}} & \mathbf{0} \\ \boldsymbol{\Upsilon}_{\text{q}} & \mathbf{0} \\ \mathbf{0} & \mathbf{I} \end{bmatrix}, \tag{D.2}$$

where $\boldsymbol{\Upsilon}_{\text{p}}$ is the transformation matrix of the $\boldsymbol{\theta}, \boldsymbol{\phi}$ and $\boldsymbol{\tau}$ to $\mathbf{o}$ and $\mathbf{p}$, $\boldsymbol{\Upsilon}_{\text{q}}$ is the transformation matrix of the $\boldsymbol{\theta}, \boldsymbol{\phi}$ and $\boldsymbol{\tau}$ to $\mathbf{q}$, the vector of the parameters that depend on the DOA, DOD and TOA, such as scatterers location in the multipath case. Note that the transformation from $\boldsymbol{\beta}$ to $\boldsymbol{\beta}$ is obtained by the identity matrix $\mathbf{I}$. Consequently, the EFIM of $\mathbf{o}$ and $\mathbf{p}$ can be obtained using the EFIM $\boldsymbol{\theta}, \boldsymbol{\phi}$ and $\boldsymbol{\tau}$ computed as the Schur's

complement of $\mathbf{J}_{\boldsymbol{\varphi}}$ as follows:

$$\mathbf{J}_{\mathbf{o},\mathbf{p},\mathbf{q}} = \begin{bmatrix} \boldsymbol{\Upsilon}_{\mathrm{p}} \\ \boldsymbol{\Upsilon}_{\mathrm{q}} \end{bmatrix} \underbrace{(\mathbf{J}_{\mathrm{Ch}} - \mathbf{J}_{\mathrm{Ch},\boldsymbol{\beta}} \mathbf{J}_{\boldsymbol{\beta}\boldsymbol{\beta}}^{-1} \mathbf{J}_{\mathrm{Ch},\boldsymbol{\beta}}^{\mathrm{T}})}_{\triangleq \mathbf{J}_{\mathrm{Ch}}^{\mathrm{e}}} \begin{bmatrix} \boldsymbol{\Upsilon}_{\mathrm{p}}^{\mathrm{T}} & \boldsymbol{\Upsilon}_{\mathrm{q}}^{\mathrm{T}} \end{bmatrix} = \begin{bmatrix} \boldsymbol{\Upsilon}_{\mathrm{p}} \mathbf{J}_{\mathrm{Ch}}^{\mathrm{e}} \boldsymbol{\Upsilon}_{\mathrm{p}}^{\mathrm{T}} & \boldsymbol{\Upsilon}_{\mathrm{p}} \mathbf{J}_{\mathrm{Ch}}^{\mathrm{e}} \boldsymbol{\Upsilon}_{\mathrm{q}}^{\mathrm{T}} \\ \boldsymbol{\Upsilon}_{\mathrm{q}} \mathbf{J}_{\mathrm{Ch}}^{\mathrm{e}} \boldsymbol{\Upsilon}_{\mathrm{p}}^{\mathrm{T}} & \boldsymbol{\Upsilon}_{\mathrm{q}} \mathbf{J}_{\mathrm{Ch}}^{\mathrm{e}} \boldsymbol{\Upsilon}_{\mathrm{q}}^{\mathrm{T}} \end{bmatrix} \tag{D.3}$$

Then,

$$\mathbf{J}_{\mathbf{o},\mathbf{p}}^{(\mathrm{e})} = \boldsymbol{\Upsilon}_{\mathrm{p}} \mathbf{J}_{\mathrm{Ch}}^{\mathrm{e}} \boldsymbol{\Upsilon}_{\mathrm{p}}^{\mathrm{T}} - \boldsymbol{\Upsilon}_{\mathrm{p}} \mathbf{J}_{\mathrm{Ch}}^{\mathrm{e}} \boldsymbol{\Upsilon}_{\mathrm{q}}^{\mathrm{T}} (\boldsymbol{\Upsilon}_{\mathrm{q}} \mathbf{J}_{\mathrm{Ch}}^{\mathrm{e}} \boldsymbol{\Upsilon}_{\mathrm{q}}^{\mathrm{T}})^{-1} \boldsymbol{\Upsilon}_{\mathrm{q}} \mathbf{J}_{\mathrm{Ch}}^{\mathrm{e}} \boldsymbol{\Upsilon}_{\mathrm{p}}^{\mathrm{T}}. \tag{D.4}$$

The EFIM of $\mathbf{o}$ and $\mathbf{p}$ can also be obtained by direct transformation of the full FIM of the channel parameters and then using Schur's complement as follows:

$$\mathbf{J}_{\mathbf{o},\mathbf{p},\mathbf{q},\boldsymbol{\beta}} = \boldsymbol{\Upsilon} \mathbf{J}_{\boldsymbol{\varphi}} \boldsymbol{\Upsilon}^{\mathrm{T}} = \begin{bmatrix} \boldsymbol{\Upsilon}_{\mathrm{p}} \mathbf{J}_{\mathrm{Ch}} \boldsymbol{\Upsilon}_{\mathrm{p}}^{\mathrm{T}} & \boldsymbol{\Upsilon}_{\mathrm{p}} \mathbf{J}_{\mathrm{Ch}} \boldsymbol{\Upsilon}_{\mathrm{q}}^{\mathrm{T}} & \boldsymbol{\Upsilon}_{\mathrm{p}} \mathbf{J}_{\mathrm{Ch},\boldsymbol{\beta}} \\ \boldsymbol{\Upsilon}_{\mathrm{q}} \mathbf{J}_{\mathrm{Ch}} \boldsymbol{\Upsilon}_{\mathrm{p}}^{\mathrm{T}} & \boldsymbol{\Upsilon}_{\mathrm{q}} \mathbf{J}_{\mathrm{Ch}} \boldsymbol{\Upsilon}_{\mathrm{q}}^{\mathrm{T}} & \boldsymbol{\Upsilon}_{\mathrm{q}} \mathbf{J}_{\mathrm{Ch},\boldsymbol{\beta}} \\ \mathbf{J}_{\mathrm{Ch},\boldsymbol{\beta}}^{T} \boldsymbol{\Upsilon}_{\mathrm{p}}^{\mathrm{T}} & \mathbf{J}_{\mathrm{Ch},\boldsymbol{\beta}} \boldsymbol{\Upsilon}_{\mathrm{q}}^{\mathrm{T}} & \mathbf{J}_{\boldsymbol{\beta}\boldsymbol{\beta}} \end{bmatrix}. \tag{D.5}$$

Therefore,

$$\mathbf{J}_{\mathbf{o},\mathbf{p}}^{(\mathrm{e})} = \boldsymbol{\Upsilon}_{\mathrm{p}} \mathbf{J}_{\mathrm{Ch}} \boldsymbol{\Upsilon}_{\mathrm{p}}^{\mathrm{T}} - \begin{bmatrix} \boldsymbol{\Upsilon}_{\mathrm{p}} \mathbf{J}_{\mathrm{Ch}} \boldsymbol{\Upsilon}_{\mathrm{q}}^{\mathrm{T}} & \boldsymbol{\Upsilon}_{\mathrm{p}} \mathbf{J}_{\mathrm{Ch},\boldsymbol{\beta}} \end{bmatrix} \begin{bmatrix} \boldsymbol{\Upsilon}_{\mathrm{q}} \mathbf{J}_{\mathrm{Ch}} \boldsymbol{\Upsilon}_{\mathrm{q}}^{\mathrm{T}} & \boldsymbol{\Upsilon}_{\mathrm{q}} \mathbf{J}_{\mathrm{Ch},\boldsymbol{\beta}} \\ \mathbf{J}_{\mathrm{Ch},\boldsymbol{\beta}}^{\mathrm{T}} \boldsymbol{\Upsilon}_{\mathrm{q}}^{\mathrm{T}} & \mathbf{J}_{\boldsymbol{\beta}\boldsymbol{\beta}} \end{bmatrix}^{-1} \begin{bmatrix} \boldsymbol{\Upsilon}_{\mathrm{q}} \mathbf{J}_{\mathrm{Ch}} \boldsymbol{\Upsilon}_{\mathrm{p}}^{\mathrm{T}} \\ \mathbf{J}_{\mathrm{Ch},\boldsymbol{\beta}}^{\mathrm{T}} \boldsymbol{\Upsilon}_{\mathrm{p}}^{\mathrm{T}} \end{bmatrix}, \tag{D.6}$$

Using the matrix inverse lemma,

$$\begin{bmatrix} \boldsymbol{\Upsilon}_{\mathrm{q}} \mathbf{J}_{\mathrm{Ch}} \boldsymbol{\Upsilon}_{\mathrm{q}}^{\mathrm{T}} & \boldsymbol{\Upsilon}_{\mathrm{q}} \mathbf{J}_{\mathrm{Ch},\boldsymbol{\beta}} \\ \mathbf{J}_{\mathrm{Ch},\boldsymbol{\beta}}^{\mathrm{T}} \boldsymbol{\Upsilon}_{\mathrm{q}}^{\mathrm{T}} & \mathbf{J}_{\boldsymbol{\beta}\boldsymbol{\beta}} \end{bmatrix}^{-1} = \begin{bmatrix} (\boldsymbol{\Upsilon}_{\mathrm{q}} \mathbf{J}_{\mathrm{Ch}}^{\mathrm{e}} \boldsymbol{\Upsilon}_{\mathrm{q}}^{\mathrm{T}})^{-1} & -(\boldsymbol{\Upsilon}_{\mathrm{q}} \mathbf{J}_{\mathrm{Ch}}^{\mathrm{e}} \boldsymbol{\Upsilon}_{\mathrm{q}}^{\mathrm{T}})^{-1} \boldsymbol{\Upsilon}_{\mathrm{q}} \mathbf{J}_{\mathrm{Ch},\boldsymbol{\beta}} \mathbf{J}_{\boldsymbol{\beta}\boldsymbol{\beta}}^{-1} \\ -\mathbf{J}_{\boldsymbol{\beta}\boldsymbol{\beta}}^{-1} \mathbf{J}_{\mathrm{Ch},\boldsymbol{\beta}}^{\mathrm{T}} \boldsymbol{\Upsilon}_{\mathrm{q}} (\boldsymbol{\Upsilon}_{\mathrm{q}} \mathbf{J}_{\mathrm{Ch}}^{\mathrm{e}} \boldsymbol{\Upsilon}_{\mathrm{q}}^{\mathrm{T}})^{-1} & \mathbf{J}_{\boldsymbol{\beta}\boldsymbol{\beta}}^{-1} + \mathbf{J}_{\boldsymbol{\beta}\boldsymbol{\beta}}^{-1} \mathbf{J}_{\mathrm{Ch},\boldsymbol{\beta}}^{\mathrm{T}} \boldsymbol{\Upsilon}_{\mathrm{q}} (\boldsymbol{\Upsilon}_{\mathrm{q}} \mathbf{J}_{\mathrm{Ch}}^{\mathrm{e}} \boldsymbol{\Upsilon}_{\mathrm{q}}^{\mathrm{T}})^{-1} \boldsymbol{\Upsilon}_{\mathrm{q}} \mathbf{J}_{\mathrm{Ch},\boldsymbol{\beta}} \mathbf{J}_{\boldsymbol{\beta}\boldsymbol{\beta}}^{-1} \end{bmatrix}, \tag{D.7}$$

Substituting above leads to

$$\begin{aligned} \mathbf{J}_{\mathbf{o},\mathbf{p}}^{(\mathrm{e})} = \boldsymbol{\Upsilon}_{\mathrm{p}} \mathbf{J}_{\mathrm{Ch}} \boldsymbol{\Upsilon}_{\mathrm{p}}^{\mathrm{T}} &- [\boldsymbol{\Upsilon}_{\mathrm{p}} \mathbf{J}_{\mathrm{Ch}} \boldsymbol{\Upsilon}_{\mathrm{q}}^{\mathrm{T}} (\boldsymbol{\Upsilon}_{\mathrm{q}} \mathbf{J}_{\mathrm{Ch}}^{\mathrm{e}} \boldsymbol{\Upsilon}_{\mathrm{q}}^{\mathrm{T}})^{-1} \boldsymbol{\Upsilon}_{\mathrm{q}} \mathbf{J}_{\mathrm{Ch}} \boldsymbol{\Upsilon}_{\mathrm{p}}^{\mathrm{T}} \\ &- \boldsymbol{\Upsilon}_{\mathrm{p}} \mathbf{J}_{\mathrm{Ch},\boldsymbol{\beta}} \mathbf{J}_{\boldsymbol{\beta}\boldsymbol{\beta}}^{-1} \mathbf{J}_{\mathrm{Ch},\boldsymbol{\beta}}^{\mathrm{T}} \boldsymbol{\Upsilon}_{\mathrm{q}} (\boldsymbol{\Upsilon}_{\mathrm{q}} \mathbf{J}_{\mathrm{Ch}}^{\mathrm{e}} \boldsymbol{\Upsilon}_{\mathrm{q}}^{\mathrm{T}})^{-1} \boldsymbol{\Upsilon}_{\mathrm{q}} \mathbf{J}_{\mathrm{Ch}} \boldsymbol{\Upsilon}_{\mathrm{p}}^{\mathrm{T}} \\ &- \boldsymbol{\Upsilon}_{\mathrm{p}} \mathbf{J}_{\mathrm{Ch}} \boldsymbol{\Upsilon}_{\mathrm{q}}^{\mathrm{T}} (\boldsymbol{\Upsilon}_{\mathrm{q}} \mathbf{J}_{\mathrm{Ch}}^{\mathrm{e}} \boldsymbol{\Upsilon}_{\mathrm{q}}^{\mathrm{T}})^{-1} \boldsymbol{\Upsilon}_{\mathrm{q}} \mathbf{J}_{\mathrm{Ch},\boldsymbol{\beta}} \mathbf{J}_{\boldsymbol{\beta}\boldsymbol{\beta}}^{-1} \mathbf{J}_{\mathrm{Ch},\boldsymbol{\beta}}^{\mathrm{T}} \boldsymbol{\Upsilon}_{\mathrm{p}}^{\mathrm{T}} + \boldsymbol{\Upsilon}_{\mathrm{p}} \mathbf{J}_{\mathrm{Ch},\boldsymbol{\beta}} \mathbf{J}_{\boldsymbol{\beta}\boldsymbol{\beta}}^{-1} \mathbf{J}_{\mathrm{Ch},\boldsymbol{\beta}}^{\mathrm{T}} \boldsymbol{\Upsilon}_{\mathrm{p}}^{\mathrm{T}} \\ &+ \boldsymbol{\Upsilon}_{\mathrm{p}} \mathbf{J}_{\mathrm{Ch},\boldsymbol{\beta}} \mathbf{J}_{\boldsymbol{\beta}\boldsymbol{\beta}}^{-1} \mathbf{J}_{\mathrm{Ch},\boldsymbol{\beta}}^{\mathrm{T}} \boldsymbol{\Upsilon}_{\mathrm{q}} (\boldsymbol{\Upsilon}_{\mathrm{q}} \mathbf{J}_{\mathrm{Ch}}^{\mathrm{e}} \boldsymbol{\Upsilon}_{\mathrm{q}}^{\mathrm{T}})^{-1} \boldsymbol{\Upsilon}_{\mathrm{q}} \mathbf{J}_{\mathrm{Ch},\boldsymbol{\beta}} \mathbf{J}_{\boldsymbol{\beta}\boldsymbol{\beta}}^{-1} \mathbf{J}_{\mathrm{Ch},\boldsymbol{\beta}}^{\mathrm{T}} \boldsymbol{\Upsilon}_{\mathrm{p}}^{\mathrm{T}}], \end{aligned} \tag{D.8}$$

$$
\begin{aligned}
&= \boldsymbol{\Upsilon}_{\mathrm{p}} \mathbf{J}^{\mathrm{e}}_{\mathrm{Ch}} \boldsymbol{\Upsilon}^{\mathrm{T}}_{\mathrm{p}} - \boldsymbol{\Upsilon}_{\mathrm{p}} \mathbf{J}_{\mathrm{Ch}} \boldsymbol{\Upsilon}^{\mathrm{T}}_{\mathrm{q}} (\boldsymbol{\Upsilon}_{\mathrm{q}} \mathbf{J}^{\mathrm{e}}_{\mathrm{Ch}} \boldsymbol{\Upsilon}^{\mathrm{T}}_{\mathrm{q}})^{-1} \boldsymbol{\Upsilon}_{\mathrm{q}} \mathbf{J}^{\mathrm{e}}_{\mathrm{Ch}} \boldsymbol{\Upsilon}^{\mathrm{T}}_{\mathrm{p}} \\
&\qquad + \boldsymbol{\Upsilon}_{\mathrm{p}} \mathbf{J}_{\mathrm{Ch},\boldsymbol{\beta}} \mathbf{J}^{-1}_{\boldsymbol{\beta}\boldsymbol{\beta}} \mathbf{J}^{\mathrm{T}}_{\mathrm{Ch},\boldsymbol{\beta}} \boldsymbol{\Upsilon}_{\mathrm{q}} (\boldsymbol{\Upsilon}_{\mathrm{q}} \mathbf{J}^{\mathrm{e}}_{\mathrm{Ch}} \boldsymbol{\Upsilon}^{\mathrm{T}}_{\mathrm{q}})^{-1} \boldsymbol{\Upsilon}_{\mathrm{q}} \mathbf{J}^{\mathrm{e}}_{\mathrm{Ch}} \boldsymbol{\Upsilon}^{\mathrm{T}}_{\mathrm{p}} \\
&= \boldsymbol{\Upsilon}_{\mathrm{p}} \mathbf{J}^{\mathrm{e}}_{\mathrm{Ch}} \boldsymbol{\Upsilon}^{\mathrm{T}}_{\mathrm{p}} - \boldsymbol{\Upsilon}_{\mathrm{p}} (\mathbf{J}_{\mathrm{Ch}} - \mathbf{J}_{\mathrm{Ch},\boldsymbol{\beta}} \mathbf{J}^{-1}_{\boldsymbol{\beta}\boldsymbol{\beta}} \mathbf{J}^{\mathrm{T}}_{\mathrm{Ch},\boldsymbol{\beta}}) \boldsymbol{\Upsilon}_{\mathrm{q}} (\boldsymbol{\Upsilon}_{\mathrm{q}} \mathbf{J}^{\mathrm{e}}_{\mathrm{Ch}} \boldsymbol{\Upsilon}^{\mathrm{T}}_{\mathrm{q}})^{-1} \boldsymbol{\Upsilon}_{\mathrm{q}} \mathbf{J}^{\mathrm{e}}_{\mathrm{Ch}} \boldsymbol{\Upsilon}^{\mathrm{T}}_{\mathrm{p}} \\
&= \boldsymbol{\Upsilon}_{\mathrm{p}} \mathbf{J}^{\mathrm{e}}_{\mathrm{Ch}} \boldsymbol{\Upsilon}^{\mathrm{T}}_{\mathrm{p}} - \boldsymbol{\Upsilon}_{\mathrm{p}} \mathbf{J}^{\mathrm{e}}_{\mathrm{Ch}} \boldsymbol{\Upsilon}_{\mathrm{q}} (\boldsymbol{\Upsilon}_{\mathrm{q}} \mathbf{J}^{\mathrm{e}}_{\mathrm{Ch}} \boldsymbol{\Upsilon}^{\mathrm{T}}_{\mathrm{q}})^{-1} \boldsymbol{\Upsilon}_{\mathrm{q}} \mathbf{J}^{\mathrm{e}}_{\mathrm{Ch}} \boldsymbol{\Upsilon}^{\mathrm{T}}_{\mathrm{p}}, \qquad \text{(D.9)}
\end{aligned}
$$

which is equivalent to (D.4).

D.2 Proof of Proposition 5.2

We start by deriving the EFIM of the location parameters for the m^{th} path. Then, we show that the overall EFIM can be written as a sum of the individual EFIM. For the m^{th} path,

$$
\mathbf{J}^{(m)}_{\mathbf{op},\mathbf{q}_m} = \boldsymbol{\Upsilon}_m \mathbf{J}^{(\mathrm{e},m)}_{\mathrm{ch}} \boldsymbol{\Upsilon}^{\mathrm{T}}_m = \begin{bmatrix} \overline{\boldsymbol{\Upsilon}}_m \mathbf{J}^{(\mathrm{e},m)}_{\mathrm{ch}} \overline{\boldsymbol{\Upsilon}}^{\mathrm{T}}_m & \overline{\boldsymbol{\Upsilon}}_m \mathbf{J}^{(\mathrm{e},m)}_{\mathrm{ch}} \overline{\overline{\boldsymbol{\Upsilon}}}^{\mathrm{T}}_m \\ \overline{\overline{\boldsymbol{\Upsilon}}}_m \mathbf{J}^{(\mathrm{e},m)}_{\mathrm{ch}} \overline{\boldsymbol{\Upsilon}}^{\mathrm{T}}_m & \overline{\overline{\boldsymbol{\Upsilon}}} \mathbf{J}^{(\mathrm{e},m)}_{\mathrm{ch}} \overline{\overline{\boldsymbol{\Upsilon}}}^{\mathrm{T}} \end{bmatrix}. \qquad \text{(D.10)}
$$

Consequently, for $\mathbf{o}$ and $\mathbf{p}$, by Schur's complement,

$$
\mathbf{J}^{(m)}_{\mathbf{o},\mathbf{p}} = \overline{\boldsymbol{\Upsilon}}_m \mathbf{J}^{(\mathrm{e},m)}_{\mathrm{ch}} \overline{\boldsymbol{\Upsilon}}^{\mathrm{T}}_m - \overline{\boldsymbol{\Upsilon}}_m \mathbf{J}^{(\mathrm{e},m)}_{\mathrm{ch}} \overline{\overline{\boldsymbol{\Upsilon}}}^{\mathrm{T}}_m \left(\overline{\overline{\boldsymbol{\Upsilon}}} \mathbf{J}^{(\mathrm{e},m)}_{\mathrm{ch}} \overline{\overline{\boldsymbol{\Upsilon}}}^{\mathrm{T}} \right)^{-1} \overline{\overline{\boldsymbol{\Upsilon}}}_m \mathbf{J}^{(\mathrm{e},m)}_{\mathrm{ch}} \overline{\boldsymbol{\Upsilon}}^{\mathrm{T}}_m. \qquad \text{(D.11)}
$$

Recall that for $m = 1$ the second term above is undefined. For all the M paths, define

$$
\boldsymbol{\Upsilon} \triangleq \begin{bmatrix} \overline{\boldsymbol{\Upsilon}}_1 & \overline{\boldsymbol{\Upsilon}}_2 & \cdots & \overline{\boldsymbol{\Upsilon}}_M \\ \mathbf{0} & \overline{\overline{\boldsymbol{\Upsilon}}}_2 & \cdots & \mathbf{0} \\ \vdots & \vdots & \ddots & \vdots \\ \mathbf{0} & \mathbf{0} & \cdots & \overline{\overline{\boldsymbol{\Upsilon}}}_M \end{bmatrix}, \qquad \mathbf{J}^{\mathrm{e}}_{\boldsymbol{\varphi}_{\mathrm{CH}}} \triangleq \begin{bmatrix} \mathbf{J}^{(\mathrm{e},1)}_{\mathrm{ch}} & \mathbf{0} & \cdots & \mathbf{0} \\ \mathbf{0} & \mathbf{J}^{(\mathrm{e},2)}_{\mathrm{ch}} & \cdots & \mathbf{0} \\ \vdots & \vdots & \ddots & \vdots \\ \mathbf{0} & \mathbf{0} & \cdots & \mathbf{J}^{(\mathrm{e},M)}_{\mathrm{ch}} \end{bmatrix}. \qquad \text{(D.12)}
$$

Then from (5.27),

$$
\mathbf{J}_{\boldsymbol{\varphi}_{\mathrm{L}}} = \boldsymbol{\Upsilon} \mathbf{J}^{\mathrm{e}}_{\boldsymbol{\varphi}_{\mathrm{CH}}} \boldsymbol{\Upsilon}^{\mathrm{T}} = \begin{bmatrix} \sum_{m=1}^{M} \overline{\boldsymbol{\Upsilon}}_m \mathbf{J}^{(\mathrm{e},m)}_{\mathrm{ch}} \overline{\boldsymbol{\Upsilon}}^{\mathrm{T}}_m & \overline{\boldsymbol{\Upsilon}}_2 \mathbf{J}^{(\mathrm{e},2)}_{\mathrm{ch}} \overline{\overline{\boldsymbol{\Upsilon}}}^{\mathrm{T}}_2 & \cdots & \overline{\boldsymbol{\Upsilon}}_M \mathbf{J}^{(\mathrm{e},M)}_{\mathrm{ch}} \overline{\overline{\boldsymbol{\Upsilon}}}^{\mathrm{T}}_M \\ \overline{\overline{\boldsymbol{\Upsilon}}}_2 \mathbf{J}^{(\mathrm{e},2)}_{\mathrm{ch}} \overline{\boldsymbol{\Upsilon}}^{\mathrm{T}}_2 & \overline{\overline{\boldsymbol{\Upsilon}}}_2 \mathbf{J}^{(\mathrm{e},2)}_{\mathrm{ch}} \overline{\overline{\boldsymbol{\Upsilon}}}^{\mathrm{T}}_2 & \cdots & \mathbf{0} \\ \vdots & \vdots & \ddots & \vdots \\ \overline{\overline{\boldsymbol{\Upsilon}}}_M \mathbf{J}^{(\mathrm{e},M)}_{\mathrm{ch}} \overline{\boldsymbol{\Upsilon}}^{\mathrm{T}}_M & \mathbf{0} & \cdots & \overline{\overline{\boldsymbol{\Upsilon}}}_M \mathbf{J}^{(\mathrm{e},M)}_{\mathrm{ch}} \overline{\overline{\boldsymbol{\Upsilon}}}^{\mathrm{T}}_M \end{bmatrix}.
$$

By Schur's Complement and using (D.11), it is easy to verify that

$$\begin{aligned}\widetilde{\mathbf{J}}^{\mathrm{e}}_{\mathbf{o},\mathbf{p}} &= \sum_{m=1}^{M} \overline{\boldsymbol{\Upsilon}}_m \mathbf{J}^{(\mathrm{e},m)}_{\mathrm{ch}} \overline{\boldsymbol{\Upsilon}}^{\mathrm{T}}_m - \sum_{m=2}^{M} \overline{\boldsymbol{\Upsilon}}_m \mathbf{J}^{(\mathrm{e},m)}_{\mathrm{ch}} \overline{\overline{\boldsymbol{\Upsilon}}}^{\mathrm{T}}_m \left(\overline{\overline{\boldsymbol{\Upsilon}}}_m \mathbf{J}^{(\mathrm{e},m)}_{\mathrm{ch}} \overline{\overline{\boldsymbol{\Upsilon}}}^{\mathrm{T}}_m \right)^{-1} \overline{\overline{\boldsymbol{\Upsilon}}}_m \mathbf{J}^{(\mathrm{e},m)}_{\mathrm{ch}} \overline{\boldsymbol{\Upsilon}}^{\mathrm{T}}_m \\ &= \sum_{m=1}^{M} \mathbf{J}^{(m)}_{\mathbf{o},\mathbf{p}}.\end{aligned}$$

Finally, from (5.38), $\mathbf{J}^{(\mathrm{e},m)}_{\mathrm{ch}} = \mathbf{J}^{(m)}_{\mathrm{ch}} - \mathbf{J}^{(m)}_{\mathrm{ch},\beta} \left(\mathbf{J}^{(m)}_{\beta\beta} \right)^{-1} \mathbf{J}^{(m)^{\mathrm{T}}}_{\mathrm{ch},\beta}$. Therefore, it follows that

$$\begin{aligned}\widetilde{\mathbf{J}}^{\mathrm{e}}_{\mathbf{o},\mathbf{p}} \triangleq = \sum_{m=1}^{M} \overline{\boldsymbol{\Upsilon}}_m \mathbf{J}^{(m)}_{\mathrm{ch}} \overline{\boldsymbol{\Upsilon}}^{\mathrm{T}}_m - \underbrace{\sum_{m=1}^{M} \overline{\boldsymbol{\Upsilon}}_m \mathbf{J}^{(m)}_{\mathrm{ch},\beta} \left(\mathbf{J}^{(m)}_{\beta\beta} \right)^{-1} \mathbf{J}^{(m)^{\mathrm{T}}}_{\mathrm{ch},\beta} \overline{\boldsymbol{\Upsilon}}^{\mathrm{T}}_m}_{\text{path gains uncertainty}} \\ \underbrace{- \sum_{m=2}^{M} \overline{\boldsymbol{\Upsilon}}_m \mathbf{J}^{(\mathrm{e},m)}_{\mathrm{ch}} \overline{\overline{\boldsymbol{\Upsilon}}}^{\mathrm{T}}_m \left(\overline{\overline{\boldsymbol{\Upsilon}}} \mathbf{J}^{(\mathrm{e},m)}_{\mathrm{ch}} \overline{\overline{\boldsymbol{\Upsilon}}}^{\mathrm{T}} \right)^{-1} \overline{\overline{\boldsymbol{\Upsilon}}}_m \mathbf{J}^{(\mathrm{e},m)}_{\mathrm{ch}} \overline{\boldsymbol{\Upsilon}}^{\mathrm{T}}_m}_{\text{clusters locations uncertainty}}. \end{aligned} \tag{D.13}$$

Appendix E

Transformation Matrix Entries

We derive the non-zero elements of $\boldsymbol{\Upsilon}$. For the LOS case, it can be shown that

$$\frac{\partial \phi_{\mathrm{UE},1}}{\partial \phi_0} = \frac{-p_x'^2 \cos\theta_0 + (p_y \cos\phi_0 - p_x \sin\phi_0)p_y'}{p_x'^2 + p_y'^2}, \tag{E.1}$$

$$\frac{\partial \phi_{\mathrm{UE},1}}{\partial \theta_0} = -\frac{p_x' p_z'}{p_x'^2 + p_y'^2}, \tag{E.2}$$

$$\frac{\partial \phi_{\mathrm{UE},1}}{\partial \mathbf{p}} = (\mathbf{r}_2\mathbf{r}_1^{\mathrm{T}} - \mathbf{r}_1\mathbf{r}_2^{\mathrm{T}})\frac{\mathbf{p}}{p_x'^2 + p_y'^2}, \tag{E.3}$$

$$\frac{\partial \phi_{\mathrm{BS},1}}{\partial \mathbf{p}} = \frac{[-p_y, p_x, 0]^{\mathrm{T}}}{p_x^2 + p_y^2}, \tag{E.4}$$

$$\frac{\partial \theta_{\mathrm{BS},1}}{\partial \mathbf{p}} = \frac{[p_x p_z, p_y p_z, -(p_x^2 + p_y^2)]^{\mathrm{T}}}{\|\mathbf{p}\|\sqrt{p_x^2 + p_y^2}}, \tag{E.5}$$

$$\frac{\partial \theta_{\mathrm{UE},1}}{\partial \phi_0} = \frac{p_x' \sin\theta_0}{\sqrt{p_x'^2 + p_y'^2}}, \tag{E.6}$$

$$\frac{\partial \theta_{\mathrm{UE},1}}{\partial \theta_0} = -\frac{p_y'}{\sqrt{p_x'^2 + p_y'^2}}, \tag{E.7}$$

$$\frac{\partial \theta_{\mathrm{UE},1}}{\partial \mathbf{p}} = \frac{1}{\sqrt{p_x'^2 + p_y'^2}}\left(\mathbf{r}_3 + \frac{p_z'}{\|\mathbf{p}\|}\mathbf{p}\right). \tag{E.8}$$

$$\frac{\partial \tau_1}{\partial \mathbf{p}} = \frac{\mathbf{p}}{c\|\mathbf{p}\|}, \tag{E.9}$$

where $\mathbf{r}_i, 1 \leq i \leq 3$ is the i^{th} column of $\mathbf{R}(\theta_0, \phi_0)$.

For the NLOS case, we use the similarity in (5.32), (5.34), and (5.36), to obtain,

$\frac{\partial \phi_{\mathrm{UE,m}}}{\partial \phi_0}$, $\frac{\partial \phi_{\mathrm{UE,m}}}{\partial \theta_0}$, $\frac{\partial \phi_{\mathrm{UE,m}}}{\partial \mathbf{p}}$, $\frac{\partial \theta_{\mathrm{UE,m}}}{\partial \phi_0}$, $\frac{\partial \theta_{\mathrm{UE,m}}}{\partial \theta_0}$, $\frac{\partial \theta_{\mathrm{UE,m}}}{\partial \mathbf{p}}$, $\frac{\partial \tau_m}{\partial \mathbf{p}}$ by replacing $\mathbf{p}$ and $\mathbf{p}'$ in (E.1) with $\mathbf{w}_m$ and $\mathbf{w}'_m$, receptively. Note that in NLOS, $\frac{\partial \phi_{\mathrm{BS,m}}}{\partial \mathbf{p}} = \frac{\partial \theta_{\mathrm{BS,m}}}{\partial \mathbf{p}} = 0$. Finally, we obtain the following

$$\frac{\partial \phi_{\mathrm{UE,m}}}{\partial \mathbf{q}_m} = -\frac{\partial \phi_{\mathrm{UE,m}}}{\partial \mathbf{p}}, \tag{E.10}$$

$$\frac{\partial \theta_{\mathrm{UE,m}}}{\partial \mathbf{q}_m} = -\frac{\partial \theta_{\mathrm{UE,m}}}{\partial \mathbf{p}}, \tag{E.11}$$

$$\frac{\partial \phi_{\mathrm{BS,m}}}{\partial \mathbf{q}_m} = \frac{[-q_{m,y}, q_{m,x}, 0]^{\mathrm{T}}}{q_{m,x}^2 + q_{m,y}^2}, \tag{E.12}$$

$$\frac{\partial \theta_{\mathrm{BS,m}}}{\partial \mathbf{q}_m} = \frac{[q_{m,x}q_{m,z}, q_{m,y}q_{m,z}, -(q_{m,x}^2 + q_{m,y}^2)]^{\mathrm{T}}}{\|\mathbf{q}_m\|\sqrt{q_{m,x}^2 + q_{m,y}^2}}, \tag{E.13}$$

$$\frac{\partial \tau_m}{\partial \mathbf{q}_m} = \frac{\mathbf{q}_m}{c\|\mathbf{q}_m\|} - \frac{\mathbf{w}_m}{c\|\mathbf{w}_m\|}, \tag{E.14}$$

$$\mathbf{w}_m \triangleq \mathbf{p} - \mathbf{q}_m \tag{E.15}$$

Appendix F

Closed-form PEB and OEB for LOS-only

F.1 3D localization

To find the LOS SOEB and SPEB in a closed form, we note that

$$\mathbf{J}_{\mathbf{o},\mathbf{p}}^{-1} = \left(\boldsymbol{\Upsilon}\boldsymbol{\Lambda}_1^{\mathrm{e}}\boldsymbol{\Upsilon}^{\mathrm{T}}\right)^{-1} = \left(\boldsymbol{\Upsilon}^{-1}\right)^{\mathrm{T}}\left(\boldsymbol{\Lambda}_1^{\mathrm{e}}\right)^{-1}\boldsymbol{\Upsilon}^{-1} = \left(\frac{\partial\boldsymbol{\varphi}_{\mathrm{L}}^{\mathrm{T}}}{\partial\boldsymbol{\varphi}_{\mathrm{CH}}}\right)^{\mathrm{T}}\left(\boldsymbol{\Lambda}_1^{\mathrm{e}}\right)^{-1}\left(\frac{\partial\boldsymbol{\varphi}_{\mathrm{L}}^{\mathrm{T}}}{\partial\boldsymbol{\varphi}_{\mathrm{CH}}}\right), \tag{F.1}$$

where the rightmost term is obtained by the inverse function theorem [141]. Thus,

$$\mathrm{SPEB} = \mathrm{Tr}\left\{\left(\frac{\partial\mathbf{p}^{\mathrm{T}}}{\partial\boldsymbol{\varphi}_{\mathrm{CH}}}\right)^{\mathrm{T}}\left(\boldsymbol{\Lambda}_1^{\mathrm{e}}\right)^{-1}\left(\frac{\partial\mathbf{p}^{\mathrm{T}}}{\partial\boldsymbol{\varphi}_{\mathrm{CH}}}\right)\right\}. \tag{F.2a}$$

$$\mathrm{SOEB} = \mathrm{Tr}\left\{\left(\frac{\partial\mathbf{o}^{\mathrm{T}}}{\partial\boldsymbol{\varphi}_{\mathrm{CH}}}\right)^{\mathrm{T}}\left(\boldsymbol{\Lambda}_1^{\mathrm{e}}\right)^{-1}\left(\frac{\partial\mathbf{o}^{\mathrm{T}}}{\partial\boldsymbol{\varphi}_{\mathrm{CH}}}\right)\right\}. \tag{F.2b}$$

Dropping the LOS subscript "1" and using spherical coordinates, we write

$$\mathbf{p} = c\tau\left[\cos\phi_{\mathrm{BS}}\sin\theta_{\mathrm{BS}}, \sin\phi_{\mathrm{BS}}\sin\theta_{\mathrm{BS}}, \cos\theta_{\mathrm{BS}}\right]^{\mathrm{T}}. \tag{F.3}$$

For the uplink, $\boldsymbol{\varphi}_{\mathrm{CH}} = [\theta_{\mathrm{BS}}, \theta_{\mathrm{UE}}, \phi_{\mathrm{BS}}, \phi_{\mathrm{UE}}, \tau]^{\mathrm{T}}$ (Section 5.4.1). Therefore, it follows that

$$\left(\frac{\partial\mathbf{p}^{\mathrm{T}}}{\partial\boldsymbol{\varphi}_{\mathrm{CH}}}\right)^{\mathrm{T}} = c\begin{bmatrix} \tau\cos\phi_{\mathrm{BS}}\cos\theta_{\mathrm{BS}} & 0 & -\tau\sin\phi_{\mathrm{BS}}\sin\theta_{\mathrm{BS}} & 0 & \cos\phi_{\mathrm{BS}}\sin\theta_{\mathrm{BS}} \\ \tau\sin\phi_{\mathrm{BS}}\cos\theta_{\mathrm{BS}} & 0 & \tau\cos\phi_{\mathrm{BS}}\sin\theta_{\mathrm{BS}} & 0 & \sin\phi_{\mathrm{BS}}\sin\theta_{\mathrm{BS}} \\ -\tau\sin\theta_{\mathrm{BS}} & 0 & 0 & 0 & \cos\theta_{\mathrm{BS}} \end{bmatrix} \tag{F.4}$$

Defining σ^2_{xx} and $\sigma^2_{xy}, x, y \in \{\theta_{\mathrm{R}}, \theta_{\mathrm{T}}, \phi_{\mathrm{R}}, \phi_{\mathrm{T}}, \tau\}$, as respectively the CRLB of x, and the covariance of x and y, then from Appendix C.1, we can write the uplink EFIM as

$$(\mathbf{\Lambda}_1^{\mathrm{e}})^{-1} = \begin{bmatrix} \sigma^2_{\theta_{\mathrm{BS}}\theta_{\mathrm{BS}}} & 0 & \sigma^2_{\theta_{\mathrm{BS}}\phi_{\mathrm{BS}}} & 0 & 0 \\ 0 & \sigma^2_{\theta_{\mathrm{UE}}\theta_{\mathrm{UE}}} & 0 & \sigma^2_{\theta_{\mathrm{UE}}\phi_{\mathrm{UE}}} & 0 \\ \sigma^2_{\theta_{\mathrm{BS}}\phi_{\mathrm{BS}}} & 0 & \sigma^2_{\phi_{\mathrm{BS}}\phi_{\mathrm{BS}}} & 0 & 0 \\ 0 & \sigma^2_{\theta_{\mathrm{UE}}\phi_{\mathrm{UE}}} & 0 & \sigma^2_{\phi_{\mathrm{UE}}\phi_{\mathrm{UE}}} & 0 \\ 0 & 0 & 0 & 0 & \sigma^2_{\tau\tau} \end{bmatrix}. \tag{F.5}$$

Substituting in (F.2a), and simplifying the results yield

$$\mathrm{SPEB} = \|\mathbf{p}\|^2 \sigma^2_{\theta_{\mathrm{BS}}\theta_{\mathrm{BS}}} + \|\mathbf{p}\|^2 \sin^2\theta_{\mathrm{BS}} \sigma^2_{\phi_{\mathrm{BS}}\phi_{\mathrm{BS}}} + c^2\sigma^2_{\tau\tau}. \tag{F.6}$$

To obtain downlink SPEB, we need to exchange columns 1 and 3 with 2 and 4 in (F.4), respectively, while concurrently swapping the role of BS and UE angles in (F.5). Eventually, this leads to the same SPEB expression in (F.6).

We now focus on the SOEB. From the properties of spherical coordinates,

$$\cos\phi_{\mathrm{UE}} = \frac{p'_x}{\|\mathbf{p}\|\sin\theta_{\mathrm{UE}}} = -\frac{\mathbf{r}_1^{\mathrm{T}}\mathbf{p}}{\|\mathbf{p}\|\sin\theta_{\mathrm{UE}}} \Longrightarrow \cos(\phi_0 - \phi_{\mathrm{BS}}) = -\frac{\cos\phi_{\mathrm{UE}}\sin\theta_{\mathrm{UE}}}{\sin\theta_{\mathrm{BS}}}. \tag{F.7}$$

Differentiating both sides w.r.t to θ_{BS}, we have

$$-\sin(\phi_0 - \phi_{\mathrm{BS}})\frac{\partial\phi_0}{\partial\theta_{\mathrm{BS}}} = -\frac{\cos\phi_{\mathrm{UE}}\sin\theta_{\mathrm{UE}}}{\sin^2\theta_{\mathrm{BS}}}\cos\theta_{\mathrm{BS}}. \tag{F.8}$$

Consequently, using (F.7) we obtain,

$$\frac{\partial\phi_0}{\partial\theta_{\mathrm{BS}}} = \cot\theta_{\mathrm{BS}}\cot(\phi_0 - \phi_{\mathrm{BS}}). \tag{F.9}$$

Similarly, it can be shown that,

$$\frac{\partial\phi_0}{\partial\theta_{\mathrm{UE}}} = \frac{\cos\phi_{\mathrm{UE}}\cos\theta_{\mathrm{UE}}}{\sin\theta_{\mathrm{BS}}\sin(\phi_0 - \phi_{\mathrm{BS}})}, \quad \frac{\partial\phi_0}{\partial\phi_{\mathrm{BS}}} = 1, \quad \frac{\partial\phi_0}{\partial\phi_{\mathrm{UE}}} = -\frac{\sin\phi_{\mathrm{UE}}\sin\theta_{\mathrm{UE}}}{\sin\theta_{\mathrm{BS}}\sin(\phi_0 - \phi_{\mathrm{BS}})}. \tag{F.10}$$

On the other hand, we have

$$\cos\theta_{\mathrm{UE}} = \frac{-\mathbf{r}_3^{\mathrm{T}}\mathbf{p}}{\|\mathbf{p}\|} = \sin\theta_0\sin\theta_{\mathrm{BS}}\sin(\phi_0 - \phi_{\mathrm{BS}}) - \cos\theta_0\cos\theta_{\mathrm{BS}}, \tag{F.11}$$

Similarly, differentiating and simplifying the results yield

$$\frac{\partial\theta_0}{\partial\theta_{\mathrm{BS}}} = \frac{\partial\phi_0}{\partial\theta_{\mathrm{BS}}}\frac{\partial\theta_0}{\partial\phi_{\mathrm{BS}}} - \frac{\tan(\theta_0)\sin(\phi_0-\phi_{\mathrm{BS}})+\tan(\theta_{\mathrm{BS}})}{\tan(\theta_0)+\tan(\theta_{\mathrm{BS}})\sin(\phi_0-\phi_{\mathrm{BS}})}, \tag{F.12a}$$

$$\frac{\partial\theta_0}{\partial\theta_{\mathrm{UE}}} = -\frac{\sin(\theta_{\mathrm{UE}})+\sin(\theta_0)\sin(\theta_{\mathrm{BS}})\cos(\phi_0-\phi_{\mathrm{BS}})\frac{\partial\phi_0}{\partial\theta_{\mathrm{UE}}}}{\sin(\theta_{\mathrm{BS}})\cos(\theta_0)\sin(\phi_0-\phi_{\mathrm{BS}})+\sin(\theta_0)\cos(\theta_{\mathrm{BS}})}, \tag{F.12b}$$

$$\frac{\partial\theta_0}{\partial\phi_{\mathrm{BS}}} = -\frac{\tan(\theta_{\mathrm{BS}})\tan(\theta_0)\cos(\phi_0-\phi_{\mathrm{BS}})}{\tan(\theta_0)+\tan(\theta_{\mathrm{BS}})\sin(\phi_0-\phi_{\mathrm{BS}})}, \tag{F.12c}$$

$$\frac{\partial\theta_0}{\partial\phi_{\mathrm{UE}}} = \frac{\partial\theta_0}{\partial\phi_{\mathrm{BS}}}\frac{\partial\phi_0}{\partial\phi_{\mathrm{UE}}}. \tag{F.12d}$$

Note that both $\frac{\partial\theta_0}{\partial\tau}$ and $\frac{\partial\phi_0}{\partial\tau}$ are zeros. Therefore, SOEB is a weighted sum of the angular bounds. Recalling that $\partial\mathbf{o} = [\partial\theta_0, \partial\phi_0]^{\mathrm{T}}$, SOEB can be written from (F.2b) in the form

$$\begin{aligned}\mathrm{SOEB} = &\left\|\frac{\partial\mathbf{o}}{\partial\theta_{\mathrm{BS}}}\right\|^2\sigma^2_{\theta_{\mathrm{BS}}\theta_{\mathrm{BS}}} + \left\|\frac{\partial\mathbf{o}}{\partial\phi_{\mathrm{BS}}}\right\|^2\sigma^2_{\phi_{\mathrm{BS}}\phi_{\mathrm{BS}}} + 2\left(\frac{\partial\mathbf{o}^{\mathrm{T}}}{\partial\theta_{\mathrm{BS}}}\frac{\partial\mathbf{o}}{\partial\phi_{\mathrm{BS}}}\right)\sigma^2_{\theta_{\mathrm{BS}}\phi_{\mathrm{BS}}} \\ &+ \left\|\frac{\partial\mathbf{o}}{\partial\theta_{\mathrm{UE}}}\right\|^2\sigma^2_{\theta_{\mathrm{UE}}\theta_{\mathrm{UE}}} + \left\|\frac{\partial\mathbf{o}}{\partial\phi_{\mathrm{UE}}}\right\|^2\sigma^2_{\phi_{\mathrm{UE}}\phi_{\mathrm{UE}}} + 2\left(\frac{\partial\mathbf{o}^{\mathrm{T}}}{\partial\theta_{\mathrm{UE}}}\frac{\partial\mathbf{o}}{\partial\phi_{\mathrm{UE}}}\right)\sigma^2_{\theta_{\mathrm{UE}}\phi_{\mathrm{UE}}}.\end{aligned} \tag{F.13}$$

Note that applying the column swapping procedure, described after (F.6), to obtain the downlink SPEB leads to the same expression in (F.13), hence (F.13) is valid for both the uplink and downlink.

F.2 2D Localization:

For the 2D case, $\theta_{\mathrm{BS}} = \theta_{\mathrm{UE}} = \pi/2$. Thus, these two parameters can be removed from the vectors of unknown parameters, setting their CRLB to zero. Therefore, it can be seen that (F.6) and (F.13) reduce to

$$\mathrm{SPEB} = \|\mathbf{p}\|^2\sigma^2_{\phi_{\mathrm{BS}}\phi_{\mathrm{BS}}} + c^2\sigma^2_{\tau\tau}, \tag{F.14}$$

$$\mathrm{SOEB} = \left\|\frac{\partial\mathbf{o}}{\partial\phi_{\mathrm{BS}}}\right\|^2\sigma^2_{\phi_{\mathrm{BS}}\phi_{\mathrm{BS}}} + \left\|\frac{\partial\mathbf{o}}{\partial\phi_{\mathrm{UE}}}\right\|^2\sigma^2_{\phi_{\mathrm{UE}}\phi_{\mathrm{UE}}} \tag{F.15}$$

Note that, using the fact that $\phi_{\mathrm{UE}} + \phi_0 - \phi_{\mathrm{BS}} = \pi$, it can be shown from (F.10) that $\left\|\frac{\partial\mathbf{o}}{\partial\phi_{\mathrm{BS}}}\right\|^2 = \left\|\frac{\partial\mathbf{o}}{\partial\phi_{\mathrm{UE}}}\right\|^2 = 1$, leading to

$$\mathrm{SOEB} = \sigma^2_{\phi_{\mathrm{BS}}\phi_{\mathrm{BS}}} + \sigma^2_{\phi_{\mathrm{UE}}\phi_{\mathrm{UE}}}. \tag{F.16}$$

Appendix G

Derivation of the Elements of $\mathbf{J}_{\boldsymbol{\varphi}_\mathrm{D}}$

Consider backward transmission round. In this case, D_1 has the following observation:

$$\mathbf{y}_1(t) = \sqrt{N_1 N_2 E_\mathrm{t}}\beta \mathbf{W}_1^\mathrm{H}\mathbf{a}_1\mathbf{a}_2^\mathrm{H}\mathbf{F}_2\mathbf{s}_2(t-\tau^\mathrm{b}) + \mathbf{n}_1(t). \tag{G.1}$$

For the case of zero-mean additive correlated Gaussian noise, the FIM of $\boldsymbol{\varphi}_\mathrm{D}$ defined in (6.18), is given by [81]

$$J_{xy}^\mathrm{b} \triangleq \int_0^{T_\mathrm{o}} \Re\left\{\frac{\partial \boldsymbol{\mu}^\mathrm{H}(t)}{\partial x}\mathbf{R}_{\mathrm{n}1}^{-1}\frac{\partial \boldsymbol{\mu}(t)}{\partial y}\right\}\mathrm{d}t, \tag{G.2a}$$

$$\triangleq \frac{1}{N_0}\int_0^{T_\mathrm{o}} \Re\left\{\frac{\partial \boldsymbol{\mu}^\mathrm{H}(t)}{\partial x}\left(\mathbf{W}_1^\mathrm{H}\mathbf{W}_1\right)^{-1}\frac{\partial \boldsymbol{\mu}(t)}{\partial y}\right\}\mathrm{d}t, \tag{G.2b}$$

$$x, y \in \{\theta_1, \phi_1, \theta_2, \phi_2, \beta_\mathrm{R}, \beta_\mathrm{I}, \tau\}$$

where $\boldsymbol{\mu}(t)$ is the mean of the observation vector, and T_o is assumed to be long enough to receive the entire pilot signal.

Consequently, we write

$$\boldsymbol{\mu}(t) = \sqrt{N_1 N_2 E_\mathrm{t}}\beta \mathbf{W}_1^\mathrm{H}\mathbf{a}_1\mathbf{a}_2^\mathrm{H}\mathbf{F}_2\mathbf{s}_2(t-\tau^\mathrm{b}), \tag{G.3}$$

from which we write

$$\frac{\partial \boldsymbol{\mu}(t)}{\partial \theta_1} = \sqrt{N_1 N_2 E_\mathrm{t}}\beta \mathbf{W}_1^\mathrm{H}\mathbf{k}_1\mathbf{a}_2^\mathrm{H}\mathbf{F}_2\mathbf{s}_2(t-\tau^\mathrm{b}),$$
$$\frac{\partial \boldsymbol{\mu}(t)}{\partial \phi_1} = \sqrt{N_1 N_2 E_\mathrm{t}}\beta \mathbf{W}_1^\mathrm{H}\mathbf{p}_1\mathbf{a}_2^\mathrm{H}\mathbf{F}_2\mathbf{s}_2(t-\tau^\mathrm{b}),$$

$$\begin{aligned}
\frac{\partial \boldsymbol{\mu}(t)}{\partial \theta_2} &= \sqrt{N_1 N_2 E_\mathrm{t}}\beta \mathbf{W}_1^\mathrm{H}\mathbf{a}_1\mathbf{k}_2^\mathrm{H}\mathbf{F}_2\mathbf{s}_2(t-\tau^\mathrm{b}),\\
\frac{\partial \boldsymbol{\mu}(t)}{\partial \phi_2} &= \sqrt{N_1 N_2 E_\mathrm{t}}\beta \mathbf{W}_1^\mathrm{H}\mathbf{a}_1\mathbf{p}_2^\mathrm{H}\mathbf{F}_2\mathbf{s}_2(t-\tau^\mathrm{b}),\\
\frac{\partial \boldsymbol{\mu}(t)}{\partial \beta_\mathrm{R}} &= j\frac{\partial \boldsymbol{\mu}(t)}{\partial \beta_\mathrm{R}} = \sqrt{N_1 N_2 E_\mathrm{t}}\mathbf{W}_1^\mathrm{H}\mathbf{a}_1\mathbf{a}_2^\mathrm{H}\mathbf{F}_2\mathbf{s}_2(t-\tau^\mathrm{b}),\\
\frac{\partial \boldsymbol{\mu}(t)}{\partial \tau} &= \sqrt{N_1 N_2 E_\mathrm{t}}\beta \mathbf{W}_1^\mathrm{H}\mathbf{a}_1\mathbf{a}_2^\mathrm{H}\mathbf{F}_2\dot{\mathbf{s}}_2(t-\tau^\mathrm{b}),
\end{aligned}$$

where $\dot{\mathbf{s}}(\tau) \triangleq \frac{\partial \mathbf{s}(\tau)}{\partial \tau}, \mathbf{k}_\mathrm{i} = \frac{\partial}{\partial \theta_i}\mathbf{a}_\mathrm{i}, \mathbf{p}_\mathrm{i} = \frac{\partial}{\partial \phi_i}\mathbf{a}_\mathrm{i}$, such that $i \in \{1,2\}$. Note that the zeros in $\mathbf{J}_{\boldsymbol{\varphi}}^{(\mathrm{b})}$ follow from the facts that

$$\int_0^{T_\mathrm{o}} \mathbf{s}_2^\mathrm{H}(t-\tau^\mathrm{b})\dot{\mathbf{s}}_2(t-\tau^\mathrm{b})\mathrm{d}t = 0, \tag{G.4}$$

and that $\frac{\partial \boldsymbol{\mu}(t)}{\partial \beta_\mathrm{R}}$ and $\frac{\partial \boldsymbol{\mu}(t)}{\partial \beta_\mathrm{I}}$ are orthogonal. On the other hand, noting that

$$\int_0^{T_\mathrm{o}} \mathbf{s}_2(t-\tau^\mathrm{b})\mathbf{s}_2^\mathrm{H}(t-\tau^\mathrm{b})\mathrm{d}t = N_\mathrm{s}\mathbf{I}_{N_\mathrm{B}}, \tag{G.5}$$

and defining the operator $\mathbf{P}_\mathbf{A} \triangleq \mathbf{A}\left(\mathbf{A}^\mathrm{H}\mathbf{A}\right)^{-1}\mathbf{A}^\mathrm{H}$, and $\gamma \triangleq N_1 N_2 N_\mathrm{s} E_\mathrm{t}/N_0$, we can write the following

$$J^\mathrm{b}_{\theta_1\theta_1} = \gamma|\beta|^2\left(\mathbf{a}_2^\mathrm{H}\mathbf{F}_2\mathbf{F}_2^\mathrm{H}\mathbf{a}_2\right)\left(\mathbf{k}_1^\mathrm{H}\mathbf{P}_{\mathbf{W}_1}\mathbf{k}_1\right) \tag{G.6a}$$
$$J^\mathrm{b}_{\phi_1\phi_1} = \gamma|\beta|^2\left(\mathbf{a}_2^\mathrm{H}\mathbf{F}_2\mathbf{F}_2^\mathrm{H}\mathbf{a}_2\right)\left(\mathbf{p}_1^\mathrm{H}\mathbf{P}_{\mathbf{W}_1}\mathbf{p}_1\right) \tag{G.6b}$$
$$J^\mathrm{b}_{\theta_2\theta_2} = \gamma|\beta|^2\left(\mathbf{k}_2^\mathrm{H}\mathbf{F}_2\mathbf{F}_2^\mathrm{H}\mathbf{k}_2\right)\left(\mathbf{a}_1^\mathrm{H}\mathbf{P}_{\mathbf{W}_1}\mathbf{a}_1\right) \tag{G.6c}$$
$$J^\mathrm{b}_{\phi_2\phi_2} = \gamma|\beta|^2\left(\mathbf{p}_2^\mathrm{H}\mathbf{F}_2\mathbf{F}_2^\mathrm{H}\mathbf{p}_2\right)\left(\mathbf{a}_1^\mathrm{H}\mathbf{P}_{\mathbf{W}_1}\mathbf{a}_1\right) \tag{G.6d}$$
$$\begin{aligned}
J^\mathrm{b}_{\beta_\mathrm{R}\beta_\mathrm{R}} &= J^\mathrm{b}_{\beta_\mathrm{I}\beta_\mathrm{I}},\\
&= \gamma|\beta|^2\left(\mathbf{a}_2^\mathrm{H}\mathbf{F}_2\mathbf{F}_2^\mathrm{H}\mathbf{a}_{\mathrm{R}2}\right)\left(\mathbf{a}_1^\mathrm{H}\mathbf{P}_{\mathbf{W}_1}\mathbf{a}_1\right),
\end{aligned} \tag{G.6e}$$
$$J^\mathrm{b}_{\theta_1\phi_1} = \gamma|\beta|^2\left(\mathbf{a}_2^\mathrm{H}\mathbf{F}_2\mathbf{F}_2^\mathrm{H}\mathbf{a}_2\right)\left(\mathbf{p}_1^\mathrm{H}\mathbf{P}_{\mathbf{W}_1}\mathbf{k}_1\right), \tag{G.6f}$$
$$J^\mathrm{b}_{\theta_1\theta_2} = \gamma|\beta|^2\left(\mathbf{k}_2^\mathrm{H}\mathbf{F}_2\mathbf{F}_2^\mathrm{H}\mathbf{a}_2\right)\left(\mathbf{k}_1^\mathrm{H}\mathbf{P}_{\mathbf{W}_1}\mathbf{a}_1\right), \tag{G.6g}$$
$$J^\mathrm{b}_{\theta_1\phi_2} = \gamma|\beta|^2\left(\mathbf{p}_2^\mathrm{H}\mathbf{F}_2\mathbf{F}_2^\mathrm{H}\mathbf{a}_2\right)\left(\mathbf{k}_1^\mathrm{H}\mathbf{P}_{\mathbf{W}_1}\mathbf{a}_1\right), \tag{G.6h}$$
$$J^\mathrm{b}_{\theta_1\beta_\mathrm{R}} = \gamma\Re\left[\beta^*\left(\mathbf{a}_2^\mathrm{H}\mathbf{F}_2\mathbf{F}_2^\mathrm{H}\mathbf{a}_2\right)\left(\mathbf{k}_1^\mathrm{H}\mathbf{P}_{\mathbf{W}_1}\mathbf{a}_1\right)\right], \tag{G.6i}$$
$$J^\mathrm{b}_{\theta_1\beta_\mathrm{I}} = -\gamma\Im\left[\beta^*\left(\mathbf{a}_2^\mathrm{H}\mathbf{F}_2\mathbf{F}_2^\mathrm{H}\mathbf{a}_2\right)\left(\mathbf{k}_1^\mathrm{H}\mathbf{P}_{\mathbf{W}_1}\mathbf{a}_1\right)\right], \tag{G.6j}$$
$$J^\mathrm{b}_{\phi_1\theta_2} = \gamma|\beta|^2\left(\mathbf{k}_2^\mathrm{H}\mathbf{F}_2\mathbf{F}_2^\mathrm{H}\mathbf{a}_2\right)\left(\mathbf{p}_1^\mathrm{H}\mathbf{P}_{\mathbf{W}_1}\mathbf{a}_1\right), \tag{G.6k}$$
$$J^\mathrm{b}_{\phi_1\phi_2} = \gamma|\beta|^2\left(\mathbf{p}_2^\mathrm{H}\mathbf{F}_2\mathbf{F}_2^\mathrm{H}\mathbf{a}_2\right)\left(\mathbf{p}_1^\mathrm{H}\mathbf{P}_{\mathbf{W}_1}\mathbf{a}_1\right), \tag{G.6l}$$

$$J^{\mathrm{b}}_{\phi_1\beta_{\mathrm{R}}} = \gamma\Re\left[\beta^*\left(\mathbf{a}_2^{\mathrm{H}}\mathbf{F}_2\mathbf{F}_2^{\mathrm{H}}\mathbf{a}_2\right)\left(\mathbf{p}_1^{\mathrm{H}}\mathbf{P}_{\mathbf{W}_1}\mathbf{a}_1\right)\right], \tag{G.6m}$$

$$J^{\mathrm{b}}_{\phi_1\beta_{\mathrm{I}}} = -\gamma\Im\left[\beta^*\left(\mathbf{a}_2^{\mathrm{H}}\mathbf{F}_2\mathbf{F}_2^{\mathrm{H}}\mathbf{a}_2\right)\left(\mathbf{p}_1^{\mathrm{H}}\mathbf{P}_{\mathbf{W}_1}\mathbf{a}_1\right)\right], \tag{G.6n}$$

$$J^{\mathrm{b}}_{\theta_2\phi_2} = \gamma|\beta|^2\left(\mathbf{p}_2^{\mathrm{H}}\mathbf{F}_2\mathbf{F}_2^{\mathrm{H}}\mathbf{k}_2\right)\left(\mathbf{a}_1^{\mathrm{H}}\mathbf{P}_{\mathbf{W}_1}\mathbf{a}_1\right), \tag{G.6o}$$

$$J^{\mathrm{b}}_{\theta_2\beta_{\mathrm{R}}} = \gamma\Re\left[\beta^*\left(\mathbf{a}_2^{\mathrm{H}}\mathbf{F}_2\mathbf{F}_2^{\mathrm{H}}\mathbf{k}_2\right)\left(\mathbf{a}_1^{\mathrm{H}}\mathbf{P}_{\mathbf{W}_1}\mathbf{a}_1\right)\right], \tag{G.6p}$$

$$J^{\mathrm{b}}_{\theta_2\beta_{\mathrm{I}}} = -\gamma\Im\left[\beta^*\left(\mathbf{a}_2^{\mathrm{H}}\mathbf{F}_2\mathbf{F}_2^{\mathrm{H}}\mathbf{k}_2\right)\left(\mathbf{a}_1^{\mathrm{H}}\mathbf{P}_{\mathbf{W}_1}\mathbf{a}_1\right)\right], \tag{G.6q}$$

$$J^{\mathrm{b}}_{\phi_2\beta_{\mathrm{R}}} = \gamma\Re\left[\beta^*\left(\mathbf{a}_2^{\mathrm{H}}\mathbf{F}_2\mathbf{F}_2^{\mathrm{H}}\mathbf{p}_2\right)\left(\mathbf{a}_1^{\mathrm{H}}\mathbf{P}_{\mathbf{W}_1}\mathbf{a}_1\right)\right], \tag{G.6r}$$

$$J^{\mathrm{b}}_{\phi_2\beta_{\mathrm{I}}} = -\gamma\Im\left[\beta^*\left(\mathbf{a}_2^{\mathrm{H}}\mathbf{F}_2\mathbf{F}_2^{\mathrm{H}}\mathbf{p}_2\right)\left(\mathbf{a}_1^{\mathrm{H}}\mathbf{P}_{\mathbf{W}_1}\mathbf{a}_1\right)\right]. \tag{G.6s}$$

To compute $J_{\tau\tau}$, in (6.25), we extend the results in Appendix C to write

$$J_{\tau^{\mathrm{b}}} = \frac{1}{4\gamma|\beta|^2\pi^2 W_{\mathrm{eff}}^2\|\mathbf{a}_2^{\mathrm{H}}\mathbf{F}_2\|^2\left(\mathbf{a}_1^{\mathrm{H}}\mathbf{P}_{\mathbf{W}_1}\mathbf{a}_1\right)}, \tag{G.7a}$$

$$J_{\tau^{\mathrm{f}}} = \frac{1}{4\gamma|\beta|^2\pi^2 W_{\mathrm{eff}}^2\|\mathbf{a}_1^{\mathrm{H}}\mathbf{F}_1\|^2\left(\mathbf{a}_2^{\mathrm{H}}\mathbf{P}_{\mathbf{W}_2}\mathbf{a}_2\right)}, \tag{G.7b}$$

Bibliography

[1] S. Gezici and Z. Sahinoglu, "UWB, G,eolocation T,echniques for IEEE, 802.15.4a personal area networks," in *MERL Technical Report, Cambridge, MA*, vol. 2, Aug. 2004.

[2] K. Lerner and B. Lerner, *World of Earth Science: A-L*, ser. Gale virtual reference library. Thomson-Gale, 2003.

[3] The Natural Navigator , "The kamal," Nov 2011, (Accessed: Oct 2017). [Online]. Available: https://www.naturalnavigator.com/news/2011/11/how-to-use-a-kamal

[4] Marine Navigation , "Understanding Marine Sextant Principle, Readings and Maintenance," Oct 2017, (Accessed: Oct 2017). [Online]. Available: https://www.marineinsight.com/marine-navigation/what-is-a-sextant/

[5] C. L. S. Howeth, *History of Communications-Electronics in the United States Navy. Washington, D.C.* Bureau of Ships and Office of Naval History., 1963.

[6] R. J. Danchik, "An overview of transit development," *John Hopkins APL Technical Digest,*, vol. 19, no. 1, pp. 18–26, Nov 1998.

[7] C. J. Hegarty and E. Chatre, "Evolution of the global navigation satellitesystem (gnss)," *Proceedings of the IEEE*, vol. 96, no. 12, pp. 1902–1917, Dec 2008.

[8] J. M. Zagami, S. A. Parl, J. J. Bussgang, and K. D. Melillo, "Providing universal location services using a wireless E911 location network," *IEEE Communications Magazine*, vol. 36, no. 4, pp. 66–71, Apr 1998.

[9] "The nations 911 system," The Federal Communications Commission, (Accessed: Oct 2017). [Online]. Available: https://www.fcc.gov/general/9-1-1-and-e9-1-1-services

[10] U. Bareth, "Privacy-aware and energy-efficient geofencing through reverse cellular positioning," in *2012 8th International Wireless Communications and Mobile Computing Conference (IWCMC)*, Aug 2012, pp. 153–158.

[11] K. Witrisal, S. Hinteregger, J. Kulmer, E. Leitinger, and P. Meissner, "High-accuracy positioning for indoor applications: RFID, UWB, 5G, and beyond," in *2016 IEEE International Conference on RFID (RFID)*, May 2016, pp. 1–7.

[12] F. Zafari, I. Papapanagiotou, and K. Christidis, "Microlocation for internet-of-things-equipped smart buildings," *IEEE Internet of Things Journal*, vol. 3, no. 1, pp. 96–112, Feb 2016.

[13] J. Patterson, "Heliguys guide to geofencing," Feb 2017, (Accessed: Oct 2017). [Online]. Available: https://www.heliguy.com/blog/2017/02/16/heliguys-guide-to-geofencing/

[14] L. Zwirello, M. Janson, C. Ascher, U. Schwesinger, G. F. Trommer, and T. Zwick, "Localization in industrial halls via ultra-wideband signals," in *2010 7th Workshop on Positioning, Navigation and Communication*, March 2010, pp. 144–149.

[15] S. S. Saab and Z. S. Nakad, "A standalone RFID indoor positioning system using passive tags," *IEEE Transactions on Industrial Electronics*, vol. 58, no. 5, pp. 1961–1970, May 2011.

[16] P. Beinschob and C. Reinke, "Advances in 3D data acquisition, mapping and localization in modern large-scale warehouses," in *2014 IEEE 10th International Conference on Intelligent Computer Communication and Processing (ICCP)*, Sept 2014, pp. 265–271.

[17] G. Jayendra, S. Kumarawadu, and L. Meegahapola, "RFID-based anti-theft auto security system with an immobilizer," in *2007 International Conference on Industrial and Information Systems*, Aug 2007, pp. 441–446.

[18] D. Wang and F. M. Ghannouchi, "Handset-based positioning system for injured fireman rescue in wildfire fighting," *IEEE Systems Journal*, vol. 6, no. 4, pp. 603–615, Dec 2012.

[19] S. w. Lee, S. y. Cheng, J. Y. j. Hsu, P. Huang, and C. w. You, "Emergency care management with location-aware services," in *2006 Pervasive Health Conference and Workshops*, Nov 2006, pp. 1–6.

[20] N. Li and G. Chen, "Analysis of a location-based social network," in *2009 International Conference on Computational Science and Engineering*, vol. 4, Aug 2009, pp. 263–270.

[21] L. Jin, X. Long, J. B. D. Joshi, and M. Anwar, "Analysis of access control mechanisms for users' check-ins in location-based social network systems," in *2012 IEEE 13th International Conference on Information Reuse Integration (IRI)*, Aug 2012, pp. 712–717.

[22] A. Jagoe, *Mobile Location Services: The Definitive Guide*, ser. Mobile Location Services: The Definitive Guide. Prentice Hall, 2003.

[23] S. Communications, "White paper: An overview of LTE positioning," Sunnyvale, CA 94089 USA, Tech. Rep., February 2012.

[24] R. Margolies, R. Becker, S. Byers, S. Deb, R. Jana, S. Urbanek, and C. Volinsky, "Can you find me now? evaluation of network-based localization in a 4g lte network," in *IEEE INFOCOM 2017 - IEEE Conference on Computer Communications*, May 2017, pp. 1–9.

[25] H. Rydn, S. M. Razavi, F. Gunnarsson, S. M. Kim, M. Wang, Y. Blankenship, A. Grvlen, and . Busin, "Baseline performance of lte positioning in 3gpp 3d mimo indoor user scenarios," in *2015 International Conference on Location and GNSS (ICL-GNSS)*, June 2015, pp. 1–6.

[26] R. D. Taranto, S. Muppirisetty, R. Raulefs, D. Slock, T. Svensson, and H. Wymeersch, "Location-aware communications for 5G networks: How location information can improve scalability, latency, and robustness of 5G," *IEEE Signal Process. Mag*, vol. 31, no. 6, pp. 102–112, Nov 2014.

[27] P. Zhang, J. Lu, Y. Wang, and Q. Wang, "Cooperative localization in 5G networks: A survey," *ICT Express*, vol. 3, no. 1, pp. 27 – 32, 2017.

[28] A. Dammann, R. Raulefs, and S. Zhang, "On prospects of positioning in 5G," in *2015 IEEE International Conference on Communication Workshop (ICCW)*, June 2015, pp. 1207–1213.

[29] M. Koivisto, M. Costa, J. Werner, K. Heiska, J. Talvitie, K. Leppnen, V. Koivunen, and M. Valkama, "Joint device positioning and clock synchronization in 5g ultra-dense networks," *IEEE Transactions on Wireless Communications*, vol. 16, no. 5, pp. 2866–2881, May 2017.

[30] X. Cui, T. A. Gulliver, J. Li, and H. Zhang, "Vehicle positioning using 5G millimeter-wave systems," *IEEE Access*, vol. 4, pp. 6964–6973, 2016.

[31] H. Wymeersch, G. Seco-Granados, G. Destino, D. Dardari, and F. Tufvesson, "5G mm-wave positioning for vehicular networks,," *IEEE Wireless Communication Magazine*, In Press.

[32] M. A. Khan, N. Saeed, A. W. Ahmad, and C. Lee, "Location awareness in 5G networks using rss measurements for public safety applications," *IEEE Access*, vol. PP, no. 99, pp. 1–1, 2017.

[33] C. Han, X. Zhu, A. Doufexi, and T. Kocak, "Location-aided multi-user beamforming for 60 GHz WPAN systems," in *IEEE 75th Veh Technol. Conf. VTC*, May 2012, pp. 1–5.

[34] N. Akbar, S. Yan, N. Yang, and J. Yuan, "Mitigating pilot contamination through location-aware pilot assignment in massive MIMO networks," in *2016 IEEE Globecom Workshops (GC Wkshps)*, Dec 2016, pp. 1–6.

[35] D. Slock, "Location aided wireless communications," in *2012 5th International Symposium on Communications, Control and Signal Processing*, May 2012, pp. 1–6.

[36] Z. Sahinoglu, . Gezici, Sinan, and I. Guvenc, *Ultra-wideband positioning systems : theoretical limits, ranging algorithms, and protocols.* Cambridge : Cambridge University Press, 2008.

[37] Z. Farid, R. Nordin, and M. Ismail, "Recent advances in wireless indoor localization techniques and system," *Journal of Computer Networks and Communications*, vol. 2013, no. 1, pp. 1–12, 2013.

[38] A. Tahat, G. Kaddoum, S. Yousefi, S. Valaee, and F. Gagnon, "A look at the recent wireless positioning techniques with a focus on algorithms for moving receivers," *IEEE Access*, vol. 4, pp. 6652–6680, 2016.

[39] R. Campos and L. Lovisolo, *RF Positioning: Fundamentals, Applications, and Tools:*, ser. GNSS technology and applications series. Artech House, 2015.

[40] A. Lin, J. Zhang, K. Lu, and W. Zhang, "An efficient outdoor localization method for smartphones," in *2014 23rd International Conference on Computer Communication and Networks (ICCCN)*, Aug 2014, pp. 1–8.

[41] I. Guvenc and C. C. Chong, "A survey on TOA, based wireless localization and NLOS, mitigation techniques," *IEEE Commun. Surveys Tuts.*, vol. 11, no. 3, pp. 107–124, 3rd Quart. 2009.

[42] Y.-T. Chan, W.-Y. Tsui, H.-C. So, and P. chung Ching, "Time-of-arrival based localization under nlos conditions," *IEEE Transactions on Vehicular Technology*, vol. 55, no. 1, pp. 17–24, Jan 2006.

[43] K. Yu and Y. Guo, "Statistical NLOS, identification based on AOA, TOA, and signal strength," *IEEE Transactions on Vehicular Technology*, vol. 58, no. 1, pp. 274–286, Jan. 2009.

[44] S. Mazuelas, F. Lago, J. Blas, A. Bahillo, P. Fernandez, R. Lorenzo, and E. Abril, "Prior NLOS, measurement correction for positioning in cellular wireless networks," *IEEE Transactions on Vehicular Technology*, vol. 58, no. 5, pp. 2585–2591, Jun. 2009.

[45] C. Ma, R. Klukas, and G. Lachapelle, "A nonline-of-sight error-mitigation method for TOA, measurements," *IEEE Transactions on Vehicular Technology*, vol. 56, no. 2, pp. 641–651, Mar. 2007.

[46] Z. Wang and S. A. Zekavat, "Omnidirectional mobile NLOS, identification and localization via multiple cooperative nodes," *IEEE Transactions on Mobile Computing*, vol. 11, no. 12, pp. 2047–2059, Dec. 2012.

[47] M. Wylie-Green and S. Wang, "Robust range estimation in the presence of the non-line-of-sight error," in *Proc. IEEE 54th Vehicular Technology Conference, Fall 2001.*, vol. 1, 2001, pp. 101–105 vol.1.

[48] J. Riba and A. Urruela, "A non-line-of-sight mitigation technique based on ml-detection," in *2004 IEEE International Conference on Acoustics, Speech, and Signal Processing*, vol. 2, May 2004, pp. ii–153–6 vol.2.

[49] Y. Qi, H. Kobayashi, and H. Suda, "Analysis of wireless geolocation in a non-line-of-sight environment," *IEEE Transactions on Wireless Communications*, vol. 5, no. 3, pp. 672–681, March 2006.

[50] S. Venkatesh and R. Buehrer, "A linear programming approach to NLOS, error mitigation in sensor networks," in *Proc. The Fifth International Conference on Information Processing in Sensor Networks*, 2006, pp. 301–308.

[51] K. Yu and Y. Guo, "Improved positioning algorithms for nonline-of-sight environments," *IEEE Transactions on Vehicular Technology*, vol. 57, no. 4, pp. 2342–2353, Jul. 2008.

[52] W. Kim, J. G. Lee, and G. I. Jee, "The interior-point method for an optimal treatment of bias in trilateration location," *IEEE Transactions on Vehicular Technology*, vol. 55, no. 4, pp. 1291–1301, Jul. 2006.

[53] S. Venkatraman, J. Caffery, and H. R. You, "Location using LOS, range estimation in NLOS, environments," in *Proc. IEEE 55th Vehicular Technology Conference, Spring 2002.*, vol. 2, 2002, pp. 856–860 vol.2.

[54] H. Miao, K. Yu, and M. Juntti, "Positioning for NLOS, propagation: Algorithm derivations and C,ramer-R,ao bounds," *IEEE Transactions on Vehicular Technology*, vol. 56, no. 5, pp. 2568–2580, Sep. 2007.

[55] P. C. Chen, "A non-line-of-sight error mitigation algorithm in location estimation," in *Proc. IEEE Wireless Communications and Networking Conference, 1999.*, Sep. 1999, pp. 316–320.

[56] J. Caffery, *Wireless Location in CDMA Cellular Radio Systems*, ser. The Springer International Series in Engineering and Computer Science. Springer US, 2006.

[57] J. Zheng and Y. C. Wu, "Joint time synchronization and localization of an unknown node in wireless sensor networks," *IEEE Transactions on Signal Processing*, vol. 58, no. 3, pp. 1309–1320, March 2010.

[58] H. Van Trees, *Detection, Estimation, and Modulation Theory, Optimum Array Processing. Part IV*, ser. Detection, Estimation, and Modulation Theory. Wiley, 2002.

[59] M. Athanassios, *Beamforming: Sensor Signal Processing For Defence Applications*, ser. Communications And Signal Processing. World Scientific Publishing Company, 2015.

[60] N. Fistas and A. Manikas, "A new general global array calibration method," in *Acoustics, Speech, and Signal Processing, 1994. ICASSP-94., 1994 IEEE International Conference on*, vol. iv, Apr 1994, pp. IV/73–IV/76 vol.4.

[61] F. Boccardi, R. W. Heath, A. Lozano, T. L. Marzetta, and P. Popovski, "Five disruptive technology directions for 5G," *IEEE Communications Magazine*, vol. 52, no. 2, pp. 74–80, February 2014.

[62] Z. Pi and F. Khan, "An introduction to millimeter-wave mobile broadband systems," *IEEE Commun. Mag*, vol. 49, no. 6, pp. 101–107, June 2011.

[63] T. S. Rappaport, S. Sun, R. Mayzus, H. Zhao, Y. Azar, K. Wang, G. N. Wong, J. K. Schulz, M. Samimi, and F. Gutierrez, "Millimeter wave mobile commun. for 5G cellular: It will work!" *IEEE Access*, vol. 1, pp. 335–349, 2013.

[64] R. W. Heath, N. Gonzlez-Prelcic, S. Rangan, W. Roh, and A. M. Sayeed, "An overview of signal processing techniques for millimeter wave mimo systems," *IEEE J. Sel. Topics in Signal Process.*, vol. 10, no. 3, pp. 436–453, April 2016.

[65] J. G. Andrews, S. Buzzi, W. Choi, S. V. Hanly, A. Lozano, A. Soong, and J. C. Zhang, "What will 5G be?" *IEEE J. Sel. Areas Commun.*, vol. 32, no. 6, pp. 1065–1082, June 2014.

[66] M. Akdeniz, Y. Liu, M. Samimi, S. Sun, S. Rangan, T. Rappaport, and E. Erkip, "Millimeter wave channel modeling and cellular capacity evaluation," *IEEE Journal on Selected Areas in Commun.*, vol. 32, no. 6, pp. 1164–1179, June 2014.

[67] M. K. Samimi and T. S. Rappaport, "3-d millimeter-wave statistical channel model for 5G wireless system design," *IEEE Transactions on Microwave Theory and Techniques*, vol. 64, no. 7, pp. 2207–2225, July 2016.

[68] K. Witrisal, P. Meissner, E. Leitinger, Y. Shen, C. Gustafson, F. Tufvesson, K. Haneda, D. Dardari, A. F. Molisch, A. Conti, and M. Z. Win, "High-accuracy localization for assisted living: 5G systems will turn multipath channels from foe to friend," *IEEE Signal Process. Mag*, vol. 33, no. 2, pp. 59–70, March 2016.

[69] F. Guidi, A. Guerra, D. Dardari, A. Clemente, and R. D'Errico, "Environment mapping with millimeter-wave massive arrays: System design and performance," in *2016 IEEE Globecom Workshops (GC Wkshps)*, Dec 2016, pp. 1–6.

[70] B. Ma, B. Niu, Z. Wang, and V. W. S. Wong, "Joint power and channel allocation for multimedia content delivery using millimeter wave in smart home networks," in *2014 IEEE Global Communications Conference*, Dec 2014, pp. 4745–4750.

[71] J. C. Aviles and A. Kouki, "Position-aided mm-wave beam training under NLOS conditions," *IEEE Access*, vol. 4, pp. 8703–8714, 2016.

[72] M. Giordani, M. Mezzavilla, C. N. Barati, S. Rangan, and M. Zorzi, "Comparative analysis of initial access techniques in5G mmWave cellular networks," in *2016 Annual Conf. on Information Science and Systems (CISS)*, March 2016, pp. 268–273.

[73] S. P. Rao, I. Oliver, S. Holtmanns, and T. Aura, "We know where you are!" in *2016 8th International Conference on Cyber Conflict (CyCon)*, May 2016, pp. 277–293.

[74] T. 3rd Generation Partnership Project (3GPP), "First 5G NR specs approved," December 2017, (Accessed: April 2018). [Online]. Available: https://www.3gpp.org/news-events/3gpp-news/1929-nsa_nr_5g

[75] A. Manikas, *Differential Geometry in Array Processing*. Imperial College Press, 2004.

[76] C. Balanis and P. Ioannides, "Introduction to smart antennas," *Synthesis Lectures on Antennas*, vol. 5, pp. 1–179, 1 2007.

[77] D. H. Johnson and D. E. Dudgeon, *Array Signal Processing: Concepts and Techniques*. Simon & Schuster, 1992.

[78] C. Burrus and S. Pillai, *Array Signal Processing*, ser. Signal Processing and Digital Filtering. Springer New York, 2012.

[79] J. Benesty, I. Cohen, and J. Chen, *Fundamentals of Signal Enhancement and Array Signal Processing*, ser. Wiley - IEEE. Wiley, 2017.

[80] H. Krim and M. Viberg, "Two decades of array signal processing research: the parametric approach," *IEEE Signal Processing Magazine*, vol. 13, no. 4, pp. 67–94, Jul 1996.

[81] S. Kay, *Fundamentals of Statistical Signal Processing: Estimation theory*, 1st ed., ser. Fundamentals of Statistical Signal Processing, 1st Ed. Englewood Cliffs, N.J.: Prentice-Hall, 1993.

[82] H. Van Trees and K. Bell, *Detection Estimation and Modulation Theory*, ser. Detection Estimation and Modulation Theory. John Wiley & Sons, 2011, no. pt. 1.

[83] H. Poor, *An Introduction to Signal Detection and Estimation*, ser. Springer Texts in Electrical Engineering. Springer New York, 2013.

[84] Y. Shen and M. Z. Win, "Fundamental limits of wideband localization – part I: A general framework," *IEEE Trans. on Inf. Theory*, vol. 56, no. 10, pp. 4956–4980, Oct 2010.

[85] ——, "On the accuracy of localization systems using wideband antenna arrays," *IEEE Transactions on Communications*, vol. 58, no. 1, pp. 270–280, January 2010.

[86] J. Caffery and G. Stuber, "Overview of radiolocation in CDMA, cellular systems," *IEEE Communications Magazine*, vol. 36, no. 4, pp. 38–45, Apr. 1998.

[87] Y. T. Chan, H. Y. C. Hang, and P. C. Ching, "Exact and approximate maximum likelihood localization algorithms," *IEEE Transactions on Vehicular Technology*, vol. 55, no. 1, pp. 10–16, Jan. 2006.

[88] C. Chang and A. Sahai, "Estimation bounds for localization," in *First Annual IEEE Communications Society Conference on Sensor and Ad Hoc Communications and Networks,*, Oct. 2004, pp. 415–424.

[89] G. L. Sun and W. Guo, "Bootstrapping M,-estimators for reducing errors due to non-line-of-sight (NLOS,) propagation," *Communications Letters, IEEE*, vol. 8, no. 8, pp. 509–510, Aug. 2004.

[90] S. Yousefi, X. W. Chang, and B. Champagne, "Distributed cooperative localization in wireless sensor networks without NLOS, identification," in *11th Workshop on Positioning, Navigation and Communication (WPNC), 2014*, Mar. 2014, pp. 1–6.

[91] T. Qiao and H. Liu, "Improved least median of squares localization for non-line-of-sight mitigation," *IEEE Communications Letters*, vol. 18, no. 8, pp. 1451–1454, Aug. 2014.

[92] F. Yin, C. Fritsche, F. Gustafsson, and A. Zoubir, "EM,- and JMAP-ML, based joint estimation algorithms for robust wireless geolocation in mixed LOS,/NLOS, environments," *IEEE Transactions on Signal Processing*, vol. 62, no. 1, pp. 168–182, Jan. 2014.

[93] ——, "TOA,-based robust wireless geolocation and C,ramer-R,ao L,ower B,ound analysis in harsh LOS,/NLOS, environments," *IEEE Transactions on Signal Processing*, vol. 61, no. 9, pp. 2243–2255, May 2013.

[94] Y. Xie, Y. Wang, P. Zhu, and X. You, "Grid-search-based hybrid TOA/AOA, location techniques for NLOS, environments," *IEEE Communications Letters*, vol. 13, no. 4, pp. 254–256, Apr. 2009.

[95] B. Sieskul, F. Zheng, and T. Kaiser, "A hybrid SS-TOA, wireless NLOS, geolocation based on path attenuation: TOA, estimation and CRB, for mobile position estimation," *IEEE Transactions on Vehicular Technology*, vol. 58, no. 9, pp. 4930–4942, Nov. 2009.

[96] J. Borras, P. Hatrack, and N. Mandayam, "Decision theoretic framework for NLOS, identification," in *Proc. 48th IEEE Vehicular Technology Conference*, vol. 2, May 1998, pp. 1583–1587 vol. 2.

[97] L. Greenstein, V. Erceg, Y. Yeh, and M. Clark, "A new path-gain/delay-spread propagation model for digital cellular channels," *IEEE Transactions on Vehicular Technology*, vol. 46, no. 2, pp. 477–485, May 1997.

[98] A channel model for positioning. Coperation europenne dans le domaine de la recherche Scientifique et Technique (COST). (2014, Dec.). [Online]. Available: http://www.lx.it.pt/cost259/g98_20.htm

[99] A. F. Molisch, H. Asplund, R. Heddergott, M. Steinbauer, and T. Zwick, "The cost259 directional channel model-part i: Overview and methodology,"

IEEE Transactions on Wireless Communications, vol. 5, no. 12, pp. 3421–3433, December 2006.

[100] H. Asplund, A. A. Glazunov, A. F. Molisch, K. I. Pedersen, and M. Steinbauer, "The cost 259 directional channel model-part ii: Macrocells," *IEEE Transactions on Wireless Communications*, vol. 5, no. 12, pp. 3434–3450, December 2006.

[101] Z. Deng, Y. Yu, W. Guan, and L. He, "NLOS, error mitigation based on modified kaiman filter for mobile location in cellular networks," in *Proc. Int. Conf. on Wireless Communications and Signal Processing (WCSP)*, Oct. 2010, pp. 1–5.

[102] D. Tse and P. Viswanath, *Fundamentals of Wireless Communication*, 1st ed. Cambridge University Press, 2005.

[103] A. L. Garcia, *Probability and Random Processes for Electrical Engineering*, 2nd ed. Addison-Wesley Publishing, New York, 1994.

[104] A. W. Bowman and A. Azzalini., *Applied Smoothing Techniques for Data Analysis*. Oxford University Press Inc., New York, 1997.

[105] M. Hlynka and D. Loach. "G,enerating uniform random points in a regular n–sided polygon". Windsor Math and Statistics Report. (2013, Dec.). [Online]. Available: http://web2.uwindsor.ca/math/hlynka/Ngon.pdf

[106] O. Orhan, E. Erkip, and S. Rangan, "Low power analog-to-digital conversion in millimeter wave systems: Impact of resolution and bandwidth on performance," in *IEEE Inf Theory and App. Workshop (ITA), 2015*, Feb 2015, pp. 191–198.

[107] S. Sun, G. R. MacCartney, M. K. Samimi, and T. S. Rappaport, "Synthesizing omnidirectional antenna patterns, received power and path loss from directional antennas for 5G millimeter-wave commun." in *IEEE Global Commun. Conf. (GLOBECOM) 2015*, 2015, pp. 1–7.

[108] X. Yang, W. Jiang, and B. Vucetic, "A random beamforming technique for omnidirectional coverage in multiple-antenna systems," *IEEE Trans. on Veh Technol.*, vol. 62, no. 3, pp. 1420–1425, March 2013.

[109] G. Lee, Y. Sung, and J. Seo, "Randomly-directional beamforming in millimeter-wave multiuser miso downlink," *IEEE Trans. on Wireless Commun.*, vol. 15, no. 2, pp. 1086–1100, Feb 2016.

[110] G. Lee, Y. Sung, and M. Kountouris, "On the performance of random beamforming in sparse millimeter wave channels," *IEEE J. Sel. Topics Signal Process.*, vol. PP, no. 99, pp. 1–1, 2016.

[111] J. Chung, C.-S. Hwang, K. Kim, and Y. K. Kim, "A random beamforming technique in MIMO systems exploiting multiuser diversity," *IEEE J. Sel. Areas in Commun.*, vol. 21, no. 5, pp. 848–855, June 2003.

[112] V. Raghavan, J. Cezanne, S. Subramanian, A. Sampath, and O. Koymen, "Beamforming tradeoffs for initial UE discovery in millimeter-wave mimo systems," *IEEE J. Sel. Topics Signal Process.*, vol. 10, no. 3, pp. 543–559, April 2016.

[113] A. Guerra, F. Guidi, and D. Dardari, "Position and orientation error bound for wideband massive antenna arrays," in *2015 IEEE Int. Conf. on Commun. Workshop (ICCW)*, June 2015, pp. 853–858.

[114] A. Shahmansoori, G. E. Garcia, G. Destino, G. Seco-Granados, and H. Wymeersch, "5G position and orientation estimation through millimeter wave MIMO," in *Proc. IEEE Global Commun. Conf. (GLOBECOM) Workshops, 2015*, Dec 2015.

[115] S. Lin, K. B. Ng, H. Wong, K. M. Luk, S. S. Wong, and A. S. Y. Poon, "A 60GHz digitally controlled rf beamforming array in 65nm CMOS with off-chip antennas," in *Radio Frequency Integrated Circuits Symp. (RFIC), 2011 IEEE*, June 2011, pp. 1–4.

[116] A. S. Y. Poon and M. Taghivand, "Supporting and enabling circuits for antenna arrays in wireless commun." *Proc. of the IEEE*, vol. 100, no. 7, pp. 2207–2218, July 2012.

[117] H. Deng and A. Sayeed, "Mm-wave MIMO channel modeling and user localization using sparse beamspace signatures," in *IEEE 15th Int. Workshop on Signal Process. Advances in Wireless Commun. (SPAWC), 2014*, June 2014, pp. 130–134.

[118] N. Garcia, H. Wymeersch, E. G. Ström, and D. Slock, "Location-aided mm-wave channel estimation for vehicular communication," in *IEEE 17th Int. Workshop on Signal Process. Advances in Wireless Commun.*, July 2016, pp. 1–5.

[119] L. S. Muppirisetty, T. Svensson, and H. Wymeersch, "Spatial wireless channel prediction under location uncertainty," *IEEE Trans. on Wireless Commun.*, vol. 15, no. 2, pp. 1031–1044, Feb 2016.

[120] J. Li, J. Conan, and S. Pierre, "Joint estimation of channel parameters for MIMO communication systems," in *2nd Int. Symp. on Wireless Commun. Systems*, Sept 2005, pp. 22–26.

[121] M. D. Larsen, A. L. Swindlehurst, and T. Svantesson, "Performance bounds for MIMO-OFDM channel estimation," *IEEE Trans. Signal Process.*, vol. 57, no. 5, pp. 1901–1916, May 2009.

[122] Y. Shen and M. Z. Win, "Performance of localization and orientation using wideband antenna arrays," in *2007 IEEE International Conference on Ultra-Wideband*, Sept 2007, pp. 288–293.

[123] ——, "On the accuracy of localization systems using wideband antenna arrays," *IEEE Trans. on Commun.*, vol. 58, no. 1, pp. 270–280, Jan 2010.

[124] Y. Shen, H. Wymeersch, and M. Z. Win, "Fundamental limits of wideband localization – part II: Cooperative networks," *IEEE Trans. on Info Theory*, vol. 56, no. 10, pp. 4981–5000, Oct 2010.

[125] A. Shahmansoori, G. E. Garcia, G. Destino, G. Seco-Granados, and H. Wymeersch, "Position and orientation estimation through millimeter-wave mimo in 5g systems," *IEEE Transactions on Wireless Communications*, vol. 17, no. 3, pp. 1822–1835, March 2018.

[126] Y. Han, Y. Shen, X. P. Zhang, M. Z. Win, and H. Meng, "Performance limits and geometric properties of array localization," *IEEE Trans. on Inf. Theory*, vol. 62, no. 2, pp. 1054–1075, Feb 2016.

[127] A. Guerra, F. Guidi, and D. Dardari, "Single anchor localization and orientation performance limits using massive arrays: MIMO vs. beamforming," 2017. [Online]. Available: https://arxiv.org/abs/1702.01670

[128] M. Fakharzadeh, M. R. Nezhad-Ahmadi, B. Biglarbegian, and J. Ahmadi-Shokouh, "CMOS phased array transceiver technology for 60 GHz wireless applications," *IEEE Trans. Antennas Propag.*, vol. 58, no. 4, pp. 1093–1104, April 2010.

[129] V. Venkateswaran and A. J. van der Veen, "Analog beamforming in MIMO communications with phase shift networks and online channel estimation," *IEEE Trans. Signal Process.*, vol. 58, no. 8, pp. 4131–4143, Aug 2010.

[130] J. Wilkinson, "Almost diagonal matrices with multiple or close eigenvalues," *Linear Algebra and its Applications*, vol. 1, no. 1, pp. 1–12, Jan 1968.

[131] Y. Shen and M. Z. Win, "Effect of path-overlap on localization accuracy in dense multipath environments," in *2008 IEEE Int. Conf. on Commun*, May 2008, pp. 4197–4202.

[132] E. Leitinger, P. Meissner, C. Rdisser, G. Dumphart, and K. Witrisal, "Evaluation of position-related information in multipath components for indoor positioning," *IEEE J. Sel. Areas Commun.*, vol. 33, no. 11, pp. 2313–2328, Nov 2015.

[133] J. Vince, *Rotation Transforms for Computer Graphics*. Springer London, 2011.

[134] C. Gentner, T. Jost, W. Wang, S. Zhang, A. Dammann, and U. C. Fiebig, "Multipath assisted positioning with simultaneous localization and mapping," *IEEE Trans. on Wireless Commun.*, vol. 15, no. 9, pp. 6104–6117, Sept 2016.

[135] D. Fan, F. Gao, G. Wang, Z. Zhong, and A. Nallanathan, "Angle domain signal processing-aided channel estimation for indoor 60-GHz TDD/FDD massive MIMO systems," *IEEE J. Sel. Areas Commun.*, vol. 35, no. 9, pp. 1948–1961, 2017.

[136] Z. Abu-Shaban, X. Zhou, T. Abhayapala, G. Seco-Granados, and H. Wymeersch, "Error bounds for uplink and downlink 3D localization in 5G mmwave systems," *Accepted at IEEE Transactions on Wireless Communications*, April 2018.

[137] M. Pelka, D. Amann, M. Cimdins, and H. Hellbriick, "Evaluation of time-based ranging methods: Does the choice matter?" in *2017 14th Workshop on Positioning, Navigation and Communications (WPNC)*, Oct 2017, pp. 1–6.

[138] J.-Y. Lee and R. A. Scholtz, "Ranging in a dense multipath environment using an UWB radio link," *IEEE Journal on Selected Areas in Communications*, vol. 20, no. 9, pp. 1677–1683, Dec 2002.

[139] N. A. H. Duisterwinkel, Erik H. A.and Puts and H. J. Wörtche, "Asymmetric multi-way ranging for resource-limited nodes," in *Ad Hoc Networks*, Y. Zhou and T. Kunz, Eds. Cham: Springer International Publishing, 2017, pp. 50–63.

[140] V. Sark, E. Grass, and J. Gutirrez, "Multi-way ranging with clock offset compensation," in *2015 Advances in Wireless and Optical Communications (RTUWO)*, Nov 2015, pp. 68–71.

[141] W. Fleming, *Functions of Several Variables*. Springer New York, 1987.